# DESIGN AND IMPLEMENTATION OF DISPERSIVE PHOTONIC NANOSTRUCTURES

A Thesis
Presented to
The Academic Faculty

by

**Babak Momeni**

In Partial Fulfillment
of the Requirements for the Degree
Doctor of Philosophy in Electrical and Computer Engineering


Georgia Institute of Technology
August 2007

# DESIGN AND IMPLEMENTATION OF DISPERSIVE PHOTONIC NANOSTRUCTURES

Approved by:


Dr. Ali Adibi, Advisor
School of Electrical and Computer Engineering
*Georgia Institute of Technology*

Dr. Thomas K. Gaylord
School of Electrical and Computer Engineering
*Georgia Institute of Technology*

Dr. John A. Buck
School of Electrical and Computer Engineering
*Georgia Institute of Technology*

Dr. Glenn S. Smith
School of Electrical and Computer Engineering
*Georgia Institute of Technology*

Dr. W. Russell Callen, Jr.
School of Electrical and Computer Engineering
*Georgia Institute of Technology*

Dr. Rick Trebino
School of Physics
*Georgia Institute of Technology*


Date Approved: June 26, 2007

To my parents.

# ACKNOWLEDGEMENTS

I wish to thank Prof. Ali Adibi for his guidance, support, and encouragement. He and his family have been more than hospitable during these years, and I am sincerely thankful for that. I appreciate the great opportunity I had to enjoy the vision of my friends, Mohammad, Saman, and Reza, in different aspects of life and research, and I am sincerely grateful for the rewarding discussions we have had. I would like to thank Omid and Arash for always being there for me, and for always offering a helping hand. I am deeply grateful to JD and Siva for teaching me everything I know about experimental characterization and for their professional manners and research ethics. I would like to express my gratitude to Charles, Majid, Ehsan, Saeed, Murtaza, Amir Hossein, and Maysam for their friendship and for their help and support. I am also grateful for the privilege to work with a wonderful group of colleagues, including Mehdi, Ning, Sina, Jerry, Cheryl, Fengtao, Henry, Pouyan, Charlie, Ye, Ali, Qing, and Elric. I would like to acknowledge my other friends in Georgia Tech, in particular, Reza Sarvari, Nazanin Rahnavard, Reza Abdolvand, Pablo Gabolde, Pedram Javanmard, David Lindberg, and Baabak Ashuri, for making it an enjoyable experience to live here.

I also would like to sincerely thank the faculty of Georgia Tech, especially, Prof. Thomas K. Gaylord, Prof. Glenn S. Smith, Prof. John A. Buck, Prof. T. A. Brian Kennedy, Prof. Rick Trebino, Prof. W. Russell Callen Jr, Prof. William D. Hunt, Prof. Mei-Yin Chou, and Prof. Gee–Kung Chang, for their exemplary attitude both inside and outside the class. Finally, I especially would like to thank my family. Without their love and support I would not be here.

# TABLE OF CONTENTS

# LIST OF TABLES

# LIST OF FIGURES

# LIST OF SYMBOLS AND ABBREVIATIONS

| | |
|---|---|
| $a$ | Lattice constant of the photonic crystal |
| $\alpha$ | Angle of incidence |
| $\beta$ | Divergence ratio threshold for a beam excited inside a photonic crystal |
| $C$ | Compactness factor measure for wavelength demultiplexing devices |
| $C_{dc}$ | Compactness factor for demultiplexing in the diffraction compensation scheme |
| $\delta$ | Divergence angle of the optical beam inside the photonic crystal |
| $\Delta\alpha$ | Divergence angle of the incident beam |
| $E$ | Required input collimation measure for wavelength demultiplexing devices |
| $H_X$ | Limiting cross-talk parameter (Table 4.1) |
| $\eta$ | Coordinate along the direction of propagation for an optical beam |
| $K_X$ | Multiplicative cross-talk parameter (Table 4.1) |
| $\mathbf{K}$ | Reciprocal lattice vector of the photonic crystal |
| $L$ | Propagation length inside the demultiplexing region in superprism devices |
| $L_{pre}$ | Equivalent preconditioning propagation length for diffraction compensation |
| $\lambda$ | Free-space wavelength |
| $n_1$ | Refractive index of the incident region |
| $n_e$ | Effective diffractive index of periodic structures (second-order) |
| $n_{ei}$ | Generalized effective diffractive index ($i^{th}$-order; $i$ = 1,2,3,…) |
| $\theta_g$ | Angle of group velocity for a photonic crystal mode with respect to the direction normal to the interface |
| $\Theta$ | Difference between angles of propagation of adjacent wavelength channels in a superprism-based demultiplexer |
| $r$ | Radius of holes in a PC |

| | |
|---|---|
| $w_1$ | Half of the transfer-limited spot size of a Gaussian beam |
| $\omega_n$ | Normalized frequency, $a/\lambda$ |
| $X$ | Tolerable cross-talk level in a wavelength demultiplexer |
| $\xi$ | Coordinate transverse to the direction of propagation for an optical beam |
| $\psi$ | Ratio of angular separation between adjacent wavelength channels to the divergence angle of each channel in a superprism-based demultiplexer |
| $z_i$ | Rayleigh range of a Gaussian beam subject to $i^{th}$-order diffraction effects |
| 1D | One Dimensional |
| 2D | Two Dimensional |
| 3D | Three Dimensional |
| AWG | Arrayed Waveguide Grating |
| DAQ | Data Acquisition |
| DBR | Distributed Bragg Reflector |
| DUT | Device under Test |
| DWDM | Dense Wavelength Division Multiplexing |
| EASFF | Equal Angular Separation with Flexible Frequencies |
| EASSF | Equal Angular Separation with Specific Frequencies |
| EFSSF | Equal Frequency Separation with Specific Frequencies |
| FBG | Fiber Bragg Grating |
| FDTD | Finite Difference Time Domain |
| GRIN | Graded Refractive Index |
| ICP | Inductively Coupled Plasma |
| IR | Infrared |
| MBIL | Multi-Beam Interference Lithography |
| MPL | Multi-Photon Lithography |

| | |
|---|---|
| MST | Multiple Scattering Theorem |
| PBG | Photonic Bandgap |
| PC | Photonic Crystal |
| PCW | Photonic Crystal Waveguide |
| PWE | Plane Wave Expansion |
| RMS | Root Mean Square |
| SEM | Scanning Electron Microscopy |
| SMF | Single Mode Fiber |
| SOI | Silicon on Insulator |
| TD-BPM | Time Domain Beam Propagation Method |
| TE | Transverse Electric |
| TM | Transverse Magnetic |
| UC | Unit Cell |
| VCSEL | Vertical Cavity Surface Emitting Laser |
| WD | Wavelength Demultiplexing |
| WDM | Wavelength Division Multiplexing |
| WKB | Wentzel-Kramers-Brillouin |

# SUMMARY

Photonic crystals (PCs), consisting of a periodic pattern of variations in the material properties, are one of the platforms proposed as “synthetic” optical materials to meet the need for optical materials with desired properties. Recently, applications based on dispersive properties of the PCs have been proposed in which PCs are envisioned as optical materials with controllable dispersive properties. Unlike the conventional use of PCs to achieve localization, in these new applications propagation inside the photonic crystal is studied, and their dispersive properties are utilized. Among these applications, the possibility of demultiplexing light using the superprism effect is of particular interest.

Possibility of integration and compactness are two main advantages of PC-based wavelength demultiplexers compared to other demultiplexing techniques, for applications including compact spectrometers (for sensing applications), demultiplexers (for communications), and spectral analysis (for information processing systems). I develop the necessary simulation tools to study the dispersive properties of photonic crystals. In particular, I will focus on superprism-based demultiplexing in PCs, and I will define a phenomenological model to describe different effects in these structures and to study important parameters and trends. A systematic method for the optimization and design of these structures will be presented. Implementations of these structures will be experimentally demonstrated using the devices fabricated in a planar SOI platform based on designed parameters. In the next step, different approaches to improve the performance of these devices (for better resolution and lower insertion loss) will be studied, and extension of the concepts to other material platforms will be discussed.

# CHAPTER 1

# INTRODUCTION

In their quest to understand and control the nature, human beings have used different means and investigated different approaches. Among these approaches, the ones related to light, because of their close connection to "observation," have always been at the center of attention. In addition, recent technological developments have found other ways to utilize light and have extended the scope of applications. The demand for higher processing speed and higher transmission capacity, in particular, has been the motivation behind the attention toward optical systems as a viable choice in applications such as communications (telecom) [1,2] and interconnects (datacom) [2] in recent years. Different methods and material-systems for realization of desired optical systems for these applications have been proposed, and this thesis will focus on a particular set of systems relying on the dispersive properties of optical materials with submicron and nanoscale features.

## 1.1. Introduction to Photonic Crystals

A basic step in designing optical devices for different applications is to have the optical material with appropriate properties available. For years, the optical materials used in making optical devices were limited to those that were naturally available in the environment. Purification, crystallization, and more recently doping and making polymers are the main methods through which some of the optical materials have been modified to match the characteristics of interest for specific applications. But, until recently, the extent of modification obtained through such schemes has been very limited. Advances in fabrication technology in the last few years, however, have brought the

opportunity to manufacture feature sizes much smaller than the optical wavelength of operation. It has been shown that such feature sizes can greatly affect the optical properties of the material. Concepts similar to “artificial dielectrics” that were suggested and used in the microwave range to create dielectrics with controllable properties were extended then, by the progress in the fabrication techniques, to optical frequencies. This new possibility has resulted in a relatively new field of “synthetic” optical materials in which the optical properties are manipulated by controlling small-scale (tens to hundreds of nanometer) features in a material. The goal is to develop a systematic approach to design such materials and to explore their potential for various applications.

In particular, a controlled way to manipulate the optical properties is to introduce sub-wavelength periodicities in dielectric materials. This periodicity affects the optical properties of the matter (in the same manner that a periodic potential affects the behavior of an electron in a lattice) and gives rise to synthetic optical materials known as photonic crystals (PCs) [3],[4]. The ability to control the optical properties of photonic crystals offers a unique opportunity to manipulate the optical response in different material platforms. Consequently, new optical materials can be designed to show specific desired optical properties in their photonic band structure. This new opportunity has resulted in new device ideas and concepts which were not previously possible, especially in integrated platforms.

Different modes of implementation of photonic crystals have been proposed. These devices, depending on the number of non-trivial periodicity dimensions can be categorized into one-dimensional (1D), two-dimensional (2D), and three-dimensional (3D) photonic crystal structures. From another point of view, the fabrication technology used for realizing these structures can be categorized into bottom-up (e.g., self-assembly) and top-down (e.g., lithographic patterning) approaches [5]. Depending on the specific application of interest, one of these implementations will be the optimal choice. Here, I will focus on a particular type of photonic crystals, i.e., planar 2D PCs, because on one

hand they are compatible with the conventional integrated optical components, and on the other hand, they are compatible with the well-developed microelectronics fabrication techniques. Because of these reasons, planar PCs have received significant attention as the most feasible solution for integration. Figure 1.1 shows examples of two-dimensionally periodic photonic crystal structures fabricated in a planar Si platform.

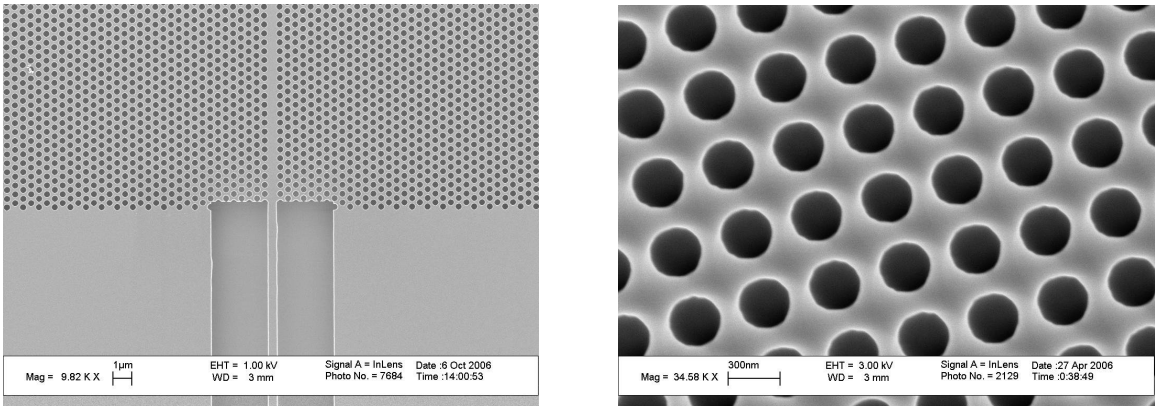


(a) (b)

Figure 1.1. Scanning electron microscope (SEM) images of (a) a PC waveguide and (b) a square lattice PC with two-dimensional periodicity fabricated in a planar platform are shown.

### 1.2. Applications of Photonic Crystals

Based on the application of interest, the role that photonic crystals are expected to play as part of the optical system can be significantly different from case to case. There are two main directions to which most of the current applications can be divided. On one side, the presence of sub-wavelength features in PCs can inhibit the propagation of light in a range of frequencies, known as photonic bandgap (PBG), and this property was proposed to achieve suppression of spontaneous emission [6-7]. Photonic crystals by prohibiting the propagation of light in their PBG range can also act as a perfect mirror for confinement of light in cavities and for guiding the light through line-defects [3-4]. Using photonic crystals in their PBG range has been widely investigated for light confinement

in PC cavities [8-10] and PC waveguides [4,11-13]. Several other applications for such a confinement have been proposed, including components for compact photonic integrated circuits [14-16], environmental sensors [17], nonlinear switches [18], and devices for cavity quantum electrodynamics [19]. On the other hand, propagation of light inside the periodic structure of a photonic crystal exhibits unique dispersive properties, and these dispersion effects can be used to realize another set of functionalities, including slow-light propagation [20], beam shaping [21], beam steering [22], open-cavity resonance [23], band-edge lasing [24-25], diffraction-free propagation [26-29], diffraction compensation [30-31], dispersion compensation [32-33], high-resolution imaging [34], and superprism-based demultiplexing [22,35-38].

In this thesis, the main focus will be on wavelength demultiplexing as one of the major applications of the unique dispersive properties of photonic crystals. The possibility of integration and compactness are two main advantages of PC-based demultiplexers, compared to other demultiplexing techniques, for applications including compact spectrometers (for sensing applications), spectral analyzers for optical information processing systems, and demultiplexers for wavelength division multiplexing (WDM) systems. The basic idea has been proposed by Kosaka et al. [39-40], and it relies on the fact that at the interface between two regions with different dispersion characteristics, with incident waves at different frequencies it is possible to excite modes that propagate in different directions, a phenomenon called the superprism effect. Because of the strong dispersive properties of photonic crystals, one can imagine that such an effect could be used to realize devices that send different wavelengths to considerably different directions. This angular separation can be used to achieve the spatial separation needed in wavelength demultiplexing. The overall scheme is schematically represented in Figure 1.2.

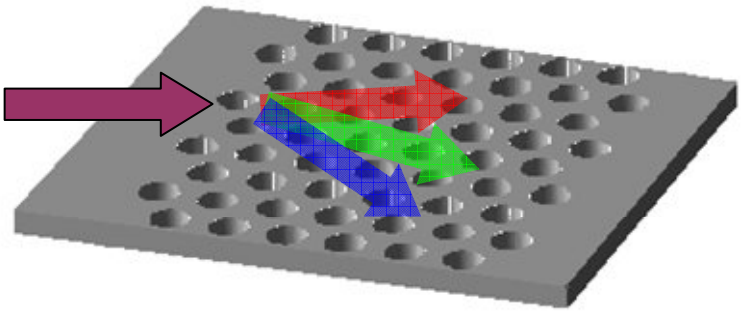

Figure 1.2. Wavelength demultiplexing in a photonic crystal structure is schematically shown. Spatial separation is obtained by mapping different wavelengths of the input signal to different propagation angles inside the PC region.

### 1.3. Devices for Wavelength Demultiplexing

Wavelength demultiplexing (or in a broader view, separation of spectral constituents of a signal) has many applications in the optical systems. Examples of these applications include spectroscopy for the investigation of the emission or absorption spectrum of materials, wavelength multiplexing for more efficient exploitation of the wide bandwidth offered at optical wavelengths, and broadband spectral analysis for information processing systems. The common module in all these applications is a component that discriminates between different wavelengths of the incoming signal and maps the input wavelength to different modes at the output.

There are two main approaches in realizing wavelength demultiplexing devices: cascaded implementation and parallel implementation. In the cascaded implementation of these devices, a series of frequency selective components are used and each of them "drops" one of the wavelength channels from the signal to a specific output port. In that sense, the cascaded implementation can be considered as a filter bank (a series of drop filters) that separates different wavelength channels. Different implementations of this idea, including those based on Fabry-Perot resonators [41], microring resonators [42], PC cavity-based drop filters [43-44], and PC couplers [45], have been proposed. The cascaded implementations offer reasonably good performance for small number of

channels, but for larger number of channels the requirement that all individual resonance effects occur exactly as designed lowers the yield and forces a stringent condition on the fabrication of these devices in practice.

The other possible implementation of optical wavelength separation devices relies on a parallel scheme. In this scheme, usually all the wavelength channels share the same medium of propagation, but the effective dispersive properties are different from one wavelength to another. As a result, propagation through such systems discriminates between different wavelengths and results in modal separation at the output plane. Several possibilities for realizing such wavelength demultiplexing devices have been proposed, among which proposals based on diffraction gratings [46-49], arrayed waveguide gratings [50-52], and the superprism effect in photonic crystals (similar to material dispersion in the conventional prisms) have received more attention. Some of these reported wavelength demultiplexing schemes are shown in Figure 1.3. The common feature between all these schemes is that the wavelength of the input signal inside the structure is mapped to some spatial feature (e.g., the angle of propagation or the location of spot) at the output of the device.

In this research, I will focus on superprism-based implementation of wavelength demultiplexing. The reason for this choice is that this implementation offers the most compact solution (for a specific resolution). In the following chapters, the ideas of implementation of compact and efficient wavelength demultiplexing devices based on the dispersive properties of photonic crystals will be proposed and assessed. Chapter 2 reviews the basic concepts of band structures of periodic media, their mode properties, and how the band structure features lead to unique dispersive properties. In Chapter 3, an approximate model for the analysis of propagation effects inside photonic crystals are developed, which will be the primary tool for efficient modeling and design of dispersive photonic structures in this work. The basic wavelength demultiplexing scheme based on the superprism effect in photonic crystals is discussed in Chapter 4. The limits of the

conventional configuration are then discussed and a modified implementation based on diffraction compensation is proposed, which enables compact and high-resolution implementation of PC wavelength demultiplexers and spectrometers.

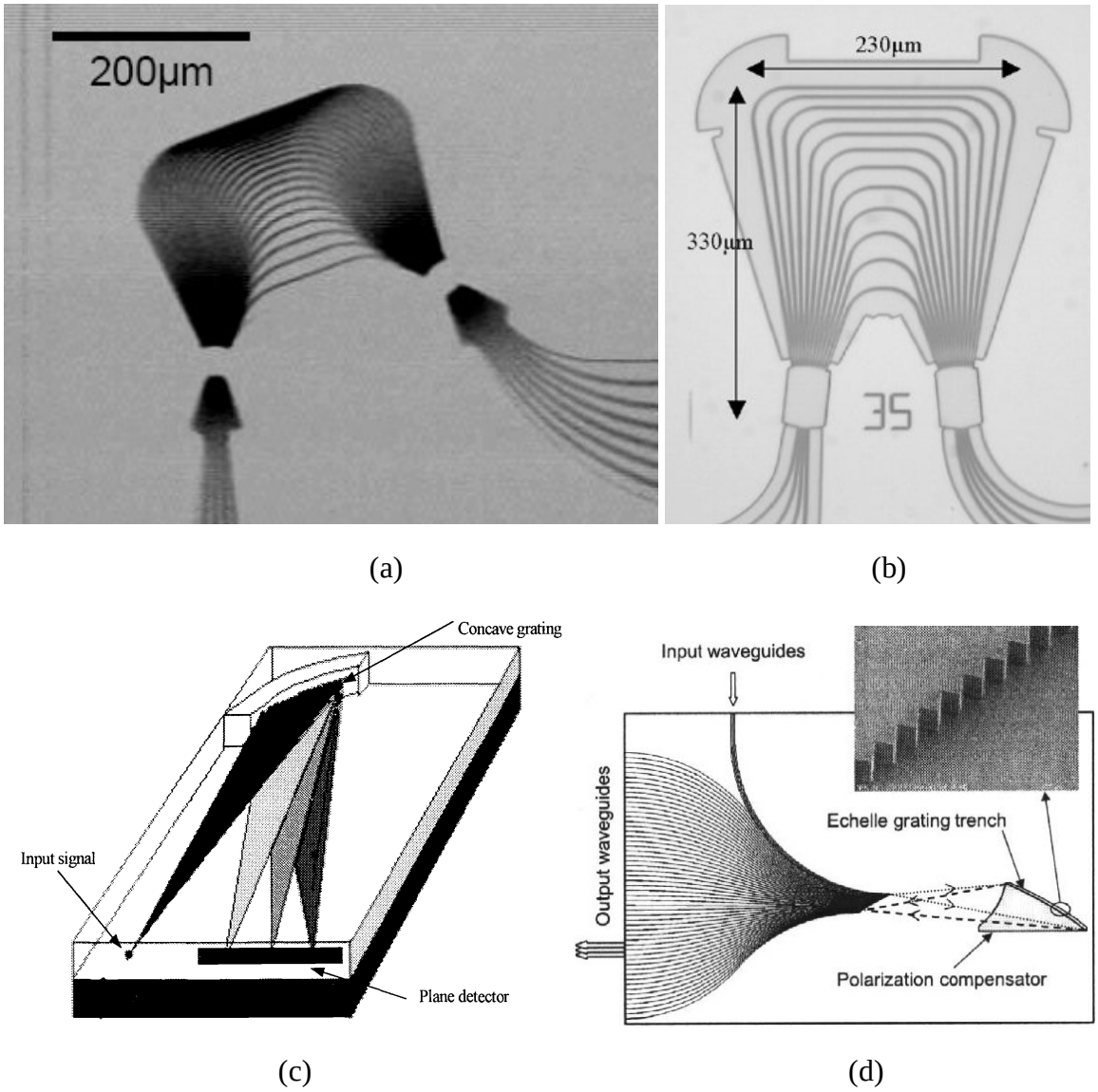


Figure 1.3. Available technologies for integrated planar demultiplexers are shown. (a) Compact AWG in silicon-on-insulator (SOI) with 8 channels, 3 nm wavelength channel spacing, cross-talk isolation better than 6 dB, and around 8 dB on-chip insertion loss [51]. (b) A 4x4 wavelength demultiplexer fabricated in InP with 400GHz channel spacing, -12 dB channel isolation, and 5 dB insertion loss [52]. (c) Schematic demonstration of planar grating spectrometer [53] based on a concave grating is shown. (d) A 48-channel grating-based wavelength demultiplexer fabricated in $SiO_2$ on Si platform [49].

Performance measures of wavelength demultiplexing are also discussed in Chapter 4, and a systematic design procedure is presented. In Chapter 5, different steps in the experimental implementation and demonstration of compact wavelength demultiplexers (i.e., fabrication and optical characterization) are presented and experimental measurement results obtained for the fabricated device are discussed. Chapter 6 deals with the issue of reflection at the interfaces of photonic crystal as one of the important factors in efficient implementation of dispersive devices. Two approaches for designing matching stages are presented that can be used to reduce the reflection loss. Chapter 7 includes other considerations to be taken into account for the practical implementation of dispersive devices for different applications. Finally, conclusions are drawn in Chapter 8, and some future directions for this research are suggested.

# CHAPTER 2

# DISPERSIVE PHOTONIC STRUCTURES

In this chapter, I will introduce the basic concepts and effects used in dispersive applications of PCs. The chapter starts with a review of the basic concepts related to the band structure of PCs. It will be followed by a brief study of structure and basic properties of modes in planar 2D PCs (which are the main implementation platform in this thesis). Finally, some propagation effects and their corresponding dispersive properties of photonic crystals will be introduced.

## 2.1. Photonic Band Structure

According to the Bloch theorem (also known as the Floquet theorem) [54], modes of a periodic structure can be expressed as a periodic envelope (with the same periodicity as the material) propagating with a propagation constant. In other word, for a structure with period *a* along the *z* direction a mode corresponding to the propagation constant *k* can be represented as

$$\begin{cases} \phi(z) = u_k(z)\exp(-jkz) \\ u_k(z+a) = u_k(z) \end{cases}. \tag{2.1}$$

In this view, the periodicity of the structure is transferred to its modes through the periodic envelope function, $u_k(z)$. Bloch theorem is the fundamental principle used in most mathematical analyses of periodic structures. We can expand the periodic envelope portion of the mode in terms of its Fourier expansion as

$$u_k(z) = \sum_n \tilde{u}_{kn}\exp(jnKz), \tag{2.2}$$

with

$$K = \frac{2\pi}{a}. \tag{2.3}$$

Figure 2.1(a) shows a one dimensionally periodic structure in the form of a stack of dielectric structures with different refractive indices. Figure 2.1(b) shows the typical spatial spectrum of $u_k(z)$ and $\phi(z)$ in such periodic structures, consisting of discrete harmonic components apart by multiples of the periodicity wavevector, *K*.

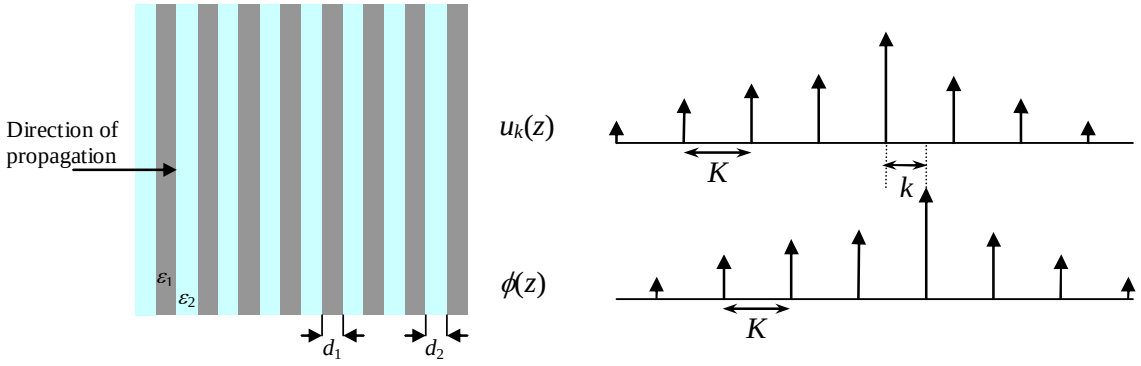


Figure 2.1. (a) A multilayer 1D photonic crystal is schematically shown. (b) Spectral representation of a mode of a 1D photonic crystal structure is illustrated. Each PC mode consists of several Bloch components.

Similar to the concept of dispersion diagrams for waveguides, the plot relating the characteristic wavevector of each mode (*k*) to the frequency of that mode is called the dispersion diagram of the periodic structure. Note that all the wavevectors differing by multiples of periodicity wavevector, *K*, are connected together in each mode. As a result the dispersion diagram of a periodic structure is periodic in wavevector. An example of the band structure of a one-dimensionally periodic structure (similar to the one in Figure 2.1 with $\varepsilon_1 = 13$, $\varepsilon_2 = 1$, and $d_1 = d_2 = a/2$) is shown in Figure 2.2(a). From this figure, it can be seen that the information in the dispersion diagram is redundant, and can be reconstructed using the contents of a single period in the wavevector domain (e.g., for $-K/2 < k < K/2$). The range of the dispersion diagram in $-K/2 < k < K/2$ that

completely expresses the entire dispersion diagram (i.e., a unit cell of the structure in the wavevector domain) is called the *Brillouin zone*. In this particular case, because of the mirror symmetry in the structure, the dispersion diagram in $-K/2 < k < 0$ is simply the mirrored version of that in $0 < k < K/2$. As a result, the complete dispersion diagram can be expressed by the $0 < k < K/2$ portion of it, which is called the *irreducible Brilluoin zone* of the periodic structure.

In the band structures shown in Figure 2.2, one can identify ranges of frequencies in which no propagating mode exists in the structure. These frequency ranges are called photonic bandgaps (in analogy with electronic bandgap in which no electronic mode exists), and multilayer periodic structures are used in this region as perfect 1D mirrors. Examples of applications of these perfect mirrors are in Bragg reflectors in vertical cavity surface emitting lasers (VCSELs) [55] and in the walls of hollow-core fibers used for high-power applications. Note that the bandgap mentioned above in these 1D structures occurs only for waves propagating in the direction perpendicular to the periodicity of structure, and waves in other directions are not necessarily prohibited in the same range of frequencies. Furthermore, using a coupled mode interpretation, the photonic bandgap opens up because of the coupling between forward- and backward-propagating modes in the structure (coupled through the periodicity of the structure), and this coupling occurs at $k = mK/2$. The same idea is also used in fiber Bragg gratings (FBGs) and distributed Bragg reflectors (DBRs) for realizing highly reflecting mirrors.

### 2.1.1. Band Structure Calculations

Most calculation methods for periodic structures are based on the application of Bloch-Floquet theorem (which gives the main form of solution for photonic crystal modes),

$$\begin{cases} \phi_k(z) = u_k(z)\exp(-jkz) \\ u_k(z+a) = u_k(z) \end{cases}. \tag{2.4}$$

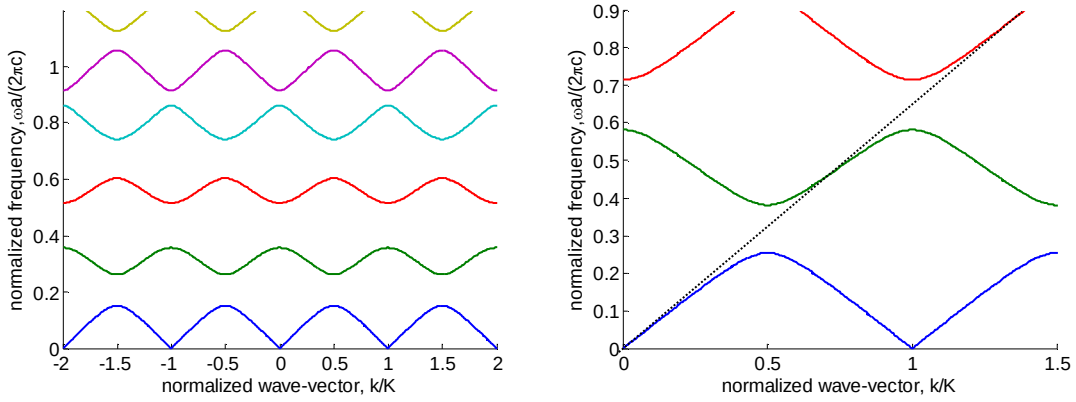


(a) (b)

Figure 2.2. (a) A typical band structure of a 1D photonic crystal is plotted. (b) Band structure of a multilayer periodic structure, as shown in Figure 2.1(a), is plotted with $\varepsilon_{r1} = 4.5$, $\varepsilon_{r2} = 1.0$, and $d_1 = d_2 = a/2$; the dotted line shows the linear dispersion of a bulk material with $\varepsilon_{r2} = 2.4$.

The direct method to find these modes is to substitute this form of the solution into the Maxwell's equations, and use the periodic boundary condition for the envelope function. Two methods that are most widely used to find the modes of PC structures are plane-wave expansion (PWE) [56] and finite-difference time domain (FDTD) [57].

In the plane wave expansion method, the periodic envelope is expanded in terms of its Fourier components (hence, the periodic boundary condition is imposed to the solution), and the resulting expansion is

$$\begin{cases} u_k(z) = \sum_m \tilde{u}_{km} \exp(-jmKz) \\ \phi_k(z) = \sum_m \tilde{u}_{km} \exp[-j(k+mK)z]\,; \quad \phi = E, H \end{cases}. \tag{2.5}$$

It is clear in this relation that the mode is expanded as a set of plane waves with wavevectors $k+mK$. Inserting this expansion into the 1D Helmholtz equation

$$\nabla^2 E + k_0^2 \varepsilon(z) E = 0, \tag{2.6}$$

results in

$$\frac{d^2}{dz^2}\sum_m \tilde{u}_{km}\exp[-j(k+mK)z]+k_0^2\varepsilon(z)\sum_m \tilde{u}_{km}\exp[-j(k+mK)z]=0\,, \tag{2.7}$$

and using

$$\varepsilon(z)=\sum_n \tilde{\varepsilon}_n \exp(-jnKz)\,, \tag{2.8}$$

we get

$$-\sum_m (k+mK)^2\tilde{u}_{km}\exp[-j(k+mK)z]+k_0^2\sum_m\sum_n \tilde{\varepsilon}_{m-n}\tilde{u}_{kn}\exp[-j(k+mK)z]=0\,. \tag{2.9}$$

Re-arranging the terms and looking at the coefficient for $\exp[-j(k+mK)z]$ terms separately, we obtain

$$-(k+mK)^2\tilde{u}_{km}+k_0^2\sum_n \tilde{\varepsilon}_{m-n}\tilde{u}_{kn}=0\,, \tag{2.10}$$

or equivalently,

$$\sum_n \frac{1}{(k+mK)^2}\tilde{\varepsilon}_{m-n}\tilde{u}_{kn}=\frac{1}{k_0^2}\tilde{u}_{km}\,. \tag{2.11}$$

This relation can be expressed in matrix representation as

$$\mathbf{Au}=\lambda\mathbf{u}\,, \tag{2.12}$$

with

$$\begin{cases}\mathbf{A}=[a_{mn}]\ ;\quad a_{mn}=\dfrac{1}{(k+mK)^2}\tilde{\varepsilon}_{m-n} \\ \lambda=\dfrac{1}{k_0^2}\end{cases} \quad \text{and} \quad \mathbf{u}=\begin{pmatrix}\tilde{u}_{k,-l}\\ \tilde{u}_{k,-l+1}\\ \vdots \\ \tilde{u}_{k,l}\end{pmatrix}. \tag{2.13}$$

which is a standard eigenvalue problem. Note that the expansion is truncated to $N=2l+1$ components to make it a finite-size matrix for numerical simulations. Solving this eigenvalue problem gives us the frequency of the mode ($\omega=k_0c$), and the profile of the envelope of the mode (through its Fourier coefficients, $u_{km}$) for a given wavevector, $k$.

Figure 2.3 shows the envelope function calculated using such simulations for the structure analyzed in Figure 1.3(b) in the first photonic band and at $k = 0.45K$.

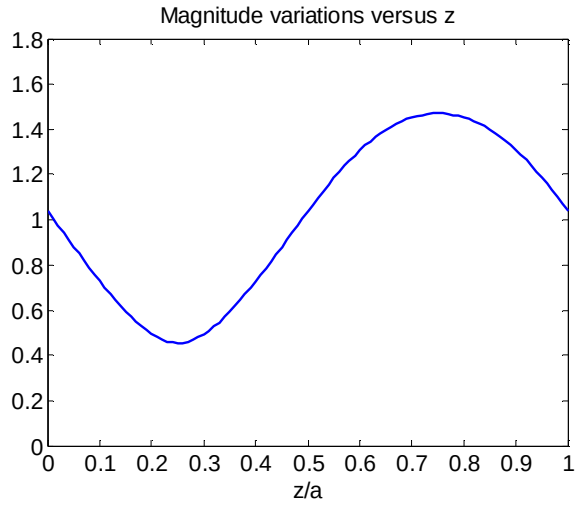


Figure 2.3. Envelope function, $u(z)$, for the first band of a multilayer periodic structure at $k$=0.45$K$ is shown ($\varepsilon_{r1} = 4.5$, $\varepsilon_{r2} = 1.0$, and $d_1 = d_2 = a/2$).

FDTD can also be used to find the modes of periodic structures. For that, again the Bloch-Floquet theorem is used to express the mode as

$$\begin{cases} \phi_k(z,t) = u_k(z)\exp(-jkz + j\omega t) \\ u_k(z+a) = u_k(z) \end{cases}. \tag{2.14}$$

Keeping only a single unit cell of the periodic structure, in this method, an initial arbitrary field profile is assumed over the unit cell. Using the boundary condition

$$\phi_k(z+a,t) = \phi_k(z,t)\exp(-jka), \tag{2.15}$$

the field is allowed to evolve for several time steps in the FDTD algorithm. Through this evolution only the modes of the structure that satisfy both the Maxwell's equations (enforced through the FDTD relations) and the specific boundary conditions survive. By saving the field over time and taking the Fourier transform of the resulting time-domain signal, the resonance peaks (corresponding to the frequencies of the modes) can be

calculated. By repeating this process for different values of *k* the complete band structure can be found.

2.1.2. Two-dimensional photonic crystals

A broader range of applications are covered when structures with two-dimensional (2D) periodicity are considered. In these structures, the material properties (e.g., permittivity) repeat in two dimensions periodically. Such structures are closely connected to 2D periodic slab-type planar photonic crystals which are one of the main platforms proposed for using photonic crystals in integrated optics. Figure 2.4 shows examples of such 2D periodic patterns created in planar structures. The unique opportunity offered by photonic crystals is that the material properties can be engineered by controlling the periodic pattern. Therefore, *synthetic* optical materials for specific needs can be realized in the integrated optical platform by designing geometrical features through fabrication, and all of this is implemented in a single optical material (e.g., in Si or III-V compounds).

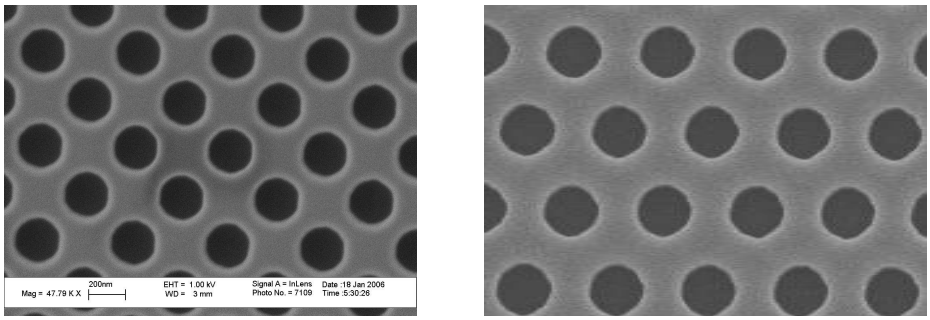


(a) (b)

Figure 2.4. (a) A square lattice and (b) a triangular lattice of air-holes fabricated in the top Si layer of a silicon-on-insulator (SOI) wafer are shown.

Two-dimensional photonic crystals are simply structures with two-dimensional periodicity in space. This 2D periodicity can be specified by a 2D unit cell and two lattice vectors. By repeating the unit cell using the two lattice vectors ($\mathbf{a_1}$ and $\mathbf{a_2}$, which define

the two lattice symmetry directions) the periodic structure can be reconstructed. Note that the choice of unit cell and lattice vectors is not unique, but there exists a primitive unit cell that is the smallest unit cell for the periodic structure (in the following material, the term unit cell usually refers to such primitive unit cells, unless otherwise stated). Figure 2.5(a) shows a square lattice structure ($\mathbf{a_1} \perp \mathbf{a_2}$ and $a_1 = a_2$) of cylindrical air inclusions in a host dielectric. Other typical lattice structures of frequent use as photonic crystal structures are triangular lattice ($\angle(\mathbf{a_1}, \mathbf{a_2}) = 60°$ and $a_1 = a_2$) shown in Figure 2.4(a) and rectangular lattice ($\mathbf{a_1} \perp \mathbf{a_2}$ and $a_1 \neq a_2$). Figure 2.5(b) shows a general 2D lattice structure in which the two lattice vectors make an arbitrary angle and $a_1 \neq a_2$.

Using the Bloch theorem, the electromagnetic modes (corresponding to a wavevector **k**) in this structure can be expressed as

$$\begin{cases} \phi_{\mathbf{k}}(\mathbf{r}) = u_{\mathbf{k}}(\mathbf{r}) \exp(-j\mathbf{k} \cdot \mathbf{r}) \\ u_{\mathbf{k}}(\mathbf{r} + \mathbf{a}) = u_{\mathbf{k}}(\mathbf{r}) \end{cases}, \tag{2.16}$$

where $\mathbf{a} = \mathbf{a_1}, \mathbf{a_2}$. Here, $\phi$ can be either the magnetic field or the electric field perpendicular to the plane of periodicity; these two cases are called H-polarization and E-polarization, respectively. Again, similar to the 1D case, the mode is divided into two parts: an envelope function that has the same periodicity as the original lattice, and an exponential term with the characteristic 2D wavevector of the mode. The reciprocal lattice vectors $\mathbf{K_1}$ and $\mathbf{K_2}$ are the k-domain counterparts of the lattice vectors (i.e., $\mathbf{a_1}$ and $\mathbf{a_2}$) and are defined such that

$$\begin{cases} \mathbf{K_i} \cdot \mathbf{a_i} = 2\pi \\ \mathbf{K_i} \cdot \mathbf{a_j} = 0 \ ; \quad i \neq j \end{cases}. \tag{2.17}$$

The reciprocal lattice vectors can be formally derived from the lattice vectors for a three-dimensionally periodic structure using the cyclic vector product as

$$\mathbf{K_1} = 2\pi \frac{\mathbf{a_2} \times \mathbf{a_3}}{(\mathbf{a_2} \times \mathbf{a_3}) \cdot \mathbf{a_1}} \qquad \mathbf{K_2} = 2\pi \frac{\mathbf{a_3} \times \mathbf{a_1}}{(\mathbf{a_3} \times \mathbf{a_1}) \cdot \mathbf{a_2}} \qquad \mathbf{K_3} = 2\pi \frac{\mathbf{a_1} \times \mathbf{a_2}}{(\mathbf{a_1} \times \mathbf{a_2}) \cdot \mathbf{a_3}} \tag{2.18}$$

For the special case of two-dimensionally periodic structures in the x-y plane, the reciprocal lattice vectors can be calculated simply by assuming a virtual periodicity with $\mathbf{a_3} = \hat{z}$ in the third direction.

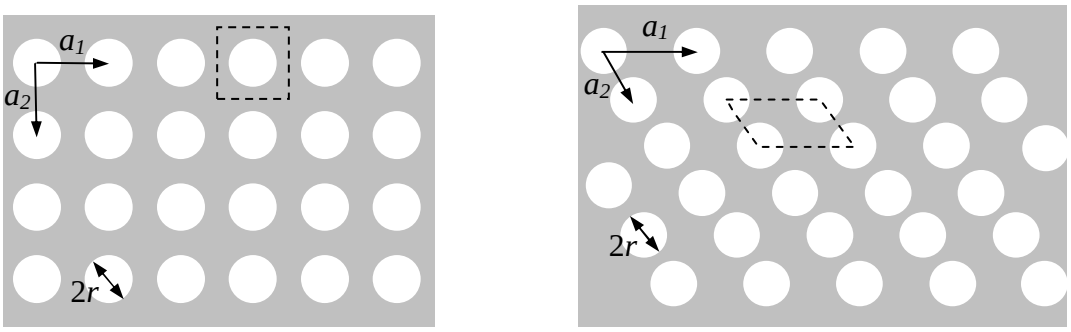


Figure 2.5. (a) A square lattice geometry and (b) an arbitrary general lattice geometry are shown schematically. The two lattice vectors of each lattice and their corresponding primitive unit cells (dashed) are depicted in these figures.

The mode properties of a periodic structure in the k-space are periodic with periods being the reciprocal lattice vectors (as already seen for the special case of 1D periodic structures). To prove this claim, starting from the general form of the mode, we have

$$\phi_{\mathbf{k}}(\mathbf{r}) = u_{\mathbf{k}}(\mathbf{r})\exp(-j\mathbf{k}\cdot\mathbf{r}) = u_{\mathbf{k}}(\mathbf{r})\exp(j\mathbf{K_i}\cdot\mathbf{r})\exp[-j(\mathbf{k}+\mathbf{K_i})\cdot\mathbf{r}]. \tag{2.19}$$

Let us define $u_{\mathbf{k}+\mathbf{K_i}}(\mathbf{r}) = u_{\mathbf{k}}(\mathbf{r})\exp(j\mathbf{K_i}\cdot\mathbf{r})$; it can be readily verified that

$$u_{\mathbf{k}+\mathbf{K_i}}(\mathbf{r}+\mathbf{a_i}) = u_{\mathbf{k}}(\mathbf{r}+\mathbf{a_i})\exp(j\mathbf{K_i}\cdot\mathbf{r})\exp(j\mathbf{K_i}\cdot\mathbf{a_i}) = u_{\mathbf{k}}(\mathbf{r})\exp(j\mathbf{K_i}\cdot\mathbf{r}) = u_{\mathbf{k}+\mathbf{K_i}}(\mathbf{r}). \tag{2.20}$$

Therefore,

$$\phi_{\mathbf{k}}(\mathbf{r}) = u_{\mathbf{k}+\mathbf{K_i}}(\mathbf{r})\exp[-j(\mathbf{k}+\mathbf{K_i})\cdot\mathbf{r}] = \phi_{\mathbf{k}+\mathbf{K_i}}(\mathbf{r}); \tag{2.21}$$

in other words, the points differing by multiples of reciprocal lattice vectors in the k-domain all represent the same electromagnetic mode.

For calculating the band structures, several methods, including PWE and FDTD (with the same principles discussed for the 1D structures), can be used. To be concise, I only describe the PWE technique here in more detail. The analysis starts again with expressing the mode of the structure using the Bloch theorem as

$$\begin{cases} \phi_{\mathbf{k}}(\mathbf{r}) = u_{\mathbf{k}}(\mathbf{r}) \exp(-j\mathbf{k}\cdot\mathbf{r}) \\ u_{\mathbf{k}}(\mathbf{r}+\mathbf{a}_{\mathbf{i}}) = u_{\mathbf{k}}(\mathbf{r}) \end{cases}. \tag{2.22}$$

Knowing that the reciprocal lattice vectors $\mathbf{K_1}$ and $\mathbf{K_2}$ express the periodicity of the structure in the k-space, we can expand the periodic envelope function, $u_{\mathbf{k}}(\mathbf{r})$, by its Fourier expansion,

$$u_{\mathbf{k}}(\mathbf{r}) = \sum_m \sum_n \tilde{u}_{\mathbf{k},mn} \exp[-j(m\mathbf{K_1} + n\mathbf{K_2})\cdot\mathbf{r}]. \tag{2.23}$$

The PC mode, therefore, in general can be expressed as

$$\phi_{\mathbf{k}}(\mathbf{r}) = \sum_m \sum_n \tilde{u}_{\mathbf{k},mn} \exp[-j(\mathbf{k} + m\mathbf{K_1} + n\mathbf{K_2})\cdot\mathbf{r}]. \tag{2.24}$$

This is the general form of the solution for the modes of this periodic structure. In what follows, I will consider the cases for E- and H-polarizations separately. For both cases we assume that the *x*-*y* plane is the plane of the periodicity and the *z* direction is perpendicular to this plane (i.e., the medium has no variation in the *z* direction). Furthermore, we assume the permittivity of the structure to be periodic, with

$$\varepsilon(\mathbf{r}) = \sum_p \sum_q \tilde{\varepsilon}_{pq} \exp[-j(p\mathbf{K_1} + q\mathbf{K_2})\cdot\mathbf{r}]. \tag{2.25}$$

### 2.1.3. Plane wave expansion for PC modes with E-polarization

In this case, $\phi = E_z$,

$$E_z(\mathbf{r}) = \sum_m \sum_n \tilde{S}_{mn} \exp[-j(\mathbf{k} + m\mathbf{K_1} + n\mathbf{K_2})\cdot\mathbf{r}], \tag{2.26}$$

and from Helmholtz equation, we have

$$\nabla^2 E_z + k_0^2 \varepsilon(\mathbf{r}) E_z = 0 . \tag{2.27}$$

Thus,

$$\sum_m \sum_n |\, \mathbf{k} + m\mathbf{K_1} + n\mathbf{K_2} \,|^2 \; \tilde{\tilde{S}}_{mn} \exp[-j(\mathbf{k} + m\mathbf{K_1} + n\mathbf{K_2}) \cdot \mathbf{r}] =$$
$$k_0^2 \left( \sum_m \sum_n \tilde{\tilde{S}}_{mn} \exp[-j(\mathbf{k} + m\mathbf{K_1} + n\mathbf{K_2}) \cdot \mathbf{r}] \right) \left( \sum_p \sum_q \tilde{\tilde{\varepsilon}}_{pq} \exp[-j(p\mathbf{K_1} + q\mathbf{K_2}) \cdot \mathbf{r}] \right) . \tag{2.28}$$

By re-arranging the terms and removing the common exponential factor from the sides, we obtain

$$-|\, \mathbf{k} + m\mathbf{K_1} + n\mathbf{K_2} \,|^2 \; \tilde{\tilde{S}}_{mn} + k_0^2 \sum_p \sum_q \tilde{\tilde{\varepsilon}}_{m-p,n-q} \tilde{\tilde{S}}_{pq} = 0 . \tag{2.29}$$

Or equivalently,

$$\frac{1}{|\, \mathbf{k} + m\mathbf{K_1} + n\mathbf{K_2} \,|^2} \sum_p \sum_q \tilde{\tilde{\varepsilon}}_{m-p,n-q} \tilde{\tilde{S}}_{pq} = \frac{1}{k_0^2} \tilde{\tilde{S}}_{mn} . \tag{2.30}$$

If we create a vector **S** of the coefficients of the electric field expansion, $\tilde{\tilde{S}}_{mn}$'s, we can represent Equation (2.30) in matrix form as

$$[\mathbf{A}_{TE}]\mathbf{S} = \frac{1}{k_0^2} \mathbf{S} , \tag{2.31}$$

which is a standard eigenvalue problem with

$$[\mathbf{A}_{TE}] = [a_{mn,pq}^{(TE)}] \;\; ; \;\; a_{mn,pq}^{(TE)} = \frac{1}{|\, \mathbf{k} + m\mathbf{K_1} + n\mathbf{K_2} \,|^2} \tilde{\tilde{\varepsilon}}_{m-p,n-q} . \tag{2.32}$$

Note that in these relations, the same indexing used to create the vector **S** (i.e., $I=I(m,n)$) is also used in the coefficients matrix. Solving the eigenvalue problem in Equation (2.31) gives us the frequencies of the PC modes ($\omega = k_0 / \sqrt{\mu_0 \varepsilon_0}$) corresponding to a given wavevector **k**. Furthermore, the eigenvector corresponding to each eigenvalue (calculated by standard methods of solving eigenvalue problems) represents the coefficients of the Bloch expansion of the mode.

2.1.4. Plane wave expansion for PC modes with H-polarization

In this case, $\phi = H_z$,

$$H_z(\mathbf{r}) = \sum_m \sum_n \tilde{U}_{mn} \exp[-j(\mathbf{k} + m\mathbf{K_1} + n\mathbf{K_2}) \cdot \mathbf{r}], \tag{2.33}$$

and the Helmholtz equation can be represented as

$$\nabla \times \left( \frac{1}{\varepsilon(\mathbf{r})} \nabla \times \mathbf{H_z} \right) = k_0^2 \mathbf{H_z}. \tag{2.34}$$

Using the vector identity

$$\nabla \times (f\mathbf{F}) = f \nabla \times \mathbf{F} - \nabla f \times \mathbf{F}, \tag{2.35}$$

we can rewrite Equation (34) as

$$-\nabla \left( \frac{1}{\varepsilon(\mathbf{r})} \right) \times (\nabla \times \mathbf{H_z}) + \frac{1}{\varepsilon(\mathbf{r})} \nabla \times (\nabla \times \mathbf{H_z}) = k_0^2 \mathbf{H_z}. \tag{2.36}$$

Now, using the vector identity

$$\nabla \times (\nabla \times \mathbf{H_z}) = \nabla (\nabla \cdot \mathbf{H_z}) - \nabla^2 \mathbf{H_z}, \tag{2.37}$$

and noting that

$$(\nabla \cdot \mathbf{H_z}) = \frac{1}{\mu_0} (\nabla \cdot \mathbf{B_z}) = 0, \tag{2.38}$$

we obtain

$$-\nabla \left( \frac{1}{\varepsilon(\mathbf{r})} \right) \times (\nabla \times \mathbf{H_z}) - \frac{1}{\varepsilon(\mathbf{r})} \nabla^2 \mathbf{H_z} = k_0^2 \mathbf{H_z}. \tag{2.39}$$

For simplicity also, we define

$$\mathbf{k}_{mn} = \mathbf{k} + m\mathbf{K_1} + n\mathbf{K_2}. \tag{2.40}$$

Thus,

$$\begin{aligned}
&\sum_m \sum_n \sum_p \sum_q \{\, (p\mathbf{K_1} + q\mathbf{K_2})\tilde{\eta}_{pq} \exp[-j(p\mathbf{K_1} + q\mathbf{K_2})\cdot\mathbf{r}]\times \\
&\qquad\qquad [\hat{x}(\mathbf{k}_{mn}\cdot\hat{y}) - \hat{y}(\mathbf{k}_{mn}\cdot\hat{x})]\tilde{U}_{mn} \exp[-j(\mathbf{k}_{mn}\cdot\mathbf{r})]\ \} \\
&+ \sum_m \sum_n \sum_p \sum_q \tilde{\eta}_{pq} \exp[-j(p\mathbf{K_1} + q\mathbf{K_2})\cdot\mathbf{r}]\,|\,\mathbf{k}_{mn}\,|^2\ \tilde{U}_{mn} \exp[-j(\mathbf{k}_{mn}\cdot\mathbf{r})] \\
&= k_0^2\left(\sum_m \sum_n \tilde{U}_{mn} \exp[-j(\mathbf{k}_{mn}\cdot\mathbf{r})]\right)
\end{aligned} \tag{2.41}$$

in which

$$\frac{1}{\varepsilon(\mathbf{r})} = \sum_p \sum_q \tilde{\eta}_{pq} \exp[-j(p\mathbf{K_1} + q\mathbf{K_2})\cdot\mathbf{r}]\,. \tag{2.42}$$

By eliminating the common exponential factor in Equation (2.41), we obtain

$$\begin{aligned}
&\sum_p \sum_q \{\tilde{\eta}_{m-p,n-q}[(m-p)\mathbf{K_1} + (n-q)\mathbf{K_2}]\times [\hat{x}(\mathbf{k}_{pq}\cdot\hat{y}) - \hat{y}(\mathbf{k}_{pq}\cdot\hat{x})]\tilde{U}_{pq}\} \\
&+ \sum_p \sum_q \tilde{\eta}_{m-p,n-q}\,|\,\mathbf{k}_{pq}\,|^2\ \tilde{U}_{pq} = k_0^2\tilde{U}_{mn}
\end{aligned}\,. \tag{2.43}$$

Similar to the E-polarization case, we can define a vector **U** of the coefficients of the magnetic field expansion, $\tilde{U}_{mn}$'s, and represent these relations in matrix form as

$$[\mathbf{A}_{TM}]\mathbf{U} = k_0^2\mathbf{U}\,, \tag{2.44}$$

which is a standard eigenvalue problem with

$$\begin{aligned}
&[\mathbf{A}_{TM}] = [a_{mn,pq}^{(TM)}] \\
&a_{mn,pq}^{(TM)} = \tilde{\eta}_{m-p,n-q}\{[(m-p)\mathbf{K_1} + (n-q)\mathbf{K_2}]\times [\hat{x}(\mathbf{k}_{pq}\cdot\hat{y}) - \hat{y}(\mathbf{k}_{pq}\cdot\hat{x})]\}\cdot\hat{z} + |\,\mathbf{k}_{pq}\,|^2
\end{aligned}\,. \tag{2.45}$$

The same procedure can be readily followed to analyze three-dimensionally periodic photonic crystals, noting that the vectorial nature of the fields in the 3D case should be preserved.

The two-dimensional dispersion of a 2D periodic structure can be represented by the dispersion relation $\omega = \omega(k_x, k_y)$ in the two-dimensional k-space. Knowing from Equation (2.21) that this information is redundant in the k-space, we can limit ourselves to one *unit cell* in the k-space, and by periodically repeating this data (using the

reciprocal lattice vectors) the entire band structure can be reconstructed. This *unit cell* region of the k-space is called the first Brillouin zone of the band structure. Figure 2.6 shows the band structure of a square lattice photonic crystal of cylindrical air holes in Si in the k-space in the form of iso-frequency contours (i.e., contours of $\omega(k_x, k_y) = \omega_0$).

Using other symmetries in the structure (e.g., 90° rotation symmetry and mirror symmetry in the square lattice with circular holes in Figure 2.6), it can be seen that the highlighted region in Figure 2.6 (marked by dotted borders) is sufficient to represent the entire band structure. This region is called the reduced Brillouin zone of the band structure.

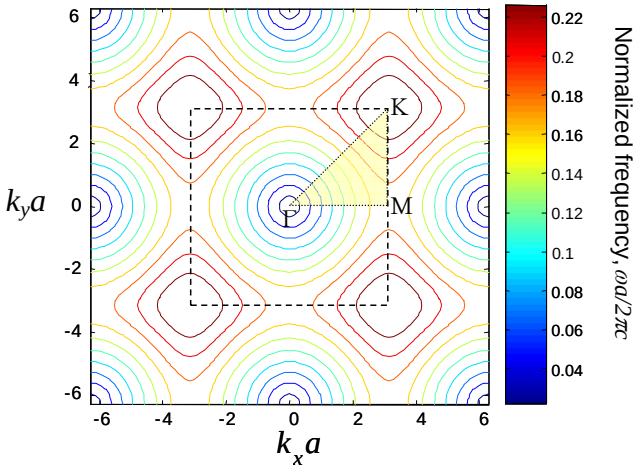


Figure 2.6. Band structure of a square lattice photonic crystal of air holes (with *r/a*=0.35) in Si (with $\varepsilon_r = 11.4$) for H-polarization is shown in the form of iso-frequency contours. The first Brillouin zone of the structure is marked by the dashed lines. It can be observed that by repeating the first Brillouin zone in the principal lattice directions (the *x* and *y* directions) the entire band structure will be generated.

The boundaries of the reduced Brillouin zone of the band structure are usually the points with the strongest effect of periodicity. As a result, to investigate the properties of the modes, usually only the dispersion of the 2D PC along these boundaries is studied. Figure 2.7 shows an alternative representation of the band structure of a 2D PC as in

Figure 2.6, calculated over the boundary of the reduced Brillouin zone. Note that these boundaries for a square lattice PC are usually marked with the crystallographic lattice directions Γ, M, and K, as shown in Figures 2.6 and 2.7.

In the band structure as shown in Figure 2.7, it can be observed that there are frequency bands, in which no electromagnetic mode is allowed. These frequency bands are called 2D photonic bandgap (PBG) in analogy with the concept of electronic bandgap. The existence of the PBG is one of the most important properties of the photonic crystals. Photonic crystals in their PBG have been proposed to achieve tight confinement of light in photonic crystal waveguides (PCWs) and photonic crystal cavities. They have been also proposed in this range for suppressing spontaneous emission.

The representation of band structure over the boundary of the irreducible Brillouin zone as depicted in Figure 2.7 is useful in PBG applications of photonic crystals, in which the existence and the location of PBG is of main interest. In dispersive applications of photonic crystals, however, such representations are of little use. Instead, a more complete visualization of the band structure in the form of iso-frequency contours in k-space (as shown in Figure 2.6) conveys more information about the dispersive properties of PC modes. A more complete (but harder to interpret) representation of photonic band structure is the direct three-dimensional plot of the frequencies of the modes in the k-space (which is the direct extension of the conventional dispersion plot in 1D structures). Figure 2.8 shows such visualization of the band structure for the first two E-polarized PC bands of a square lattice PC of circular air holes (with $r/a$ = 0.34) in a dielectric with relative permittivity of $\varepsilon_r = 9.1$ (same structure as in Figure 2.7). Note that the bands are shown only in the first Brillouin zone and the bands in the rest of the k-space can be found by repeating these bands periodically. Furthermore, note that in this

case the second photonic band is the extension of the first band folded back into the first Brillouin zone, and as a result its dispersion is considerably different from that of an ordinary bulk medium.

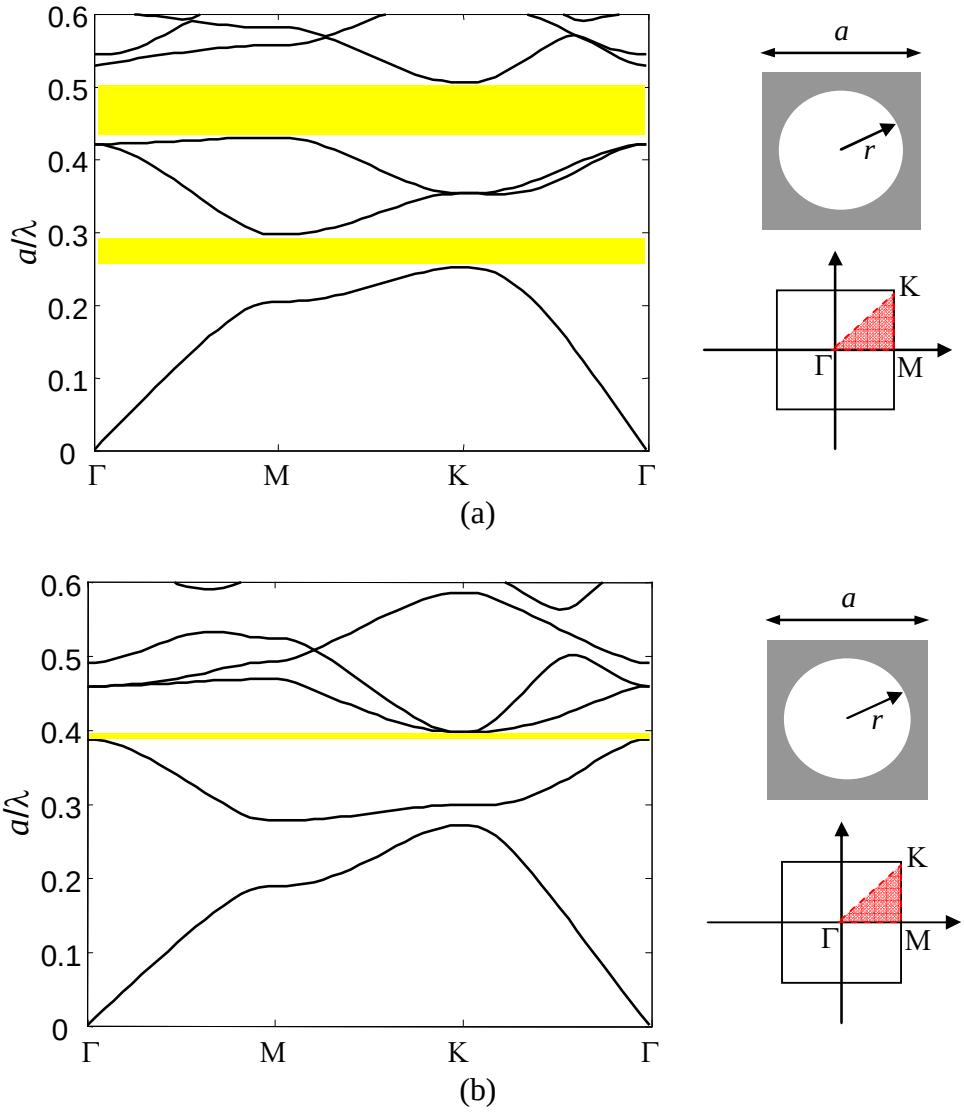


Figure 2.7. Band structure of the 2D square lattice PC, similar to the one in Figure 2.6, with $r/a$ = 0.34 and relative permittivity $\varepsilon_r$ = 9.1 is calculated and plotted over the boundary of the reduced Brillouin zone for (a) E-polarization and (b) H-polarization. Photonic bandgap regions are shown by yellow strips. Normalized frequency is defined as $a/\lambda$ in this figure, where $a$ is the lattice constant of the PC, and $\lambda$ is the free-space wavelength corresponding to the operation frequency.

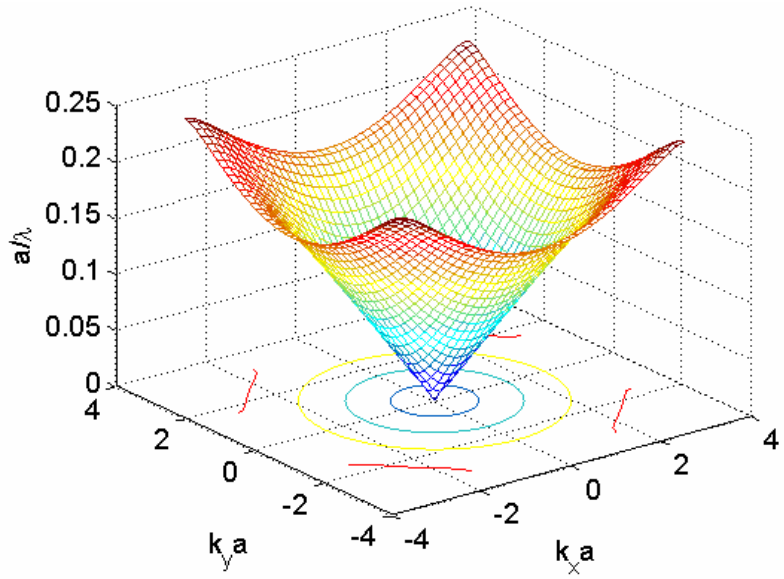


(a)

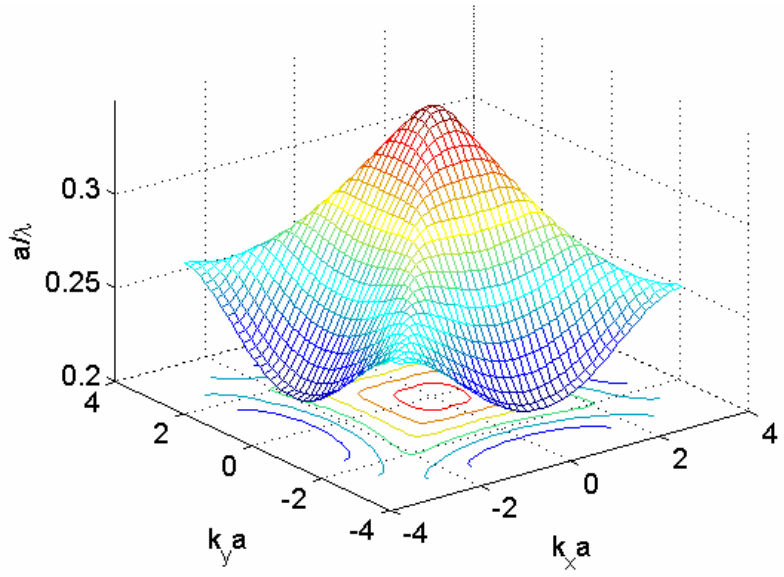


(b)

Figure 2.8. Band structure of E-polarized modes of a 2D square lattice PC similar to the one in Figure 2.7 (with $r/a$ = 0.34 and relative permittivity $\varepsilon_r$ = 9.1) is calculated and plotted over the 2D k-space. (a) The first photonic band (with lowest frequency) and (b) the second photonic band are depicted. In both cases, corresponding iso-frequency contours in the 2D k-plane are also plotted.

## 2.2. Structure of Modes in Planar 2D PCs

A more feasible implementation platform is a slab-type PC structure in which the light is confined in a slab of a dielectric material (with relatively large permittivity) and the slab is patterned by a periodic array of holes. In these structures, confinement in the vertical direction (normal to the plane of the slab) is achieved by total internal reflection, similar to unpatterned slab waveguides [58-59]. Figure 2.9(a) shows such confinement in a periodically patterned slab. The slab-type implementation of PC structures [60-69] is advantageous over other platforms since it is compatible with available well-developed microelectronic fabrication technology as well as with previously developed concepts in integrated optics.

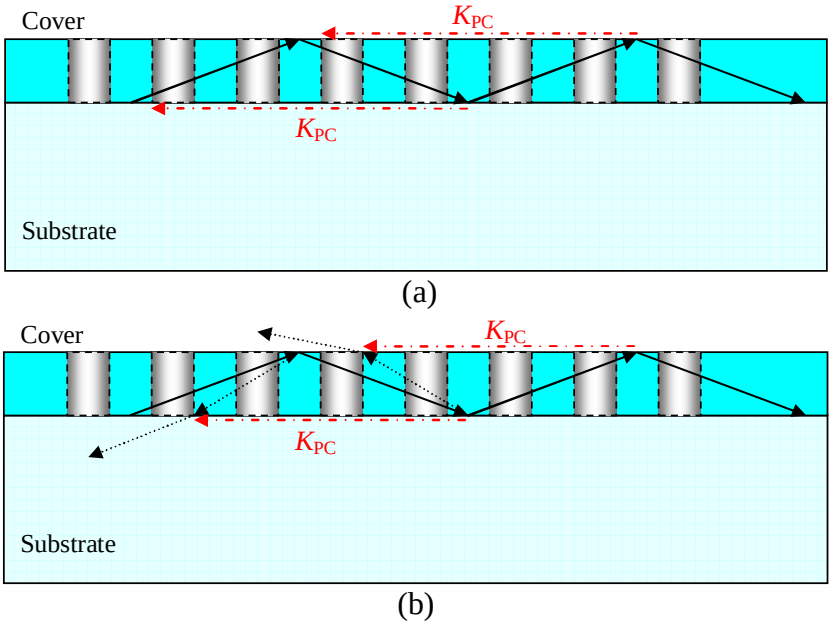


Figure 2.9. Confinement and leakage in a slab-type photonic crystal are schematically represented. (a) Solid arrows show confinement by total internal reflection in the slab. (b) In a periodically patterned slab, at higher frequencies, the periodicity wavevector of the photonic crystal, $K_{PC}$, can couple the modes of the structure to wavevectors that are no longer confined by total internal reflection (shown by dotted arrows); these photonic crystal modes are not confined, and their propagation in the slab-type PC involves propagation loss caused by leakage to the substrate or cover regions.

Depending on the frequency of light, the periodicity wavevector of the photonic crystal may couple the light to the propagating modes of the substrate and/or cover regions, as shown in Figure 2.9(b). In this case, the wave "leaks" to the outside of the slab, and propagation loss is relatively large. To ensure confinement of light in the slab region, it is essential that all of the Bloch components generated inside the slab have tangential wavevectors that are larger than the amplitude of the wavevectors in the substrate and cover regions. The region that does not satisfy this condition is usually marked out of the band structure, since it cannot be used for low-loss manipulation of light in photonic crystals. The border line that separates confined modes from those that are not confined is usually referred to as the *light line*.

In 2D and symmetric slab-type structures, photonic crystal modes can be separated into two groups of orthogonal polarizations [65], i.e., transverse electric (TE) modes and transverse magnetic (TM) modes; in these cases, usually the band structures of these two sets of modes are studied separately (since either set of modes can be selectively excited and used for the operation of photonic devices). In asymmetric slab-type photonic crystal structures, these sets of modes are not pure, and in general, one needs to consider all the hybrid modes. However, there are cases in which the definition of TE-like and TM-like modes applies to these structures, and a single dominant polarization for the range of operation can be considered [65,70]. Note that the convention based on which TE and TM polarizations are defined has been different in some reports for 2D and planar structures. To avoid confusion, throughout this work, TE is defined as the case with dominant magnetic field in the direction perpendicular to the plane of periodicity in a slab-type structure. In 2D structures, the term H-polarization is used for the same case (highlighting the fact that the magnetic field has a single component perpendicular to the plane of periodicity). Similarly, TM and TM-like polarizations have a dominant electric field in the direction perpendicular to the plane of

periodicity in a slab-type structure, and will be referred to as E-polarization in 2D structures.

For the analysis of the mode structure in slab-type PCs, the direct method is to simulate the complete 3D structure using either FDTD [57], or plane-wave expansion (PWE) using the supercell method [65]. Both these approaches require relatively large memory and involve intensive computations. An approximate (yet efficient) approach for faster simulation of slab-type PCs is the use of effective index. In the effective index simulations, the dielectric confinement in the direction normal to the interfaces of the slab (or the plane of periodicity of the PC) is neglected, and instead, an effective index (corresponding to this confinement) is used for the dielectric region. Therefore, the slab-type PC problem is reduced to a 2D PC structure that can be readily solved using any of the standard approaches [71].

The modes of these structures in principle are slab-type modes (i.e., the modes of an unperturbed slab structure) that are modified because of the in-plane periodicity. The effect of periodicity appears as band folding (which in some cases results in band crossing, and possibly mode splitting in that vicinity) and band deformations. These effects are in nature similar to what we see in 2D PC structures, with the main difference being that the original unperturbed modes of the structure are the modes of a slab waveguides, and that the range of operation is restricted to the confined modes below the substrate light cone.

The main design consideration is the proper choice of the thickness of the slab relative to the lattice constant of the PC. For PBG applications, usually the thickness of the slab is chosen in a way to maximize the gap (which is the useful range of operation in these applications). However, if we are considering the PC for propagation of the beam, maximizing the PBG may not be the best criterion. In general, as the ratio of the

thickness to the lattice constant increases, the modes are shifted to lower normalized frequencies, and therefore, a larger portion of the band structure lies below the light cone (this is an advantage, since parts of the band structure above the light cone are not confined and thus, cannot be used despite their possibly attractive dispersive properties). On the other hand, for larger normalized thickness the structure becomes multimode in the range of interest. Figure 2.10 shows these trends by comparing the band structure of four different photonic crystals.

In the calculations for Figure 2.10, a 3D PWE technique incorporating a supercell is used to find the modes of the structure. The size of the supercell in the vertical *z* direction (i.e., the direction perpendicular to the plane of periodicity) is chosen to be 12 times the thickness of the slab region to ensure optical isolation. Also, in these simulations 19 orders in the *z* direction were retained for acceptable representation of the actual structure. Note that in practice, the thickness of the film layer is mainly dictated by the availability of the wafers, and the other parameters of the PC have to be chosen accordingly.

### 2.3. Propagation Effects

The main phenomena of interest in applications based on the dispersive properties of PCs are the effect of propagation on the spatial profile of an optical beam and the dependence of these propagation effects on the wavelength of the optical beam. The main propagation effect in ordinary bulk media is the diffraction effect and most conventional device concepts rely on the effects at the interfaces of regions with different refractive indices. However, in photonic crystals the optical material shows a variety of unique dispersive properties with direct impact on the profile of an optical beam propagating through this structure. In what follows, a brief background on the approach for

understanding these effects is provided, and then, some of unique dispersive properties of PCs are surveyed.

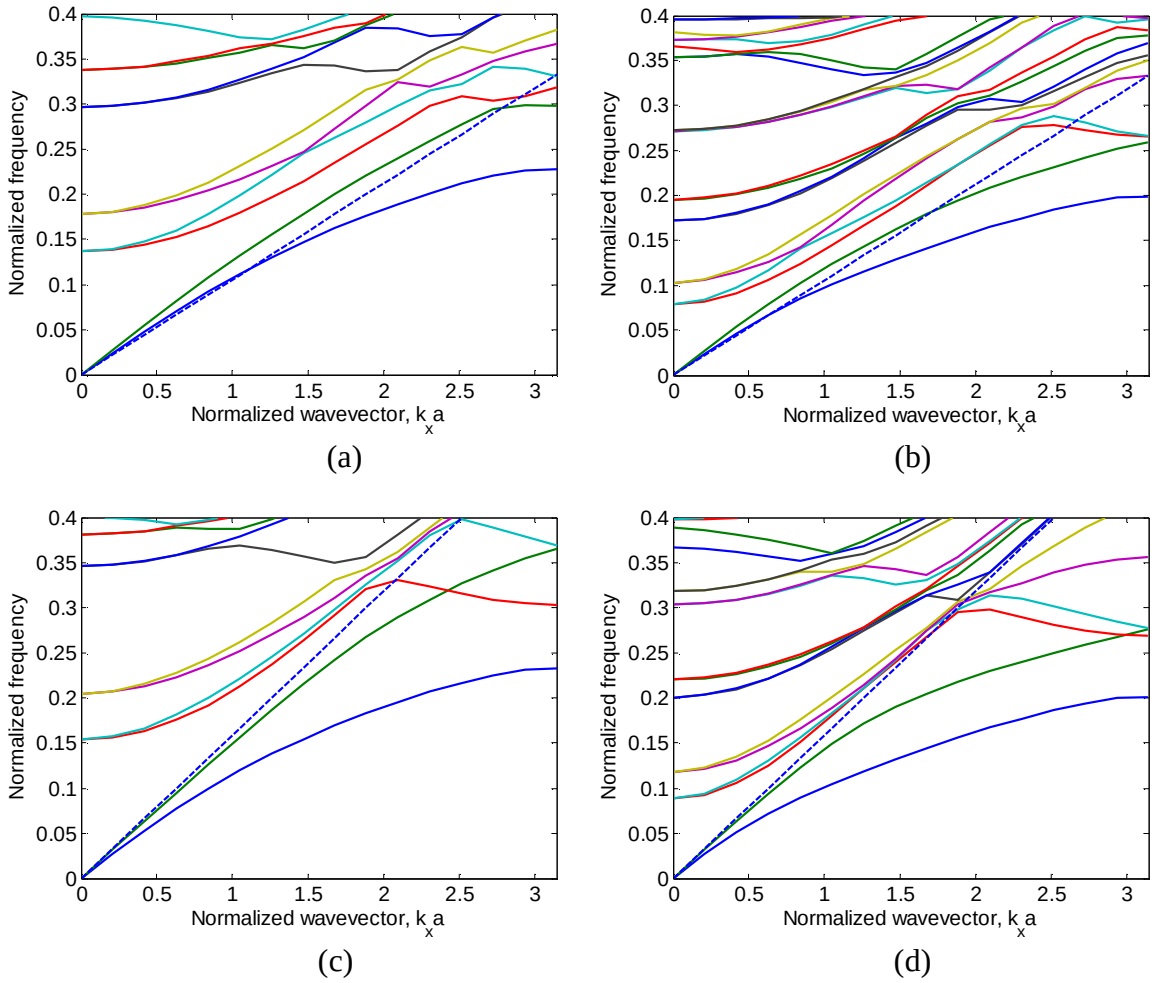


Figure 2.10. Band structures in the in-plane ΓM direction for a square lattice of air-holes with $r/a$ = 0.3 in SOI wafers are shown. The thickness of the film Si layer in all cases is $h$ = 220 nm, and the results are related to (a) Si film on oxide with $h/a$ = 0.4, (a) Si film on oxide with $h/a$ = 0.7, (c) undercut Si with $h/a$ = 0.4, and (d) undercut Si with $h/a$ = 0.7. The dashed line shows the light line (for the substrate or air) and is the border for confined modes.

Propagation effects for a monochromatic beam propagating inside a dispersive medium can be understood by drawing an analogy between the resulting effects and those caused by the propagation of a pulse through a dispersive medium in the time domain. The already well-developed analysis tools developed for the propagation of an optical

pulse in time-domain (e.g., those presented in [72]) can be readily extended to the space domain. In this analogy, the time is transformed to the coordinate along which the beam profile is monitored, as shown in Figure 2.11. Each spatial spectrum component (characterized by a wavevector, *k*) has a specific direction of propagation that is governed by the direction of group velocity of that component. This direction corresponds to a shift in the space domain in the output plain in analogy with the time-delay in the temporal (i.e., shift along time coordinate) counterpart. Note that the wavelength dependence in investigation of dispersive effects in space is more elaborate compared to its time-domain counterpart. Even though at each specific wavelength the nature of the propagation in the time and space domains are similar, there are a variety of unique concepts and phenomena when the difference between different wavelengths for the propagation effects in the space domain is considered.

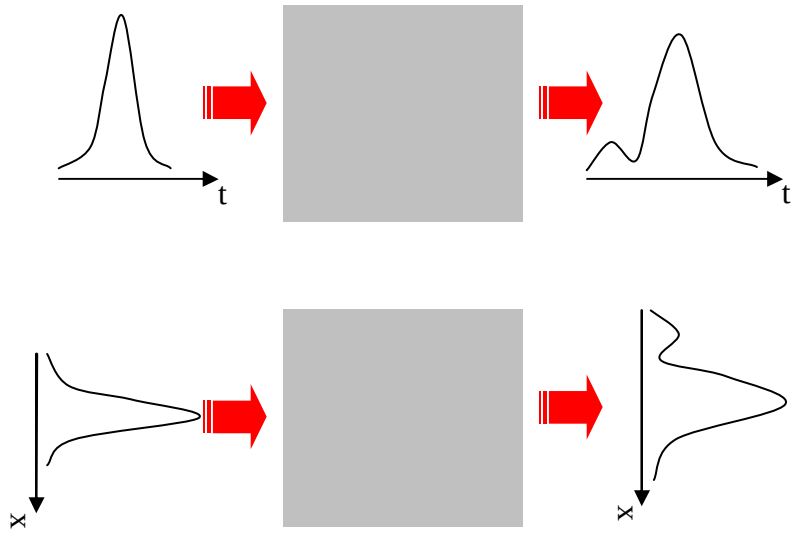


Figure 2.11. Analogy between beam propagation effects in the time domain (top) and in the space domain (bottom) is graphically illustrated.

In the applications based on the dispersive properties of PCs, the periodic subwavelength patterning of the material changes the dispersive properties discussed

above for an optical beam propagating through the photonic crystal structure [73]. By changing the material properties through patterning the material, a wider range of optical properties in integrated optical platforms will become available. Access to the materials with different optical properties (e.g., different diffractive index) in this fashion is achieved with the conventional microelectronic fabrication technology, and as a result, it eliminates the need for material growth or other sophisticated processes to bring the optical material property of interest to the integrated platform. Furthermore, by engineering the PC modes through fabrication, some dispersive properties can be achieved that have no counterpart in ordinary bulk optical materials. Therefore, this approach brings up the opportunity to manipulate optical properties of the material and to develop "synthetic" optical materials with dispersive properties of interest, relying only on the well-developed fabrication technologies.

In specific cases, when the period of the PC lattice is much smaller than the wavelength of the light (i.e., working in the first photonic band, away from the band edge), an effective medium theory [74] can be applied to analyze the properties of the PC structure. In the effective medium approximation, the PC region can be replaced by a bulk material with an average index that imitates the band structure of the periodic structure. In more elaborate cases (e.g., in the vicinity of the gaps or at higher photonic bands) at which the dispersion effects are stronger, a simple effective medium theory is not applicable anymore, and a more careful treatment is needed, which will be discussed in the next chapter.

### 2.3.1. Super-collimation

One of the first proposed applications of the dispersive properties of photonic crystals was the possibility of optical beam propagation with little or no diffraction through a photonic crystal region. This property of photonic crystals has been investigated by several groups [31,28,36,75-76], and is proposed along with unique reflection properties

[77-78] for routing the signal through an integrated platform. Specifically, the possibility of routing the signal with no "physical" guiding boundaries and the opportunity to achieve beam crossing with no cross-talk make the photonic crystal in super-collimation regime a viable candidate for signal routing in optical interconnects [79].

Flat regions of the band structure, a typical example of which is shown in Figure 2.12, are used for this purpose. In these regions, propagation of a beam from input to output in the PC structure showing super-collimation property adds the same spectral phase to all spatial-spectrum components of the beam; therefore, the optical beam is not affected by propagation through the photonic crystal structure and the shape of the beam is preserved.

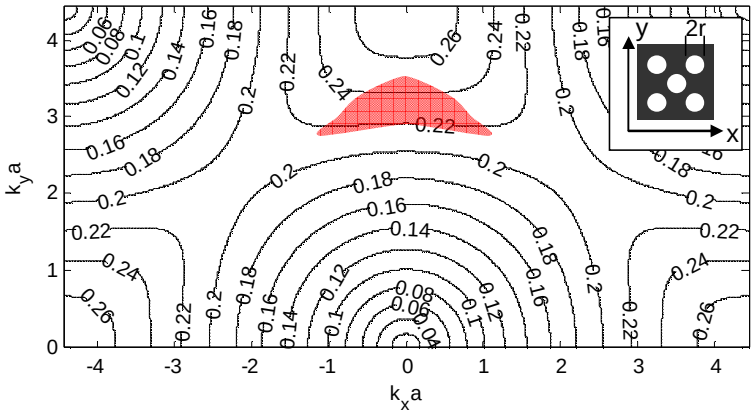


Figure 2.12. Band structure of a rotated square lattice slab-type PC structure of air-hole in Si in the form of iso-frequency contours in the 2D in-plane k-space is shown. The inset shows the lattice structure and the definition of coordinates (with $r/a$ = 0.30 in this structure). The lattice constant, $a$, is the distance between the centers of the closest neighbor holes, and the numbers marked on the contours are the corresponding normalized frequencies, $a/\lambda$. The shaded region is the range of band structure with super-collimation property (i.e., with small diffractive broadening effects).

The idea has been also combined with other properties of PCs for more functional devices. For example, the difference between the dispersion of two PCs in this range has been used to realize a dispersive integrated beam splitter [128]. It should be noted that the super-collimation property of the photonic crystals occurs in a limited bandwidth, and

that bandwidth (along with the corresponding spatial bandwidth of the beam) should be considered for successful implementation of the idea in different applications.

### 2.3.2. Negative refraction

Because of band folding effects, it is possible, for certain ranges of excitation, to have the refracted beam inside the photonic crystal structure on the same side as the incident beam coming from a bulk medium, as shown in Figure 2.13. Such an effect is referred to as negative refraction, but it should not be mixed with negative refractive index material with negative permittivity and negative permeability, as the physical origin of the effect is different.

Negative refraction in photonic crystals is closely related to the interface of the photonic crystal used for excitation. In other words, at a certain excitation condition light can be coupled to a PC mode with a direction of group velocity showing negative refraction. In that sense, negative refraction condition in photonic crystals is associated with the direction of group velocity of PC modes compared to that of a plane-wave in the bulk incident region for a specific interface of the photonic crystal. Note that the propagation of the PC mode inside the structure (apart from excitation) is then the ordinary propagation of a Bloch mode in a periodic structure. The idea of negative refraction in photonic crystals was used for realization of an open cavity structure [23]. It has also been used for isolation of signal from unwanted contributions in a photonic crystal demultiplexer [80]. Note that the term “negative refraction” is also used in the optical community in the context of imaging, but the term in those cases in fact refers to negative diffraction in photonic crystals, which will be discussed in the next section.

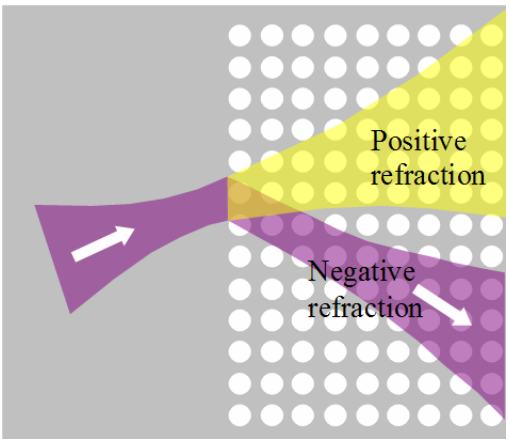


Figure 2.13. The positive and negative refraction properties in a PC are schematically demonstrated.

### 2.3.3. Negative diffraction

One of the unique properties of photonic crystals is the propagation effects for optical beams inside the periodic structure. It can be shown [31] that the diffraction of the envelope of an optical beam inside the photonic crystal is governed by the curvature of the band structure at the operation point (which is defined by the wavelength and the direction of propagation). Therefore, the diffraction properties of the beam propagation in photonic crystals can be controlled to have the desired features by designing the PC structure, i.e., by changing its properties (e.g., lattice type, size of the holes, shape of the holes, etc.) or by choosing the proper point on the band structure. In particular, operation at a point on the band structure with curvature of the band negative to that of ordinary bulk media exhibits the negative diffraction effect. Using negative diffraction at a certain propagation length, it is possible to compensate the propagation effects (e.g., diffractive beam broadening) caused by propagation in an ordinary bulk material (with a normal "positive" diffraction effect). Figure 2.14(a) schematically shows the diffraction compensation by negative diffraction effect inside a PC structure. The diffraction compensation effect has been discussed in the context of one-dimensional PC structures

[81], and its effect for focusing the optical beams has been investigated and discussed in detail in several reports [31,82-83].

Figure 2.14 shows the results for the propagation of a E-polarized Gaussian beam ($a/\lambda$=0.30) through a two-stage PC structure composed of two square lattices of air-holes in Si with $r_1/a$ = 0.40 and $r_2/a$ = 0.35 with the same lattice constant, as shown in Figure 2.14(b). The first PC region has a positive diffractive index. Thus, the propagation through the first PC region results in diffractive beam broadening. The resulting beam then enters the second PC region, which is designed to have a negative diffractive index. As a result, the diffraction effects in the second region, after some propagation length, cancel those introduced by propagation through the first region. The variations of the beamwidth of the Gaussian beam in the first and the second PC regions are shown in Figures 2.14(c) and 2.14(d), respectively. As seen in Figure 2.14, the original beamwidth is retrieved at $y=y_2$ using the propagation in the second PC. Further propagation in the second region adds more quadratic phase, which broadens the beam again. The negative diffractive index is related to the negative curvature of the bands of the PC, and can occur in both positive and negative refraction regimes.

The possibility of coupling evanescent components of an optical source to photonic crystal modes and transferring them to the output brings about the opportunity to perform imaging with resolutions beyond the diffraction limit. This topic has been subject to detailed investigations because of its potentially useful and significant applications, and proof of principle demonstrations have shown some of its capabilities under the broad title of subwavelength imaging [84,34].

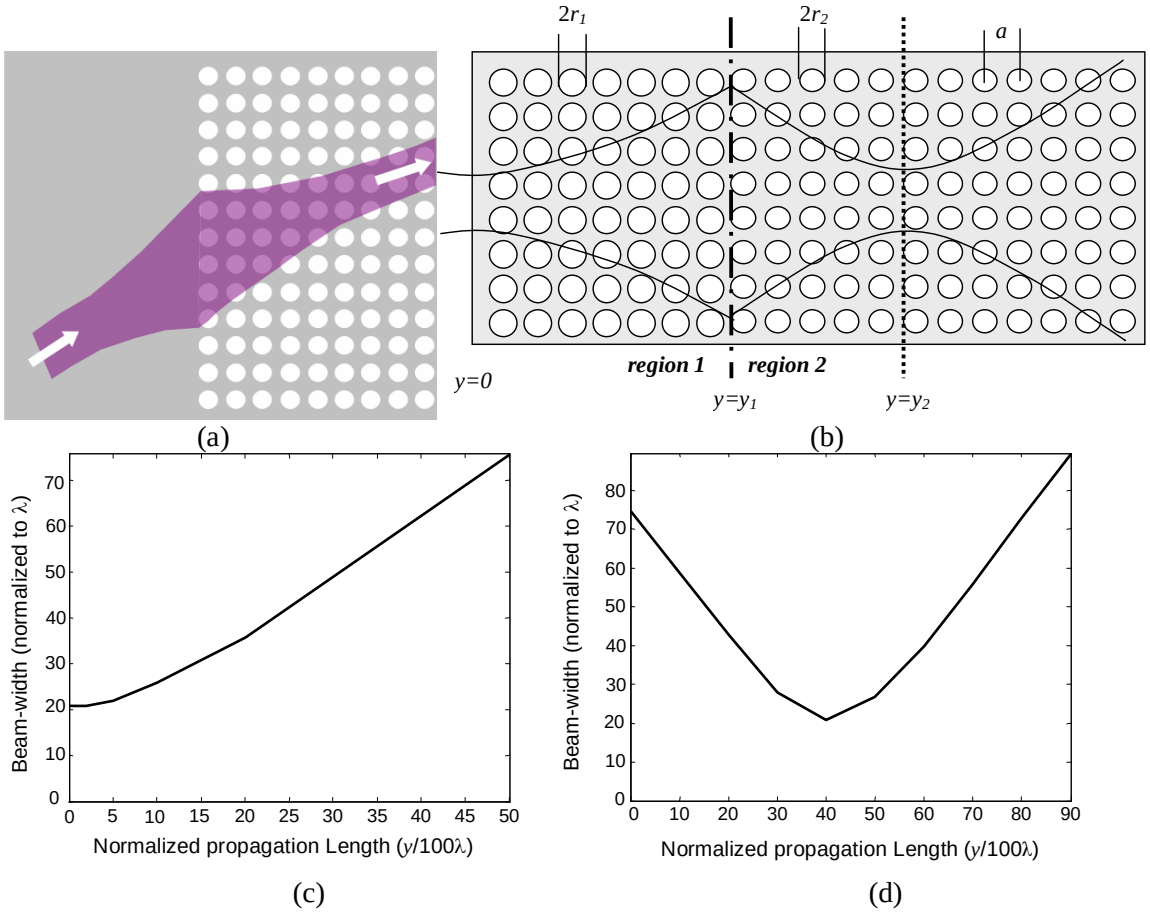


Figure 2.14. (a) The negative diffraction effect and diffraction compensation in a PC are schematically demonstrated. Beamwidth behavior is plotted for a Gaussian beam propagating in a two stage PC structure. (b) Beam variations inside the structure are illustrated. (c) Beamwidth in a square lattice of air-holes in Si ($r_1/a$ = 0.40), and (d) beamwidth of the resulting beam from (b) in a square lattice of air-holes in Si ($r_2/a$ = 0.35) are plotted. The initial width of the Gaussian beam entering region 1 at $y$=0 is 20$\lambda$, and $a/\lambda$ = 0.30 and E-polarization are considered.

## 2.3.4. Superprism effect

One interesting property of photonic crystals is their ability to spatially separate different wavelengths, similar to what a prism does. This phenomenon, called the superprism effect, arises from two facts. First, the dispersive properties of the PCs can be much different from those of the incident region; hence, incident waves with slightly different properties (e.g., small difference in wavelength) can excite much different PC modes inside the periodic region. Second, the direction of propagation of the optical beams inside the PC is governed by the direction of group velocity of the corresponding

PC mode. Photonic crystals can show strong (spatial) dispersion, in other words, the direction of group velocity can vary significantly in these structures, which can result in large angular dispersion (i.e., large change in the angle of group velocity when changing the wavelength) that leads to much stronger spatial separation of different wavelength channels compared to a conventional prism that relies on material dispersion. The overall concept is schematically shown in Figure 2.15(a). Figure 2.15(b) shows the region on the band structure with a strong superprism effect in a 45°-rotated square lattice PC. The superprism effect can be used to achieve spatial separation of different wavelength components of an incident beam in a photonic crystal.

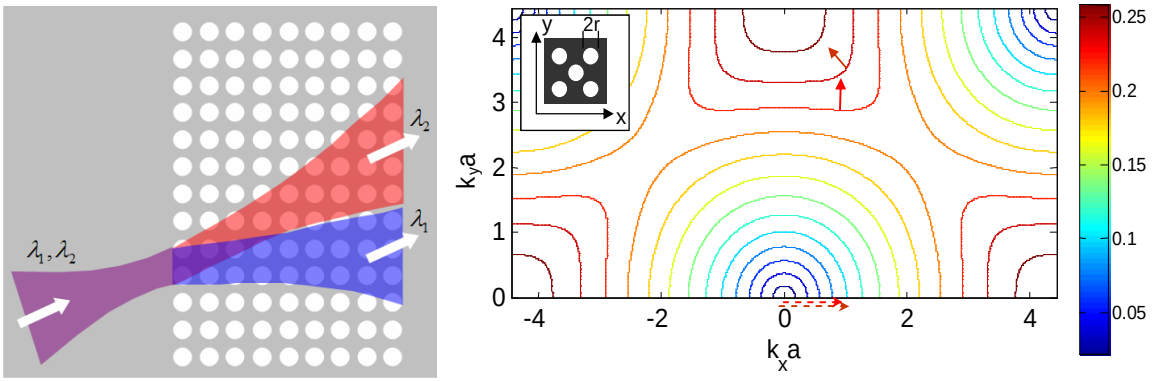


(a) (b)

Figure 2.15. (a) The superprism effect in a PC is schematically demonstrated. (b) In-plane band structure of a 45°-rotated square lattice PC structure on an SOI wafer is shown. The inset shows the lattice structure and the definition of coordinates (with r/a = 0.30 in this structure, a being the lattice constant), and the color coding of the contours represents the corresponding normalized frequencies, a/λ. Two PC modes excited by a plane wave coming from the unpatterned slab at an angle of 15° are shown on the band structure. The dashed arrows show the tangential wavevector of the excitation wave along the interface, and the solid arrows show the group velocity directions of the modes excited inside the PC structure.

Kosaka et al. suggested the potential behavior based on anomalous dispersion property of photonic crystals [39] and proposed a highly sensitive phenomenon, named the superprism effect, for wavelength demultiplexing applications [35]. The basic theory has been developed based on the group velocity direction and its relation to the PC band structure [73,85]. The implementation of wavelength separation in a planar PC structure

has been demonstrated with good agreement with the theory [37]. Also, some of the implementation issues and basic limitations and considerations of superprism-based demultiplexers have been addressed and discussed [86-87].

The idea of using the PC superprism effect for wavelength demultiplexing was discussed and experimentally demonstrated [22,88-94,80] by different groups in different operation ranges. An alternative approach, making use of the phase velocity of the photonic crystal modes, has also been proposed for improved performance of photonic crystal demultiplexers [95-97].

### 2.3.5. Slow light propagation

The distributed resonance effect (i.e., continuous inter-coupling of Bloch orders) results in a slow-wave property in the vicinity of photonic mode gaps. Intuitively, this effect can be related to multiple reflections of light (at a working region close to the Bragg condition) inside the structure during propagation, as schematically shown in Figure 2.16. Such a property makes photonic crystals a good candidate for a slow-wave structure with several potential applications like delaying light and field amplitude enhancement for nonlinear optical applications. Even though this effect has not been directly used to slow down light in practical applications, the resulting improved density of states has been used in applications such as band-edge lasing [24-25].

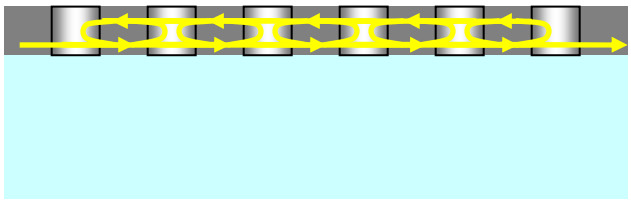

Figure 2.16. Multiple reflections of light in a PC structure are schematically shown. The distributed resonance effect in this structure results in lower effective group velocity values and enhanced field amplitudes.

# CHAPTER 3

# ANALYSIS TOOLS FOR DISPERSIVE APPLICATIONS OF PHOTONIC CRYSTALS

New device concepts that emerge from the unique dispersive properties of photonic crystals and new demands for applications arising from those concepts need new tools for efficient modeling of these structures. In developing such analysis tools, it is of particular importance to have a method that, in addition to direct analysis of the structure (i.e., finding the solution for a particular case), provides us with some insight on the physics of the problem. Such an insight is crucial in the design process, where solutions and modifications for specific goals are desired.

The analysis of photonic crystal structures for their dispersive properties is inefficient using direct electromagnetic wave simulators that use numerical techniques such as FDTD method [57], time-domain beam propagation method (TD-BPM) [98], or Multiple Scattering Technique (MST) [99]. The reason is that the required size of the structure for observing the desired dispersive effects is relatively large; however, there are sub-wavelength variations in the material properties that require a fine simulation grid. Thus, there are intensive memory, computation and time costs in direct simulation of the structure. Spectral methods based on modal expansion of the field are advantageous for the analysis of these structures [100]. The reason for modal approaches (based on the properties of the modes) being more efficient in modeling these devices is that they eliminate the unnecessary calculations for the simulation of the beam throughout the structure and limit it to the input and output planes. There are still potentials to simplify the analysis since in most practical applications only the envelope of the beam (not its exact profile calculated in modal approach) is needed. In particular, a diffractive index model can be used [31] to analyze beam propagation effect inside

photonic crystals using simple geometrical optics methods; furthermore, this approximate method gives insight into the beam propagation process and will be helpful to avoid a mass of computations for each particular case.

In this chapter, I will investigate these propagation effects inside PCs using modal expansion and derive a simple (approximate) diffractive index model for the applications mentioned before. I will show that diffractive index model only requires numerical simulation for the calculation of band structure, which is typically performed by analyzing only a unit cell of the PC. After finding the diffractive index, the propagation of electromagnetic waves inside the PC can be analyzed using the well-known analytic formulas for bulk media. Thus, the diffractive index model proposed here reduces the computation time for the analysis of electromagnetic wave propagation inside PCs by several orders of magnitude. Using this model, I will also explain how diffraction control devices can be implemented by designing proper PC structures.

### 3.1. Modal Approach

The most common method for analyzing propagation effects is to use modal approach. In this method, the signal is expanded over the modes of the structure and knowing the propagation properties of each mode and by superposition of the modes after propagation at the output, the resulting signal is found. The only requirement for validity of this process is the validity of mode expansion and superposition, which is satisfied in linear systems. This approach can be used to analyze the propagation effects in photonic crystals as well, as schematically demonstrated in Figure 3.1.

To briefly formulate the relations, the beam profile at the input plane, $p_1(x)$, and at the output plane, $p_2(x)$, can be represented as

$$p_1(x) = \int_{k_x} \sum_{k_y(k_x)} a(\mathbf{k})\, f_{\mathbf{k}}(x, y_1) dk_x \,, \tag{3.1}$$

and

$$p_2(x) = \int_{k_x} \sum_{k_y(k_x)} a(\mathbf{k}) f_{\mathbf{k}}(x, y_2) dk_x \ , \tag{3.2}$$

in which, the integration over $k_x$ covers the spatial spectrum of the beam in the transverse direction, and the summation represent all modes of the photonic crystal structure (both real and complex) for each $k_x$. The weight function, $a(\mathbf{k})$, is the amplitude of each mode excited at the input and is found by mode matching of the input beam to photonic crystal modes. Note that in this representation the propagation effects are included in properties of each mode (through $f_{\mathbf{k}}$ functions), and these propagation effects can be found simply by referring to the Bloch theorem for PC modes which states that

$$f_{\mathbf{k}}(x, y) = U_{\mathbf{k}}(x, y) e^{jk_x x} e^{jk_y y} \ , \tag{3.3}$$

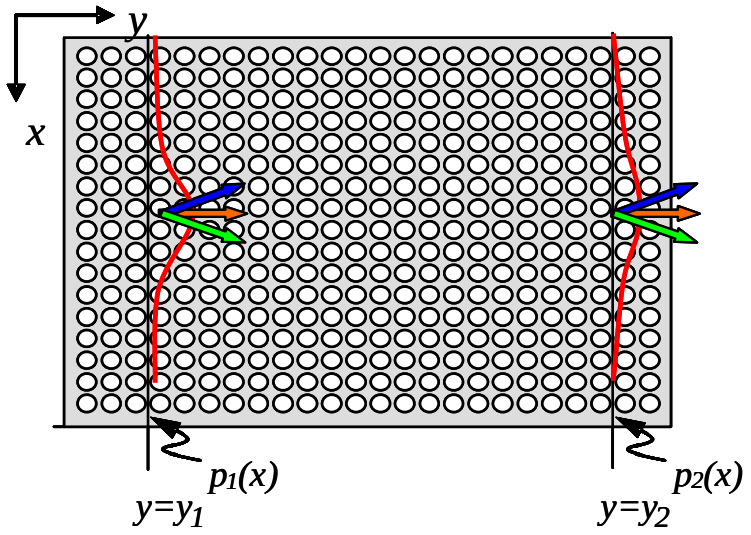


Figure 3.1. The operation principle of the modal approach for the analysis of beam propagation in PCs is demonstrated. The input beam is expanded over photonic crystal modes, and the resulting output beam is found using the same expansion and by including the propagation effects of each of the constituent modes.

For the actual implementation of this method, all PC modes are found using one of the standards methods for PCs (In this work, I have used PWE technique; see Appendix B for calculation of PC modes at a certain frequency and for a given transverse

wavevector). However, direct application of modal approach suffers limitations in practice, since it requires finding all eigenvalues and eigenmodes of the structure. This process of finding the modes and projecting the input signal on them can still be computationally intensive in practice. Figure 3.2 shows the calculated beam profiles at different propagation lengths inside a square lattice 2D PC (air holes in Si, $r/a$=0.4) for an E-polarized input Gaussian beam. As it can be observed from Figure 3.2, the exact beam profile has fine spatial features that are related to the microscopic variations of the beams in the inhomogeneous PC region (through dielectric regions and hole regions of the PC). Such exact solutions of the beam profile at the output are not needed in most practical cases. In the following sections, I will introduce further simplifications for the analysis tools to reduce the computations by focusing only on the envelope of the beam which is the main characteristic of interest in most dispersive applications of PCs.

### 3.2. Envelope Transfer Function

Knowing that the envelope of the beam is of main interest in dispersive application of PCs, we can model the propagation effect inside the PC as an input-output system, with envelopes of the input and output beams being the signals through these systems. For simplicity, the structures we consider here are two-dimensional photonic crystals and the optical beams are at one of the orthogonal E- or H-polarization (with electric or magnetic field perpendicular to the plane of periodicity, corresponding to TM and TE polarizations in planar 2D PCs, respectively). Also, we limit our discussion to in-plane propagation effects that can be either in a 2D photonic crystal or a slab-type planar photonic crystal. Nonetheless, it can be shown that a similar treatment can be used for other periodic structures as well. For generality, we represent the field as $f$, which can be the transverse component of either the electric field or the magnetic field inside the structure. Using Bloch theorem, a photonic crystal mode corresponding to the wavevector $\mathbf{k} = \hat{x}k_x + \hat{y}k_y$ in its plane-wave expansion representation can be written as

$$f_{\mathbf{k}}(x,y) = U_{\mathbf{k}}(x,y)e^{jk_x x}e^{jk_y y}, \tag{3.4}$$

$$U_{\mathbf{k}}(x,y) = \sum_m \sum_n \tilde{f}_{mn} e^{jm\mathbf{K}_u\cdot\mathbf{r}} e^{jn\mathbf{K}_v\cdot\mathbf{r}}. \tag{3.5}$$

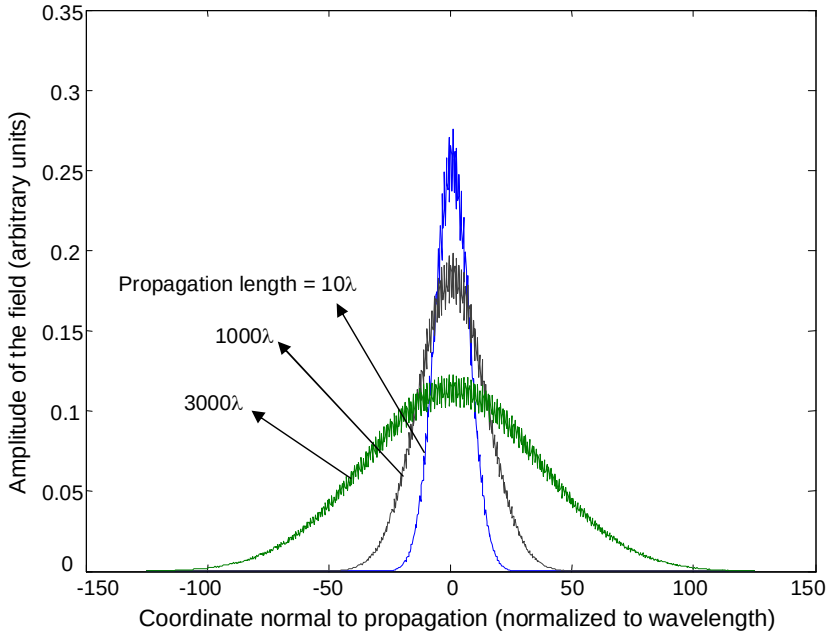


Figure 3.2. Beam profiles are plotted for a Gaussian beam normally incident on a square lattice PC (air holes in Si, $r/a$=0.4) at different propagation lengths inside the PC (E-polarization at $a/\lambda$=0.3).

We assume, as shown in Figure 3.3, that the input beam excites PC modes around point $O$ in the band structure. We define $\xi$ and $\eta$ as the coordinates in the directions tangent and normal to the constant frequency contour at point $O$ (Figure 3.3). Thus, the direction of group velocity (or wave propagation) at point $O$ is along the $\eta$ direction. Lattice wavevectors of this photonic crystal are given by

$$\begin{cases} \mathbf{K}_u = \mathbf{x}K_u \sin\theta + \mathbf{y}K_u \cos\theta \\ \mathbf{K}_v = \mathbf{y}K_v \end{cases}. \tag{3.6}$$

Assume we have an initial distribution $p_1(u)$ along the $u$-axis inside the PC. We can expand this distribution over photonic crystal modes as

$$
\begin{aligned}
p_1(x) &= \int A(k_x) U_{\mathbf{k}}(x, y_1) \exp(jk_x x) \exp(jk_y y_1) dk_x \\
&= \int A(k_x) \left( \sum_m \sum_n \tilde{f}_{mn}(k_x) \exp(jmK_x x) \exp(jnK_y y_1) \right) \exp(jk_x x) \exp(jk_y y_1) dk_x \qquad (3.7) \\
&= \int A(k_x) \left( \sum_m \sum_n \tilde{f}_{mn}(k_x) \exp[j(k_x + mK_u \sin\theta)x] \exp[j(k_y + mK_u \cos\theta + nK_v) y_1] \right) dk_x
\end{aligned}
$$

The Fourier transform of this distribution can be calculated as

$$
P_1(k) = \sum_m \sum_n A(k - mK_u \sin\theta) \tilde{f}_{mn}(k - mK_u \sin\theta) e^{jk_y (k - mK_u \sin\theta) y_1} e^{j(mK_u \cos\theta + nK_v) y_1} . \qquad (3.8)
$$

The details of these derivations are presented in [31]. Note that the spectral content is assumed to be band-limited around $k_{x0}$, in that sense, the actual spatial profile of the beam (excluding the phase term) is determined by $\hat{A}(k) = A(k + k_{x0})$. To find the envelope of the beam distribution, only the low frequency portion of $P_1(k + k_{x0})$ should be kept. For the low-frequency portion of the signal, if the signal is band-limited to $[k_{x0} - K_u \sin\theta/2, k_{x0} + K_u \sin\theta/2]$, we can eliminate the terms with $m \neq 0$ in Equation (3.8). The spectrum of the envelope of the beam profile (excluding the phase term), $\hat{P}_1(k)$ can be found as

$$
\hat{P}_1(k) = A(k + k_{x0}) \exp[jk_y (k + k_{x0}) y_1] \sum_n \tilde{f}_{0n}(k + k_{x0}) \exp(jnK_y y_1) . \qquad (3.9)
$$

Now if we consider the same beam at the plane $y = y_2$, we have

$$
\hat{P}_2(k) = A(k + k_{x0}) \exp[jk_y (k + k_{x0}) y_2] \sum_n \tilde{f}_{0n}(k + k_{x0}) \exp(jnK_y y_2) . \qquad (3.10)
$$

If $y_2$-$y_1$=$2\pi l/K_y$, then

$$
\hat{P}_2(k) = \hat{P}_1(k) \exp[jk_y (k + k_{x0})(y_2 - y_1)], \qquad (3.11)
$$

which means that the effect of propagation from $y=y_1$ to $y=y_2$ can be represented as a phase change in the spatial spectral domain similar to plane-wave-type propagation with

propagation constant $k_y$. Thus, the main effect of propagation in PCs is the phase variations of PC modes from initial plane to the observation plane.

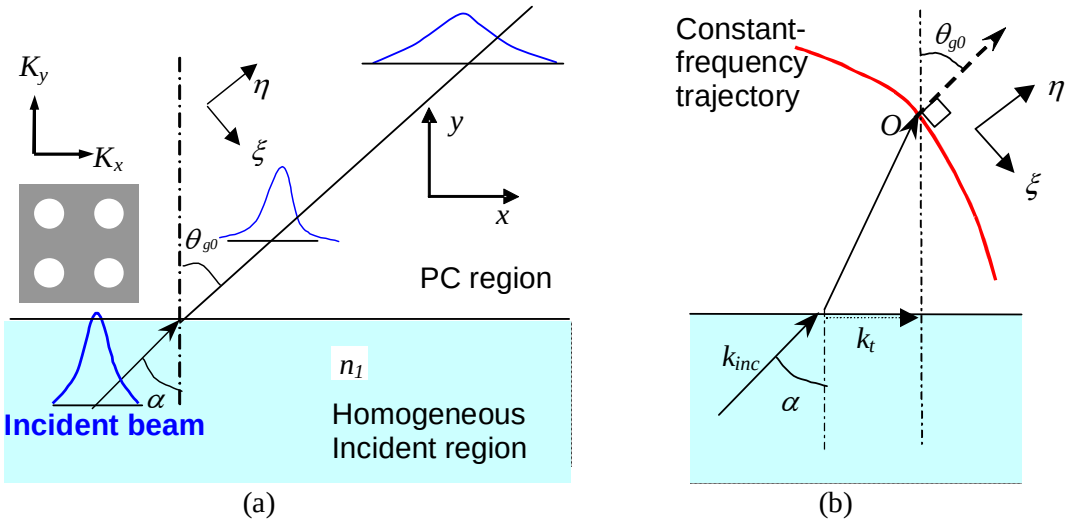


Figure 3.3. (a) The interface of a PC with a homogeneous incident region (with refractive index $n_1$) is shown and the corresponding parameters are introduced. $\alpha$ is the angle of incidence and $\theta_{g0}$ is the angle of group velocity inside the PC region corresponding to the main component of the incident beam. (b) Relevant wavevectors corresponding to the incident wave and the PC mode are depicted.

Based on the derivations given above, we can write the transfer function for the envelope of an optical beam propagating through the structure from $y=y_1$ to $y=y_2$ plane as

$$H(k) = \frac{\hat{P}_2(k)}{\hat{P}_1(k)} = \exp[jk_y(y_2 - y_1)], \tag{3.12}$$

where $k_y = k_y(k_x)$ is related to $k_x$ through the dispersion relation of the structure at the constant temporal frequency of the beam. The relation is exactly the same if we monitor the propagation in a bulk medium. Based on this similarity, we extend the relation for a beam propagating in the bulk medium along the $\eta$ direction (Figure 3.3) to the photonic crystal case, and write the propagation relation for the beam propagating along the direction $\eta$ as [31]

$$H(k_\xi) = \frac{\hat{P}_2(k_\xi)}{\hat{P}_1(k_\xi)} = \exp[jk_\eta(k_\xi)(\eta_2 - \eta_1)], \tag{3.13}$$

in which $\eta$ and $\xi$ are the coordinates along the directions parallel and normal to the direction of propagation, respectively, as shown in Figure 3.3. $H(k_\xi)$ is the envelope transfer function describing the evolution of the envelope of the beam in propagation through a periodic structure.

In Figure 3.4 the results for the exact simulation of the properties of a Gaussian beam incident on a square lattice photonic crystal at different propagation lengths inside the PC region are compared with those calculated using the envelope transfer function. It can be observed that the approximate model represents the envelope of the beam inside the structure with very good accuracy.

### 3.3. Diffractive Index Model

Using the envelope transfer function, the analysis of evolution of the envelope of the optical beams inside photonic crystals reduces to a standard spectral-domain analysis. We can further simplify the problem based on its analogy with ordinary bulk media and find a diffractive index that describes the diffraction of the optical beams in these structures. The importance of such an approximate method is two-fold: on one hand, it converts the wave propagation in PC to a conventional case in geometrical optics, and enables us to extend and use all the available insight of the ordinary wave propagation phenomena to photonic crystals. In addition, by using simple Gaussian beams relations in the PC structures, we can find analytical and semi-analytical formulas describing the basic properties of the devices under investigation (e.g., cross-talk level, required propagation length, …), which are crucial in quantifying the performance of the devices and for engineering the design parameters.

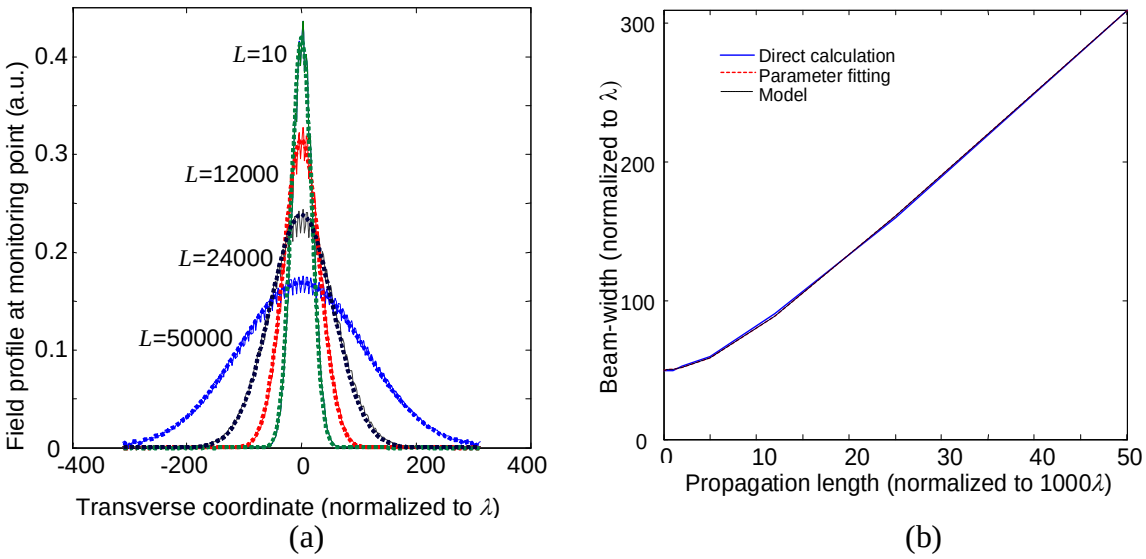


Figure 3.4. (a) Beam profiles (normal to the direction of propagation) for the propagation of a Gaussian beam through a square lattice photonic crystal (air-holes in Si, $r/a$=0.4 at normalized temporal frequency $\omega_n=a/\lambda$=0.3) are shown for different propagation lengths ($L$) inside the PC. The field has E-polarization, and the initial beamwidths (at $L$=0) are 50$\lambda$. Solid lines are the results of exact simulations using a modal approach (based on PWE technique), and dotted lines are those calculated using the envelope transfer function method. (b) The beamwidth variation with propagation length inside the PC is shown. The solid line is found directly from exact modal approach, the dashed line is found by fitting the parameters to Gaussian beam propagation model, and the dotted line is the one calculated using the approximate method presented in this chapter.

In transition from the envelope transfer function model to an approximate diffractive index model, there is an extra assumption involved that requires the spatial spectrum response of the structure (represented by the spectral phase in the envelope transfer function) to vary slowly over the range of interest. Knowing that the constant-frequency contour is smooth around the operation point, we can approximate the transfer function by the first three terms of its Taylor expansion,

$$H(k_\xi) = \exp\left\{j[\Phi_0 + (k_\xi - k_{\xi 0})\Phi_1 + (k_\xi - k_{\xi 0})^2 \Phi_2]\right\}, \tag{3.14}$$

where we have

$$\Phi_0 = (\eta_2 - \eta_1)k_\eta(k_{\xi 0}), \tag{3.15}$$

$$\Phi_1 = (\eta_2 - \eta_1)\frac{\partial k_\eta}{\partial k_\xi}\bigg|_{k_\xi = k_{\xi 0}}, \tag{3.16}$$

$$\Phi_2 = \frac{1}{2}(\eta_2 - \eta_1)\frac{\partial^2 k_\eta}{\partial k_\xi^2}\bigg|_{k_\xi = k_{\xi 0}} . \tag{3.17}$$

These terms can be used to describe the beam propagation effects inside photonic crystals. The first term in Equation (3.15) is a simple phase change that does not affect the shape of the beam. The first-order spectral phase term in Equation (3.16) represents a shift in the location of the beam with respect to the selected coordinates as the beam propagates through the structure. In other words, it represents the direction of propagation of the optical beam inside the structure. The second-order term is related to the chirp parameter (*b*) [72] that is defined as

$$b = \Phi_2 = \frac{1}{2}(\eta_2 - \eta_1)\frac{\partial^2 k_\eta}{\partial k_\xi^2}\bigg|_{k_\xi = k_{\xi 0}} . \tag{3.18}$$

The chirp parameter is essentially responsible for beam broadening during propagation, similar to its time-domain counterpart [72].

If we define $\Theta = \partial k_\eta / \partial k_\xi$, then the angle of the group velocity direction (i.e., normal to the constant frequency contour) with respect to the normal to the interface of the PC and the incident medium can be written as

$$\theta_g(k_\xi) = \theta_{g0} + \tan^{-1}(\partial k_\eta / \partial k_\xi) . \tag{3.19}$$

where $\theta_{g0}$ is the angle of group velocity for $k_{\xi 0}$, as shown in Figure 3.3. Since $\Theta(k_{\xi 0}) = 0$, using the definition of the direction of group velocity, it is found that

$$\frac{\partial \theta_g}{\partial k_\xi}\bigg|_{k_\xi = k_{\xi 0}} = \left(\frac{1}{1+\Theta^2}\frac{\partial \Theta}{\partial k_\xi}\right)\bigg|_{k_\xi = k_{\xi 0}} = \frac{\partial^2 k_\eta}{\partial k_\xi{}^2}\bigg|_{k_\xi = k_{\xi 0}} . \tag{3.20}$$

Therefore,

$$b = \frac{1}{2}(\eta_2 - \eta_1)\frac{\partial \theta_g}{\partial k_\xi}\bigg|_{k_\xi = k_{\xi 0}} , \tag{3.21}$$

which suggests that the diffraction property of the medium depends basically on the local value of $\partial\theta_g/\partial k_\xi$ (or equivalently, the curvature of the constant frequency contour) in the 2D *k*-plane. For a bulk homogeneous medium with refractive index *n* and free-space wavevector $k_0$, direct calculations result in

$$\left.\left(\frac{\partial\theta_g}{\partial k_\xi}\right)\right|_{k_\xi=k_{\xi 0}} = \frac{1}{k_0 n}. \tag{3.22}$$

We use this relation to define the diffractive index of the medium as

$$n_e = \frac{1}{k_0\left(\partial\theta_g/\partial k_\xi\right)_{k_\xi=k_{\xi 0}}}. \tag{3.23}$$

Noting that $\left(\partial k_t/\partial k_u\right)_{k_\xi=k_{u0}} = \cos\theta_{g0}$ and $k_t = n_1 k_0 \cos\alpha$ ($k_t$ is the component of the incident wavevector that is parallel to the interface, as shown in Figure 3.3), Equation (3.23) can be rewritten as

$$n_e = \frac{1}{k_0\left(\partial\theta_g/\partial k_t\right)_0 \cos\theta_{g0}} = \frac{n_1\cos\alpha}{\left(\partial\theta_g/\partial\alpha\right)_0 \cos\theta_{g0}}, \tag{3.24}$$

in which subscript "0" is used to emphasize that these values are local values calculated at the point for which Taylor expansion is written (i.e., at $k_\xi = k_{\xi 0}$). Note that both the magnitude and the sign of $n_e$ are important. The magnitude determines how much phase chirp is added to the beam, and the sign is either positive (positive chirp, as in ordinary dielectric media) or negative (negative chirp). The negative chirp has no counterpart in the conventional wave propagation phenomena in dielectric medium and can be used to compensate the effect of ordinary diffraction. If the assumptions for the above derivation are satisfied, the diffractive index model can be used for describing all the important properties of beam propagation inside PCs. This provides better understanding of wave propagation phenomena in PCs, and eliminates the need for massive direct electromagnetic simulations.

To verify the applicability of the method, we consider the structure shown in Figure 3.1. There are two different issues to be justified. First, that the envelope function used here is a good representation of the extent of the optical beam inside the photonic crystal; and second, that the model accurately describes the behavior of the envelope of the beam during the propagation. As a reference of comparison for both cases, we use a brute-force method of analysis for the beam inside the structure and compare the results with those obtained using our approximate method. In the brute-force method, we use a modal expansion for the propagation, and a mode-matching scheme for the interface to obtain the transmitted field inside the photonic crystal region.

The structure we analyze is a two-dimensional square lattice photonic crystal of air-holes in Si. The holes have a radius of $r = 0.35a$, where $a$ is the lattice constant. The incident beam has a Gaussian profile (at $\lambda = a/0.30$ and with a waist of $2w_0 = 4\lambda$) and is incident from air to the photonic crystal. The polarization of the incident beam is assumed to be E-polarized (i.e., electric field parallel to the axis of cylindrical holes). We also assume that the interface is parallel to one of the primary lattice directions of the photonic crystal. We first calculate the properties of this beam as it propagates through the structure using brute-force technique. Figure 3.5(a) shows the beam profiles at the initial plane ($y$=10$a$) and final plane ($y$=5000$a$). Note that the effects caused by the mismatch at the boundary are vanished at the initial plane after propagation for ten unit cells and the initial field distribution is related solely to propagating modes of the structure. In Figure 3.5(b) the envelopes of the field profiles at different propagation lengths are calculated and shown using a low-pass filter which keeps only the low spatial frequency portion of the beam profile. It can be observed that all these envelope functions have Gaussian spatial distribution and propagation in the structure has the same broadening effect as in the conventional homogeneous media.

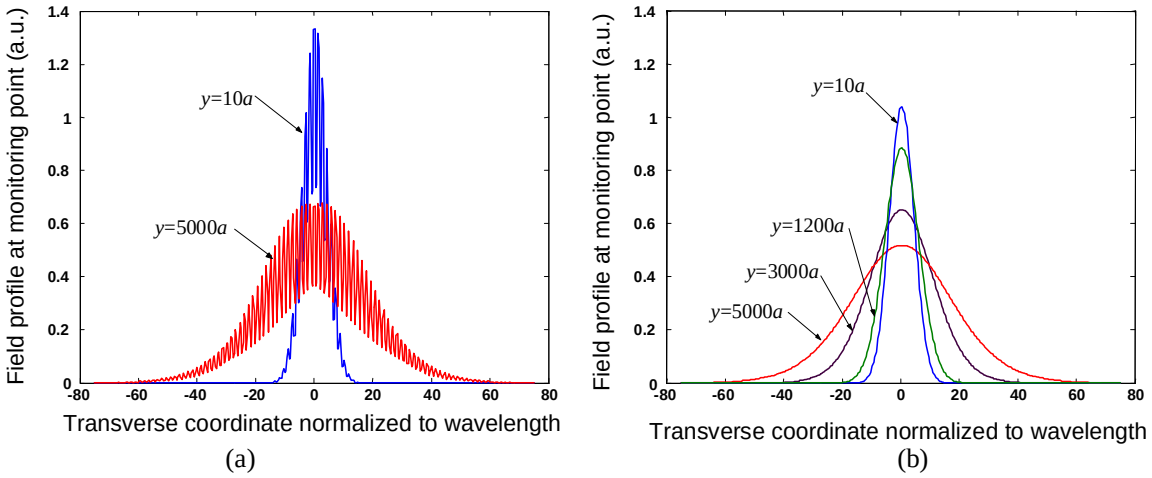


Figure 3.5. (a) Field profiles at initial point ($y$=10$a$) and final point ($y$=5000$a$) are shown. (b) Calculated envelopes of beam profiles at different propagation lengths inside the photonic crystal structure are shown. These envelopes are in good agreement with those obtained by a diffractive index model (with $n_e$=13.5).

To check the validity of the diffractive index model, we first calculate the effective diffraction index at different points in the band structure (iso-frequency contours in the k-space). Using the diffractive index calculated for the structure analyzed in Figure 3.5 (i.e., $n_e$=13.5) and assuming a Gaussian beam propagation, we calculate the beamwidth at different propagation distances ($L$). The band structure of this photonic crystal is shown in Figure 3.6(a). We also calculate the beamwidths at different propagation lengths using the brute-force simulation and compare the results obtained using the two techniques in Figure 3.6(b). As it can be seen from Figure 3.6(b), the beamwidth variation has the same behavior as that of a Gaussian beam propagating in a homogeneous medium with refractive index of 13.5 [which is the value we obtain using Equation (3.23)]. Note that this effective diffraction index ($n_e$=13.5) is much different from the refractive index of Si (which is 3.38) and the average refractive index of the structure (which is 2.7).

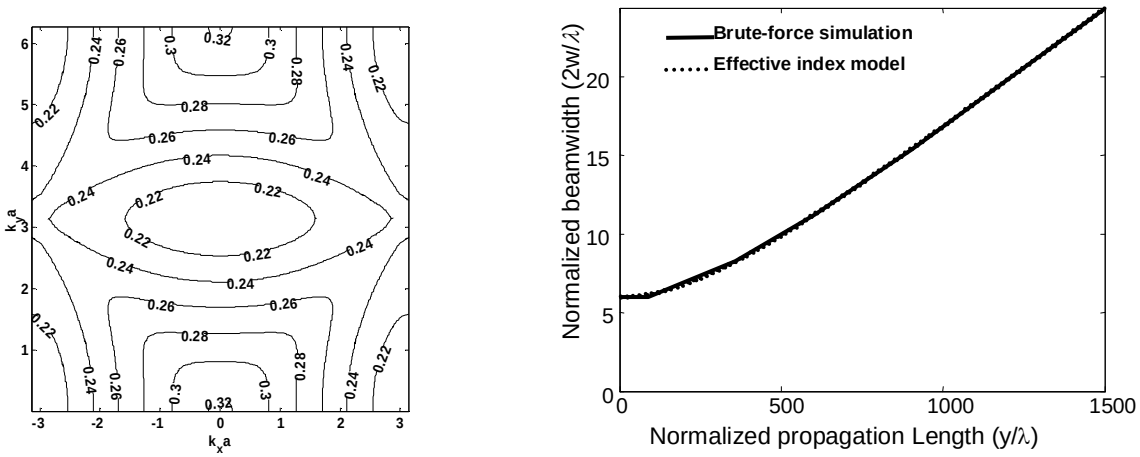


(a) (b)

Figure 3.6. (a) Band structure of the square lattice photonic crystal structure under consideration is shown in the form of iso-frequency contours in k-space. (b) Variations of the beamwidth during the propagation through the structure are shown for both the direct simulation results (solid line) and the results obtained by a Gaussian beam approximation and the diffractive index model (dashed line).

We repeat the same procedure in a square lattice photonic crystal of air-holes in Si ($r/a$=0.40) with an incident Gaussian beam with a beamwidth of 10λ and E-polarization. I have repeated the simulations for different normalized frequencies ($\omega_n = a/\lambda$) and compared the results for the diffractive index and the normalized Rayleigh range obtained from the diffractive index model with those obtained by curve-fitting into the data obtained from brute-force simulations. The results are shown in Table 3.1. It can be seen that the agreement is good and the model is valid for all practical purposes.

Table 3.1. Comparison of diffractive index and Rayleigh range values obtained from simulations with those obtained from the diffractive index model.

| $\omega_n$ | $n_{e,sim}$ | $n_e$ | $z_{0,sim}/\lambda$ | $z_0/\lambda$ |
|---|---|---|---|---|
| 0.23 | 1.13 | 1.17 | 370 | 368 |
| 0.24 | 1.90 | 1.92 | 600 | 603 |
| 0.25 | 2.29 | 2.27 | 720 | 713 |
| 0.26 | 2.61 | 2.63 | 780 | 826 |
| 0.27 | 2.86 | 2.94 | 900 | 924 |
| 0.28 | 3.13 | 3.23 | 1020 | 1015 |
| 0.29 | 3.49 | 3.57 | 1050 | 1122 |
| 0.30 | 4.18 | 4.17 | 1250 | 1310 |

### 3.4. Generalized Diffractive Index Model

There are cases in which either the second-order spectral phase term is very small (compensated in propagation through regions with opposite diffraction effects) or higher-order terms are considerably large (bands deformed drastically from their original quadratic forms). In these cases, the effect of higher-order terms comes into the picture and results in further beam broadening. Some measures are needed to quantify this broadening so that they can be used in practical designs. Unlike the second-order case, the effect of broadening for higher-order terms is not simply the main lobe of the beam profile getting wider. Side-lobes usually appear, and the measure has to change (Clearly, the full-width at half-maximum measure does not work anymore). A good measure of how distributed the beam has become is the root-mean-square (rms) beam size defined as

$$w_{rms}^2 = \frac{\int_x x^2 I(x)dx}{\int_x I(x)dx}, \tag{3.25}$$

where $I(x)$ is the intensity of the beam (amplitude squared). Using this measure, the beam size for a third-order spectral phase term is calculated and shown in Figure 3.7(a). The behavior is very similar to the ordinary second-order spectral phase [31], and this similarity suggests that one can assign a corresponding diffractive index to it. A similar behavior is seen for the case with a dominant fourth-order spectral phase as plotted in Figure 3.7(b).

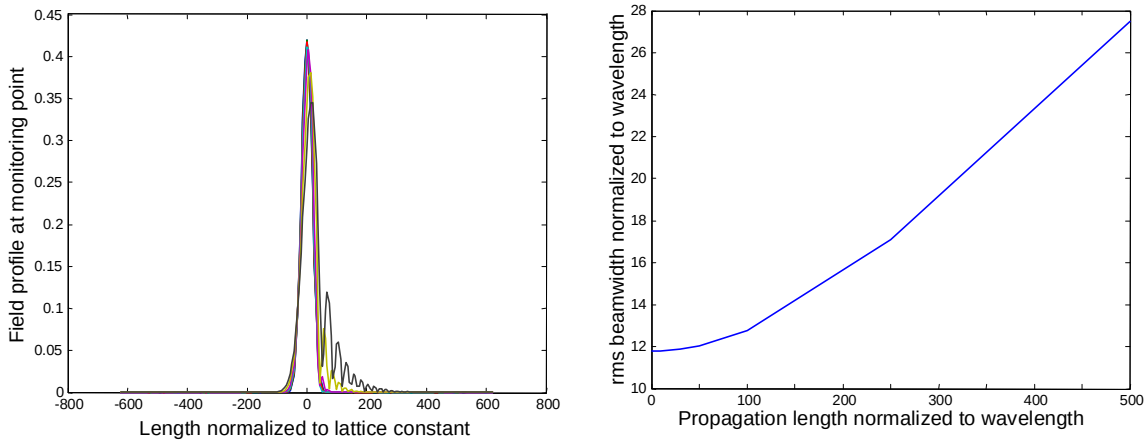


(a)

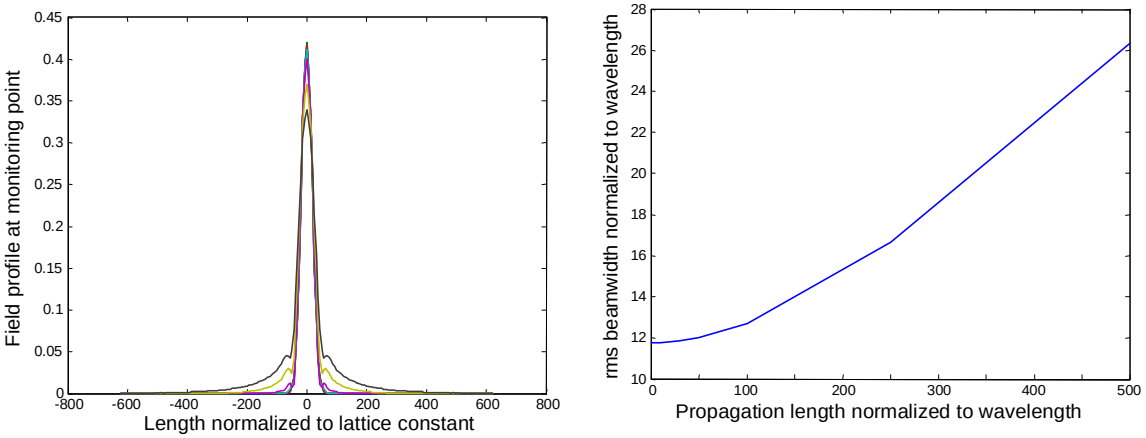


(b)

Figure 3.7. Beam profile and variation of beamwidth versus propagation length are plotted for (a) the third-order and (b) the fourth-order spectral phase terms.

If $A(k_\xi)\exp[\,j\Phi(k_\xi)]$ is the normalized spatial Fourier transform of the beam profile with

$$\int_{k_\xi} A(k_\xi)^2\,dk_\xi = 1, \tag{3.26}$$

the rms-beamwidth of the beam can be found as [72]

$$w_{rms}^2 = \int_{k_\xi} A'(k_\xi)^2\,dk_\xi + \int_{k_\xi} A(k_\xi)^2\,\Phi'(k_\xi)^2\,dk_\xi\,, \tag{3.27}$$

in which $A'(k_\xi)$ and $\Phi'(k_\xi)$ are the first derivatives of $A(k_\xi)$ and $\Phi(k_\xi)$ (with respect to $k_\xi$), respectively. To analyze the beam propagation effects, we assume that the amplitude of each spectral component of the beam remains intact (which is valid if there is no loss, no gain, and no coupling between modes in the system). The spectral phase term $\Phi(k_\xi)$ is caused by the spatial dispersion during propagation of the optical beam. Starting with a minimum phase Gaussian beam with a beam waist of $2w_0$, given by

$$A(k_\xi) = \left(\frac{w_0}{\sqrt{2\pi}}\right)^{1/2} \exp\left(-\frac{1}{4} w_0^2 k_\xi^2\right), \tag{3.28}$$

entering a material with second-order spectral phase $\Phi(k_\xi) = b_2 k_\xi^2$ and length $L$, the output rms beamwidth can be directly calculated from Equation (3.27) as

$$w_{rms,2}^2 = \frac{w_0^2}{4} + \frac{4b_2^2}{w_0^2}, \tag{3.29}$$

with

$$b_2 = \frac{1}{2}\frac{d^2\Phi}{dk_\xi^2} = \frac{1}{2}\frac{d^2 k_\eta}{dk_\xi^2} L = \frac{L}{2k_0 n_{e2}}, \tag{3.30}$$

where $n_{e2} = \left(k_0\, d^2 k_\eta \big/ dk_\xi^2\right)^{-1}$ is the diffractive index as defined in the previous section. Equation (3.29) can be rewritten as

$$w_{rms,2}^2 = \frac{1}{4} w_0^2 \left(1 + \frac{L^2}{z_{02}^2}\right), \tag{3.31}$$

with $z_{02} = k_0 n_{e2} w_0^2 / 2$ being its effective Rayleigh range.

Equation (3.31) represents the variation (or broadening) of the size of a Gaussian beam in an ordinary medium. This equation also governs the size of the output beam in a conventional PC demultiplexer. There are cases, however, that either because of diffraction compensation the second-order effect is canceled out, or because of strong

spatial dispersion, higher-order diffraction effects are important. Thus, to calculate the output beam size in such structures, we need to use the third-order spectral phase term (i.e., $\Phi(k_\xi) = b_3 k_\xi^3$) in Equation (3.27) to obtain

$$w_{rms,3}^2 = \frac{w_0^2}{4} + \frac{w_0}{\sqrt{2\pi}} \int_{k_\xi} \exp\left(-\frac{1}{2} w_0^2 k_\xi^2\right) (9 b_3^2 k_\xi^4) dk_\xi = \frac{w_0^2}{4} + \frac{27 b_3^2}{w_0^4}, \tag{3.32}$$

where

$$b_3 = \frac{1}{6} \frac{d^3\Phi}{dk_\xi^3} = \frac{1}{6} \frac{d^3 k_\eta}{dk_\xi^3} L . \tag{3.33}$$

Combining Equations (3.32) and (3.33) results in

$$w_{rms}^2 = \frac{w_0^2}{4} + \frac{3L^2 \left(d^3 k_\eta / dk_\xi^3\right)^2}{4 w_0^4} . \tag{3.34}$$

We can define

$$z_{03} = \frac{1}{\sqrt{3}} \left(d^3 k_\eta / dk_\xi^3\right)^{-1} w_0^3, \tag{3.35}$$

to simplify Equation (3.34) as

$$w_{rms,3}^2 = \frac{1}{4} w_0^2 \left(1 + \frac{L^2}{z_{03}^2}\right). \tag{3.36}$$

This is in an exact analogy with the second order form given in Equation (3.31). Based on this analogy, we can define the third-order Rayleigh range as

$$z_{03} = \frac{1}{2} k_0 n_{e3} w_0^2, \tag{3.37}$$

to define a third-order diffractive index as

$$n_{e3} = \frac{2 w_0}{\sqrt{3} k_0} \left(d^3 k_\eta / dk_\xi^3\right)^{-1} . \tag{3.38}$$

The beamwidth behavior inside the structure follows the same behavior as in the ordinary second-order case, with one major distinction that the third-order diffractive index ($n_{e3}$) depends linearly on the beam waist ($2w_0$) and inversely on the third-order curvature of the bands. Figure 3.8 shows the beam profiles calculated in a 45°-rotated square lattice PC (air holes in Si, $r/a$=0.40) using a direct modal approach compared to that found using a third-order diffractive index model. In this case, the setup is chosen such that the second-order diffraction has no contribution at the output screen (the second-order contributions from the incident bulk region and the PC region cancel out each other). It can be observed that the envelope of the beam calculated using the higher-order diffractive index (found by curve fitting to the band structure in the range of excitation) is in good agreement with the envelope of the beam calculated using a direct modal approach.

Similar to the third-order case, the rms beamwidth for the fourth-order diffraction can be calculated using the fourth-order spectral phase term as

$$w_{rms,4}^2 = \frac{1}{4} w_0^2 \left( 1 + \frac{L^2}{z_{04}^2} \right), \tag{3.39}$$

with

$$z_{04} = \frac{1}{2} k_0 n_{e4} w_0^2, \tag{3.40}$$

$$n_{e4} = \frac{2\sqrt{3} w_0^2}{\sqrt{5} k_0} \left( d^4 k_\eta \big/ dk_\xi^4 \right)^{-1}. \tag{3.41}$$

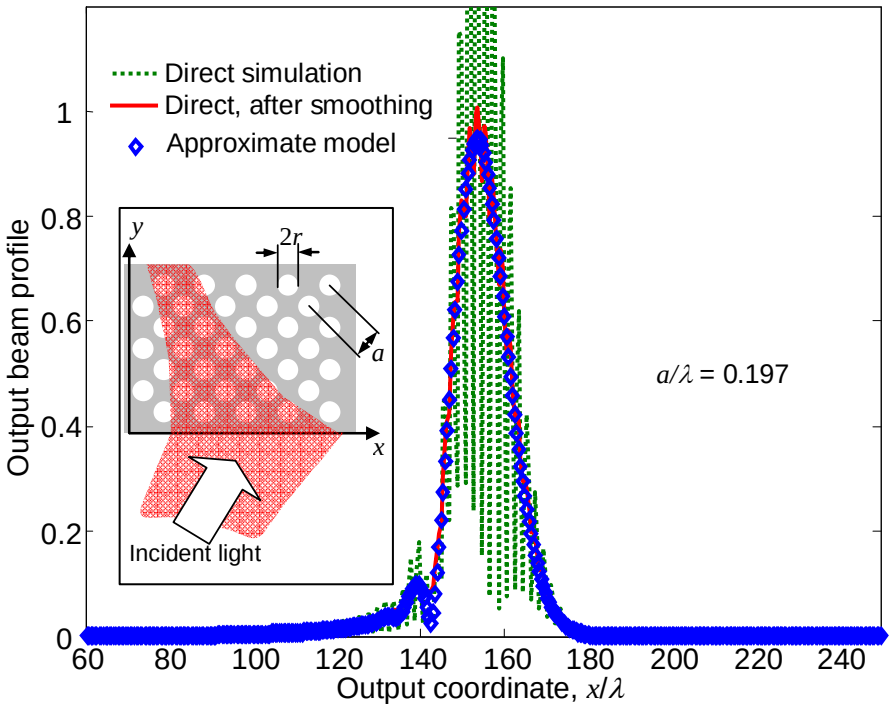


Figure 3.8. For a 45°-rotated 2D square lattice PC (air holes in Si, $r/a$=0.40) the profile of the beam envelope at the output is calculated using direct mode matching method (solid line) and the approximate diffractive index method (diamond marker). The incident light in this calculation is a preconditioned (i.e., broadened) Gaussian beam at normalized wavelength a/λ = 0.197, which illuminates the structure at an angle of 12° with respect to the normal to the interface. The preconditioning is performed so that the effect of the second-order diffraction term vanishes at the output of the PC structure. The accurate and approximate results are in good agreement.

In general, for $\nu$-th order spectral phase, we can calculate the main parameters describing the beam propagation effects as

$$w_{rms,\nu}^2 = \frac{1}{4} w_0^2 \left( 1 + \frac{L^2}{z_{0\nu}^2} \right), \tag{3.42}$$

$$z_{0\nu} = \frac{1}{2} k_0 n_{e\nu} w_0^2, \tag{3.43}$$

$$n_{e\nu} = \frac{(\nu-1)!}{\sqrt{(2\nu-3)!!}} \frac{w_0^{\nu-2}}{k_0} \left( d^{\nu} k_{\eta} / dk_{\xi}^{\nu} \right)^{-1}, \tag{3.44}$$

where $(2\nu-3)!!$ stands for factorial over odd numbers up to $2\nu-3$ (i.e., 1, 3, 5, …, $2\nu-3$).

Note that for a PC structure, all derivatives in the $k_\xi - k_\eta$ plane (e.g., $d^3k_\eta / dk_\xi^3$) are calculated at the operation point on the PC band structure and at the specific frequency of operation. Thus, by dispersion engineering (i.e., by designing the PC to have appropriate dispersion properties at the operation point), we can greatly affect the propagation of an optical beam. Note also that the overall behavior of the beamwidth of a given beam inside materials with third-, fourth-, or higher-order spectral phase terms can be calculated using similar formulas as that of an ordinary Gaussian beam propagating in a bulk medium if we use the appropriate diffractive index. In that sense, the analysis reduces to simple geometrical optics calculations which are extremely fast and efficient to perform, comparing to direct electromagnetic wave simulations (that require huge amount of time, processing, and memory). I will use this approximate model in analyzing the beam propagation effects in photonic crystal structures for dispersion-based applications and in particular, for the analysis and design of superprism-based demultiplexers.

# CHAPTER 4

# DEMULTIPLEXING BASED ON THE SUPERPRISM EFFECT IN PHOTONIC CRYSTALS

To effectively exploit the demultiplexing capabilities of PCs in different configurations and for different applications, a few basic steps are necessary. First, we should have an understanding of the physical concepts of the effect, including the dispersive properties of PCs and the wave propagation effects inside PCs. Second, a meaningful measure of the performance of the device has to be defined based on our design goals. Finally, we should be able to systematically design the parameters of the structure to achieve our desired design goals. I cover these issues in this chapter to design and implement photonic crystal demultiplexers based on the wavelength separation properties of PCs.

The superprism demultiplexing in photonic crystals relies on the difference between the angles of group velocities of photonic crystal modes excited by different incident wavelength components. In principle, the same effect is observed at the interface of two dielectric regions of different refractive indices, as in regular prisms. However, the distinction between different wavelengths in regular prisms is limited to the material dispersion offered by the dielectric that the prism is made of. This distinction can be substantially larger in photonic crystals in which the dispersion effects induced by periodicity are considerably stronger. After Lin et al. [101] proposed the effective prism structure using PC synthetic materials, the idea of superprism phenomenon was developed [39-40,35] and the physical concept behind it was described [73]. This idea has been implemented in one-dimensional (1D) and planar 2D PCs [93-94,37], which show different spatial distributions of the light for different wavelength channels at the output. However, a detailed assessment of these devices for wavelength demultiplexing

showed that there are limitations for using these devices in their basic configuration for high spectral resolutions [86-87]. The limitation is also observed in the previous demonstrations of the demultiplexers relying on the basic superprism effect [89,22,37]. Alternative implementations have been proposed, utilizing other differences in the properties of beams passing through photonic crystals to boost the wavelength separation characteristics. Examples of such effort include utilizing the difference between wavevectors of the beams at different wavelengths [95-97], and using cavities to improve the cross-talk isolation [102]. However, demonstration of these ideas faces practical implementation difficulties.

Figure 4.1 shows the basic property for different incident wavevectors (i.e., different incident wavelengths). The angle of group velocity in the structure can vary considerably from one wavelength to another wavelength as a result of the anomalous dispersive properties of the photonic crystal. Knowing that the optical power at each wavelength propagates in the direction of corresponding group velocity, this relatively large angular difference is what forms the basis of the superprism effect. In a more realistic situation, however, the actual optical beams need to be considered in these systems instead of the abstract view of interpretation in terms of wavevectors. There are two main considerations that come into the picture when the limited spatial extension of the optical beams is included in the model. Both the angular separation between adjacent channels and the divergence angle of each channel are important in the propagation length required for adjacent beams inside the structure required to achieve a certain level of cross-talk. We need a quantitative measure of the propagation length required in terms of the properties of the optical beam and the properties of the medium on one side and the angular separation and the desired cross-talk level on the other side.

We can use the approximate diffractive index model in the previous section to create a clear picture of the beam propagation inside photonic crystal structures, and to relate the design parameters to the desired performance characteristics. We consider a

two-dimensional photonic crystal structure with a typical band structure shown in Figure 4.1. In this figure, each contour corresponds to the allowed photonic crystal mode at a certain wavelength and with all possible wavevectors ($k_x$,$k_y$). In what follows the band structures under discussion may be related to two-dimensional photonic crystals or in-plane propagation in a planar slab-type photonic crystal. The discussions are similar in both cases.

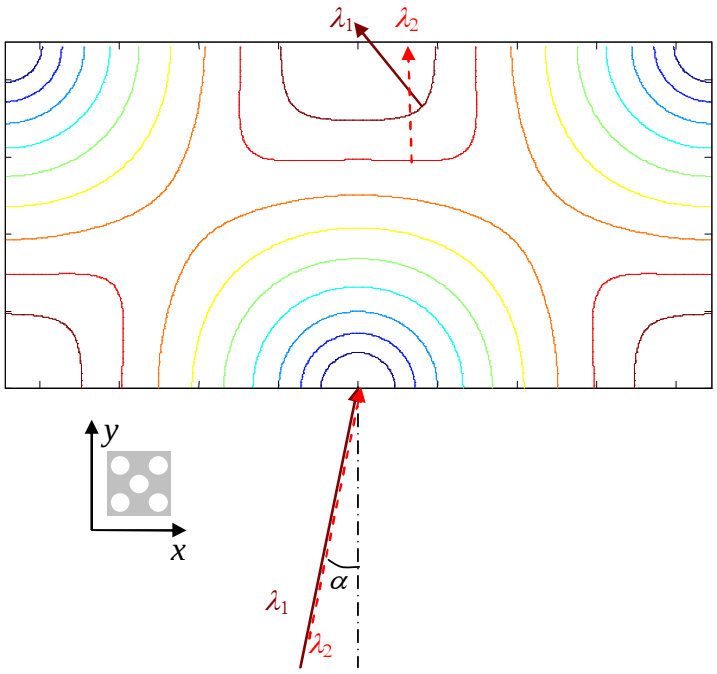


Figure 4.1. Iso-frequency contours of the first band of a rotated square lattice PC in a planar SOI wafer is shown ($r/a$ = 0.30). Coordinates are rotated by 45° with respect to the principal lattice vectors of the PC as shown in the inset. The direction of the group velocity in the strong superprism effect range varies significantly for the two different wavelengths considered here.

### 4.1. Dispersion in Space-Domain

The concept of dispersion in the space domain is a unique possibility in photonic crystals with no simple counterpart in ordinary bulk materials. In principle, similar phenomenon can be observed in anisotropic materials in which diffraction properties deviate from the well-known effects. However, naturally occurring anisotropy is

relatively weak, and those dispersive properties are of little practical application. In contrast, the coupling between Floquet-Bloch orders in photonic crystals (caused by the strong periodicity in the material) results in band folding and strong band deformations, both of which can be the source of unique dispersive properties.

The dispersive properties of photonic crystals in a sense can be considered as generalization and extension of temporal dispersion effects. The ability to control the shape of the bands and their wavelength dependence offers a unique opportunity to realize optical processing functionalities. Here, in particular, the focus will be on the possibility to map different wavelengths in the incident beam to different angles in space, and thus, achieving the spatial separation needed for wavelength demultiplexing.

### 4.2. Basic Configuration for Wavelength Separation

The basic configuration for the PC wavelength demultiplexer is shown in Figure 4.2. The PC is illuminated by a collimated input beam from a homogeneous medium with a refractive index $n_1$. Because of the anomalous dispersion of the PC, different wavelengths are spatially separated at the output (i.e., wavelength demultiplexing). For a given incident angle, the photonic crystal modes excited at different wavelengths can be calculated by equating the tangential components of the wavevector at the interface. Using the tangential component of the mode, and at each given wavelength, the corresponding mode (i.e., corresponding point of operation on the band structure) can be found. The direction of propagation of an optical beam excited at each point of the band structure can be found using the direction normal to the iso-frequency contours of the band structure,

$$\mathbf{v}_g = \nabla_{\mathbf{k}} \omega \,. \tag{4.1}$$

In addition, using Equation (3.24) for the diffractive index, we can estimate how each wavelength channel at a given angle diverges as a result of diffraction, as it propagates through the structure. Because of the unique dispersive properties of photonic crystals,

the change in the angle of group velocity with a change in the wavelength of the incident beam can be considerably large (compared to that in other mechanisms, e.g., in a reflection grating configuration). This mapping from wavelength to the spatial direction of propagation of beam is the main mechanism we use for wavelength demultiplexing.

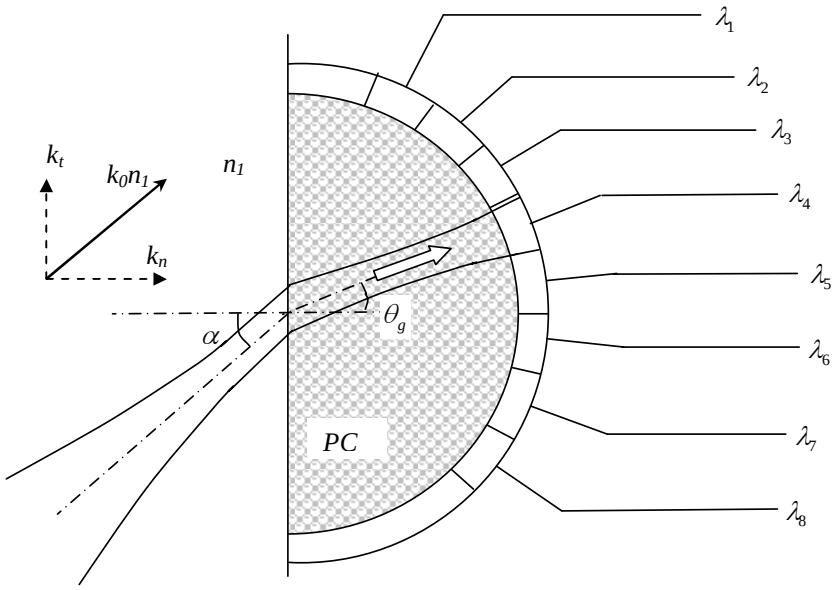


Figure 4.2. Geometry of the structure used for superprism demultiplexing in the conventional configuration is shown.

The relative extent of two adjacent wavelength channels inside the PC is schematically shown in Figure 4.3(a), assuming that the two adjacent channels have equal divergence angles $\delta$. The overlap of the two beams depends on both the angular separation between these channels and the propagation length inside the PC. We define the cross-talk between channels as the total power of each channel at the position of other channels. Assuming the beams inside the PC to be Gaussian (which is a good approximation for most practical applications [31]), and the angular separation between the two adjacent channels (calculated at their center frequencies) to be $\Theta$, the propagation length required to limit cross-talk to a desired value $X$ is found approximately as [103]

$$\begin{cases} L(X) = \zeta(X) z_0 \\ \zeta(X) = \dfrac{K_X}{\psi - H_X} \end{cases}. \tag{4.2}$$

where $z_0 = 4\lambda_0/(\pi n_e \delta^2)$ is the Rayleigh range for the beam [127], $\lambda_0$ is the free-space wavelength, and $\psi = \Theta/\delta$ is the angular separation factor.

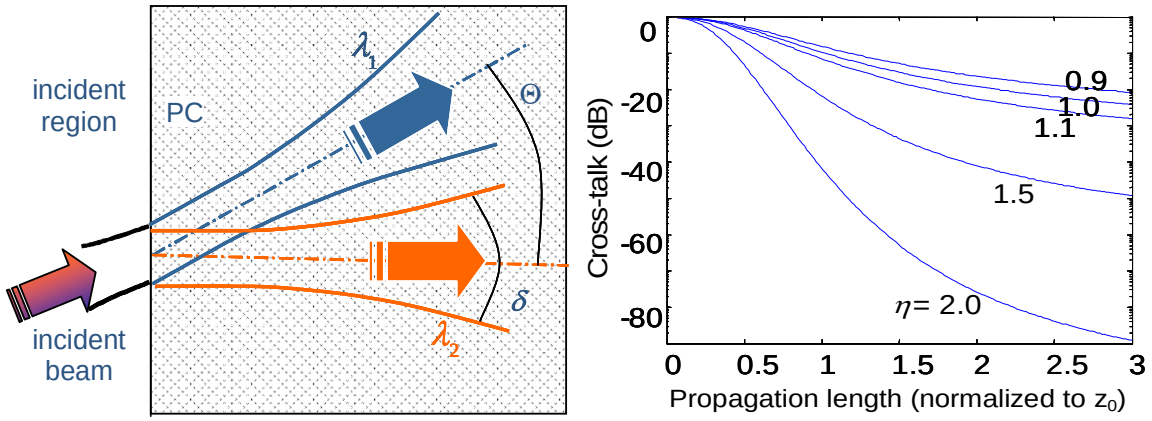


(a) (b)

Figure 4.3. (a) Schematic evolution of beam profiles of two adjacent wavelength channels inside the PC structure is illustrated. $\Theta$ is the angular spacing between the group velocity directions of the center frequencies of these two channels, and $\delta$ is the divergence angle of each channel inside the PC region. (b) The behavior of the cross-talk versus the propagation length for different values of $\eta = \Theta/\delta$ is plotted. The Gaussian beam approximation is used in all cases.

Equation (4.2) is found by interpolating the simulated data. The coefficients $K_X$ and $H_X$ in Equation (4.2) depend only on the cross-talk $X$, and not on other design parameters; their values are listed in Table 4.1. To find $K_X$ and $H_X$, we calculated the cross-talk (assuming Gaussian beams) for several different device lengths ($L$) and angular separation factors ($\Theta/\delta$). A subset of the results appears in Figure 4.3(b), which shows the variations of cross-talk versus propagation length for different angular separation factors, $\psi$. We then fitted the data to Equation (4.2) to obtain values of $K(X)$ and $H(X)$ for each value of cross-talk, $X$. The error in this curve fitting for all cases in the range of interest was less than 5%. Since the propagation inside the PC is modeled using the

diffractive index technique, the results in Figure 4.3(b) and Table 4.1 are independent of the choice of PC. The importance of this equation is in that it relates the required propagation length, $L$ (which is directly related to the physical size of the demultiplexer) to other parameters (i.e., beam divergence, $\delta$, and angular separation between channels, $\Theta$) based on the acceptable cross-talk level.

Table 4.1. Cross-talk parameters.

| Cross-talk level, $X$ (dB) | $K_X$ | $H_X$ |
|---|---|---|
| -20 | 0.9 | 0.56 |
| -30 | 0.9 | 0.83 |
| -40 | 0.9 | 1.04 |
| -50 | 0.9 | 1.22 |

### 4.3. Performance Analysis for the Basic Configuration

To design efficient wavelength demultiplexing devices, we need to analyze the performance of these devices in terms of practical measures. The main performance measures of interest in wavelength demultiplexing devices are cross-talk isolation, wavelength resolution, and size of the device. In this section, I will derive the basic relations between these main performance measures, and find the fundamental trends and trade-offs in these devices. Such relations on one side enable us to compare the performance of superprism-based PC demultiplexers with other demultiplexing schemes in terms of compactness and resolution, and on the other side, provide a way to design optimal devices by engineering the geometry and configuration.

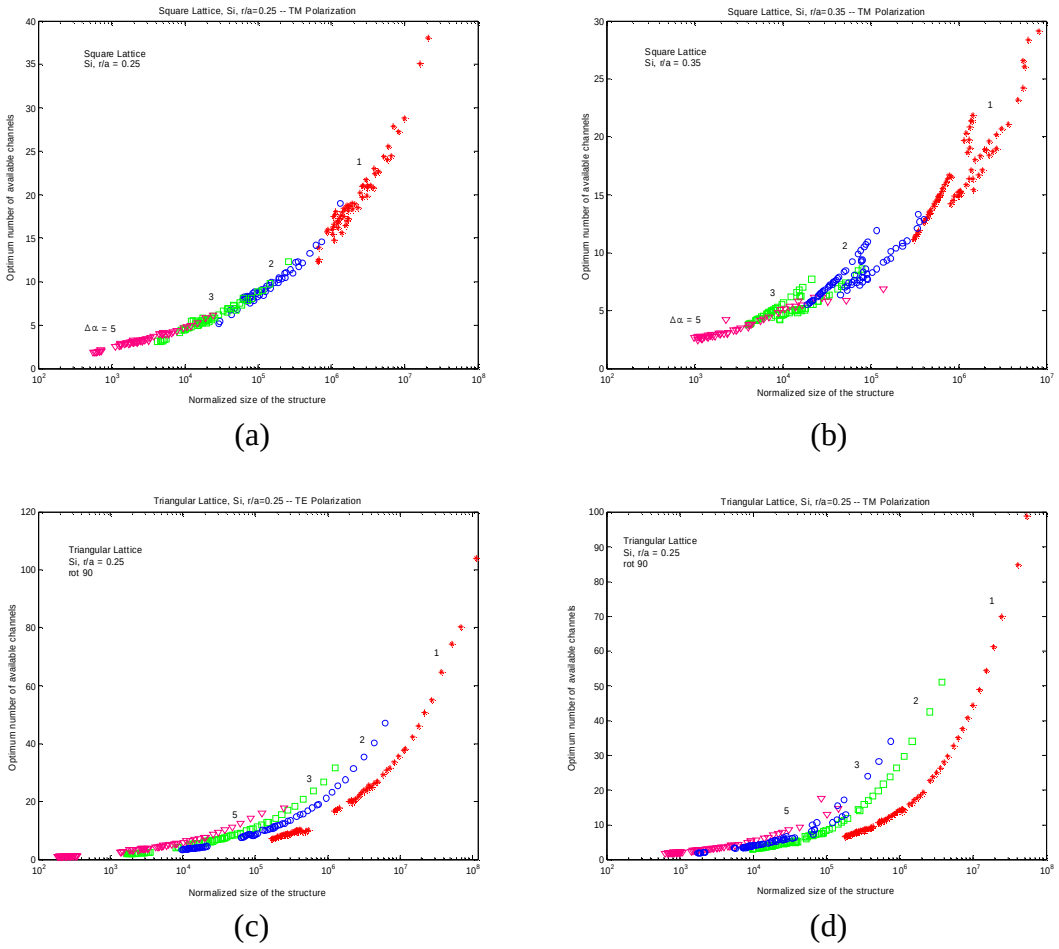


Figure 4.4. The relation between the size of the structure and the number of channels are shown for different PC lattices of air holes in Si. (a) H-polarization in a square lattice PC with $r/a = 0.25$, (b) H-polarization in a square lattice PC with $r/a = 0.35$, (c) E-polarization in a triangular lattice PC with $r/a = 0.25$, and (d) H-polarization in a triangular lattice PC with $r/a = 0.25$. In each case, star, circular, square, and triangular markers stand for incident divergence angles of $\Delta\alpha$ = 1°, 2°, 3°, and 5°, respectively.

For arbitrary frequency separation between adjacent channels, for each structure, we calculate the angle of group velocity versus frequency and angle of incidence for each structure, and also the angular sensitivity parameter, $\partial\theta_g/\partial\alpha$, for the structure. Now, for a specific beam divergence in incident beam, $\Delta\alpha$, we consider a range of values for channel separation angle, $\Delta\theta_g$, and based on that we find the optimum angle of incidence in the sense that the number of available channels per unit area is maximized (in fact, the

merit function to be maximized is $N_{av}\cos^2\alpha$). Figure 4.4 shows the relation between the size of the structure and the number of wavelength channels (i.e., wavelength demultiplexing resolution) in four different photonic crystal structures. These values for different values of $\Delta\alpha$ and $\Delta\theta_g$ are marked in each graph, and the trend in each graph represents the potentials of the corresponding structure. It can be induced that first, there are optimal designs in each lattice that offer the most compact devices for any desired resolution. Second, there is a significant difference between the demultiplexing performances of different lattices. These graphs suggest that a more rigorous analysis is required to compare different PC lattice structures, geometries, and design parameters for better demultiplexing performance.

To be able to compare the performance of different demultiplexing structures, we can define figures of merit to quantify their performance. The two primary merits describing the performance of these structures that we consider here are the compactness of the structure and the divergence angle requirement for the incident (or input) beam. Compactness is one of the main advantages of the superprism-based demultiplexers and an optimum design must result in as compact a structure as possible. The smaller the area of the structure is, the higher the yield; the lower the cost; and the less the complications caused by the nonuniformity of the structure would be. Moreover, scattering loss, which is still one of the major issues in planar PC structures, increases as the size of the structure is increased. On the other hand, to avoid huge cross-talk and realize spatial separation of channels in a PC structure with reasonable size (or alternatively, to achieve the desired resolution), some limitations must be imposed on the divergence angle of the incident beam. It is practically difficult to launch very large beam sizes with very small divergence angles into the planar PC structure. Designing structures that can effectively work with incident beams with reasonable divergence angles is essential for realizing

practical PC demultiplexers. Therefore, compactness and incident divergence angle are considered here as the main features for which figures of merit are defined.

The physical area is a reasonable measure for the compactness of a PC demultiplexer. Note that the required propagation lengths of different channels for achieving a certain level of cross-talk are in general different. For calculating the area of the structure, the worst case (i.e., the channels with largest propagation length) must be considered. Thus, we can use (4.2) to define $L$, the minimum propagation length for achieving the required cross-talk level ($X$), as

$$L \cong \max_{channels}\left\{\frac{4\zeta(X)\lambda}{\pi n_e \delta^2}\right\}, \tag{4.3}$$

where $\max_{channels}$ refers to maximum value over all wavelength channels in the demultiplexer. If the total angular range of operation over which all separated wavelength channels exist inside the PC are represented by $\theta_T$, the area of the structure will be

$$A = \frac{1}{2}\theta_T L^2 \cong \frac{\theta_T}{2}\left(\max_{channels}\left\{\frac{4\zeta(X)\lambda}{\pi n_e \delta^2}\right\}\right)^2 \tag{4.4}$$

Using Equations (4.2) and (4.4) we obtain

$$A \cong \frac{8\lambda^2\theta_T}{\pi^2}\left(\max_{channels}\left\{\left(\frac{K_X}{\eta - H_X}\right)\frac{\left(\partial\theta_g/\partial\alpha\right)\big|_\omega \cos\theta_g}{n_1 \cos\alpha\,\delta^2}\right\}\right)^2, \tag{4.5}$$

in which $X$-dependence in $K_X$ and $H_X$ is implicit. Using $\eta=\Theta/\delta$, we can simplify $A$ to

$$A \cong \frac{8\lambda^2 K_X^2\theta_T}{n_1^2\pi^2\cos^2\alpha}\left(\max_{channels}\left\{\frac{\left(\partial\theta_g/\partial\alpha\right)\big|_\omega \cos\theta_g}{(\Theta - H_X\delta)\delta}\right\}\right)^2. \tag{4.6}$$

Combining $\delta = \left(\partial\theta_g/\partial\alpha\right)\big|_\omega(\Delta\alpha)$ and Equation (4.6), we get

$$A \cong \frac{8\lambda^2 K_X^2 \theta_T}{n_1^2 \pi^2 \cos^2 \alpha}\left(\frac{1}{\Delta\alpha}\right)^2\left(\max_{channels}\left\{\frac{\cos\theta_g}{\Theta - H_X\left(\partial\theta_g/\partial\alpha\right)\big|_\omega \Delta\alpha}\right\}\right)^2. \qquad (4.7)$$

4.3.1. Figures of merit

The case that we consider here is a demultiplexer with equal angular separation but with no restriction on the wavelength of the channels, which will be denoted as equal angular separation with flexible frequencies (EASFF). This scheme is of interest when we have a set of equally-spaced detectors at the output, for example in a spectrometer, but the wavelength spacing between channels are flexible since the spectrum will be later processed and extracted from the readings of the array of detectors. In this case, the angular spacing, $\Theta$, has to be chosen for the worst channels (the largest value) and is the same for all channels. For design purposes, the regions in the PC band structure with smaller values for $\left(\partial\theta_g/\partial\alpha\right)\big|_\omega$ are advantageous for this scheme. If we limit this value to a threshold $\beta$ (i.e., $\left(\partial\theta_g/\partial\alpha\right)\big|_\omega < \beta$) as discussed in [87], then

$$A \cong \frac{8\lambda^2 K_X^2 \theta_T(\alpha,\beta)}{n_1^2 \pi^2 \cos^2 \alpha}\left(\frac{1}{\Delta\alpha}\right)^2\left(\max_{channels}\left\{\frac{\cos\theta_g}{\Theta - H_X \beta\Delta\alpha}\right\}\right)^2. \qquad (4.8)$$

Using simple calculus, it can be shown that the area $A$ is minimized by setting $\Delta\alpha = \Theta/(2H_X\beta)$ which results in

$$A \cong \frac{8\lambda^2 K_X^2 \theta_T}{n_1^2 \pi^2 \cos^2 \alpha}\left(\frac{4H_X^2\beta^2}{\Theta^2}\right)\left(\frac{4\cos^2\theta_{gm}}{\Theta^2}\right), \qquad (4.9)$$

where $\theta_{gm}$ is the propagation angle in the range of interest which maximizes $\cos^2\theta_g$. For $N$ demultiplexed channels, $\theta_T = N\Theta$, thus

$$A \cong \frac{128\lambda^2 K_X^2 H_X^2}{n_1^2 \pi^2}\left(\frac{\beta^2 \cos^2\theta_{gm}}{\theta_T^3(\alpha,\beta)\cos^2\alpha}\right)N^4. \qquad (4.10)$$

This basically tells us that in these demultiplexers the area of the structure is proportional to the fourth power of the number of channels. The coefficient of this relation can be defined as the compactness factor, $C_{EASFF}$, with

$$C_{EASFF} = \left( \frac{n_1^2 \pi^2}{128 K^2 H^2} \frac{\theta_T^3(\alpha,\beta)\cos^2\alpha}{\beta^2 \cos^2\theta_{gm}} \right); \quad \frac{A}{\lambda^2} \cong \frac{N^4}{C_{EASFF}}. \tag{4.11}$$

Compactness factor, as defined in Equation (4.11), depends on the PC structure (through $\theta_T$), and on the parameters $\alpha$ and $\beta$. To realize an $N$-channel demultiplexer in this scheme, the larger the compactness factor is, the more compact the structure will be. Therefore, $C_{EASFF}$ can be used as a measure of compactness of the structure to compare different designs. In the process of minimizing the area of the structure, we obtained

$$\Delta\alpha = \Theta/(2H\beta). \tag{4.12}$$

By re-arranging this formula and using $\theta_T = N\Theta$ we get

$$\Delta\alpha = \frac{\theta_T(\alpha,\beta)}{2H\beta}\frac{1}{N}, \tag{4.13}$$

which means that for a given design in this scheme the required incident divergence angle decreases as the number of channels increases. Reducing the incident divergence angle usually requires more sophisticated optical design; therefore, a design with less strict requirement for the divergence angle of input beam is more favorable. We define the other performance measure (which depends on both the PC and the design parameters) as incident divergence factor, $E_{EASFF}$, where

$$E_{EASFF} = \frac{\theta_T(\alpha,\beta)}{2H\beta}; \quad \Delta\alpha = \frac{E_{EASFF}}{N}. \tag{4.14}$$

4.3.2. Resolution limit

Even though the initial structures proposed based on the basic superprism effect looked promising, more careful analysis revealed that resolution of the photonic crystal superprism in the conventional basic configuration is limited for compact devices [86].

Also, as it has been shown above, there is a large cost for going to higher resolutions, i.e., the size of the structure grows as the fourth power of the number of demultiplexing wavelength channels [87], as shown in Equation (4.41). These facts showed the limitations of the conventional superprism-based demultiplexers for high-resolution applications. Table 4.2 lists the results of optimization for superprism-based PC demultiplexers in the basic configuration. The calculated compactness factor, *C*, can be used to derive the required size for desired number of wavelength channels.

Table 4.2. Results of optimization (over $\alpha$, $\omega_{n0}$, and radius) in the EASFF scheme.

| Lattice type | Pol. | *r/a* | $\alpha_{opt}$ | $\beta_{opt}$ | $\theta_{T,opt}$ | $C_{opt}$ |
|---|---|---|---|---|---|---|
| Square | TE | 0.35 | 16° | 2.75 | 19.4° | 0.017 |
| | TM | 0.30 | 14° | 2.44 | 22.1° | 0.032 |
| Triangular (ΓM) | TE | 0.27 | 9° | 0.11 | 10.0° | 1.56 |
| | TM | 0.20 | 4° | 1.96 | 21.4° | 0.047 |
| Triangular (ΓK) | TE | 0.40 | 8° | 7.5 | 92.8° | 0.26 |
| | TM | 0.40 | 4° | 16 | 90.7° | 0.054 |

Figure 4.4(a) shows the response of an optimal structure designed in a square lattice PC of air-holes in Si with H-polarization. The resulting beam profiles at the output of the designed structure, shown in Figure 4.4(b), confirm the required spatial separation at the output of the device. From these beam profiles, we can see that the nonuniformity of the diffractive index in this range of operation results in considerable broadening of some of the wavelength channels.

The design objective can be modified to cover other cases, including equal frequency separation between channels with fixed or variable operation bandwidth, which are covered in the Appendix A. The results for other design objectives show the same basic relations between parameters, i.e., the size of structure grows as the fourth

power of wavelength (or frequency) resolution, and the required divergence angle of the input beam is inversely proportional to the desired resolution.

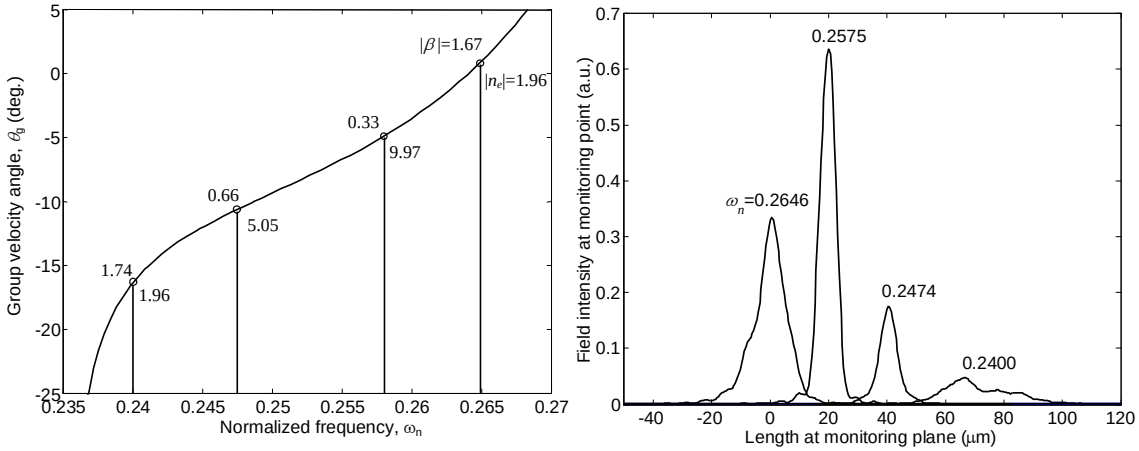


(a) (b)

Figure 4.5. (a) Variations of the angle of group velocity versus normalized frequency for a square lattice PC with H-polarization is shown in an optimal structure for the EASFF scheme. The number above each channel shows the value of $\partial\theta_g/\partial\alpha$ for that channel, and the number below it shows its corresponding value for the diffractive index. (b) The field intensities of four frequency channels at the output plane of the superprism-based demultiplexer designed in Figure 4(a) are plotted. The ratio of the hole radius to the lattice constant is $r/a$=0.30, the incident angle $\alpha$=14°, and $\beta_{opt}$=2.44. The angular spacing between adjacent channels for $X$=-20dB is $\Theta$=5.6°, and the input divergence angle is $\Delta\alpha$=3.2°. For this design, at $\lambda$=1550nm, propagation length is $L$=210μm.

The reason behind the limitations in the basic configuration is identified to be the divergence of the optical beams inside the photonic crystal region [86-87]. In the basic configuration, the incident beam is at its waist at the entrance to the photonic crystal region, and as it propagates the beam size becomes larger. As a result, the angular separation between adjacent channels needs to be at least of the order of divergence angle of each channel. This requirement limits the resolution of the device and puts stringent conditions on the collimation of the input beam. I will propose solutions to this issue in the following section.

### 4.4. Diffraction Compensation for Improving the Demultiplexing Performance

As discussed in the previous section, the demultiplexing concept using the superprism effect in photonic crystals relies on the change in the direction of group velocities of the beams at different wavelengths. Spatial separation of the beams at the output plane in such a scheme requires relatively long propagation lengths inside the dispersive material. A more efficient implementation can be achieved if the diffractive beam broadening is suppressed. To achieve this in a PC wavelength demultiplexing device, one option is to allow the incident optical beam (with multiple channels) to propagate (and diffract) in the unpatterned Si before entering into the PC region. This propagation results in a second-order spectral phase term in the spatial spectrum of the beams (and therefore, beam broadening), which we refer to as preconditioning. As the beams propagate through the PC, they experience two effects: the superprism effect and negative diffraction. Beams of different wavelengths propagate in different directions inside the PC (the superprism effect), and at the same time, the second-order spectral phase term is decreased (since the PC second-order diffraction is opposite to that of the unpatterned Si) until it completely vanishes at the output (diffraction compensation), retrieving the minimum spot size for the beams at the output ports. Using this scheme, the spatial separation needed inside the PC region can be of the order of the minimum spot size of the incident beams, which is much smaller than its broadened version observed in the basic configuration of superprism-based demultiplexer.

In another view, the main limitation in the basic configuration of superprism-based wavelength demultiplexing is the dependence between the angular dispersion factor ($\partial\theta_g/\partial\lambda$) and the beam divergence factor ($\partial\theta_g/\partial\alpha$), which is posed by the band structure itself. If we eliminate this dependence by compensating the diffraction effects (and hence, making the response independent of the beam divergence factor), the trends in the structure change, and wavelength separation can be achieved in a much more

compact structure. Schematic demonstration of the devices considered here is shown in Figure 4.6 in which both the diffraction compensation and superprism effects are illustrated.

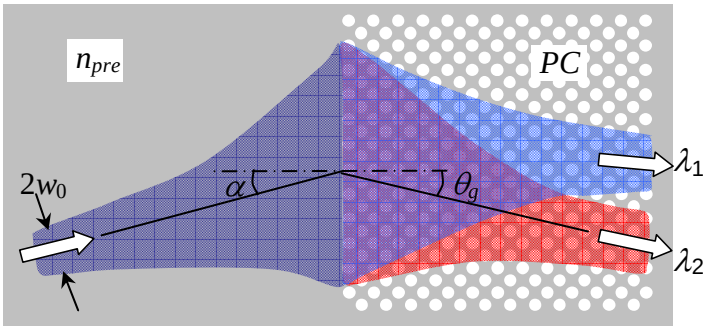


Figure 4.6. Schematic view of a preconditioned photonic crystal demultiplexer and the definition of parameters are shown for an incident beam coming at an angle $\alpha$.

### 4.5. Performance Analysis for the Diffraction-Compensated Configuration

We use two of the unique dispersion properties of photonic crystals, namely, the superprism effect and diffraction compensation to achieve compact demultiplexers. Two main objectives to be considered are: first, different wavelengths should be spatially separated (by steering them to different directions using the superprism effect), and second, the beam broadening caused by normal diffraction should be eliminated (to avoid the limitations of the conventional superprism configuration).

To design superprism demultiplexers, we follow a two-step scheme. First, by defining a compactness factor as the figure of merit describing the performance of the photonic crystal demultiplexer in preconditioning regime, we find the proper photonic crystal structure and an appropriate operation point. In the next step, in the vicinity of that operation point, we find the design parameters (i.e., length of the structure and divergence of the incident beam) to give us the required cross-talk level at the resolution of interest for all demultiplexing wavelength channels.

The main difference in the analysis of the preconditioned PC demultiplexers comparing the conventional ones (investigated in detail in [103]) is the replacement of the second-order spectral phase with the third-order spectral phase. Furthermore, as demonstrated in Chapter 3, the main wave propagation features remain the same as ordinary second-order case, when third-order diffraction is the dominant effect (by choosing the appropriate diffractive index). The substitution of the third-order diffractive index instead of the second-order diffractive index in this scheme is shown in Figure 4.7.

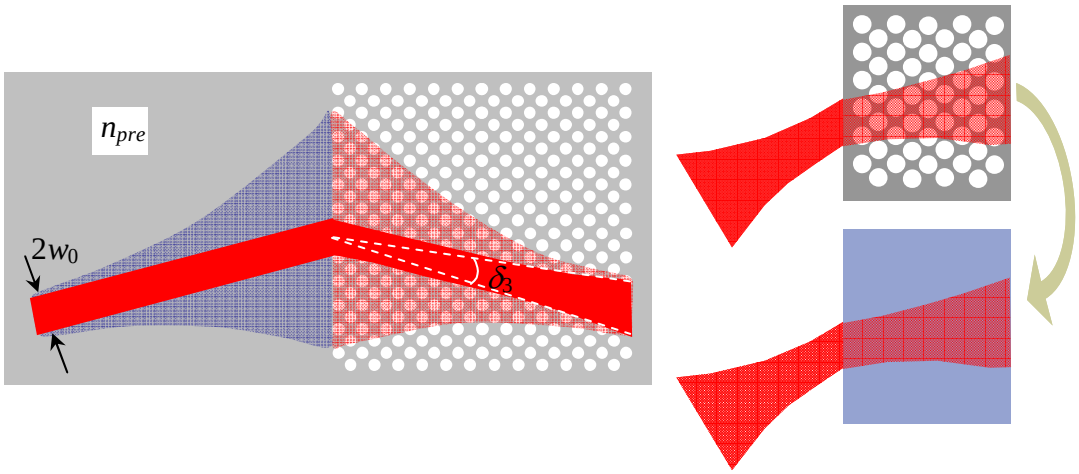


Figure 4.7. A preconditioned photonic crystal demultiplexer that uses propagation in a bulk incident region for diffraction compensation is schematically illustrated. Dark beam trace shows the evolution of an optical beam at a single wavelength throughout the structure without the effect of second order diffraction. In this case, $\delta_3$ is the divergence angle of the beam caused by the third-order diffraction.

Using the formulation of Section 2, we can apply the same formalism as in the conventional case [103] for the calculation of the cross-talk in a preconditioned PC device, by using the third-order diffractive index. As a result, we can calculate the required propagation length, $L$, for achieving a certain level of cross-talk as

$$L = \frac{K_X}{\eta_3 - H_X} z_3 . \tag{4.15}$$

In these relations, $z_3$ is the Rayleigh range corresponding to the third order spectral phase term, $\eta_3 = \Delta/\delta_3$ is the ratio of angular separation between adjacent channels ($\Delta$) to divergence angle of each channel caused by the third-order diffraction effect inside the PC (shown in Figure 4.7), and $K_X$=0.9 and $H_X$=0.56 are constants chosen to achieve a cross-talk better than -20dB between channels. Equation (4.15) represents the spatial separation condition for the preconditioned superprism devices. The diffraction compensation condition that describes the cancellation of the overall quadratic phase can be written as

$$\frac{L_{pre}}{n_{pre}\cos^2\alpha} = \frac{L}{n_{e2}\cos^2\theta_g} \tag{4.16}$$

To assess the performance of the preconditioned superprism demultiplexers, here, we calculate the size of these structures for a given angular channel spacing, Δ. Starting from Equations (3.36)-(3.38) for a beam propagating in a medium with third-order diffraction effects, we have $\delta_3 = 2\lambda/(\pi \mid n_{e3} \mid w_{PC})$ and $z_3 = \frac{1}{2} k_0 \mid n_{e3} \mid w_{PC}^2$. By inserting these relations into Equation (4.15) one obtains [91]

$$L = \frac{2K_X w_{PC}^3}{w_{PC}^2\Delta - 2\sqrt{3}H_X\left|\partial^3 k_\eta / \partial k_\xi^3\right|}. \tag{4.17}$$

The area of the photonic crystal taken by each channel can be estimated as

$$A = \left(\frac{w_{PC}}{z_2} L\right)L = \frac{8K_X^2 w_{PC}^5\left|\partial^3 k_\eta / \partial k_\xi^3\right|}{\left[w_{PC}^2\Delta - 2\sqrt{3}H_X\left|\partial^3 k_\eta / \partial k_\xi^3\right|\right]^2} \tag{4.18}$$

The area in Equation (4.18) depends explicitly on the diffraction-limited beam waist of the channel inside the PC, $2w_{PC}$; thus, we can minimize the area directly with respect to this parameter by using $\partial A/\partial w_{PC} = 0$ to obtain

$$(w_{PC})_{opt} = \left[ \frac{10\sqrt{3}H_X}{\Delta} \left| \frac{\partial^3 k_\eta}{\partial k_\xi^3} \right| \right]^{1/2} \tag{4.19}$$

which consequently gives

$$L_{opt} = \frac{5K_X}{2\Delta}(w_{PC})_{opt} \tag{4.20}$$

$$A_{opt} = \frac{25K_X^2}{2k_0 n_{e2}\Delta^2}(w_{PC})_{opt}. \tag{4.21}$$

In terms of the physical parameters of the structure, one can find [91]

$$\frac{A_{opt}}{\lambda^2} = \frac{25\sqrt{10\sqrt{3}H_X}K_X^2}{8\pi^2}\left[ \frac{\cos\theta_g}{n_1\cos\alpha}\left( \frac{\partial n_{e2}}{\partial \alpha} \right) \right]^{1/2} \frac{1}{n_{e2}^2}\left( \frac{\partial \theta_g}{\partial \omega} \right)^{-5/2} (\Delta\omega)^{-5/2}, \tag{4.22}$$

in which we have used $\Delta = (\partial\theta_g/\partial\omega)\Delta\omega$ as the separation between adjacent channels. From these relations, we can see that the area of the structure scales as $(\Delta\omega)^{-5/2}$, which grows considerably slower than the $(\Delta\omega)^{-4}$ dependence in the conventional superprism-based demultiplexers [87].

We can define the compactness factor for the diffraction compensated structures as

$$C_{dc} = \frac{8\pi^2 n_{e2}^2}{25\sqrt{10\sqrt{3}H_X}K_X^2}\left[ \frac{\cos\theta_g}{n_1\cos\alpha}\left( \frac{\partial n_{e2}}{\partial \alpha} \right) \right]^{-1/2}\left( \frac{\partial \theta_g}{\partial \omega} \right)^{5/2}, \tag{4.23}$$

which simply relates the angular spacing between channels to their optimum area through

$$\frac{A_{opt}}{\lambda^2} = \frac{(\Delta\omega)^{-5/2}}{C_{dc}}. \tag{4.24}$$

Also, it is straightforward to find from Equation (4.19) that

$$\Delta\alpha = \frac{2\lambda\cos\theta_g}{\pi n_1\cos\alpha}\left[ \frac{(\partial\theta_g/\partial\omega)}{10\sqrt{3}H_X\left|\partial^3 k_\eta/\partial k_\xi^3\right|} \right]^{1/2}(\Delta\omega)^{1/2} = E_{dc}(\Delta\omega)^{1/2}, \tag{4.25}$$

which grows considerably slower than the $\Delta\alpha = E_{EASFF}(\Delta\omega)$ in the basic configuration of the superprism-based demultiplexers [103].

Equations (4.24) and (4.25) summarize the improvements achieved by modifying the basic configuration to a diffraction compensated configuration. A comparison between the two schemes show that there is a clear advantage in adopting the diffraction compensated scheme since both the size and divergence requirements become less stringent. The difference becomes more drastic as we move to the high-resolution devices needed for current demanding applications in demultiplexing and sensing.

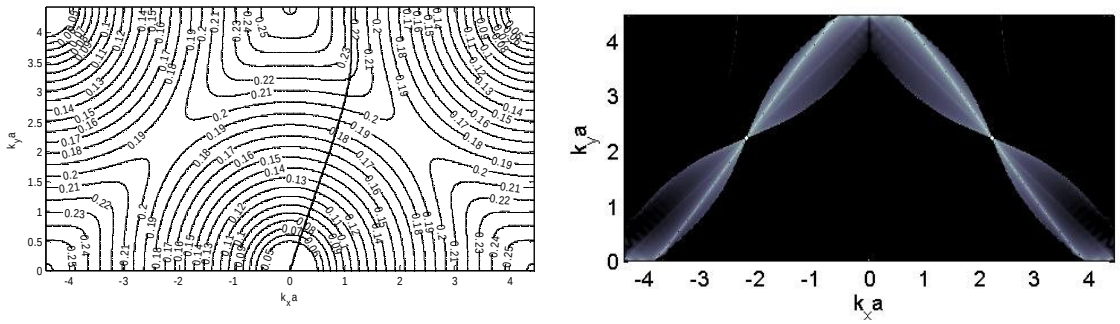


Figure 4.8. (a) The band structure of a 45°-rotated (interface at a 45° angle with respect to the interface of the PC with the incident region) square lattice planar PC with lattice constant $a$=333nm, normalized radius of holes of $r/a$=0.23, and thickness of Si guiding layer of $h$=200nm is shown for the first TE-like polarization (electric field perpendicular to the axes of holes). (b) The compactness factor is calculated and shown in a logarithmic scale for the band structure in part (a); bright regions are appropriate for designing preconditioned superprism demultiplexers.

## 4.6. Design Steps for Wavelength Demultiplexing in the Diffraction-Compensated Configuration

Having the main focus on the compactness of the structure, we can consider $C_{dc}$ as a first measure to locate the appropriate operation points on the band structure of a given photonic crystal. From a graph similar to Figure 5(b), one can determine the operation point that can potentially provide good demultiplexing performance. Selecting this point

specifies the center frequency of operation, as well as the incident angle of the input beam. However, the actual required propagation length to get to the desired level of cross-talk for all channels requires extracting the related parameters for individual wavelength channels. These parameters describe the propagation behavior for each channel (i.e., the direction of propagation, sensitivity to frequency, and the divergence caused by the third-order spectral phase term). To get the required cross-talk for all channels, the original diffraction-limited waist of the incident beam ($w_i$) should be found in such a way that the maximum propagation length required over all channels is minimized. This can be directly performed by reformulating Equation (4.17) as

$$L_j = \frac{2K_X w_i^3 \cos^3\theta_{gj}}{w_i^2 \Delta_j \cos^2\theta_{gj} \cos\alpha - 2\sqrt{3}H_X \left|\partial^3 k_\eta / \partial k_\xi^3\right|_j \cos^3\alpha}, \tag{4.26}$$

in which subscript $j$ stands for the parameters calculated for the $j$-th channel. After finding $w_i$ from this process, it is straightforward to set

$$L = \max_j \{L_j(w_i)\}. \tag{4.27}$$

As an example, for a four channel demultiplexer with channel spacing of 0.5 nm in a SOI wafer the required propagation lengths for all channels are plotted together in Figure 4.9(a). It can be observed that in this case wavelength channels 2 and 3 which are at the center of operation point (closer to the optimal design point) show better performance and are separated at shorter propagation lengths. To achieve the required -20dB cross-talk for all channels, however, we need a propagation length of at least 2.05 mm(and a diffraction-limited input spot size of 29 μm) to satisfy the requirements for all wavelength channels. Figure 4.9(b) shows another advantage of designing the photonic crystal demultiplexing structure in this operation range, which is the invariance of the

diffractive index over the bandwidth of interest (close to the optimum operation point). This property is important since it results in refocusing of all wavelength channels at the same plane in the output of the device, where output waveguides can be placed to carry the separated channels.

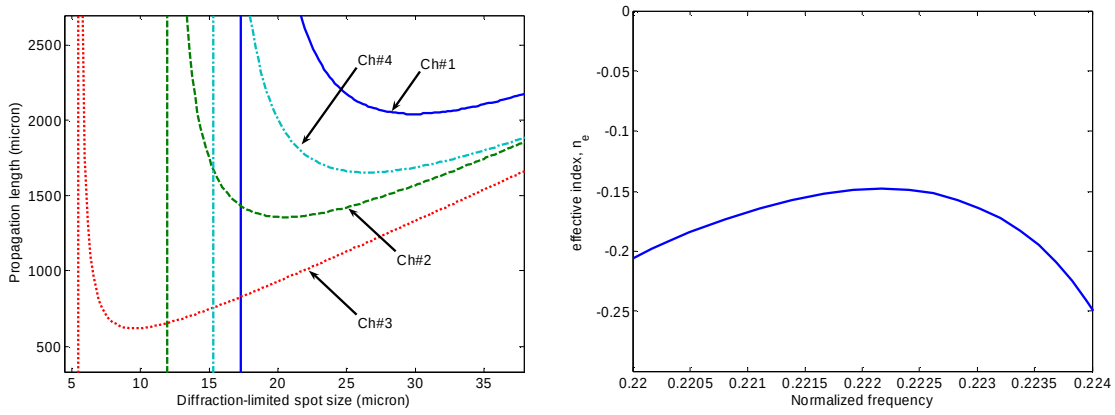


(a) (b)

Figure 4.9. (a) For an incident angle of $\alpha = 17°$, and normalized frequency of operation of $\omega_{nc} = 0.22215$ (both found from choosing an operation point in Figure 4.8), the relation between the original diffraction limited waist of the incident beam and the required propagation length for achieving a cross-talk better than -20dB is plotted for four demultiplexing wavelength channels with a channel spacing of $\delta\lambda = 0.5$ nm. From these plots, minimum acceptable propagation length is found to be 2.05 mm for a four channel demultiplexer. Corresponding required waist for the incident beam is found to be $w_0 = 30$ μm. (b) The diffractive index for a range of frequencies at the incident angle of $\alpha = 17°$ is plotted showing a region with small variation of negative diffractive index in the vicinity of the operation point ($\omega_{nc} = 0.22215$).

Using the performance merits introduced in this chapter, and following the design procedure we can find the device parameters of the optimal structure for desired design objectives. Note that the analysis of the structure and assessing the demultiplexing performance in our approach is based on simple geometrical optics considerations; nonetheless, since we are using the band structure for the actual planar PC, the model is in good agreement with the actual structure. In the following chapters, experimental demonstration of these devices and additional considerations to improve their performance will be discussed.

# CHAPTER 5

# EXPERIMENTAL DEMONSTRATION OF WAVELENGTH DEMULTIPLEXING IN PHOTONIC CRYSTALS

In this chapter, experimental realization of wavelength demultiplexing devices in a planar platform is the main focus. As discussed in Chapter 4, a combination of the superprism effect and negative diffraction can offer a solution for compact wavelength demultiplexing in photonic crystals. However, in a practical implementation of such devices, without proper considerations, the unwanted contributions (other polarization of light or other wavelengths) and stray light will directly appear at the same location as the desired signal at the output, as schematically shown in Figure 5.1(a). This effect is detrimental to the proper operation of the wavelength demultiplexing device, especially when these devices are being used as spectrometers for sensing applications (where the presence of unwanted input light is inevitable). To avoid this problem, one can use the negative refraction property of the photonic crystals to isolate the signal of interest from the stray light. One implementation of this idea is imaginable if the designed photonic crystal of interest has the negative refraction property in addition to the superprism effect and negative diffraction. In that case, the signal in the bandwidth and polarization of interest can be steered away from stray light by refracting in the negative regime (while all other input waves experience a positive refraction at the interface), as demonstrated in Figure 5.1(b).

Note that in this way, the "synthesized" optical material is behaving in contrary to the ordinary bulk optical materials in three ways: it send different wavelengths to drastically different directions (the superprism effect), it diffracts the light reverse to that of ordinary bulk media (negative diffraction), and it refracts the signal at the interface to the opposite direction, compared to ordinary materials (negative refraction). And these

three effects, when combined, result in a close-to-ideal optical material for wavelength demultiplexing in a way that was not available before.

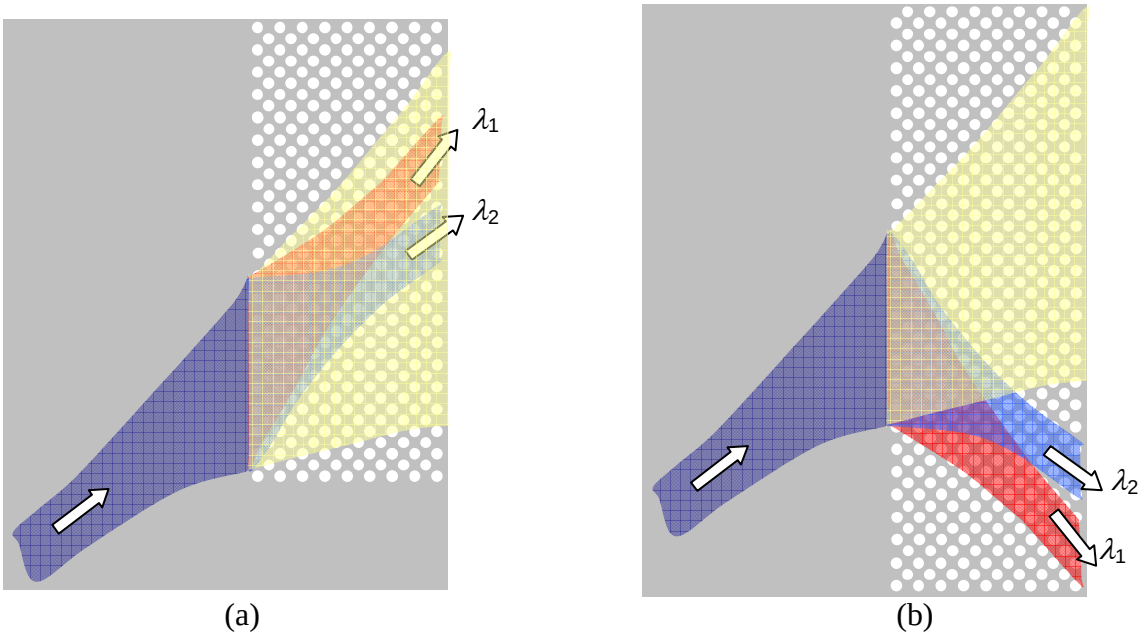


Figure 5.1. Diffraction compensated wavelength demultiplexing in photonic crystals is schematically demonstrated for operation in the (a) positive refraction regime and (b) negative refraction regime.

The basic ideas of the three effects that are combined in our design are shown in Figure 5.2. Figure 5.2(a) shows a typical planar PC fabricated by etching a two-dimensional (2D) array of air holes in Si. Figure 5.2(b) shows the superprism effect, in which the PC separates wavelength channels by directing them into different angles. Figure 5.2(c) shows the application of the negative diffraction property of PCs for diffraction compensation. Propagation of an optical beam in a PC with negative diffraction index compensates for the diffraction caused by propagation through a normal (i.e., positive diffraction index) material. The negative refraction at the PC interface is shown in Figure 5.2(d). As Figure 5.2(d) shows, the desired signal is refracted away from the direction of the incident signal (causing the separation of the desired signal from stray signals).

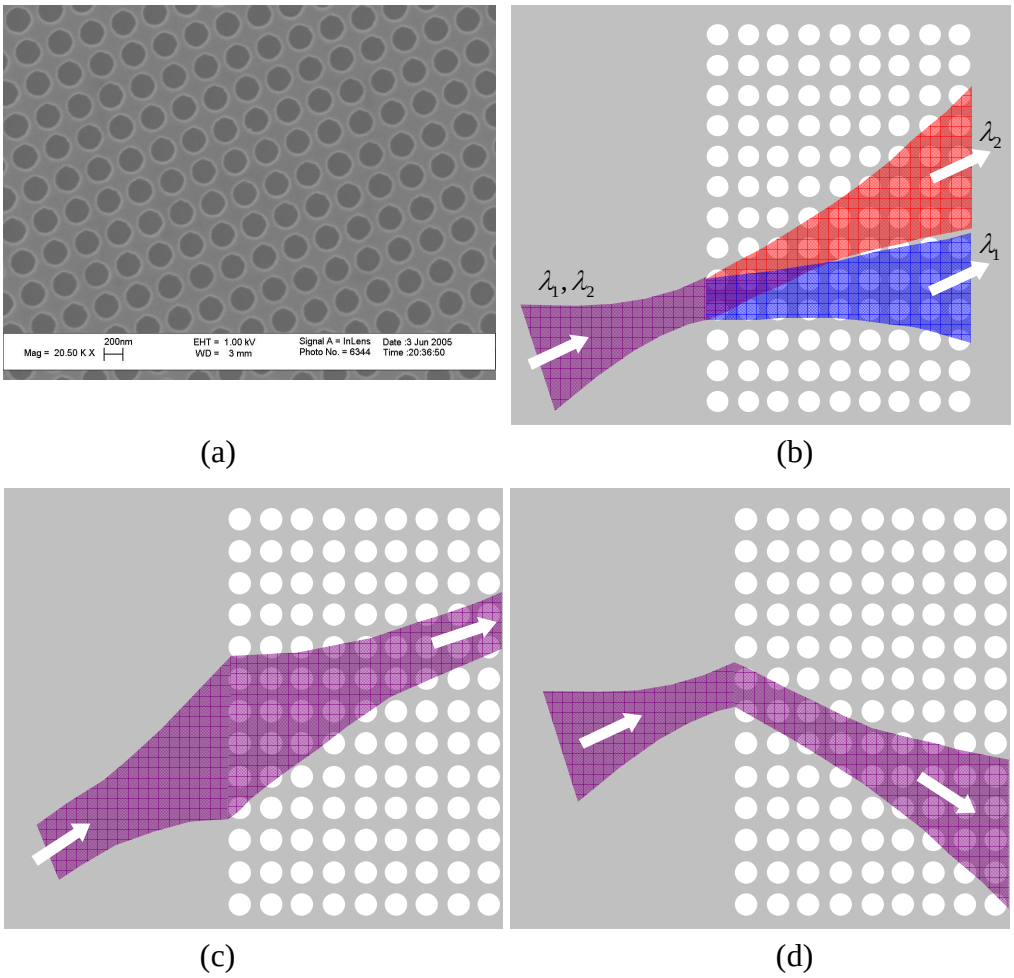


Figure 5.2. (a) An SEM image of a square lattice PC fabricated in SOI is shown. (b) Schematic plot of the superprism-based demultiplexing in the conventional configuration is shown. (c) Schematic plot of diffraction compensation (PC is designed in negative diffraction regime) is shown. (d) Schematic plot of negative refraction at the interface of PC is shown.

## 5.1. Planar Photonic Crystals

In this implementation, I will focus on planar structures since this is the most feasible option for photonic crystals because of their compatibility with the well-developed microelectronic fabrication techniques. Unlike simulation techniques based on direct electromagnetic wave propagation that their computation cost considerably grows as we go to three-dimensional structures, the diffractive index model, described in this

work, only requires the band structure of the photonic crystal, which can be calculated once for all further calculation steps. This allows us to directly perform a three-dimensional analysis on the more realistic planar structures. One main difference between the three-dimensional planar case and the two-dimensional model is that in two dimensional case the incident region is assumed to be a homogeneous medium with a given refractive of index (material dispersion can be neglected in the relatively narrow bandwidth of operation); however, in planar structures, the incident wave comes through a slab waveguide and the modal dispersion of this waveguide affects the modes that can be excited inside the photonic crystal region. Figure 5.3(a) shows the calculated dispersion curve (effective guiding index with respect to frequency) for the first TE-like and TM-like modes of this slab waveguide. For the dispersion diagram in Figure 5.3(a), a SOI wafer is assumed with top silicon layer of thickness of 220 nm on a 3 μm of $SiO_2$. The silicon oxide layer is assumed to isolate the guiding layer from the thick silicon substrate. Figure 5.3(b) shows the loci of the modes excited inside a square lattice photonic crystal made in the same wafer with a lattice constant of $a$=355nm and holes of diameter 213nm, when the light comes from the unpatterned slab at different angles.

Figure 5.4 shows the band structure of the first TE-like photonic band of a square lattice PC of air-holes in Si in an SOI wafer. The interface of this PC is at a 45° angle with respect to the primary lattice directions as shown in the inset of Figure 5.4. Different regions of the band structure with a strong superprism effect, the negative diffraction property, and the negative refraction property are marked on this band structure, showing that a range of operation with all the three properties is possible. I have used the methodology in Chapter 4 to find the optimal operation point, and design a 4-channel wavelength demultiplexer around 1550 nm in this structure. The resulting design

parameters are: $r/a$ = 0.25, $h/a$ = 0.6, $\alpha$ = 15°, L = 70 μm, and $2w_0$ = 10.5 μm. This design was then used in the fabrication process that follows.

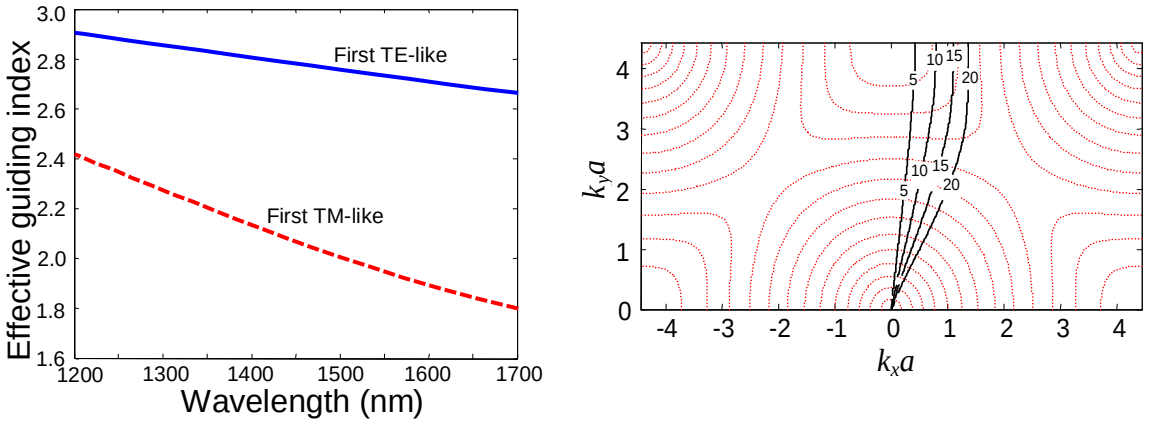


(a) (b)

Figure 5.3. (a) The dispersion diagram for guiding in an unpatterned SOI wafer with $h$=220nm is plotted. (b) The band structure (dotted lines) of a slab-type PC in an SOI wafer (square lattice, $r/a$=0.30, $h/a$=0.62) and the loci of PC modes (solid lines) excited for incident waves coming from an unpatterned slab at different incident angles are shown.

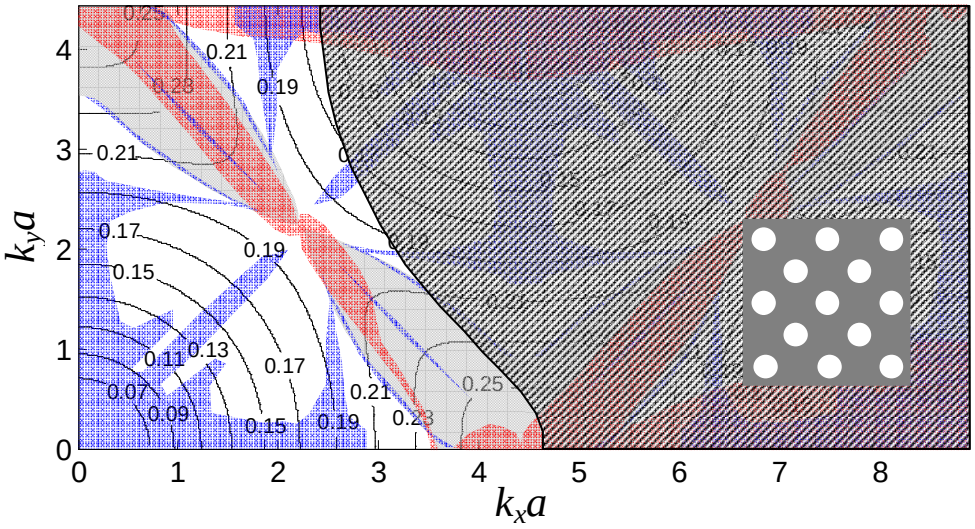


Figure 5.4. Calculated of iso-frequency contours of the first TE-like band in a planar square lattice PC ($r/a$ = 0.25 on SOI wafer) with the principal lattice direction at 45° with respect to the interface. Regions of the band structure with different dispersive properties are marked as gray for negative diffraction; red for a strong superprism effect; blue for low third-order diffraction; and hatched for regions not excitable from the input slab waveguide.

## 5.2. Fabrication Process

The optimal structure found by dispersion engineering of the PC according to the guidelines mentioned in the previous section was fabricated on a SOI wafer with 3 μm of $SiO_2$ sandwiched between a thick Si substrate and a 220 nm layer of Si (on top) covered by 70 nm of $SiO_2$ that is used as a hard-mask during the fabrication process. The 2D PC pattern is lithographically written on the top $SiO_2$ layer using a JEOL JBX-9300FS 100kV electron beam lithography system and then etched using a Plasma-Therm inductively coupled plasma (ICP) system. Figure 5.5 shows the schematic view of the fabricated structure. Light is end-coupled into the structure through one of a series of 10.6 μm wide input waveguides each exciting the PC structure at a unique incident angle in the range of 13 to 17 degrees. The PC region (found through optimization) has a 45°-rotated square lattice geometry with a lattice constant of 367 nm and with holes of 180 nm in diameter, as shown in the inset of Figure 5.5. The propagation through the 1100 μm long unpatterned Si region (schematically shown in Figure 5.5) preconditions the beam with positive second order phase. Beam blocks are used at the entrance of the PC region to limit the spatial-spectral content of the input beam (i.e., to spatially filter out some of the higher-order beams that are excited by higher order modes of the multimode input waveguide) and also to prevent stray incident light from reaching the output end. The output light of the PC region is coupled into an array of 5 μm wide waveguides (with 1 μm distance between neighboring waveguides) to obtain better spatial resolution (note that the size of beam for each wavelength channel is around 11 μm at the output). The spatial extent of the light in each wavelength channel in the PC demultiplexer output corresponds to two output waveguides. Each output waveguide is tapered down to 2 μm at the output end of the devices. Two of the wavelength channels are schematically shown on Figure 5.5 as red and blue curves.

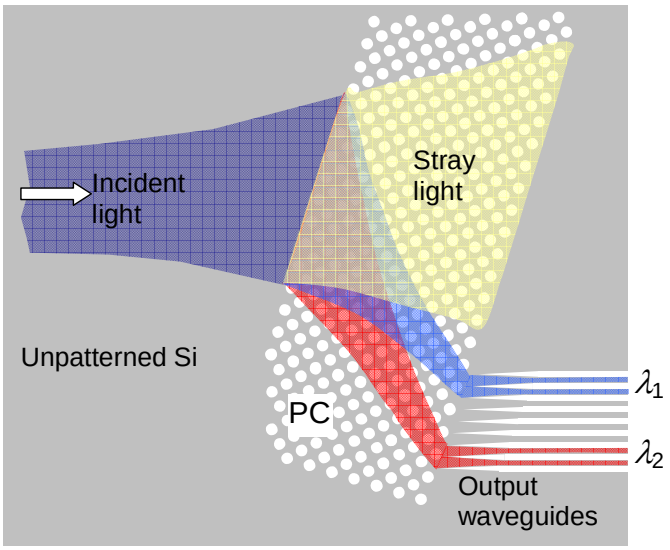


Figure 5.5. A schematic view of the wavelength demultiplexing structure combining three dispersive properties of photonic crystals, i.e., the superprism effect, negative diffraction, and negative refraction, is demonstrated.

We have fabricated a preconditioned photonic crystal superprism demultiplexer designed using the process in Section 4.6 in a silicon-on-insulator (SOI) wafer. The initial wafer has a 220 nm layer of Si sandwiched between a 70nm of $SiO_2$ top layer (used as a hard-mask during fabrication process) and a 3 μm $SiO_2$ layer underneath. Electron-beam lithography and ICP etching are used to pattern the top $SiO_2$ hard mask layer, and a chlorine-based chemistry is used afterwards to pattern the Si layer. Scanning electron microscopy (SEM) images of the fabricated photonic crystal structure and its interface are shown in Figure 5.6(a) and Figure 5.6(b), respectively. The overall view of the structure is shown in Figure 5.6(c). The optical beam from the input waveguide goes through a preconditioning region to initially undergo the required preconditioning diffraction [shown schematically as beam broadening in Figure 5.6(c)]. This diffraction is subsequently compensated by propagation of the beam through the photonic crystal region, so that the optical beams are focused again at the output interface of the photonic crystal region. Figure 5.7 shows an SEM image of the output edge of the sample after

cleaving. This SEM image shows the arrangement of different layers of the SOI wafer used for the fabrication, as well as the quality of end-faces of the output waveguides.

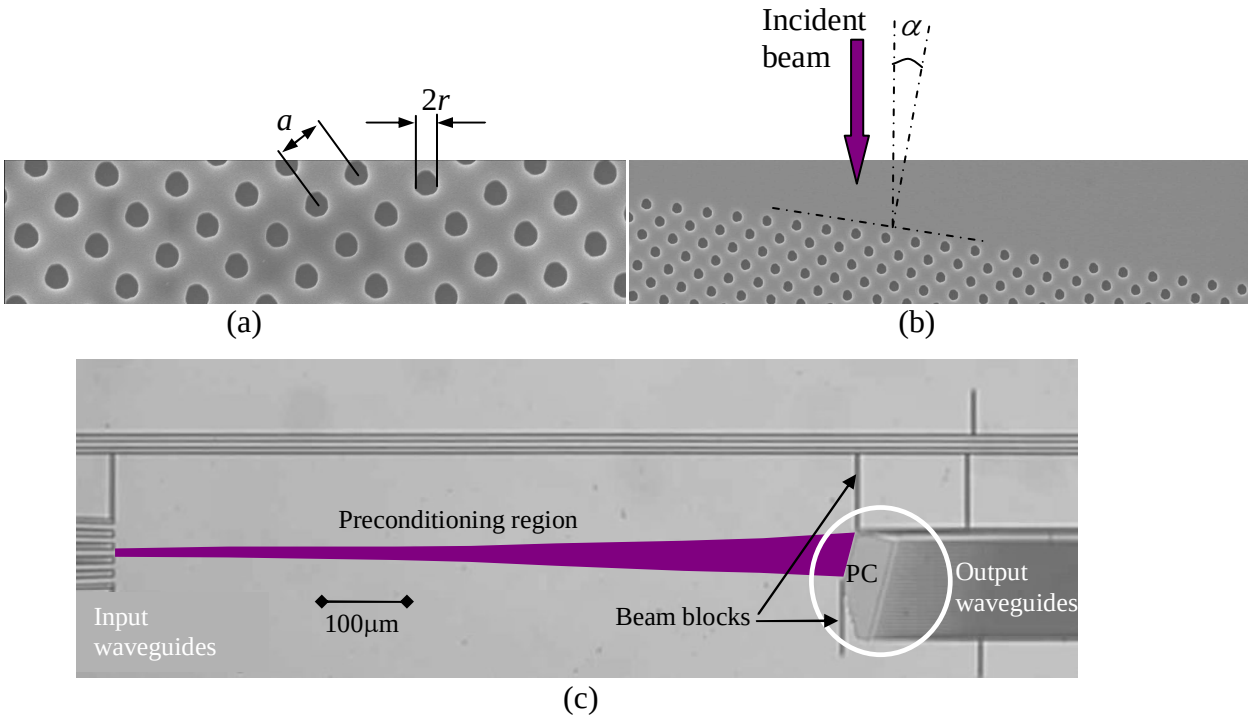


Figure 5.6. (a) An SEM image of the fabricated device is shown. A rotated square lattice PC with $r/a$ = 0.24 in a planar SOI platform is used. (b) An SEM image of the interface of the PC is shown. (c) Overview of the demultiplexing device is shown. Five input waveguides are used to test the response of the device under different incident angles. Waveguides at the output are used to sample the beam profile of the optical beams coming out of the PC.

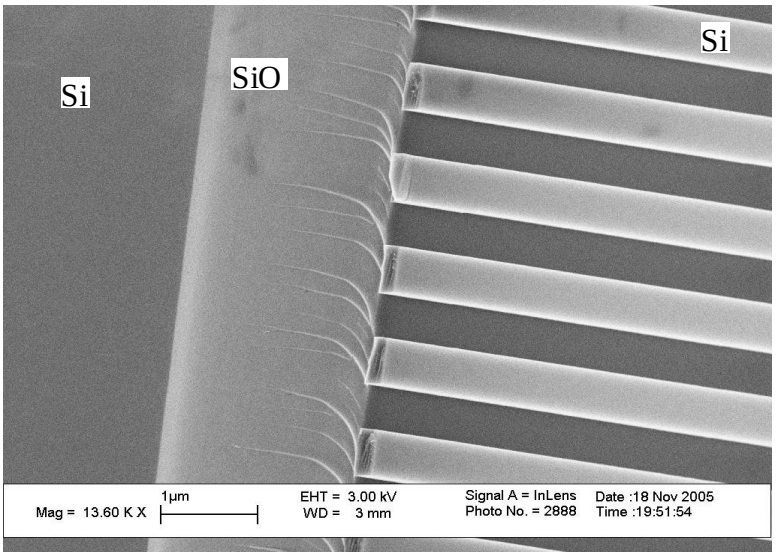


Figure 5.7. An SEM image of the cleaved edge of the output waveguides is shown. Some nonuniformity in the quality of the end-faces of these output waveguides is clear. The three layers of this SOI wafer, i.e., the film Si, the isolating $SiO_2$, and the substrate Si, are also visible in this image.

### 5.3. Characterization Setup

In our measurement setup, shown in Figure 5.8, a set of tunable lasers (81672B, 81600B, 81680A, and 81640A from Agilent Technologies, covering 1260 nm to 1640 nm wavelength range) are coupled through fiber couplers to a graded refractive index (GRIN) fiber lens and the collimated beam is directed through a broadband polarizer to assure the proper polarization of input beam. A 40x objective lens is used to end-couple the light into one of the input waveguides of the devices. The sample is placed on a sample holder on top of a precision translation/tilt stage (561-XYZT precision stage from Newport). An infrared (IR) camera (SU320 NIR, from Sensors Unlimited, Inc.) connected to a long working distance microscope (Mytutoyo FS-70 microscope head, with 20x and 50x near infrared long working distance lenses) is used to monitor the coupling to the input waveguide from the top. The output edge of the device is imaged using a 20x objective lens on another IR camera (Merlin NIR from Indigo Corp.). Figures 5.9(a) and 5.9(b) show the actual characterization setup that is used in this research.

Figure 5.9(c) shows the arrangement of these three lenses around the device under test (DUT). Figure 5.9(d) shows the image taken by an IR camera of the input edge of the sample under test, showing the scattering of the laser spot from the input facet of the sample and coupling of light to the waveguides.

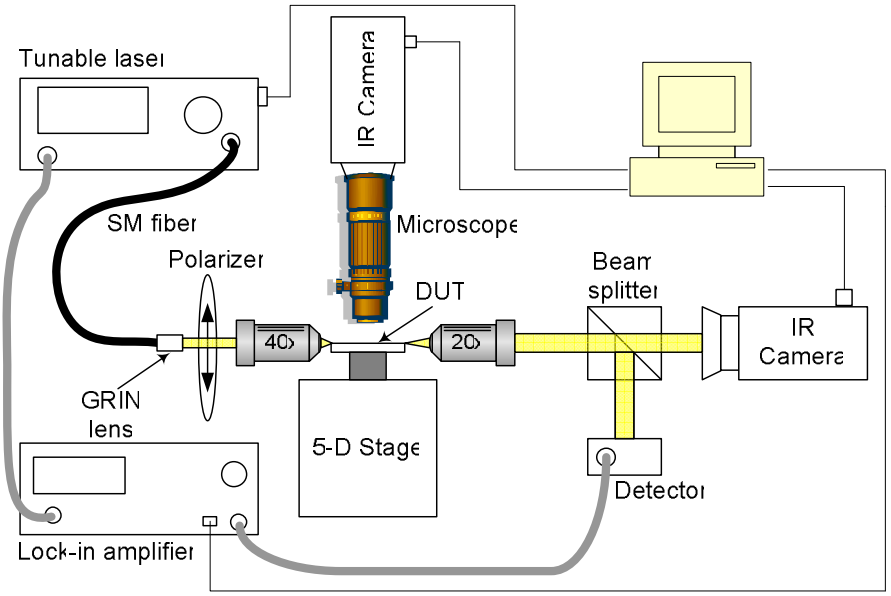


Figure 5.8. Overall view of the experimental setup for characterization of the planar PC structures.

The output light intensity is also directed to an IR detector (New Focus #2033 with 30 kHz bandwidth) that is connected to a lock-in amplifier with a modulation frequency of 20 kHz (Stanford Research Systems, SR830) to enhance the signal-to-noise ratio of the channel response measurements [104]. The LabVIEW software (from National Instruments) is used for controlling all the experiments. It is used to capture the images from cameras, and to systematically sweep the wavelength and measure the transmission spectrum over the desired wavelength range (in the available tunable laser range of 1260 nm to 1640 nm). All the data is stored in the computer either using a data acquisition card (DAQ) or using a GPIB card for further processing.

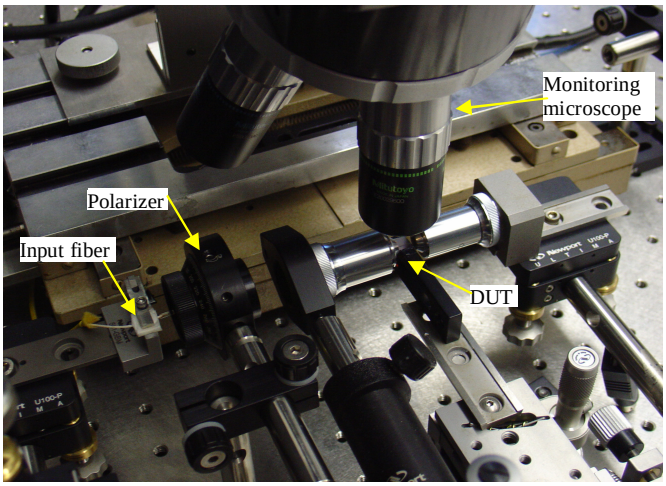


(a)

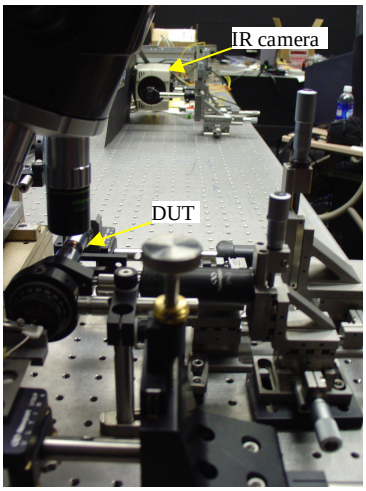


(b)

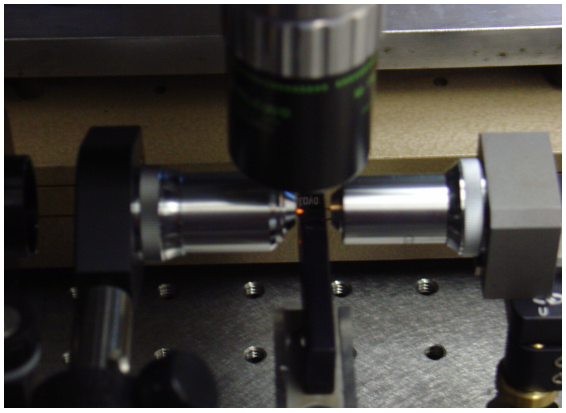

(c)

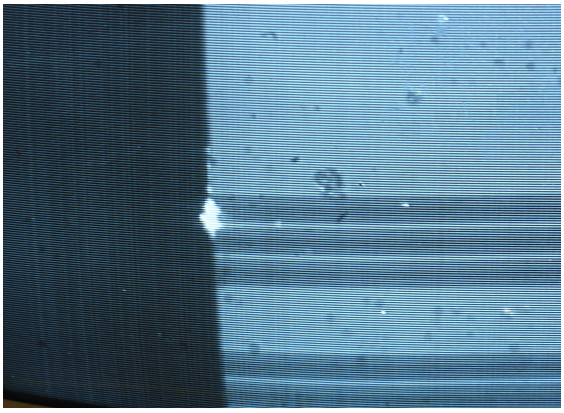

(d)

Figure 5.9. (a) An image of the actual characterization setup, with light passing from left to right, shows the input fiber, the polarizer, the objective lens to couple the light into the device under test (DUT), and the output lens to image the output edge of the sample. A long working distance microscope on top (connected to an IR camera) is used for alignment purposes in this case. (b) Imaging at the output with high magnification is used, as shown in this figure, to isolate and resolve individual output waveguides. (c) The image of the DUT shows the configuration of the input and output lenses as well as the long working distance lens connected to the microscope for alignment inspection. (d) Picture taken by an IR camera shows the laser spot at the input interface and coupling of light to one of the input waveguides.

## 5.4. Experimental Measurement Results

Figure 5.10(a) shows the image of the output waveguides at four discrete wavelengths with input in TE-like polarization (electric field parallel to the plane of periodicity). Good separation of these wavelength channels can be clearly seen in Figure 5.10(a). In addition, the desired small spot obtained by the diffraction compensation

effect is evident from these images (Note that the size of the input beam at the entrance to the PC region is around 60μm). Another evidence for dramatic minimization of the output spot size comes from the comparison of the focusing TE-like beams with TM-like beams for which neither the superprism effect nor the diffraction compensation effect occur.

In Figure 5.10(b), we show the measured output distributions for TM-like polarization for the same set of wavelengths used in Figure 5.10(a). It can be easily seen that the overall output beam profiles of all TM-like channels are very broad, covering more than 10 output waveguides. Comparing Figures 5.10(a) and 5.10(b), the effect of negative diffraction in refocusing the TE-like polarization beams at the output end is evident. Also, it can be clearly observed that by designing the device in the negative refraction regime for the TE polarization, the unwanted polarization (TM) is successfully isolated from the desired signals (i.e., all TM signals in the wavelength range of operation appear in a separate set of output waveguides). To measure the power in each output waveguide, a pinhole in the far-field of the device output is used to select only a single waveguide and to reduce the scattered light from the background.

The normalized measured power for four of the output waveguides at 15° incident angle from the input waveguide are shown in Figure 5.11(a). Four channels are separated in this device with a wavelength spacing of 8 nm, and channel isolations (sum of contributions of other channels at the location of the desired one) are better than 6.5 dB. This is to the best of our knowledge the first demonstration of an integrated superprism-based demultiplexing device with such channel separation in a 4500 $\mu m^2$ (i.e., 50μm×90μm) PC structure. Using the same scheme, a 64-channel demultiplexer with channel spacing of 0.5 nm can be realized in a 4 $mm^2$ PC structure.

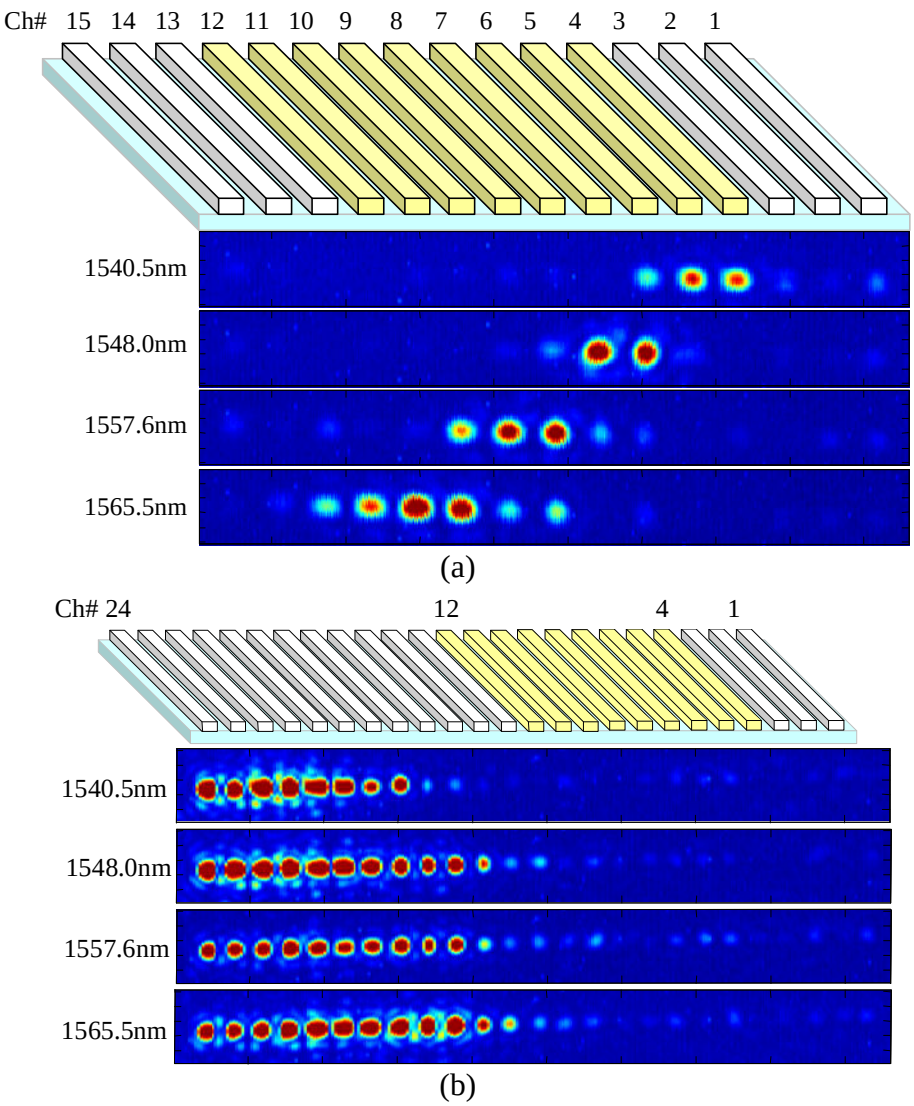


Figure 5.10. (a) Output images for the TE-like polarization show power distributions in the output waveguides at four discrete wavelengths. (b) For the same wavelengths as part (a), power distributions in the output waveguides for the TM-like polarization are shown. It can be seen that for this polarization diffraction compensation does not occur, and the output beams have extended distributions. Moreover, there is negligible interference from this polarization at the location of demultiplexing channels highlighted in this figure.

Note that in general, the power level for different channels is not uniform (1.5 dB variation over the channels is shown in Figure 5.11) because of the wavelength-dependent intrinsic loss of the PC, the wavelength-dependent nonuniformity in excitation, or the quality of end-face of output waveguides corresponding to different channels. Note also that for the fourth channel (at 1563 nm in Figure 5.11) the focusing is not as good as the other channels. Possible reasons for the side-lobe appearing on one side of the

spectrum [visible on the two channels on the right in Figure 5.11(b)] are distortion in the incident beam and diffraction effects from beam blocks at the entrance to the PC region, and residual third-order spatial diffraction effects (possibly caused by imperfections in fabrication that deviate the fabricated structure from the optimum operation point with low spatial dispersion effects). The total insertion loss for the sample demonstrated in this measurement is estimated to be 13 dB by comparing the output power level to that of a straight ridge waveguide on the same substrate. Note that a large portion of this loss (approximately 6 dB) is due to the multimode nature of the input waveguide and can be considerably reduced by using a tapered input waveguide. The preconditioning region in Figure 5.6 is chosen to be an unpatterned Si slab for simplicity of demonstration. In a practical device, this function can be implemented using a curved mirror with appropriate curvature to further reduce the size.

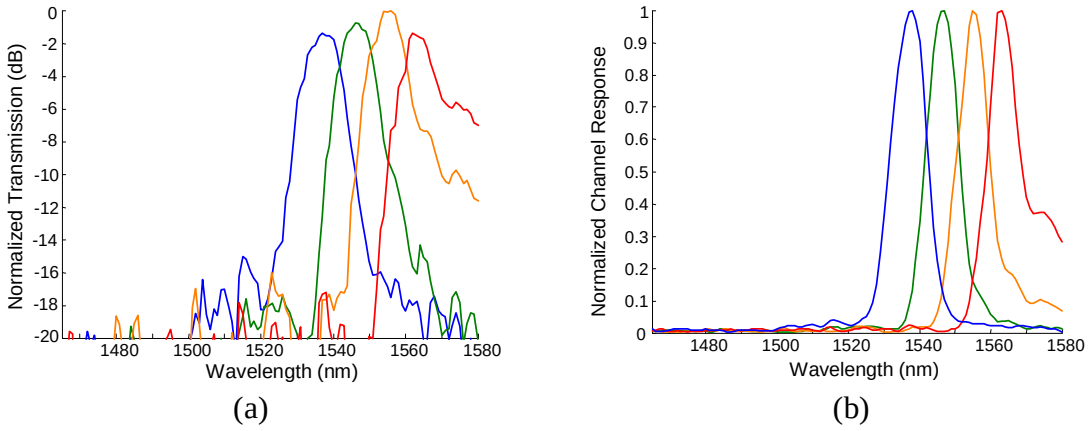


Figure 5.11. (a) The measured transmitted powers of four output waveguides (channels 5, 7, 9, and 11) are plotted. (b) Channel responses for the waveguides in (a) are shown. In this case, incidence is at 15° (middle input waveguide is used for excitation), and input wave has a TE-like polarization.

Looking at the operation range in Figure 5.4, we can see that for incident angles slightly different from the designed value, the same basic properties for wavelength demultiplexing are still satisfied. To confirm this observation, another sample was used (with similar parameters as above, with slightly smaller holes of 175 nm in diameter)

with extra input waveguides to send the light to the photonic crystal at three incident angles (i.e., 13°, 15°, and 17°). The channel responses for these three incident angles are shown in Figure 5.12. By comparing the results obtained at different incident angles, it can be observed that: first, the diffraction compensation is not complete at $\alpha$ = 13° (because the preconditioning length is designed for another incident angle), resulting in wider spectral lines, compared to other incident angles. Second, the third-order diffraction effects are stronger (for this particular set of parameters) at $\alpha$ = 15°, compared to $\alpha$ = 17°, resulting in more pronounced side-lobes in the channel responses. Finally, the bandwidth of operation shifts as the incident angle is changed, and this effect can be used to extend the operation bandwidth of the device. All these observations are in agreement with theoretical predictions, and confirm the validity of the approximate model used to describe the dispersive effects in these PC structures. Up to this point, the main focus has been on the demonstration of the principle wavelength demultiplexing effect in PCs. In the following chapters, additional considerations for improving the performance of these devices (e.g., reducing insertion loss) will be addressed.

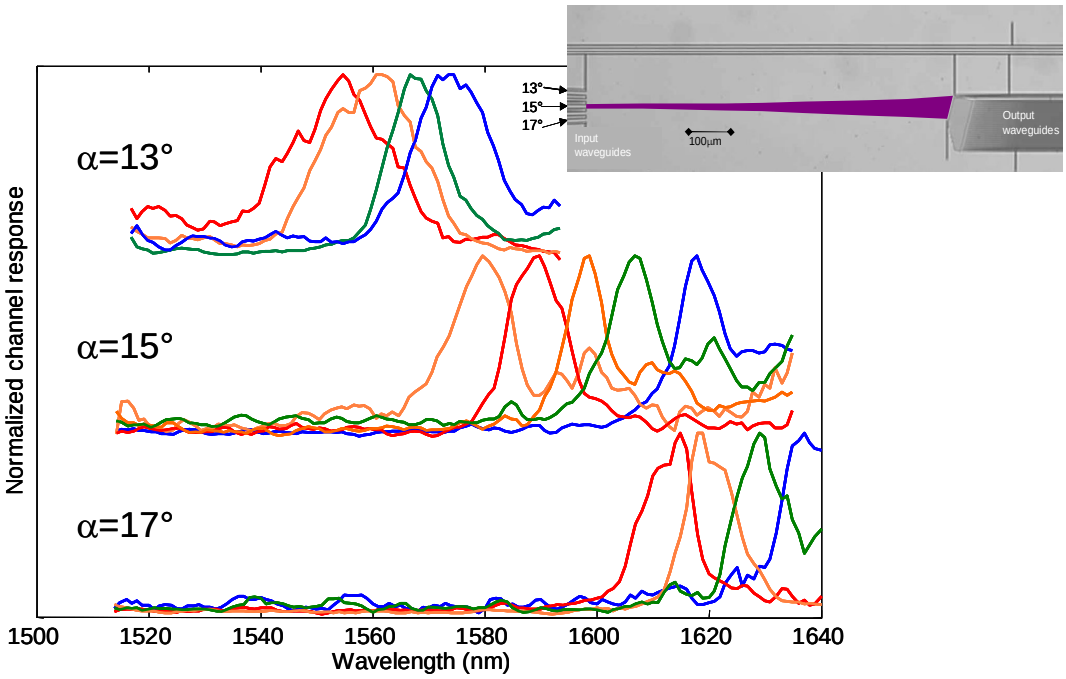


Figure 5.12. Transmission channel responses for a sample fabricated in SOI (a 45°-rotated square lattice geometry with a lattice constant of 367 nm and with holes of 175 nm in diameter) are shown at three different incident angles of $\alpha$ =13°, 15°, and 17°.

# CHAPTER 6

# EFFICIENT COUPLING OF LIGHT TO DISPERSIVE PHOTONIC STRUCTURES

One crucial issue in implementing dispersion-based PC devices is to overcome the reflection loss in coupling the light into or out of the PC structures. Improper coupling and considerable reflection at the interfaces of these devices disrupt efficient operation of dispersive photonic structures by increasing the insertion loss in these devices and by contributing to unwanted responses caused by coupling to unwanted modes (e.g., multiple reflections or increased cross-talk). These factors especially become important in realizing a system consisting of multiple components. In this chapter, a direct method for the analysis of these reflection effects at the interfaces of photonic crystals will be provided. Also, two approaches for designing matching stages to reduce unwanted reflections, namely, adiabatic matching and impedance matching, will be discussed.

## 6.1. Analysis of Reflection at the Interface of Photonic Crystals

In this section, I will limit the analysis of reflection at the interface of PCs to the case of 2D PCs, because of their close relation to the planar structures we study in this research. The reflection at the interfaces of planar PCs can be decomposed to the effects caused by the lateral mode profile of the wave and those caused by the in-plane effects of the PC. The lateral mode profile mismatch between the incident and the PC regions results in scattering loss to out-of-plane radiation modes in addition to in-plane reflection. However, since the mismatch is mainly due to the difference between the degrees of confinement in the two regions, the resulting reflection and scattering is not the dominant factor in the insertion loss. Furthermore, since we are focusing on reducing the reflection loss in this work, and tapering the modes have proven to be useful in reducing these

effects in planar PCs, the focus in the remaining of the discussions will be on analyzing the in-plane reflection effects.

The in-plane reflection effects in planar PCs can be efficiently modeled by comparing the effects to those in 2D PCs. To make the 2D model resemble more to the actual planar structure, a diffractive index is used in the 2D model, which describes the effective confinement of the light to the planar film layer [105]. The geometry of the structures that will be considered in the rest of this section is shown in Figure 6.1. In this figure, a plane wave is incident on the interface of the PC at an angle, $\alpha$, and excites transmitted modes inside the PC region as well as modes reflecting back from the interface. The wavevectors of all the excited modes are connected to each other by phase matching condition along the interface. The PC structure is assumed to have arbitrary lattice direction denoted by $\mathbf{a}_1$ and $\mathbf{a}_2$, as shown in Figure 6.1. To address most common practical cases, I will focus on the case where one of the periodicity lattice vectors (here, $\mathbf{a}_1$) is along the interface, even though the method can be readily extended to the more general case of arbitrary interface.

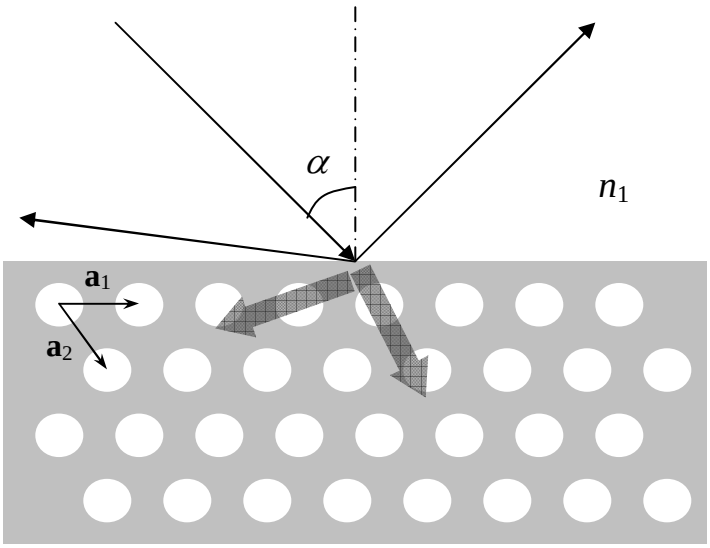


Figure 6.1. The geometry of the setup for calculating the reflection at the interface of a 2D PC is illustrated.

To perform this analysis, I use a direct mode matching process. This process consists of calculating all significant modes in both the incident region and the PC region, and then finding the relative amplitude of these modes by applying the electromagnetic boundary conditions along the interface. This is a very general method, and variations of it can be applied to other cases of interest such as reflection at the interface between two PCs or reflection of a wave coming from a PC to a bulk medium.

The first step in the analysis is finding the possible modes in the two regions when the incident wavevector is present in the setup. The reflected wavevectors are found directly by applying the phase matching condition along the interface (by considering the tangential components of reciprocal lattice vectors of the PC). To find the modes inside the PC, we use a modified version of the plane-wave expansion method. In this modified version, using the Floquet-Bloch theorem, the field is expanded as

$$f(\mathbf{r}) = \sum_m \sum_n \tilde{f}_{mn} \exp[-j(k + m\mathbf{K_1} + n\mathbf{K_2}) \cdot \mathbf{r}], \tag{6.1}$$

and this expansion is inserted into the Maxwell's equations. In this case, the frequency of the mode and one of the components of the wavevector (i.e., the component along the interface) are known. The relations are then re-arranged to form an eigenvalue problem for the other component of the wavevector. By solving the resulting eigenvalue problem, all PC modes that are excited with the given incident wave are calculated (See Appendix B for the details of this process).

After finding the modes in the two regions, the continuity of tangential components of the electric and magnetic field along the interface is applied. This results in a linear system of equations with the unknowns being the amplitude of different transmitted and reflected modes in the structure. The solution of this linear system gives us these amplitudes, from which the relative power in each mode can be found. The details of this process and the related formulations are discussed in Appendix B.

Figure 6.2 shows an example of calculated reflections over a range of frequency for a square lattice PC structure, with incident wave coming at normal incidence with H-polarization. The stop bands marked in Figure 6.2(a) match with the complete reflection regions in Figure 6.2(b). Furthermore, as one would expect, the normalized frequencies close to the band edge show relatively high reflection, which means the mismatch between the incident wave and PC modes in this range is high. Also, note that at very small normalized frequencies the reflection approaches the value obtained by the average index method (large wavelength limit).

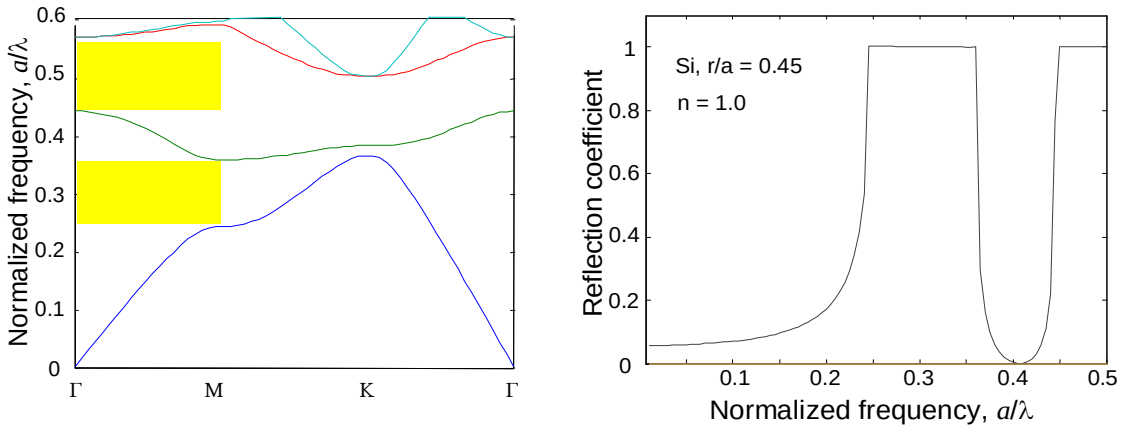


(a) (b)

Figure 6.2. (a) The band structure of the PC modes with H-polarization in a square lattice PC of air-holes ($r/a$ = 0.45) in Si is shown. (b) The calculated reflection coefficient is plotted for a plane wave coming from air to the PC in (a) at normal incidence.

The method explained above will be used as the reference point for calculating the reflection of waves at the interfaces of PCs and for investigating the related effects. In the following sections, methods will be discussed to reduce such reflections. Eliminating reflection reduces the insertion loss and removes the complication arising from multiple travels of light through the system. Without inter-stage reflections, the implementation of dispersive photonic structures is considerably simplified, and a systematic multi-level approach can be used for realizing different properties in such systems.

## 6.2. Adiabatic Matching

Different techniques that have been proposed to reduce this reflection can be divided into three groups: methods based on direct mode matching [106], methods based on interference (e.g., in [107]), and those based on gradual change [108-109]. Interference-based methods are those in which multiple reflections throughout the matching stage are used to achieve a destructive interference for the reflection wave (e.g., in anti-reflection multilayer coatings). In the matching stages based on gradual change (also known as adiabatic transition), however, the initial mode passes through slightly modified intermediate steps that transform it into the final mode, keeping the reflection low at all intermediate stages. A main concern in proposed interference-based techniques to date is the small range of frequencies or incident angles over which low reflection is achieved. In this section, we present a design for a reflection reduction stage based on adiabatic transition that is wideband (in frequency), tolerant to fabrication imperfections, compatible with planar fabrication technologies, and has a wide acceptance angle.

In this section, I present a matching stage for reflection reduction based on the principle of gradual change to efficiently couple light to propagating modes of photonic crystals (PCs). In adiabatic transitions in electromagnetic structures the characteristic properties of the medium vary smoothly in a way that there is negligible coupling of the initial mode to other modes (reflecting or of different properties) of the structure. In theory, for such a smooth variation, in the limit for an infinitely long transition region, complete transfer of energy is possible. In practice, however, the length of the transition stage is limited, and an approximation to the ultimate adiabatic case is achieved. Furthermore, relatively strong dispersion effects in the behavior of modes of the PC make it necessary to consider smooth variation of mode properties in addition to the smooth variation of geometrical features.

In the following discussions we will restrict ourselves to 2D PCs of air holes in a dielectric material with a fixed permittivity to comply with the practical limitations in fabricating planar PC devices. Thus, design parameters are the radius of holes and the aspect ratio (ratio of the lattice vector in the two perpendicular directions). Assuming that the variations are slow and following the basic approximation in Wentzel-Kramers-Brillouin (WKB) method [110] the wave in the transition region can be considered to be the local mode of the corresponding PC at each location. Thus, to design a smooth transition, one needs to know how large the mismatch in any of the intermediate interfaces is. To get this information, we first consider the reflection at the interface of two slightly different PCs shown in the inset of Figure 6.3. Assuming that the difference between field profiles of the modes at the interface is negligible, the field in these two regions can be written as

$$\begin{cases} f_1(\mathbf{r}) = u_1(\mathbf{r})\exp(-j\mathbf{k}_i \cdot \mathbf{r}) + \rho u_1(\mathbf{r})\exp(-j\mathbf{k}_r \cdot \mathbf{r}) \\ f_2(\mathbf{r}) = \tau u_2(\mathbf{r})\exp(-j\mathbf{k}_t \cdot \mathbf{r}) \end{cases}, \tag{6.2}$$

where the field is $f_n(\mathbf{r}) = \sqrt{\varepsilon_n(\mathbf{r})}E_{n,z}(\mathbf{r})$ ($n$ = 1,2 shows the region that field corresponds to) for E-polarization (electric field perpendicular to the plane of periodicity), and $f_n(\mathbf{r}) = \sqrt{\mu_0}H_{n,z}(\mathbf{r})$ for H-polarization (magnetic field perpendicular to the plane of periodicity). The coefficients $\rho$ and $\tau$ represent the reflection and transmission relative field amplitudes, and $u_1(\mathbf{r})$ and $u_2(\mathbf{r})$ are the Bloch envelope functions corresponding to the PC modes. In addition, $\mathbf{k}_i$, $\mathbf{k}_r$, and $\mathbf{k}_t$ are the incident, reflected, and transmitted wavevectors, respectively.

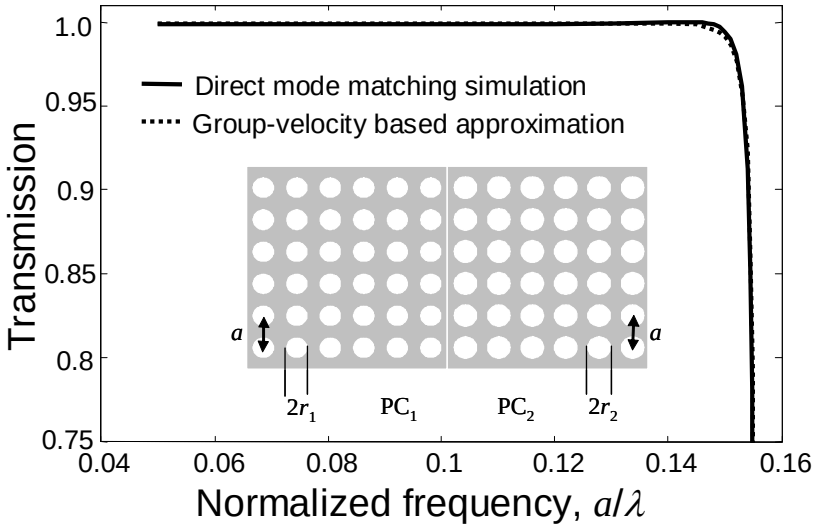


Figure 6.3. Transmission coefficients (E-polarization) for the light coupling between two 2D square lattice PCs with slightly different parameters ($r_1/a$ = 0.30 and $r_2/a$ = 0.35, as shown in the inset) using the direct mode matching simulation and group-velocity-based approximation are compared.

Assuming $S_i$, $S_r$, and $S_t$ to be the component of Poynting vector normal to the interface corresponding to incident, reflected, and transmitted contributions, respectively, the boundary conditions at the interface can be written as

$$\begin{cases} f_1(\mathbf{r})\big|_{\text{interface}} = f_2(\mathbf{r})\big|_{\text{interface}} \\ S_i\big|_{\text{interface}} = S_r\big|_{\text{interface}} + S_t\big|_{\text{interface}} \end{cases}. \tag{6.3}$$

The Poynting vector can be related to the group velocity using $\mathbf{S} = \mathrm{E}\mathbf{v}_g$, in which E is the average energy density of the mode, given by

$$\mathrm{E} = 2\int_{uc} |f(\mathbf{r})|^2 \mathbf{dr} \Big/ \int_{uc} \mathbf{dr} = 2\int_{uc} |u(\mathbf{r})|^2 \mathbf{dr} \Big/ \int_{uc} \mathbf{dr}, \tag{6.4}$$

where the integration is performed over a unit cell (*uc*) of the PC. Starting from this relation for incident, reflected, and transmitted waves, and using the assumption that the field profiles in the two regions have negligible difference, one can directly deduce that $\rho$

and $\tau$ are real-valued and that $\int_{uc}|u_1(\mathbf{r})|^2\,\mathbf{dr} \approx \int_{uc}|u_2(\mathbf{r})|^2\,\mathbf{dr}$. Therefore, $\mathrm{E}_{1,i} = \mathrm{E}_{1,r}/\rho^2 = \mathrm{E}_{2,t}/\tau^2$, and substituting this into (6.3) results in

$$\begin{cases} 1+\rho = \tau \\ \tau^2 v_{g2,n} + \rho^2 v_{g1,n} = v_{g1,n} \end{cases}, \tag{6.5}$$

where $v_{g1,n}$ and $v_{g2,n}$ are the components of group velocities normal to the interface for the PC modes in regions 1 and 2, respectively. Using Equation (6.5) one can obtain the reflection coefficient as [126]

$$\rho = (v_{g1,n} - v_{g2,n})/(v_{g1,n} + v_{g2,n}). \tag{6.6}$$

This relation relates the reflection at the interface between slightly different PCs to the mismatch in the group velocity of their modes. To verify the validity of (6.6), we analyze the reflection for TE polarized light between two 2D square lattice PCs of air-holes in Si ($\varepsilon_r = 11.4$) with $r_1/a$ = 0.30, $r_2/a$ = 0.35, as shown in Figure 6.3. The results for direct calculations (using plane-wave expansion and mode matching method [31]) are compared with those obtained by group-velocity approximation in Equation (6.6), as shown in Figure 6.6. Transmission coefficients (i.e., transmitted power divided by the incident power) calculated using the approximate relation in this case agrees well (within a relative error less than 1%) with those of the exact calculations.

In PCs, the reflection between slightly different regions can be attributed to two sources: the difference between their group velocities and the difference between their field profiles. Thus, design of a smooth transition region (i.e., designing the pattern of variation for the radius of holes and aspect ratio) should be performed in two aspects: 1) smooth variation in field profile, and 2) smooth variation in group velocity. Here the

focus is on coupling from an incident homogeneous region to a PC structure. For this case, the strategy that we propose involves 1) initially changing the geometry of the PC structure smoothly keeping the group velocity intact until we reach a PC structure with low dispersion effects, and 2) in the second step, changing the structure to match the group velocity of the incident region. Using this scheme, the field profile matching is done at first, and then group velocity matching is performed in the regime that dispersion effects are no longer strong. To demonstrate this design scheme, coupling at normal incidence from a homogeneous Si region to a square lattice PC of air-holes in Si with $r/a = 0.40$ under TE polarization is considered. For this lattice type, constant group velocity contours with respect to different values of hole size and aspect ratio are plotted in Figure 6.4. Normalized frequency ($\omega_n = a_x/\lambda$, $a_x$ being the lattice constant parallel to the interface) of 0.15 is assumed for the calculation of the results shown in Figure 6.4 The path proposed for the adiabatic transition is shown by a dashed line in this figure. Point A in Figure 6.4 corresponds to the PC structure that we plan to efficiently couple light to (target PC). The path between A and B falls on a constant group velocity contour, and each point shown by an open circle corresponds to one of the intermediate PC layers. The path from B to C is chosen to have equal reflection at all intermediate stages.

The approximate length of the matching stage, *L*, for long transition regions, $k_0 L >> c/v_{g2,n}$, can be obtained based on general approximations of adiabatic transition [110], as

$$L \approx (1/2k_0)(c/v_{g2,n})\ln(1/R_g), \tag{6.7}$$

in which $R_g$ is the desired (or acceptable maximum) power reflection, $c$ is the velocity of light in vacuum, and $k_0$ is the free-space wavenumber. Equation (6.7) for a PC structure is different from the formula for adiabatic transition in bulk materials (given in [110]) by a factor $2\pi$ which was calculated by interpolation the simulation results to include the effects of the discretization of the properties of the PC structures (i.e., layered structure instead of a continuous adiabatic change), and the difference between initial and final field profiles in the PC structure (which is not present for bulk structures in [110]).

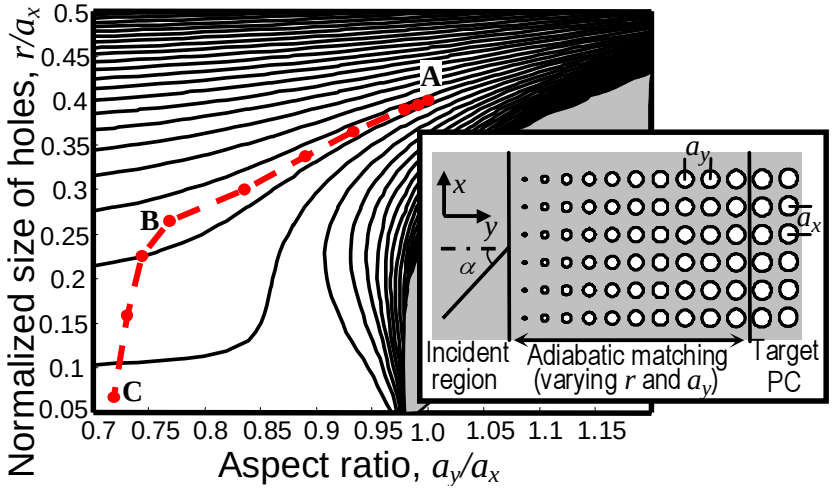


Figure 6.4. Contours of constant group velocities (at $a_x/\lambda = 0.15$ with E-polarization) for different design parameters of 2D rectangular lattice PCs are plotted. The lattice constant parallel to the interface, $a_x$, is kept intact and normal incidence (along the *y* direction) is considered. The dashed line shows the suggested path for an adiabatic transition and circles highlight the designed parameters for the successive layers. The gray shaded region represents PC structures for which the operation frequency lies inside the bandgap.

Figure 6.5(a) shows the reflection performance of the matching stages designed for different lengths of the transition for the PC structure described in Figure 6.4. A combination of plane-wave expansion and multilayer-grating analysis is used to calculate the reflection in these structures. The exponential reduction in reflection by adding the

buffer layer can be qualitatively seen from Figure 6.5(a) at each normalized frequency as suggested by Equation (6.7). Figure 6.5(a) shows that a buffer stage with small size (less than 10 lattice constants) results in considerable reflection reduction over a wide frequency range. The reflection in Figure 6.5(a) saturates below $10^{-3}$, and we believe the reason is the discretization error in the numerical technique. Figure 6.5(b) compares the angular reflection response of the PC structure having a 10-layer adiabatic matching stage with that of the structure with no matching stage. The incident region is a homogeneous Si medium. It can be observed from Figure 6.5(b) that in a wide range of angle two orders of magnitude reflection reduction is achieved by adding the buffer stage with only 10 layers. To study the robustness of the adiabatic matching stage under fabrication imperfection, Figure 6.5(c) shows the reflection performance of a 12-layer adiabatic matching stage and 50 different randomly perturbed versions of it obtained by randomly varying the radii of holes in all layers by up to 5% using a random variable with uniform distribution. Figure 6.5(c) shows that at the center frequency of $\omega_n = a/\lambda = 0.15$, the reflection remains at the same order of magnitude as the original design. Furthermore, the modified structures maintain the wideband performance expected from an adiabatic design.

To summarize, basic physical considerations in designing these matching stages are investigated and a systematic yet simple design procedure is suggested. We show that matching stages obtained using this method are wideband in frequency, have a wide acceptance angle, and are robust against fabrication imperfections. Therefore, they are the preferred choice in general-purpose matching stages to be used along with dispersion-based PC devices.

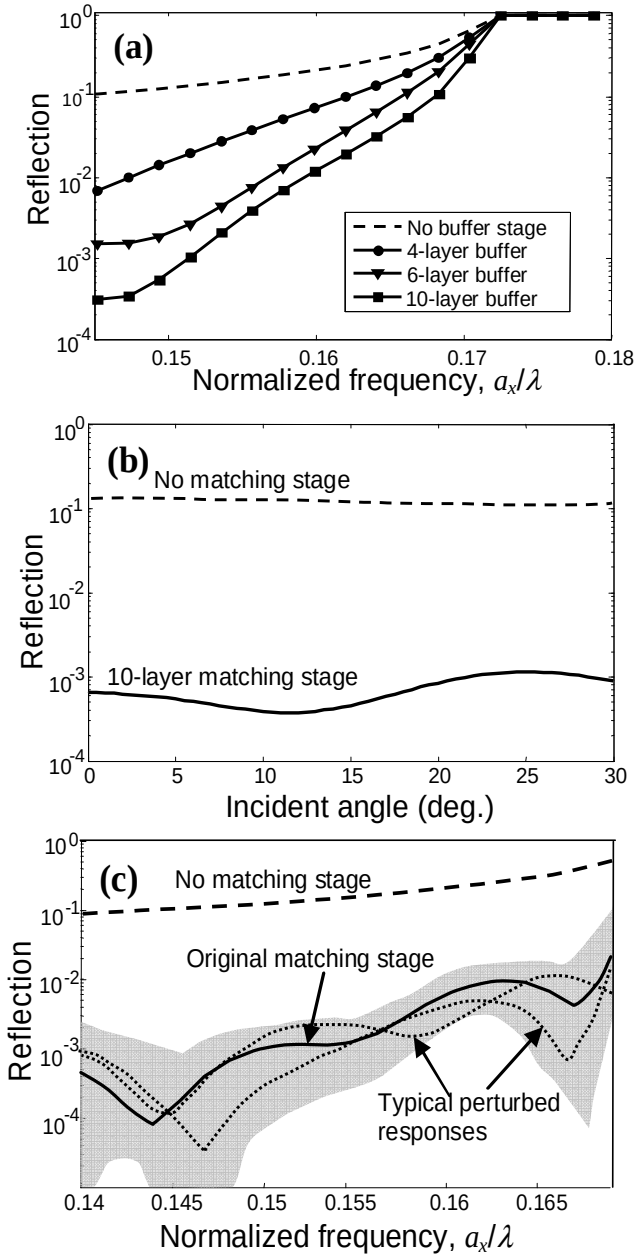


Figure 6.5. (a) Reflection from a square lattice PC structure (circular air-holes in Si, $r/a = 0.40$) is shown with no matching stage and with adiabatic matching stages. (b) For the same structure, the angular response of the 10-layer matching at $a_x/\lambda$=0.15 is compared with that of the PC with no matching stage. (c) The shaded region shows reflections for 50 different random buffer stages (with 12 PC layers) with up to 5% perturbation in the sizes of holes compared to the original design.

## 6.3. Impedance Matching

The brute-force approach of calculating the reflection at the interfaces of the PC regions usually, as discussed before, involves either direct electromagnetic simulation of the structure in the time domain [107] or using modal approach [111]. Both these approaches require massive calculations and give little insight into the physics of the coupling process from the incident region to the PC mode. Here, we propose an approximate effective impedance model that can be used to estimate the reflection at the interface of a PC structure. We will show that this model has two main attractive features: first, it is independent of the properties of the incident region, and second, it can be readily applied to analyze different terminations of the PC interface (i.e., location of the interface relative to the PC unit cell). A different impedance model, inspired by the rigorous definition of impedance, has been already reported by Biswas et al. [112]. We use an alternative definition here based on the continuity of power and field that provides more insight into the physics of reflection and enables us to optimize the structure at the interface to reduce reflection.

### 6.3.1. Definition of the effective impedance for PC interfaces

To find the reflection at the interface between two distinctive materials, the common practice is to apply the continuity of electromagnetic field (transverse components of electric and magnetic fields) along the interface. Alternatively, one can use a combination of these fields as new parameters to apply the electromagnetic boundary conditions. We limit our discussion to 2D PC structures with E-polarization field excitation (i.e., electric field perpendicular to the plane of periodicity). In this particular case, we choose continuity of the tangential electric field and continuity of the

normal Poynting vector at the interface as the boundary conditions. The choice of the continuity of the Poynting vector at the interface, encouraged by the physical concepts of the continuity of power, proves to be more suitable for PCs since the Poynting vector has the aggregated effect of the periodicity of the structure included in it. Using the analogy with homogeneous bulk media, the effective impedance for propagating modes of a PC can be defined as [113]

$$\eta = \left| \left\langle E_{\text{int}} \right\rangle^2 \right| \Big/ (2S_n), \tag{6.8}$$

where $\left\langle E_{\text{int}} \right\rangle$ is the spatial average amplitude of the electric field along the interface, and $S_n$ is the time averaged component of the Poynting vector normal to the interface. For the equivalent impedance model to be valid the incident and transmitted regions need to be single mode (or they need to have a dominant mode). Furthermore, the accuracy of the model degrades when the variations of the field along the interface in the two regions (i.e., incidence and transmission regions) differ significantly. These considerations limit the range of structures that our effective impedance model covers, but the model remains valid in the vicinity of the first photonic bandgap of the PCs, on which most of the activity in the PC dispersion engineering has been focused.

To verify the effective impedance model, we consider a 2D structure in which light is incident from a dielectric region to an interface of a square lattice PC. The PC structure consists of a periodic array of air holes in a dielectric with normalized radii of $r/a$ = 0.35 ($a$ being the lattice constant), and its band structure in the direction normal to the interface is shown in Figure 6.6(a). Since we analyze the structure using a 2D model, the effect of the finite PC thickness is taken into account by selecting the effective permittivity of $\varepsilon_r = 7.4$ for Si as the dielectric material. Here, normal incidence is

assumed, and the PC termination at the interface is assumed to go through the middle of the holes [i.e., $y_0 = a/2$, as shown in the inset of Figure 6.6(b)]. The transmission results are shown in Figure 6.6(b) for direct simulation (by modifying a cascaded grating analysis [129] to incorporate termination to a periodic structure) and for those calculated using our proposed approximate effective impedance model ( $R = |(\eta_i - \eta_{pc})/(\eta_i + \eta_{pc})|^2$ where $\eta_i$ and $\eta_{pc}$ are the effective impedance of the incident region and that of the PC interface, respectively). To calculate the effective impedance, we use plane wave expansion method to find the eigenmodes of the structure, and then the effective impedance for each PC mode is found directly from Equation (6.8) for any given location of interface. Figure 6.6(b) shows that the effective impedance model provides a very good estimate of the transmission coefficient up to the point that the reflected grating orders appear (at $a/\lambda = 0.37$). In particular, the transmission characteristics in the vicinity of the stop band are accurately represented by the effective impedance model.

One main advantage of the effective impedance model is that it is independent of the permittivity of the incident region and is defined only by the properties (permittivity, geometry, lattice type, etc.) of the PC region. To verify this, the same PC structure in Figure 6.6 is used when light is incident from air. Figure 6.7 shows the transmission coefficient calculated with air as the incident region with different terminations of the PC with good agreement between the effective impedance model and direct numerical simulation visible.

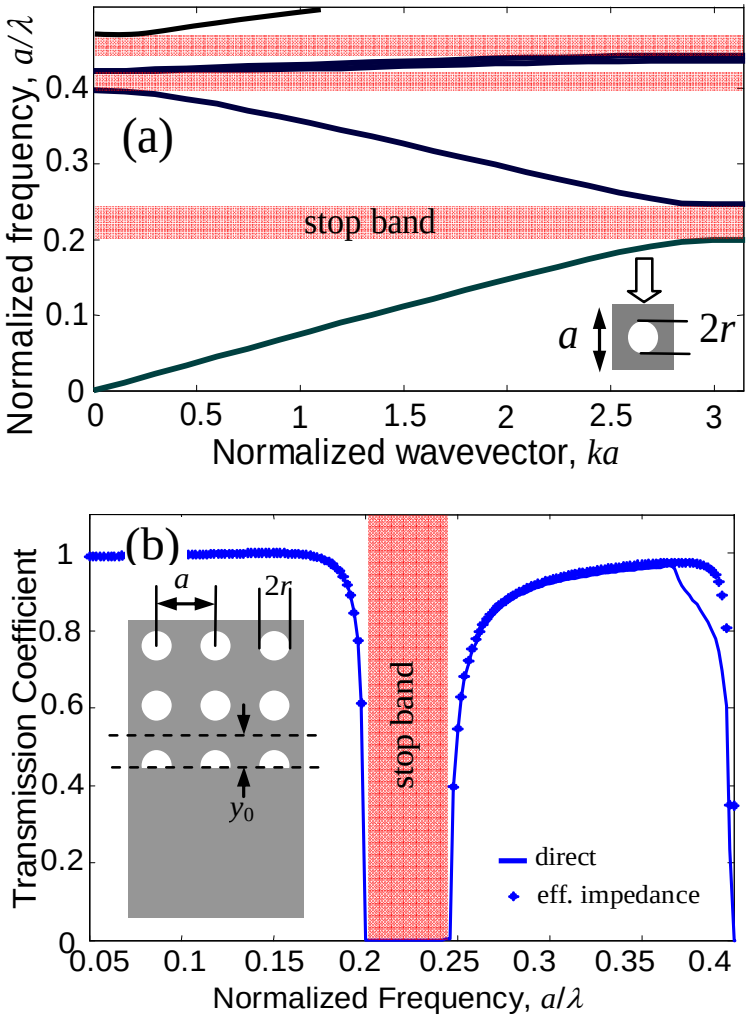


Figure 6.6. (a) The band structure of a square lattice PC of air holes ($r$=0.35$a$) in a dielectric with $\varepsilon_r = 7.4$ is shown for the direction specified by the arrow in the inset. (b) The transmission coefficient (i.e., transmitted power divided by the incident power, $T = 1 - R$) of light from the incident region ($\varepsilon_r = 7.4$) to the PC in part (a) using a direct grating analysis and the effective impedance model are plotted. The interface is located half way through the holes (i.e., $y_0$=$a$/2).

Figure 6.7 shows the existence of high transmission zones in the vicinity of the stop band (around $a/\lambda$ = 0.19 in Figure 6.7(a) and around $a/\lambda$ = 0.26 in Figure 6.7(b)). Such a behavior is of special interest in the dispersion-based applications of PCs, where coupling of light to PC modes with low group velocity is desired. Figure 6.8 shows the electric field profile of the relevant mode of the PC studied in this section at frequencies

close to the stop band in Figure 6.7. To calculate the PC effective impedance, we use Equation (6.8) and note that the Poynting vector is related to the group velocity normal to the interface ( $v_{gn}$ ), and the average energy density stored in the medium ($W_E$) as

$$S_n = W_E v_{gn}. \tag{6.9}$$

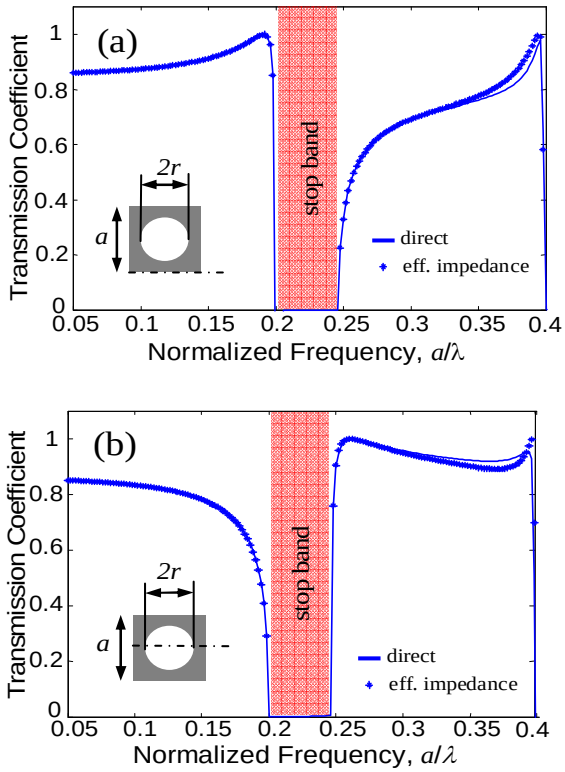


Figure 6.7. The transmission coefficient of light incident from air ( $\varepsilon_{air} = 1.0$ ) to the square lattice PC in Figure 6.6 is calculated using the direct grating analysis and the effective impedance model. The interface (dash-dot line) is at (a) $y_0 = 0$ and (b) $y_0 = a/2$, with $y_0$ defined in Figure 6.6.

In Equation (6.9), the average stored energy over a unit cell, $W_E$ , is given by

$$W_E = \frac{1}{2}\iint_{u.c.} \mathbf{dr}\varepsilon(\mathbf{r})\left|E(\mathbf{r})\right|^2, \tag{6.10}$$

where $\varepsilon(\mathbf{r})$ represents the permittivity, and the 2D integration is performed over a PC unit cell (i.e., the structure in Figure 6.8(a)). Combining Equations (6.8) and (6.9) results in

$$\eta = \left|\langle E_{\text{int}} \rangle^2\right| \Big/ (2W_E v_{gn}). \tag{6.11}$$

In Figure 6.8(a) the electric field is more concentrated in the dielectric around the edges of the unit cell where the interface is located. Continuity of the electric field along the interface states that the field along this line is the same inside the PC and in the air. Therefore, using Equation (6.10) one can see that $\left(\left|\langle E\rangle_{\text{int}}^2\right| / W_E\right)_{air} > \left(\left|\langle E\rangle_{\text{int}}^2\right| / W_E\right)_{PC}$ because of the large value of $W_E$ in the PC region caused by higher permittivity, $\varepsilon(\mathbf{r})$. Combining this result with Equation (6.11), it is clear that impedance matching at the PC-air interface requires a small group velocity for the PC mode compared to air. This can be realized by using the PC in the frequencies close to the edge of the stop band. Similarly, in the frequencies above the first stop band, the field is more concentrated in the dielectric in the middle of the PC unit cell as shown in Figure 6.8(b). Therefore, for these frequencies and for an interface going through the middle of the unit cell [as shown in Figure 6.8(b)], again $\left(\left|\langle E\rangle_{\text{int}}^2\right| / W_E\right)_{air} > \left(\left|\langle E\rangle_{\text{int}}^2\right| / W_E\right)_{PC}$, and by using frequencies close to the edge of the stop band and thus lowering the group velocity in the PC, effective PC impedance of unity for impedance matching to the incident region (i.e., air in this case) can be achieved. Another important behavior in the vicinity of the stop band can be seen when the field profile of the PC mode goes to zero along the interface (e.g., $y_0 = a/2$ interface and $y_0 = 0$ interface in Figures 6.8(a) and 6.8(b), respectively). In this case,

$\left(\left|\langle E\rangle_{\text{int}}^2\right| / W_E\right)$ has a second order zero at the band edge, while $v_{gn}$ has a first order zero; therefore, as we approach the bandgap, the effective impedance of the structure goes to zero.

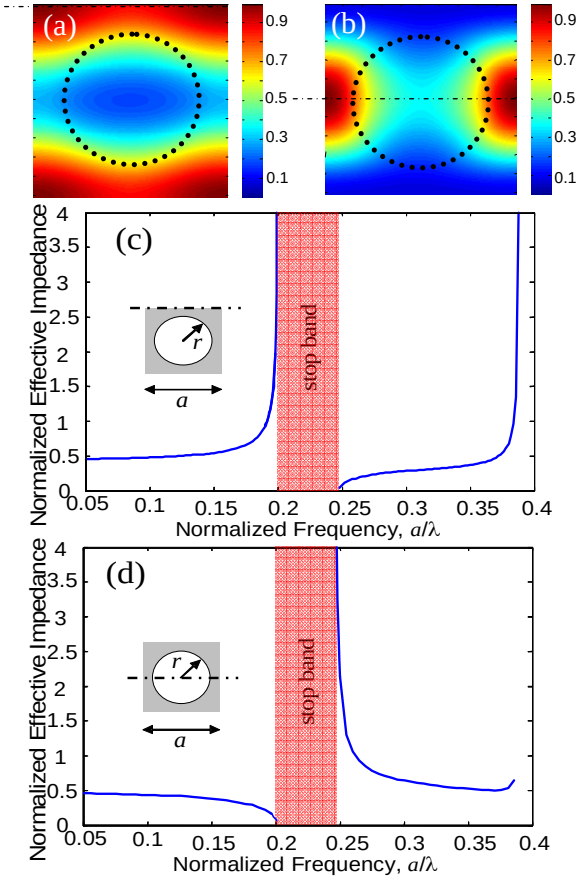


Figure 6.8. Electric field profiles of the PC modes at high transmission points are shown for (a) $a/\lambda$ = 0.19 and (b) $a/\lambda$ = 0.26. Dash-dot lines show the relative location of the interface for low reflection, when the incident light is coming from air in each case. The effective impedance of the PC under study (normalized to that of air) is shown for the interface with (c) $y_0 = 0$ and (d) $y_0 = a/2$.

Our results clearly show that the PC effective impedance can be considerably varied by the PC termination at the interface. The possibility to approach both zero and infinite effective impedances (and thus, any impedance value in between) based on the PC termination at the interface provides the opportunity to impedance-match the PC to

any incident region by proper choice of the interface. In many dispersion-based applications of PCs, a low group-velocity mode of the PC is of interest and impedance matching discussed above provides a practical way to achieve reflection-free coupling of light to these modes. The bandwidth of the high transmission window (>95%) in this case is around 10% of the operation wavelength which is wide enough for almost all practical purposes. Note that this particular impedance matching happens in the vicinity of the bandgap, where other matching schemes face complications.

### 6.3.2. Approaches for impedance matching

The effective impedance concept can be used to estimate the reflection at the interfaces of PCs with acceptably low error for most practical cases. The fact that an effective impedance value can be assigned to a PC interface (regardless of the properties of the incident region) makes it possible to assess the reflection for a given PC mode without going into lengthy simulations and to find the proper termination or intermediate stage to suppress the impedance mismatch. The use of the effective impedance model enables us to describe a unique impedance matching condition for reflection-free coupling to PCs, which is of significant value in designing heterostructure dispersion-based PC devices. Finally, since the impedances of the PC mode for different terminations are not necessarily equal, there is a unique opportunity in photonic crystals to have a PC stage with different impedances at the input and output planes. Such a concept does not exist in ordinary bulk materials, and can be used to directly implement an impedance matching PC layer.

Note that the definition of an impedance value to a PC mode requires that mode to be the dominant mode of the structure in the range of interest. As a result, the effective

impedance model discussed in this section works well only for single-mode regime in the incidence and transmission regions. However, the requirement for single-mode operation is also enforced in almost all practical implementations of dispersive photonic devices, and as a result, this condition does not limit the applicability of the effective impedance model for practical cases.

# CHAPTER 7

# ADDITIONAL CONSIDERATIONS FOR THE IMPLEMENTATION OF DISPERSIVE PHOTONIC STRUCTURES AND SYSTEMS

In this chapter, I will discuss other issues that are important in practical implementation of dispersive photonic devices. Three main issues in planar 2D PCs, i.e., loss mechanisms, multimode operation, and cross-polarization coupling, will be studied. In each case, the related possible complications will be reviewed and possible approaches to avoid them will be proposed.

## 7.1. Propagation and Scattering Losses

One of the main issues in practical implementation of dispersive photonic structures is the insertion loss in these structures. There are three main possible sources of loss in these structures: intrinsic propagation loss, scattering loss, and coupling loss. The issue of coupling loss and some approaches to reduce the reflection loss at the interfaces have been discussed in Chapter 6, showing that these losses can be reduced considerably by using appropriate matching stages. Here, the other sources of loss will be considered.

The intrinsic propagation loss in planar PC structures has two main sources: coupling to leaky modes above the light line, and power leakage to the substrate. Power leakage to the substrate refers to the case that the optical isolation between the film layer (in which the main portion of the light is confined; e.g., the top Si layer in SOI wafers) and the substrate (e.g., the main Si substrate in SOI wafers) is not complete. As a result, some light leaks to the wafer substrate during propagation in the planar structure. This loss in SOI wafers is more when the oxide layer is kept and for smaller thicknesses of the isolating oxide layer. However, this loss is not significant in most practical cases (typically much less than 1 dB/cm in SOI wafers), and can be further reduced by using

wafers with a thicker layer of oxide. The more important source of intrinsic loss in planar PCs is coupling to leaky waves above the light line. Coupling to leaky modes occurs when we use portions of the band structure above the light line, for which one or more of Floquet-Bloch orders can radiate to the cover or substrate region. In this case, the light is not essentially confined to the film layer, and the power is constantly lost to out-of-plane modes. The loss in this case can be large (~ 10 dB/cm), but can be simply avoided if we limit out range of operation on the band structure to the regions far enough from the light line. Figure 7.1 shows a typical band structure of a square lattice photonic crystal in SOI on which the regions of leaky substrate and cover modes are marked. Avoiding these leaky regions is essential in implementing a low-loss dispersive device in this platform. It can be readily observed from this figure that by undercutting the structure (which brings the leaky condition to that of the air) the range of possible low-loss operation is considerably expanded.

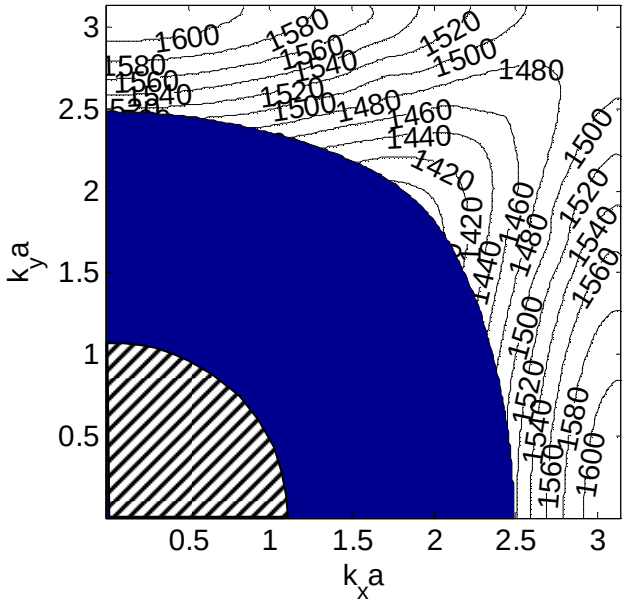


Figure 7.1. The iso-frequency contours of the second TE band of a square lattice planar 2D PC in SOI are shown (each contour is marked with its corresponding wavelength). The PC has a lattice constant of 400 nm, and holes of 200 nm in diameter. The thickness of the film Si layer is 240 nm. The regions of leaky coupling to the oxide substrate and to the air are marked with solid and hashed shadings.

The scattering loss in PC structures is caused by nonuniformity of the structure and presence of defects in the structure that locally scatter light to unwanted or radiation modes. The scattering loss in PCs is mainly determined by the quality of fabrication and is ultimately limited to the imperfections in each fabrication technology. Figure 7.2(a) shows one of the fabricated structures through the process explained in Chapter 5, for which some side-wall roughness and imperfection can be observed. Figure 7.2(b) shows an SEM image of the top view of one of fabricated structures. It can be observed in Figure 7.2(b) that the shape of the holes is not perfectly circular. The deviation is caused by the exposure pattern of the electron beam writing process in which some resist regions are exposed more. The two type of imperfection illustrated in Figure 7.2 have different effects on the scattering loss through the structure. Systematic deformations caused by e-beam exposure do not, in principle, affect the performance of the device. The may cause slight deviation from the originally designed structures, but as long as the periodicity of the structure (even with deformed unit cell) is retained no scattering loss is present. However, local defects, side-wall roughness, or nonuniformities in the structure (caused either by patterning process or etching process) will result in scattering loss.

Another loss mechanism in these structures is the out-of-plane loss caused by the mismatch in the lateral direction of field profiles between two regions (e.g., at the interface between an unpatterned Si region with a planar PC). This loss can dominate if one tried to couple directly two modes of different lateral symmetry. However, in most practical cases, the lateral mismatch is not a significant source of loss, and it can be reduced by an adiabatic transition between the two regions.

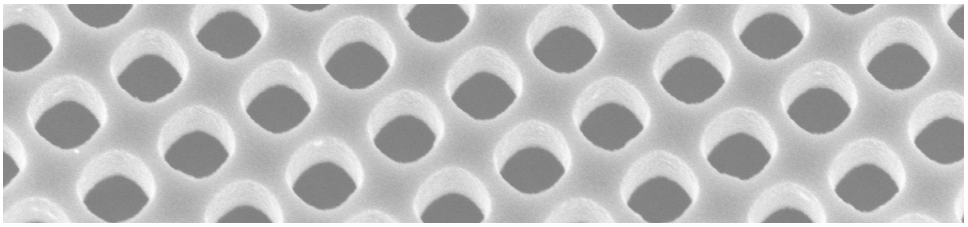

(a)

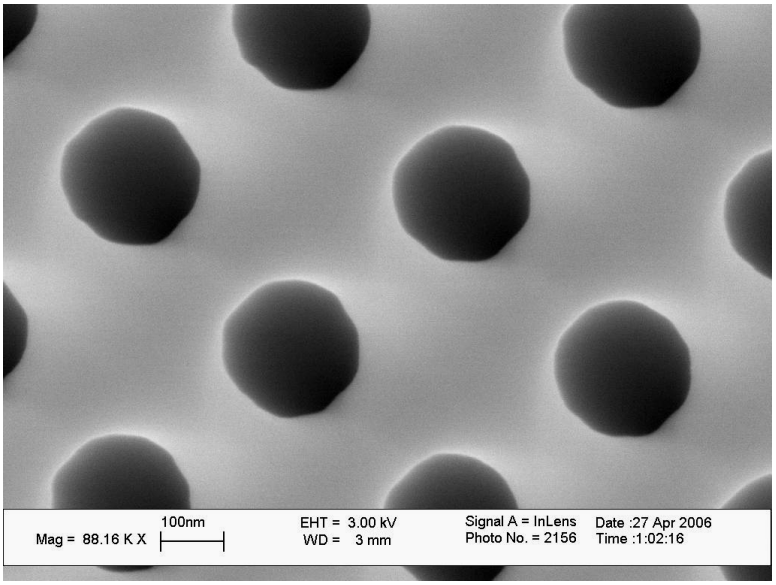


(b)

Figure 7.2. (a) Side-wall roughness can be seen in an SEM image of a fabricated structure in SOI. (b) Top view of a fabricated sample in SOI shows systematic deformations caused by the vicinity effects in the electron beam exposure.

In designing dispersive systems, one of the main decisions to be made is the choice of the photonic band to work in. As a general guideline, working at lower photonic bands suffers less insertion loss (from all sources, including propagation loss, scattering loss, reflection loss, and other sources of intrinsic loss) and is easier to implement. Furthermore, in the lowest order mode there is a possibility to work with a band which is always confined to the planar structure. The drawbacks are that first, working at lower bands (and thus, lower normalized frequencies) requires better fabrication resolution to pattern the PC. Second, in the lower photonic bands the

dispersion effects are in general weaker than higher photonic bands. The choice of operation photonic band has to be made considering these trade-offs.

### 7.2. Multimode Behavior

To have control over the dispersive properties of light, it is essential to keep the signal single-mode throughout the platform. Coupling to unwanted modes in a multimode structure can degrade the performance of the system by adding extra insertion loss (the power in unwanted modes), and by presence of the interfering signal at the output, which can be treated as extra cross-talk in the wavelength demultiplexing devices.

In planar implementation of dispersive devices, the unpatterned slab region is the medium usually used for transfer of light between different stages of the system. Therefore, it is necessary to make sure that the slab remains single-mode in these applications. Figure 7.3 shows the range of single-mode operation for a planar slab in SOI wafers.

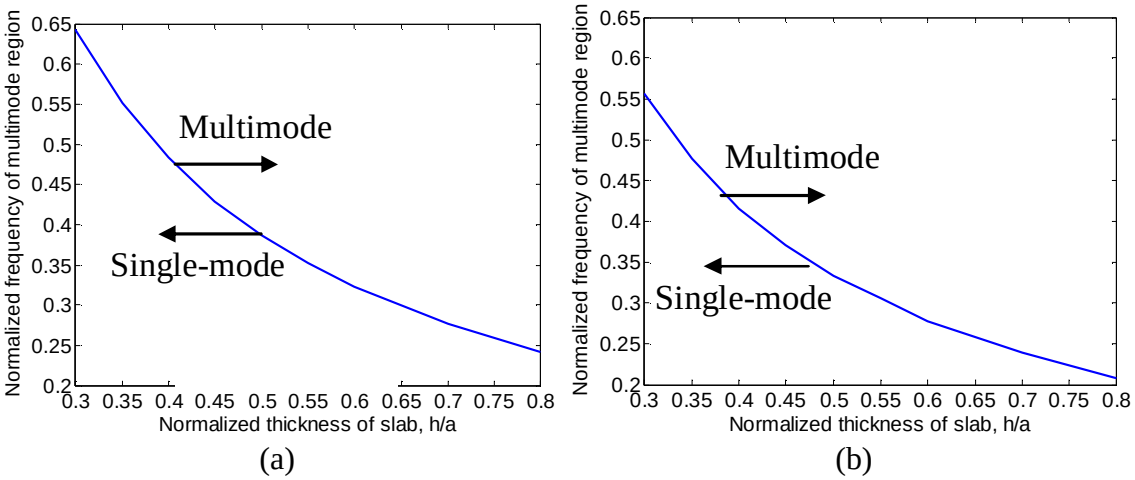


Figure 7.3. The range of single-mode operation of the unpatterned slab in SOI is shown for (a) Si on substrate and (b) air-bridge structure (after removing the oxide layer).

Depending on the operation point in the band structure, it is also possible that a single-mode input excites more than one PC mode. Figure 7.4 shows an example of such

occurrence in a square lattice planar PC excited by a beam incident from the unpatterned slab. The two modes marked in this figure are both excited in the structure and carry the light in different directions (and with different dispersive properties) inside the PC. It is also possible for a single PC mode at the output interface of a PC structure to excite more than one wave in the unpatterned region. This latter case happens when at higher frequencies the grating-type orders resulting from the phase matching at the interface are not in the cut-off condition.

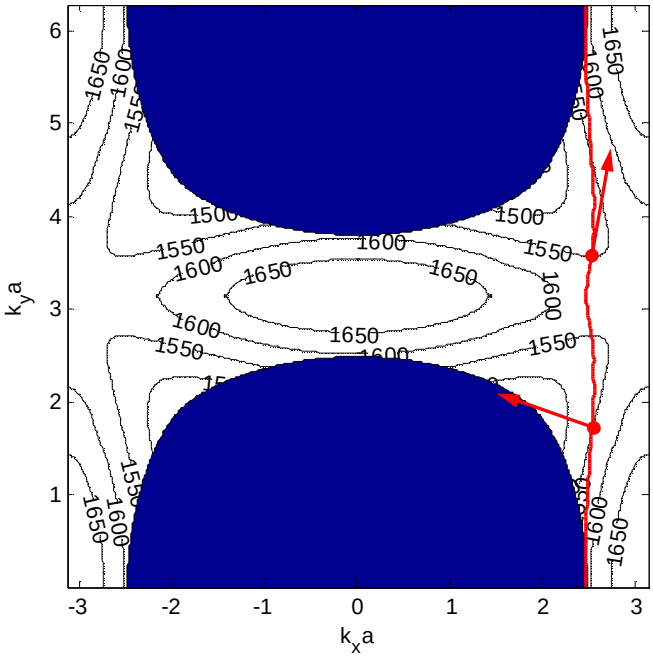


Figure 7.4. The band structure of a square lattice PC in SOI is shown (each contour is marked with its corresponding wavelength). The PC has a lattice constant of 420 nm, and holes of 210 nm in diameter. The thickness of the film Si layer is 250 nm. The red line indicates the range of modes at different wavelengths excited by an incident plane wave coming from the unpatterned slab on the same planar structure at an incident angle of 32°. Marked arrows show the direction of propagation of two PC modes excited at the wavelength of 1550 nm for the above-mentioned incident wave.

### 7.3. Cross-polarization Coupling

Another issue to be considered in planar implementation of dispersive PC devices is the cross-coupling between different polarizations. As described in Chapter 2, in

presence of holes in the planar 2D PC, the modes of the structure are not pure TE or TM polarized, and in general, can be considered as hybrid modes. Therefore, band folding caused by the periodicity of the structure, can result in coupling between the TE-like and TM-like modes of the structure. In symmetric slab structures, these effects vanish because of different symmetry of the field components in the lateral dimension (i.e., the direction perpendicular to the plane of periodicity). However, this is not the case for asymmetrical slabs (e.g., structures in SOI wafers without undercutting) [70]. For such asymmetric planar PCs, the coupling between TE-like and TM-like bands, when they intersect each other, opens a stop band and deforms locally the shape of the bands. Such stop bend, if located within the range of operation, can disrupt the normal function of dispersive PC elements. Figure 7.5 shows an example of such coupling between the TE and TM polarizations for a square lattice PC in an SOI wafer.

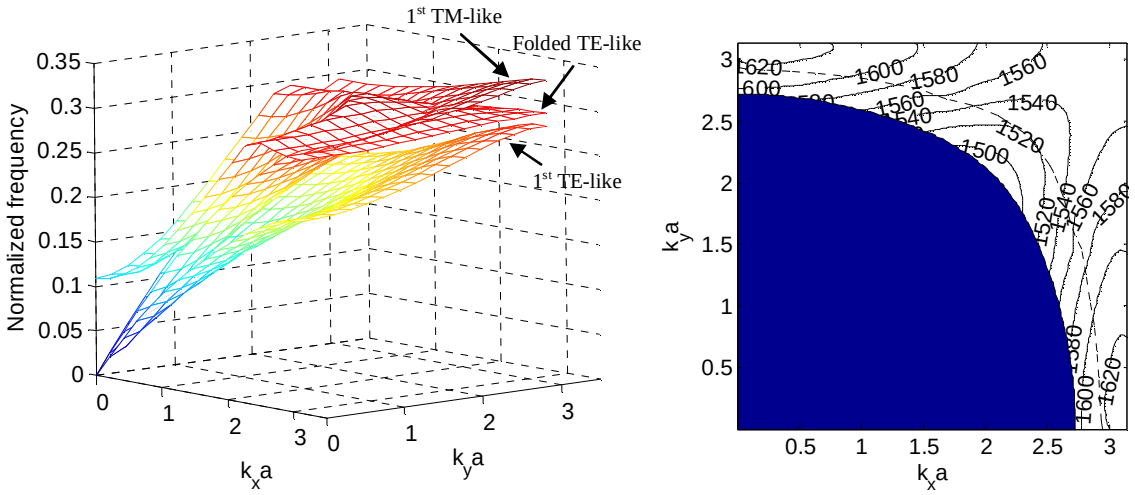


Figure 7.5. (a) The first three photonic bands of a square lattice planar PC in SOI (asymmetric structure with air on top and $SiO_2$ underneath) are shown. The PC structure has air-holes of diameter 290 nm, lattice constant of 480 nm, and slab thickness of 240 nm. The band crossing between the folded TE-like mode and the lowest TM-like mode can be seen from this figure. (b) Contours of the folded TE-like band in the in-plane k-space are plotted, and the crossing line with the TM-like mode is marked by a dashed line. In this figure, band splitting (and thus, opening a stop band) at the intersection line results in band deformation in that vicinity.

### 7.4. Solutions and Challenges

The issues mentioned above require a clear strategy for designing dispersive PC components and systems. One approach is to undercut the planar structure (e.g., using wet etching for SOI wafers) to have a patterned slab surrounded by air. Undercutting the planar structure and hence, making a symmetric slab PC with air on both sides, decouple the modes with different lateral symmetry and also relaxes the confinement condition imposed by working below the light cone. The drawbacks in transforming the structure to an air-bridge slab are: first, the structure is less stable mechanically, and second, there are some losses associated with the interface between the undercut and on-the-substrate regions. Also, in a system with multiple components, selective undercutting a portion of the device adds more steps to the fabrication process. Figure 7.6(a) shows SEM image of the output end-face of an undercut SOI wafer. In this figure, an array of waveguides is carrying the light to the output, and partial undercutting is used to leave supporting $SiO_2$ posts for the silicon waveguides (to add to mechanical stability and avoid cross-talk between the output waveguides). Another issue that may happen for large area PCs is the bending of the top silicon layer after undercutting. Figure 7.6(b) shows an undercut PC region in SOI. The silicon layer is slightly bent as can be seen in the etched trench in this image; as a result, further away from the regions supported by the oxide underneath, the silicon layer falls on the substrate of the wafer if no additional support is included.

Another factor discussed in the challenges was that at higher normalized frequencies (e.g., when working in higher PC bands) multiple waves will be excited as a result of phase matching at the interface of the PC. This multimode behavior disrupts the designed operation of the dispersive device by transmitting some of the power to the unwanted modes of the slab. The range for which other plane waves are generated can be simply found from phase matching at the interface as

$$K_t < k_0 n_{slab} (1 + \sin\alpha), \tag{7.1}$$

in which $K_t$ is the smallest tangential wavevector that is generated by the periodicity of the PC structure, $a$ is the in-plane incident angle, $k_0$ is the free-space wavevector of the field, and $n_{slab}$ is the effective index for in-plane propagation in the unpatterned slab. In the multimode region, because of the presence of multiple modes that can potentially carry the light in the reflected region, it is hard to implement an efficient matching stage. To avoid all these difficulties, one option is to use another photonic crystal in the incident region to push the unwanted plane waves to cut-off. Here, we propose the inclusion of another photonic crystal with smaller period at the surface. This additional PC buffer stage, effectively performs as a region with smaller index, and prevents the propagation of unwanted waves. To avoid new wavevectors in the system, the period of the buffer stage is chosen to be half of the target PC. Note that because of the small period in this buffer stage, the normalized frequency of operation for this region is small, and therefore, the effective index approximation can be used in the operation range. Figure 7.7(a) shows the incorporation of such a buffer stage along with a PC. For these structures, the range of multimode operation is changed to

$$K_t < k_0 (n_{buffer} + n_{slab} \sin \alpha), \tag{7.2}$$

where $n_{buffer}$ is the effective index in the buffer region. By choosing the size of the holes in the buffer region to be large, this effective index will become small and therefore, the range of single-mode operation will be extended. This process, in fact, brings the opportunity to realize regions with smaller (and controllable) refractive index into the integrated platform of the dispersive PC device simply by patterning the slab. Note that the size of the holes and the periodicity in the buffer stage will be limited to the achievable spatial resolution and feature sizes in the fabrication process.

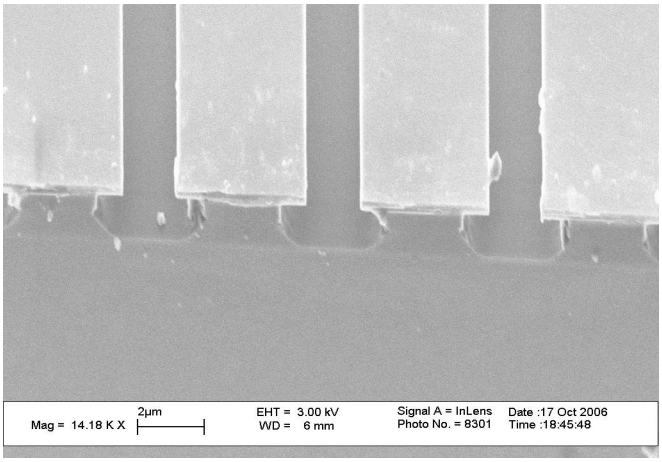


(a)

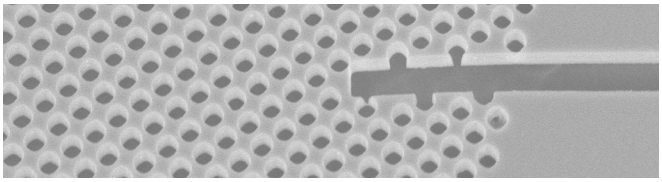

(b)

Figure 7.6. (a) An SEM image of end-face of an SOI sample compromising of multiple parallel waveguides is shown. The structure is partially undercut to retain the mechanical support for the waveguides. (b) An SEM image of a large area PC (in an SOI substrate) after undercutting is shown. Bending of the top silicon layer after undercutting is visible in this image.

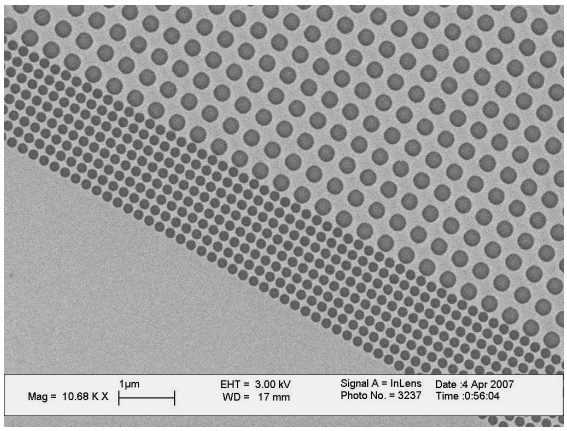


Figure 7.7. An SEM image of a PC buffer stage used along with a dispersive PC device is shown. The period of the buffer stage is half of the original target PC, and it effectively operates as a region with smaller index in this system.

The solutions briefly discussed above are examples of opportunities available by exploiting the possibilities of “designing” appropriate materials in the integrated platform of our system to achieve better performance and more versatile functionalities in dispersive PCs. The available solutions are not, of course, limited to these suggestions, and other methods can be thought of to solve particular problems faced in implementation of these devices for each application.

# CHAPTER 8

# FUTURE DIRECTIONS

The possibility of exploiting the dispersive properties of photonic crystal structures to “design” an optical material with properties of interest is the main direction proposed in this research. A compact and efficient wavelength demultiplexing device as an example of such applications is designed and demonstrated showing the potential of this approach to implement functionalities with a performance superior to other available device concepts. Developing new device concepts and implementing them in different platforms for existing and future desired optical systems is the natural direction that can be imagined as the foreseen future of this work. In what follows, I will briefly address some extensions to this work.

## 8.1. Integrated Spectrometers for Sensing Applications

Compact on-chip spectrometers are essential components for integrated optical sensing that can be considered as a natural application of the wavelength demultiplexing devices developed in this research. Implementation of such devices requires strong dispersion in the optical materials, which can be realized using unique dispersive properties of PCs. Possibility of integration, compactness, and compatibility with different host materials are the main advantages of PC-based spectrometers compared to other techniques.

The main difference between the operation of the device as a demultiplexer and as a spectrometer is that in demultiplexers, the spatial overlap of the beams at different wavelength channels directly correspond to the cross-talk, while in spectrometers it is possible to use a post-processing step to eliminate or suppress such cross-talk effects. The

design objective in an on-chip spectrometer for sensing applications is to be able to recognize specific spectral features in the transmission response of the interaction device (e.g., a transmission peak in the spectrum). Environmental changes (e.g., change in the refractive index of the region next to a resonator) alter the spectrum of the interacting device, and this change needs to be detected using the spectrometer. The scheme that I propose is to find the correlation of output signal with training data to recognize the signature in the spectral response. The schematic view of such sensing platform is shown in Figure 8.1.

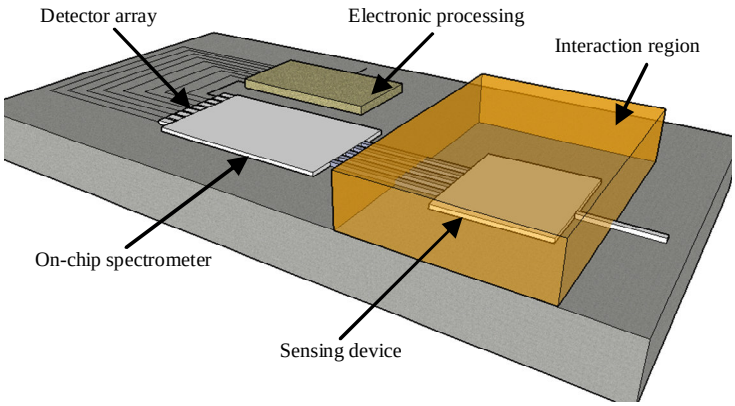


Figure 8.1. Overview of an integrated optical sensing device employing an integrated on-chip spectrometer for spectral interrogation of the signal is demonstrated. The optical signal is affected in the interaction region by the sensing mechanism, and the output from this stage is analyzed over a range of spectrum using the on-chip spectrometer to recognize the unique signatures left by the sensing process.

We have fabricated PC demultiplexing structures and tested the performance of these devices as on-chip spectrometers. Figures 8.2(a) and 8.2(b) show the response of the structure and the SEM image of the fabricated structure tested for this purpose, respectively. To investigate the performance of these devices, the training data is obtained by recording the output power distributions in output waveguides at different wavelengths. The measurement is performed over 60 nm of wavelength bandwidth with 50 pm wavelength grid spacing in the training data. A subset of this training data is

shown in Figure 8.2(a). An additive Gaussian noise is then added to this data and by correlating the noise-affected version with all the training data, the wavelength is estimated using a maximum likelihood scheme. Figure 8.2(c) shows the estimated error in locating a spectral peak at the output at different noise levels (the noise level ratio is defined as the ratio of the noise power at the output to the average of the signal power in all output waveguides of interest). Estimation error in this case is the standard deviation of error (the difference between estimated location and the actual location of the spectral peak) for an ensemble of 60 events. It can be observed that the PC spectrometer in this case is capable of determining the location of the spectral peak with an average estimation error of 50 pm (at a relatively high noise level ratio of 0.15), as shown in Figure 8.2(c). Note that the PC structure for this example is only 100 μm by 200 μm in size. This clearly shows the potential of PCs for implementation of compact on-chip spectrometers.

Note that the optimal operation point of these devices as spectrometers is different from that of the wavelength demultiplexing device. More detailed analysis of these structures (see for example, [114]) is needed to explore the possibilities and find the optimum operation range for these devices. Considering the current demand for sensitive, accurate, and efficient integrated sensing devices and the unique opportunity offered by photonic crystals, this is one of the main directions that the current work can be extended to for practical applications of immediate interest.

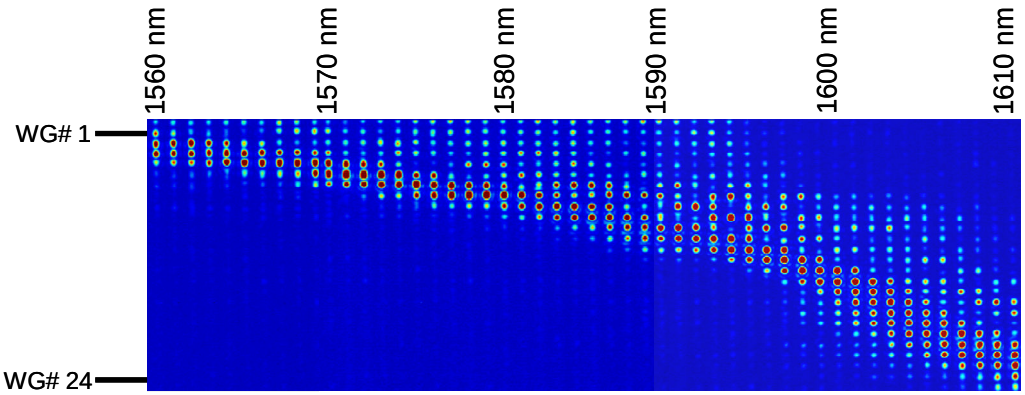


(a)

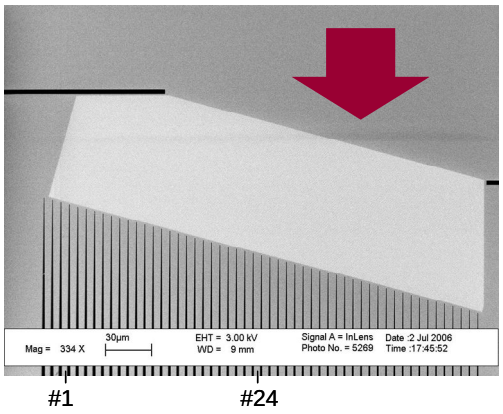


(b)

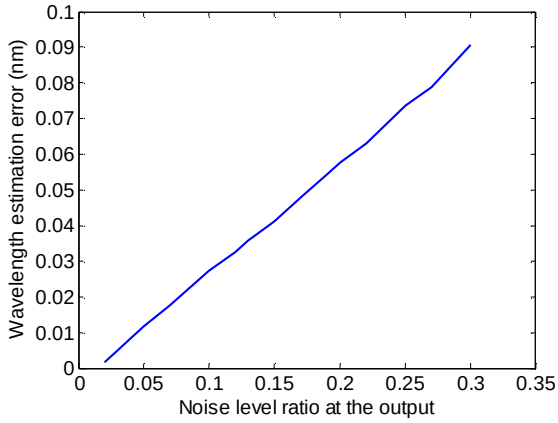


(c)

Figure 8.2. (a) A subset of the training data for a fabricated PC spectrometer (obtained by imaging the output plane of the fabricated device and recording it at different wavelengths) is shown. (b) An SEM image of the photonic crystal spectrometer is shown. An array of waveguides is used to sample the beam profile at the output plane of the photonic crystal region. (c) The performance of the PC spectrometer in locating a spectral peak in the spectrum is shown in the form of wavelength estimation error with respect to the output noise level.

## 8.2. Multistage Photonic Crystal Devices

Practical implementation of optical systems usually requires interplay of several components, and naturally requires utilizing both guided and dispersive photonic structures. Such implementations, in the particular case of dispersive photonic crystal structures, require complete control over the dispersion throughout the system. The main challenges to overcome to reach that point are the issues of compatibility and reliability. On one side, different components should be designed for operation in the same

consistent platform (e.g., a planar 2D PC with the same thickness), and the modal properties of the signals between different stages of the system should be compatible. On the other side, as the number of components of the system increases, in order for the entire structure to work as desired, more reliability for each component (compared to the case with only a single component in the system) is needed. In this context, designs that are more robust against possible sources of error (e.g., fabrication imperfection, modeling error, unwanted interference, etc) become more attractive.

Figure 8.3 shows an example of a two-stage PC demultiplexer. In this device both PC regions operate in the strong superprism region, but the PC on the top in this figure operates in the second photonic band and has a positive diffractive index, while the other PC is designed in the first photonic band and has a negative diffractive index. Spatial separation of wavelengths is achieved in both stages, but the diffraction effects are cancelled out by proper choice of lengths of the two stages. This example demonstrates a more compact implementation of wavelength demultiplexing devices, and shows some of the possibilities of dispersive systems consisting of multiple stages.

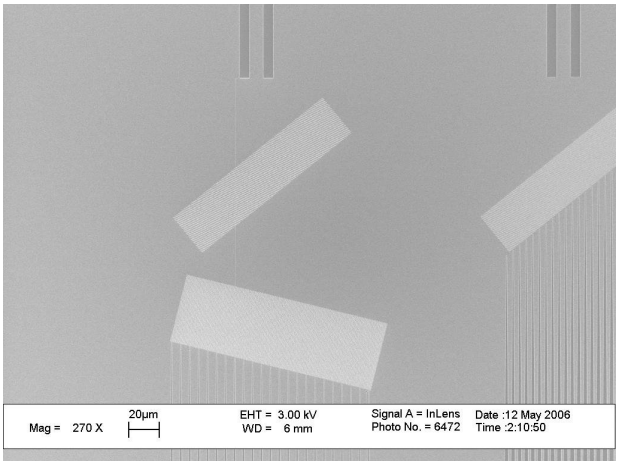


Figure 8.3. The overview of a two-stage PC demultiplexer (fabricated in SOI) based on the superprism effect and diffraction compensation is shown.

### 8.3. Inhomogeneous Photonic Crystal Structures

In this research the main focus has been on the dispersive properties of a PC with fixed parameters. There is, however, a variety of applications that can benefit from utilizing another degree of freedom obtained by varying the parameters of the PC and creating inhomogeneous PC structures. The possibility to have spatial variations in an integrated platform adds significantly to their capabilities for implementing systems based on dispersive application of PCs. Figure 8.4 show an implementation of a PC lens in SOI by gradually changing the size of holes in a square lattice PC. Our preliminary experimental results show the effectiveness of such an approach for realizing on-chip lenses in integrated platforms (focusing of a collimated beam is observed using such lenses). Continuation of this work for new device concepts can lead to unique and efficient solutions for a variety of functionalities and applications for spatial-spectral manipulation of optical beams in the planar integrated platform.

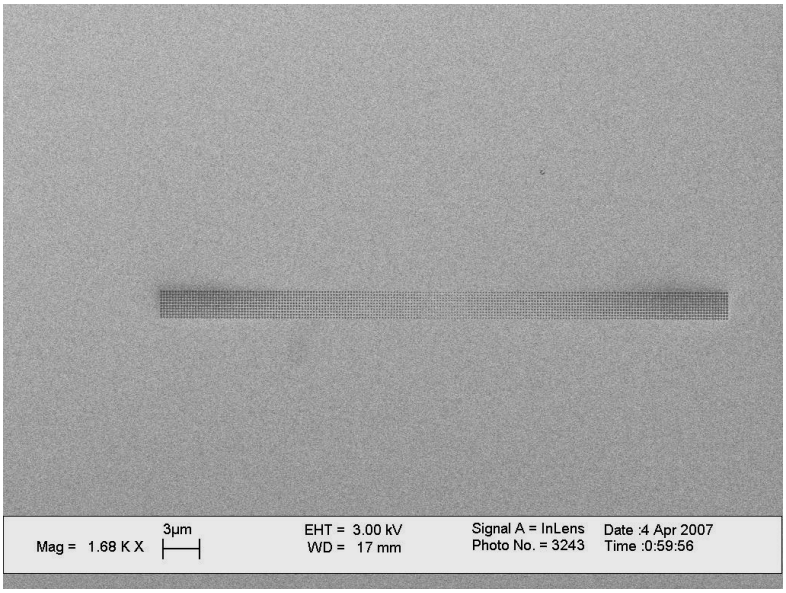


Figure 8.4. A PC lens fabricated in SOI is shown. The effective index of the material is changed in different locations of the lens by changing the size of holes in a square lattice PC structure.

## 8.4. Implementation in Other Material Platforms

A major advantage of the implementation of optical systems through patterning the structures (as it is done in forming photonic crystal structures) is that the device concepts are not limited to a specific material. Even though the majority of the discussion in this research was focused on the implementation of devices in SOI wafers, the choice of platform is not limited to SOI. The same concepts can be applied to other material platforms with the only considerations being the optical properties of the material in the range of interest (e.g., material absorption and refractive index) and the existence of the required fabrication techniques to perform the patterning. In particular, two interesting platforms that can be considered for such implementations are the PCs in III-V semiconductors (for the possibility of incorporation of active devices in the system) and the PCs in silicon-nitride (for the possibility of operation in the visible range of wavelengths). The main tools for this extension are already developed in this work. Important applications that can extensively benefit from such extensions include lab-on-a-chip sensing platforms at visible and UV wavelength as well as active integrated photonic circuits. Figure 8.5 shows a PC structure fabricated in silicon nitride using electron beam lithography and dry etching.

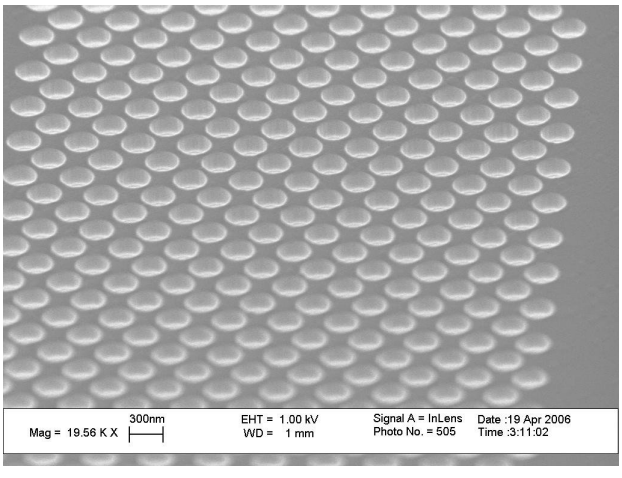


Figure 8.5. An SEM image of a photonic crystal structure fabricated in silicon-nitride is shown.

### 8.5. Extension to Three-Dimensional Photonic Crystals

For the analysis of the beam propagation, the same model (that was developed for 2D structures) applies to three-dimensional (3D) structures by extending the diffractive index model to the 3D case and by using the same methodology as before. It can be shown that for each photonic crystal mode in 3D PCs there are two principal axes and two effective diffraction indices. By controlling the properties of the PC, these indices can be tailored, and this effect can lead to interesting properties in 3D PC structures. A major advantage of three-dimensional PC structures over the slab-type structures is that the coupling of light to 3D structures is much easier, and they offer more flexibility in design. On the other hand, fabrication techniques for 3D structures are not as mature as the slab-type structures that rely on the well-developed microelectronics fabrication technology. The possibility of using 3D PC structures as dispersive elements expands the range of applications that can be covered and brings new potentials and concepts that need further investigation. Some immediate practical applications of such 3D PC structures with engineering dispersion include spectroscopy, pulse shaping, spatial-spectral mapping of optical signals, and dispersion compensation. Appendix C includes more details on extension of the analysis tools to 3D structures (both the diffractive index model and the effective impedance model).

# CHAPTER 9

# CONCLUSIONS

In this research, the main focus has been on the implementation and applications of dispersive photonic crystal structures. To achieve this goal, in the first step, a simplified analysis tool for modeling these structures is developed with its main emphasis being on the spatial distribution of optical beams propagating through photonic crystals. The resulting diffractive index model avoids very long calculations involved in direct simulation of the devices and transforms the beam propagation effects to the well-known propagation effects in the time and space domains. Using this model and focusing on wavelength demultiplexing as the application of interest, the superprism effect in photonic crystals is used as the main physical phenomenon for realizing compact wavelength demultiplexing devices. I have introduced analytical relations to describe the performance of these wavelength demultiplexing devices, which show that the size of these structures in the basic implementation of the superprism-based demultiplexers grows rapidly for higher resolutions. It is then shown that by combining the superprism effect with two other dispersive applications of PCs (namely, the negative diffraction effect and the negative refraction effect), it is possible to realize more compact demultiplexers and avoid stray light at the output of these devices. Both of these features are crucial in practical implementation of wavelength demultiplexing devices. The optimization and systematic design are then performed for these devices.

For implementation of these devices, an integrated planar platform in SOI wafers is chosen. Based on 3D simulations of the band structure and using the diffractive index model, a PC demultiplexer is designed and fabricated. The performance of the device is then verified by optical characterization. The measurement results confirm all the

physical concepts based on which the device has been designed. The demonstrated demultiplexer (based on combination of the superprism effect with negative diffraction and negative refraction) shows the possibility of realizing the most compact demultiplexers. A main contribution of this research is the demonstration of the most compact PC demultiplexer with at least two orders of magnitude smaller size compared to all demonstrated PC demultiplexing structures reported to date. This is the result of modeling and development of systematic design techniques for PC structures in which multiple unique dispersive properties of PCs are simultaneously utilized (and optimized). Additional techniques for more efficient implementation of these devices have also been proposed and developed. Among these techniques, two main contributions are the development of matching stages for reducing the reflection loss and investigation of higher photonic bands for improving the resolution of the wavelength demultiplexing devices. Finally, important issues for practical implementation of dispersive PCs for different applications in general have been addressed. This research open up a new avenue for the application of PC structures as dispersive devices in which it is possible to engineer the dispersive properties by optimally selecting the PC geometrical parameters (periodicity, size of holes, etc.). Thus, it is possible to use and extend the results of this research for multiple applications in which delicate dispersive properties are needed.

This new approach that enables “effective” optical materials with different properties in a single host material brings a new life to the integrated optical platforms and enables efficient implementation of devices needed for optical information processing and sensing. Possibility to migrate to other material platforms (e.g., other geometries such as 3D PCs or other host materials such as silicon nitride) with minimal effort is another advantage of the design concepts developed in this research. Developing the necessary components to enable the integration of multiple functionalities in a single platform is one of the main directions to be taken to bring the dispersive photonic structures to real applications.

A brief summary of contributions of this research follows:

- Development of an efficient systematic approach for the analysis of the envelope of the optical beams propagating inside photonic crystal structures.
- Development of an approximate diffractive index model for efficient and intuitive analysis of the diffraction effects inside periodic structures
- Developing the idea and systematically designing photonic crystal devices based on dispersion compensation (more compact and higher in resolution compared to the conventional implementation).
- Experimental demonstration of the designed photonic crystal structures based on combined dispersive effects experimentally (first demonstration of a diffraction-compensated superprism effect with considerably better performance compared to the conventional basic configuration of superprism-based demultiplexers).
- Development of a systematic approach to design efficient adiabatic matching stages for dispersive applications of PCs.
- Development of an effective impedance model for efficient analysis and design of impedance matching stages in PCs.
- Development of the model and concepts for dispersive applications in 3D photonic crystal structures.

# APPENDIX A

# DESIGNING PHOTONIC CRYSTAL DEMULTIPLEXERS IN DIFFERENT REGIMES

In Chapter 4 the optimization and design process for a specific scheme, equal angular spacing with flexible frequencies (EASFF), were discussed. Such a scheme is of interest for realizing a spectrometer with post-processing. There are other applications, however, that require equal frequency spacing. These applications, mainly encountered in communications systems, may require certain specifications on channel spacing as in dense wavelength division multiplexing (DWDM), or can work in a range of channel spacing, for example in a point-to-point coarse WDM system. We will develop the design procedure for these two cases in what follows. Similar to Chapter 4, the area of the structure plays an important role, given by

$$A \cong \frac{8\lambda^2 K^2 \theta_T}{n_1^2 \pi^2 \cos^2 \alpha} \left( \frac{1}{\Delta\alpha} \right)^2 \left( \max_{channels} \left\{ \frac{\cos\theta_g}{\Theta - H\left(\partial\theta_g / \partial\alpha\right)\big|_\omega \Delta\alpha} \right\} \right)^2 . \tag{A.1}$$

## A.1. Equal Frequency Separation with Specified Frequencies (EFSSF)

In this case, the frequency separation between adjacent channels is equal. An example for this case is a DWDM wavelength demultiplexer. The incident divergence angle can be found as

$$\Delta\alpha = \gamma \frac{\Delta\omega}{2H}, \tag{A.2}$$

with

$$\gamma = \min_{channels}\left\{\frac{\left(\partial\theta_g/\partial\omega\right)_\alpha}{\left(\partial\theta_g/\partial\alpha\right)_\omega}\right\}, \tag{A.3}$$

in which the minimum value is obtained over all wavelength channels in the frequency range of interest. Using (A.1) and (A.2) along with $\Theta = \left(\partial\theta_g/\partial\omega\right)_\alpha \Delta\omega$ for each channel, the area of the structure is

$$A \cong \frac{8\lambda^2 K^2 \theta_T}{n_1^2 \pi^2 \cos^2\alpha}\left(\frac{2H}{(\Delta\omega)^2}\right)^2 \gamma^{-2} \times \max_{channels}\left\{\frac{\cos\theta_g}{\left(\partial\theta_g/\partial\omega\right)_\alpha - \frac{1}{2}\left(\partial\theta_g/\partial\alpha\right)_\omega \gamma}\right\}^2. \tag{A.4}$$

Using $\omega_T = N\Delta\omega$, we obtain

$$A \cong \frac{32\lambda^2 K^2 H^2}{n_1^2 \pi^2 \cos^2\alpha}\left(\frac{\theta_T}{\omega_T^4}\right)\gamma^{-2} \times \max_{channels}\left\{\frac{\cos\theta_g}{\left(\partial\theta_g/\partial\omega\right)_\alpha - \frac{1}{2}\left(\partial\theta_g/\partial\alpha\right)_\omega \gamma}\right\}^2 N^4, \tag{A.5}$$

where $\omega_T$ is the total bandwidth of the designed device. It can be seen that the area of the structure increases as the fourth power of the number of channels [87].We can define a compactness factor as

$$C_{EFSFF} = \frac{n_1^2 \pi^2}{128 K^2 H^2}\frac{\omega_T^4 \gamma^2 \cos^2\alpha}{\theta_T} \times \min_{channels}\left\{\frac{\left(\partial\theta_g/\partial\omega\right)_\alpha - \dfrac{\gamma}{2}\left(\partial\theta_g/\partial\alpha\right)_\omega}{\cos\theta_g}\right\}^2, \tag{A.6}$$

with

$$\frac{A}{\lambda^2} \cong \frac{N^4}{C_{EFSFF}}, \tag{A.7}$$

and the incident divergence factor as

$$E_{EFSFF} = \frac{\omega_T \gamma}{2H} \;; \quad \Delta\alpha = \frac{E_{EFSFF}}{N}. \tag{A.8}$$

The quantities $C_{EFSFF}$ and $E_{EFSFF}$ are considered as the figures of merit for superprism-based PC demultiplexers in this scheme.

## A.2. Equal Angular Separation with Specified Frequencies (EASSF)

The main difference here, compared to the flexible frequency scheme, is that the frequency range of operation of the device is given. In applications such as spectroscopy, one of the main performance measures for the demultiplexer is the frequency resolution (i.e., how close the frequencies that it can resolve are located with respect to each other). Knowing the number of channels by itself does not express the resolution since it has no information about the distribution of channels in frequency. For a single channel, normalized resolution can be defined as center frequency of the channel ($\omega_j$) divided by frequency separation of that channel from its adjacent channels ($\Delta\omega_j$); i.e., $\omega_j/\Delta\omega_j$ for j-th channel. For a demultiplexer with multiple arbitrarily spaced channels, we need to combine these individual normalized resolutions ($\omega_j/\Delta\omega_j$) to obtain a reasonable performance measure that can be used to compare different designs. To represent the performance over the entire spectrum of operation, we define the resolution measure, $R$, as

$$R = \sum_{channels(j)} \frac{\omega_j}{\Delta\omega_j}. \tag{A.9}$$

This parameter, the frequency resolution (or resolution) of the device, is considered here as a main figure of merit for the demultiplexer. We use an averaged version of the resolution to reflect the behavior in the entire frequency range of interest. Assuming that the device is designed for a specified frequency range $\Omega$, then

$$R = N\left(\frac{\omega_0}{\Delta\omega}\right)_{avg} \cong N\frac{\omega_0 \int_\Omega (1/\Delta\omega) d\omega}{\int_\Omega d\omega}, \tag{A.10}$$

The size of the structure is another performance measure of interest in this case as well. We will use the resolution per unit area as our figure of merit for the following discussions. Having equal angular separation ($\Theta$) between channels results in

$$\frac{1}{(\Delta\omega)_j} = \left(\frac{\partial\theta_g}{\partial\omega}\right)\Big|_{\alpha,j} \frac{1}{\Theta}, \tag{A.11}$$

where $\left(\partial\theta_g/\partial\omega\right)\big|_{\alpha,j}$ and $(\Delta\omega)_j$ are the values corresponding to each channel ($j$=1,…, $N$). Hence, the normalized resolution per device area is defined using (A.1), (A.10), and (A.11) as

$$R_n = \frac{R\lambda^2}{A} = \frac{n_1^2\pi^2\cos^2\alpha}{8K^2} \frac{N\omega_0 \int_\Omega \left(\partial\theta_g/\partial\omega\right)\big|_\alpha d\omega}{\omega_T\theta_T\Theta} \times \left(\min_\Omega\left\{\Theta - H\left(\partial\theta_g/\partial\alpha\right)\big|_\omega \Delta\alpha\right\}\right)^2 (\Delta\alpha)^2 \ . \tag{A.12}$$

Similar to the EASFF case, $R_n$ can be maximized by setting

$$\Delta\alpha = \frac{\Theta}{2H\max_\Omega\left(\partial\theta_g/\partial\alpha\right)\big|_\omega} = \frac{\theta_T}{2H\max_\Omega\left(\partial\theta_g/\partial\alpha\right)\big|_\omega}\frac{1}{N}, \tag{A.13}$$

which results in

$$R_n = \frac{n_1^2\pi^2}{128K^2H^2} \frac{\omega_0\theta_T^3\cos^2\alpha}{\omega_T\left(\max_\Omega\left\{\left(\partial\theta_g/\partial\alpha\right)\big|_\omega\right\}\right)^2}\frac{1}{N^2}. \tag{A.14}$$

From this relation, it can be observed that the resolution per unit area decreases as the second power of number of channels ($N$) in this scheme. We can define the resolution factor as

$$\rho_\omega = \frac{n_1^2\pi^2}{128K^2H^2} \frac{\omega_0\theta_T^3\cos^2\alpha}{\omega_T\left(\max_\Omega\left\{\left(\partial\theta_g/\partial\alpha\right)\big|_\omega\right\}\right)^2} \ ; \quad R_n = \frac{\rho_\omega}{N^2}, \tag{A.15}$$

and this value, $\rho_\omega$, will be used as the main figure of merit in our designs.

# APPENDIX B

# CALCULATION OF REFLECTION AT THE INTERFACES OF PHOTONIC CRYSTALS

The basic approach for analyzing reflection effects at PC interfaces is to find the photonic crystal modes inside the periodic region and match them to plane waves in homogeneous medium through electromagnetic boundary conditions. If a plane wave is incident at the interface, the result of such an analysis is the amplitude of photonic crystal modes and amplitude of reflected plane waves.

We assume that the photonic crystal has an arbitrary lattice, but one of its lattice vectors is parallel to the interface. The two lattice vectors are shown in Figure B.1 as $\mathbf{a}_1$ and $\mathbf{a}_2$. The corresponding reciprocal lattice vectors will be

$$\begin{cases} \mathbf{K}_1 = \mathbf{x}K_{1x} + \mathbf{y}K_{1y} \\ \mathbf{K}_2 = \mathbf{y}K_2 \end{cases} \tag{B.1}$$

The angle of incidence is assumed to be $\alpha$, and the refractive index in homogeneous region is $n_i$. Also, the interface is located at $y = y_0$ with respect to the edge of the unit cell.

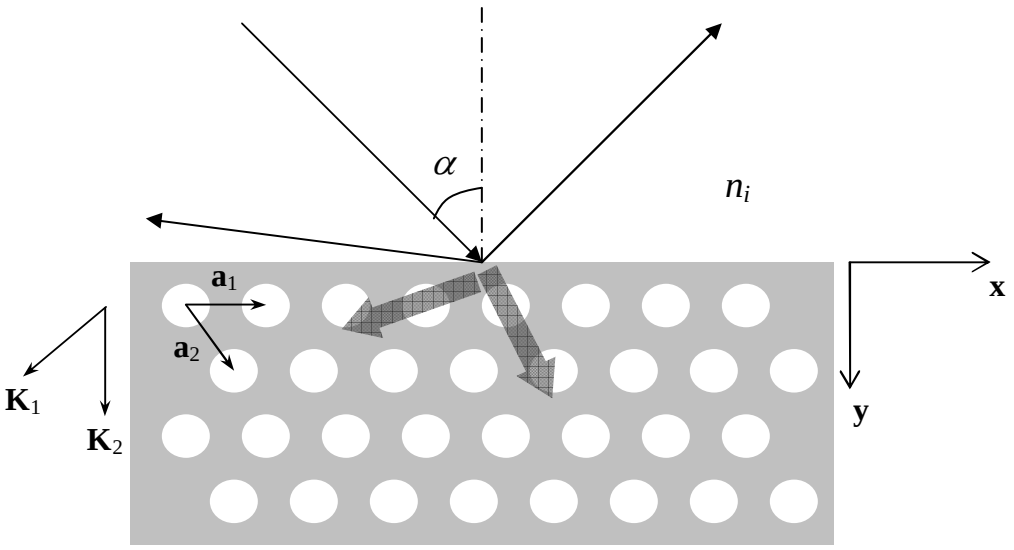


Figure B.1. The geometry of the setup for calculating the reflection at the interface of a 2D PC is illustrated.

### B.1. Formulation for E-Polarization

Considering E-polarization in the system shown in Figure B.1, the incident wave can be written as

$$E_i = \exp[-jk_{xi}x - jk_{yi}(y-y_0)] = \exp[-j(k_{xi}x + \sqrt{n_i^2k_0^2 - k_{xi}^2}\,(y-y_0))]. \qquad \text{(B.2)}$$

Knowing these values, the general solution in homogeneous region can be written as

$$E_h = E_i + \sum_m R_m \exp[-j(k_{xi} + mK_{1x})x + jk_{my}y], \qquad \text{(B.3)}$$

in which

$$k_{my} = \begin{cases} \sqrt{n_i^2k_0^2 - (k_{xi} + mK_{1x})^2} \;;\; n_i^2k_0^2 \geq (k_{xi} + mK_{1x})^2 \\ -j\sqrt{n_i^2k_0^2 - (k_{xi} + mK_{1x})^2} \;;\; n_i^2k_0^2 < (k_{xi} + mK_{1x})^2 \end{cases}. \qquad \text{(B.4)}$$

The sign of wavevector in the *y* direction is selected in a way to satisfy conservation of power at the interface (for the propagating wave) and being bounded at infinity (for the evanescent waves).

The electric field inside the photonic crystal can be written as

$$E_p = \sum_t T_t \sum_m \sum_n \tilde{E}_{mn,t} \exp[-j(k_{xi} + mK_{1x})x - j(k_{my,t} + mK_{1y} + nK_2)y] \qquad \text{(B.5)}$$

with $T_t$ being the amplitude of $t$-th photonic crystal mode, and $k_{my,t}$ being its corresponding wavevector in the $y$ direction. $\tilde{E}_{mn,t}$ is the amplitude of $(m,n)$ component in plane-wave expansion of $t$-th photonic crystal mode. To find the modes excited inside the PC when a tangential wavevector, $k_{xi}$, is enforced at the interface, we insert the Floquet-Bloch form of the PC modes

$$\mathbf{E}(\mathbf{r}) = \mathbf{z} \sum_m \sum_n \tilde{E}_{mn} \exp(-j\mathbf{k}\cdot\mathbf{r}) \exp[-j(m\mathbf{K}_1 + n\mathbf{K}_2)\cdot\mathbf{r}], \qquad \text{(B.6)}$$

into the Helmholtz equation,

$$\nabla \times \nabla \times \mathbf{E}(\mathbf{r}) = k_0^2 \varepsilon(\mathbf{r}) \mathbf{E}(\mathbf{r}). \qquad \text{(B.7)}$$

Therefore,

$$-\mathbf{k}_{mn} \times \left(\mathbf{k}_{mn} \times \mathbf{z}\tilde{E}_{mn}\right) = \mathbf{z} k_0^2 \sum_s \sum_t \tilde{\varepsilon}_{m-s,n-t} \tilde{E}_{st}, \qquad \text{(B.8)}$$

in which

$$\mathbf{k}_{mn} = \mathbf{k} + m\mathbf{K}_1 + n\mathbf{K}_2. \qquad \text{(B.9)}$$

We can rewrite the Equation (B.8) as

$$\left[(k_x + mK_{1x})^2 + (k_y + mK_{1y} + nK_2)^2\right]\tilde{E}_{mn} = k_0^2 \sum_s \sum_t \tilde{\varepsilon}_{m-s,n-t} \tilde{E}_{st}. \qquad \text{(B.10)}$$

Equation (B.10) should be re-arranged to form an eigenvalue problem for $k_y$. If we define indices $I$ and $J$ as

$$\begin{cases} I(m,n) = mN_1 + n \\ J(s,t) = sN_1 + t \end{cases}, \qquad \text{(B.11)}$$

and coefficient matrices

$$[\boldsymbol{\varepsilon}] = [\varepsilon_{IJ}]_{N_1N_2 \times N_1N_2} \quad ; \quad \varepsilon_{IJ} = \tilde{\tilde{\varepsilon}}_{m-s,n-t}, \tag{B.12}$$

$$\mathbf{e} = [e_I]_{N_1N_2 \times 1} \quad ; \quad e_I = \tilde{\tilde{E}}_{mn}, \tag{B.13}$$

$$[\mathbf{K}_x] = [K_{x,IJ}]_{N_1N_2 \times N_1N_2} \quad ; \quad K_{x,IJ} = \begin{cases} k_x + mK_{1x} & ; \quad I = J \\ 0 & otherwise \end{cases}, \tag{B.14}$$

$$[\mathbf{K}_y] = [K_{y,IJ}]_{N_1N_2 \times N_1N_2} \quad ; \quad K_{y,IJ} = \begin{cases} mK_{1y} + nK_2 & ; \quad I = J \\ 0 & otherwise \end{cases}. \tag{B.15}$$

We can write the Equation (B.10) in matrix format as

$$k_y^2\mathbf{e} + 2k_y[\mathbf{K}_y]\mathbf{e} + ([\mathbf{K}_x]^2 + [\mathbf{K}_y]^2 - k_0^2[\boldsymbol{\varepsilon}])\mathbf{e} = 0. \tag{B.16}$$

To solve this equation (which is in the form of a generalized eigenvalue problem), we can use an auxiliary variable,

$$\mathbf{u} = k_y\mathbf{e}, \tag{B.17}$$

which transforms the Equation (B.16) to

$$\begin{cases} k_y\mathbf{u} + 2[\mathbf{K}_y]\mathbf{u} + ([\mathbf{K}_x]^2 + [\mathbf{K}_y]^2 - k_0^2[\boldsymbol{\varepsilon}])\mathbf{e} = 0 \\ k_y\mathbf{e} - \mathbf{u} = 0 \end{cases}. \tag{B.18}$$

Thus,

$$k_y\begin{pmatrix}\mathbf{u}\\ \mathbf{e}\end{pmatrix} = \begin{pmatrix} -2[\mathbf{K}_y] & k_0^2[\boldsymbol{\varepsilon}] - [\mathbf{K}_x]^2 - [\mathbf{K}_y]^2 \\ [\mathbf{I}] & [\mathbf{O}] \end{pmatrix}\begin{pmatrix}\mathbf{u}\\ \mathbf{e}\end{pmatrix}, \tag{B.19}$$

which is a standard eigenvalue problem, with [**I**] and [**O**] being the identity and zero matrices, respectively.

In this problem, the wavevector in the $x$ direction is known because of phase matching, and we solve the eigenvalue problem to find $k_y$. If we assume $N_1$ plane-waves in the $K_1$ direction, and $N_2$ plane-waves in the $K_2$ direction, we will have $2N_1N_2$ values for $k_y$. Three conditions for the selection of PC modes should be considered: (1)

real part within a single Brillouin zone (to preserve linear independence, since wavevector differing by a reciprocal lattice in fact represent the same PC mode), (2) for complex modes, imaginary part must be negative for the modes to decay away from the interface, and (3) for real modes, the direction of Poynting vector must be away from the interface to satisfy conservation of power.

The correct sign of real or imaginary parts of the wavevector eliminates half of the $2N_1N_2$ modes that are found by solving the eigenvalue equation in (B.19). Also, the remaining $N_1N_2$ modes can be divided into $N_1$ groups of $N_2$ modes, each group representing one PC mode. We choose one wavevector, $k_y$, out of each group (preferably those which are less affected by truncation) and use the resulting $N_1$ modes for the mode-matching process.

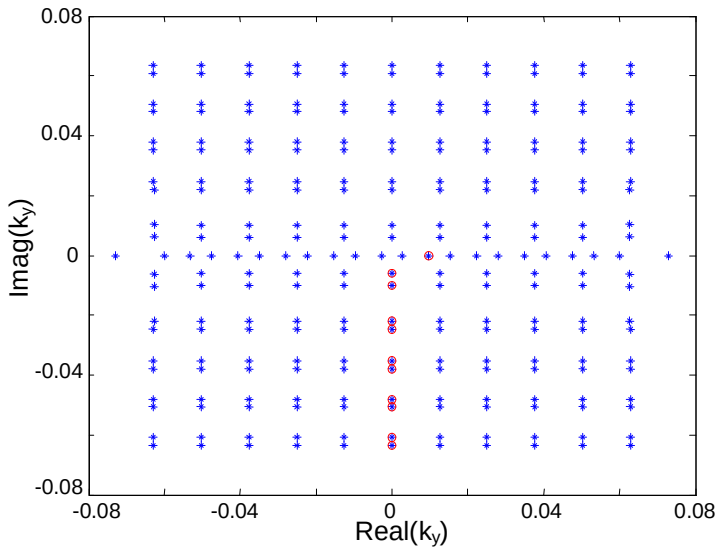


Figure B.2. Calculated normal components of the wavevector inside the PC structure for a square lattice of air-holes in Si are marked by stars in the complex plane. Circular markers highlight the wavevectors that satisfy the conditions for mode selection; these PC modes will be used in the mode-matching process for calculating the reflection.

Note that the Poynting vector mentioned above is the space-averaged Poynting vector of the mode. Unlike wave propagation in uniform media, the local Poynting vector for a PC mode is neither necessarily real, nor spatially uniform. To calculate the space-averaged Poynting vector for an arbitrary 2D PC, starting with

$$\mathbf{E}(\mathbf{r}) = \mathbf{z}\sum_m \sum_n \tilde{E}_{mn} \exp(-j\mathbf{k}\cdot\mathbf{r}) \exp[-j(m\mathbf{K}_1 + n\mathbf{K}_2)\cdot\mathbf{r}], \tag{B.20}$$

$$\begin{aligned}\mathbf{H}(\mathbf{r}) &= \frac{j}{\omega\mu}\nabla\times\mathbf{E} \\ &= \frac{1}{\omega\mu}\sum_m\sum_n (\mathbf{k}+m\mathbf{K}_1+n\mathbf{K}_2)\times\mathbf{z}\tilde{E}_{mn}\exp(-j\mathbf{k}\cdot\mathbf{r})\exp[-j(m\mathbf{K}_1+n\mathbf{K}_2)\cdot\mathbf{r}]\end{aligned}, \tag{B.21}$$

the complex local Poynting can be found as

$$\begin{aligned}\mathbf{S} &= \frac{1}{2}\mathbf{E}\times\mathbf{H}^* \\ &= \frac{1}{\omega\mu}\sum_m\sum_n\sum_s\sum_t \mathbf{z}\times[(\mathbf{k}+s\mathbf{K}_1+t\mathbf{K}_2)\times\mathbf{z}]\tilde{E}_{mn}\tilde{E}^*_{st}\exp\{-j[(m-s)\mathbf{K}_1+(n-t)\mathbf{K}_2)]\cdot\mathbf{r}\} \\ &= \frac{1}{\omega\mu}\sum_m\sum_n\sum_s\sum_t (\mathbf{k}+s\mathbf{K}_1+t\mathbf{K}_2)\tilde{E}_{mn}\tilde{E}^*_{st}\exp\{-j[(m-s)\mathbf{K}_1+(n-t)\mathbf{K}_2)]\cdot\mathbf{r}\}\end{aligned} \tag{B.22}$$

By averaging over the space (over a unit cell) we obtain

$$\langle\mathbf{S}\rangle = \frac{1}{\omega\mu}\sum_m\sum_n (\mathbf{k}+m\mathbf{K}_1+n\mathbf{K}_2)\left|\tilde{E}_{mn}\right|^2. \tag{B.23}$$

In numerical simulations, in practice, there are occasional errors in finding the right set of PC modes. The cause of errors were either choosing a mode with the wrong direction of propagation of energy, or choosing a repeated mode near the edges of the first zone. We basically use two steps to eliminate these instabilities: first, using the formula given above for the direction of propagation of energy, only those modes with the proper direction of Poynting vector are selected. Second, we consider a slightly bigger zone, and then eliminate the extra modes with largest real part, this way the small

jitter in the location of the modes (which are due to numerical errors) does not cause missing a mode or having a duplicated mode.

To satisfy the electromagnetic boundary conditions at the interface, continuity of tangential electric and magnetic field should be satisfied, which means

$$\begin{aligned}&\exp(-jk_{xi}x)+\sum_m R_m \exp[-j(k_{xi}+mK)x] \\ &\qquad = \sum_t T_t \sum_m \sum_n \tilde{E}_{mn,t} \exp[-j(k_{xi}+mK)x - j(k_{my,t}+nK)y_0]\end{aligned} \tag{B.24}$$

and

$$\begin{aligned}&-jk_{yi}\exp(-jk_{xi}x)+\sum_m R_m(jk_{my})\exp[-j(k_{xi}+mK)x] \\ &\qquad = \sum_t T_t \sum_m \sum_n \tilde{E}_{mn,t}(-jk_{my,t} - jnK)\exp[-j(k_{xi}+mK)x - j(k_{my,t}+nK)y_0]\end{aligned} \tag{B.25}$$

Eliminating common phase factor in the *x* direction, we obtain

$$\delta_{m0} + R_m \exp(-jmKx) = \sum_t T_t \sum_n \tilde{E}_{mn,t} \exp[-jmKx - j(k_{my,t}+nK)y_0] \tag{B.26}$$

$$k_{yi}\delta_{m0} - R_m k_{my} \exp(-jmKx) = \sum_t T_t \sum_n \tilde{E}_{mn,t}(k_{my,t}+nK)\exp[-jmKx - j(k_{my,t}+nK)y_0] \tag{B.27}$$

For each *m*, the above equations give two linear equations, therefore, for $m=-n_x,...,n_x$, we have $2(2n_x+1)=2N_x$ linear equations. If we take $t=1,...,N_x$, then there are $N_x$ unknowns for photonic crystal modes and $N_x$ unknowns for reflection waves, thus we have a consistent $2N_x$ linear system of equations with $2N_x$ unknowns. This system can be solved by standard methods of solving linear system of equations, and the results give the amplitude of reflected waves and photonic crystal modes.

For the purpose of simulation, we can rewrite the foregoing system as

$$\begin{pmatrix} A_{11} & A_{12} \\ A_{21} & A_{22} \end{pmatrix} \begin{pmatrix} R \\ T \end{pmatrix} = \begin{pmatrix} b_1 \\ b_2 \end{pmatrix} \tag{B.28}$$

In which $A_{11}$ and $A_{21}$ are diagonal matrices with $a_{11,m} = -\exp(-jk_{my}y_0)$ and $a_{21,m} = k_{my}\exp(-jk_{my}y_0)$ as diagonal elements, respectively. For other coefficient matrices we have

$$a_{12,mt} = \sum_n \tilde{E}_{mn,t}\exp[-j(k_{my,t} + nK)y_0] \tag{B.29}$$

$$a_{22,mt} = \sum_n \tilde{E}_{mn,t}(k_{my,t} + nK)\exp[-j(k_{my,t} + nK)y_0] \tag{B.30}$$

Finally, constant values on the right hand side of system are $b_{1,m} = \delta_{m0}\exp(-jk_{yi}y_0)$ and $b_{2,m} = k_{yi}\delta_{m0}\exp(-jk_{yi}y_0)$. Figure B.3 shows the reflection at the interface of a square lattice PC of air-holes in Si (with *r/a*=0.20) for an incident plane wave coming from a bulk Si region with E-polarization. These results are obtained using the method described above, and for the definition of reflection coefficient, a convention similar to the concept of diffraction efficiency for gratings is used. The simulation is repeated for two cases with different number of plane waves, demonstrating the consistency of the results.

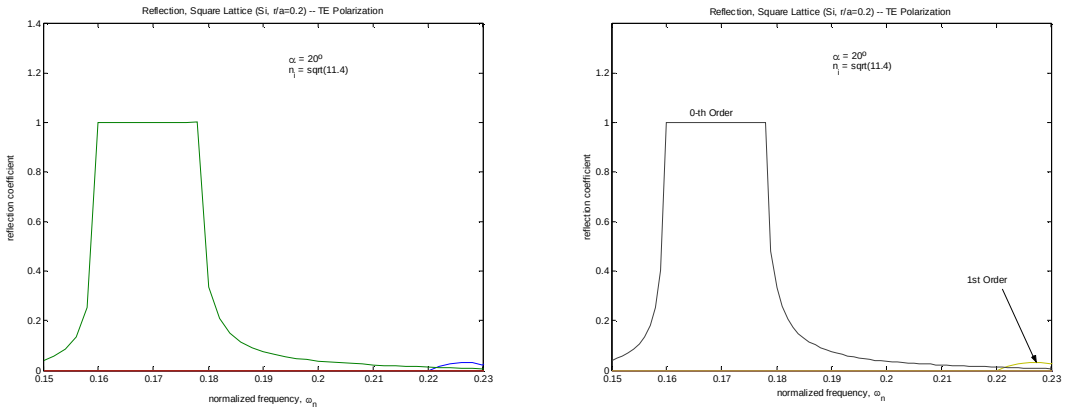


(a) (b)

Figure B.3. Calculated reflection at the interface of a square lattice PC of air-holes in Si (*r/a*=0.20) is shown with the number of Bloch components retained in the simulation being (a) $N_1$=$N_2$=17 and (b) $N_1$=$N_2$=13. The incident wave is in E-polarization and comes at an angle of $\alpha$=20° from a bulk Si region to the PC structure.

## B.2. Formulation for H-Polarization

The same procedure as discussed for the E-polarization case can be followed to calculate the reflection at PC interfaces for H-polarization. For calculating the PC modes excited inside the PC for an incident plane wave, we can expand the field components as

$$H_z(\mathbf{r}) = \sqrt{\frac{\varepsilon_0}{\mu_0}} \sum_m \sum_n \tilde{H}_{z,mn} \exp(-j\mathbf{k}\cdot\mathbf{r}) \exp[-j(m\mathbf{K}_1 + n\mathbf{K}_2)\cdot\mathbf{r}], \tag{B.31}$$

$$E_x(\mathbf{r}) = \sum_m \sum_n \tilde{E}_{x,mn} \exp(-j\mathbf{k}\cdot\mathbf{r}) \exp[-j(m\mathbf{K}_1 + n\mathbf{K}_2)\cdot\mathbf{r}], \tag{B.32}$$

$$E_y(\mathbf{r}) = \sum_m \sum_n \tilde{E}_{y,mn} \exp(-j\mathbf{k}\cdot\mathbf{r}) \exp[-j(m\mathbf{K}_1 + n\mathbf{K}_2)\cdot\mathbf{r}]. \tag{B.33}$$

By inserting these relations into the Maxwell's equations,

$$\begin{cases} \nabla \times \mathbf{E}(\mathbf{r}) = -j\omega\mu_0 \mathbf{H}(\mathbf{r}) \\ \nabla \times \mathbf{H}(\mathbf{r}) = j\omega\varepsilon(\mathbf{r})\mathbf{E}(\mathbf{r}) \end{cases}, \tag{B.34}$$

and using the matrix convention, we obtain

$$\begin{cases} [\mathbf{K}_x]\mathbf{e}_y - \left(k_y[\mathbf{I}] + [\mathbf{K}_y]\right)\mathbf{e}_x = k_0\mathbf{h}_z \\ k_0\mathbf{e}_y = [\boldsymbol{\eta}][\mathbf{K}_x]\mathbf{h}_z \\ k_0\mathbf{e}_x = -[\boldsymbol{\eta}]\left(k_y[\mathbf{I}] + [\mathbf{K}_y]\right)\mathbf{h}_z \end{cases}, \tag{B.35}$$

where $[\boldsymbol{\eta}] = [\boldsymbol{\varepsilon}]^{-1}$ contains the Fourier coefficients of the inverse permittivity of the periodic structure, and the rest of matrices follow the same definitions as in the E-polarization case. If we eliminate $\mathbf{e}_y$ from these linear relations, the result is

$$\begin{cases} k_0\mathbf{e}_x + [\boldsymbol{\eta}]\left(k_y[\mathbf{I}] + [\mathbf{K}_y]\right)\mathbf{h}_z = 0 \\ \left(\frac{1}{k_0}[\mathbf{K}_x][\boldsymbol{\eta}][\mathbf{K}_x] - k_0\right)\mathbf{h}_z - \left(k_y[\mathbf{I}] + [\mathbf{K}_y]\right)\mathbf{e}_x = 0 \end{cases}. \tag{B.36}$$

The relations in Equation (B.36) can be readily arranged to form a standard eigenvalue problem,

$$k_y \begin{pmatrix} [O] & [\boldsymbol{\eta}] \\ -[\mathbf{I}] & [O] \end{pmatrix} \begin{pmatrix} \mathbf{e}_x \\ \mathbf{h}_z \end{pmatrix} + \begin{pmatrix} k_0[\mathbf{I}] & [\boldsymbol{\eta}][\mathbf{K}_y] \\ -[\mathbf{K}_y] & \frac{1}{k_0}[\mathbf{K}_x][\boldsymbol{\eta}][\mathbf{K}_x] - k_0[\mathbf{I}] \end{pmatrix} \begin{pmatrix} \mathbf{e}_x \\ \mathbf{h}_z \end{pmatrix} = 0 . \qquad \text{(B.37)}$$

Solving this eigenvalue problem gives us the eigenvalues and corresponding eigenvectors of the modes excited inside the PC region. Following a mode selection scheme similar to the one described for the E-polarization case, we can find the set of independent and physically proper modes to be used in the mode-matching process.

# APPENDIX C

# IMPLEMENTATION OF DISPERSIVE SYSTEMS IN THREE-DIMENSIONAL PHOTONIC CRYSTALS

## C.1. Introduction

Recent advances in fabrication of three-dimensional photonic crystal structures, including layer-by-layer processing [115], direct laser writing by multi-photon lithography (MPL) [116-118], and multi-beam interference lithography (MBIL) [119-121], have made it possible to consider these structures for a variety of applications. Activities to realize photonic crystals have been mostly around planar structures because of their compatibility with well-developed microelectronic fabrication techniques, the possibility of integration in a planar platform, and their close connection to already investigated field of integrated optics. However, there are applications, including beam shaping and dispersion control, in which the optical beams to be processed are in the free space. For such cases, coupling the light into and out of a planar platform will not be a cost-efficient solution. In addition, recent advances in materials and fabrication techniques (such as MBIL, MPL, self assembly, etc) have brought the opportunity to realize high-quality three-dimensional photonic crystals at low cost that can be readily used as the optical material in these applications. These potentials are more versatile, easier to access, and more cost-efficient in three-dimensional structures, compared to two-dimensional platforms, which motivates focused research in this direction. There have been proposals for photonic crystal devices in these applications, and to realize them efficiently, it is essential to have a basic understanding of the effects and a model to describe the structures of interest.

The propagation of the optical beams inside the three-dimensional photonic crystal structures is the main effect to be studied to enable organized analysis and design of dispersion-based applications of photonic crystals. The amount of required memory and computation makes direct space-domain simulation of these structures, e.g., using finite difference time-domain (FDTD) method, highly inefficient. A modal approach is more efficient in this case by reducing both the required memory and the computation cost for large structures. It has been shown that for two-dimensional photonic crystal structures an effective diffractive index can be defined to describe beam propagation effects in the two-dimensionally periodic structures. Here, we will show that such model can be extended to three-dimensional photonic crystals as well. As a result, it will be shown that in general for any photonic crystal mode, there are two principal directions and two corresponding effective indices that describe the beam properties in the plane perpendicular to the direction of propagation. The model is used to study some dispersive applications of these structures.

### C.2. Extension of the Diffractive Index Model to 3D PCs

The problem of interest in most dispersive applications of photonic crystals is the modeling of evolution of the optical beams propagating through a periodic structure. There have been models to describe these effects in particular cases [122-123], but a more general model is still missing. We try in this section to develop an easy-to-use model that can also provide some insight into the process of beam propagation through three-dimensional periodic structures. Modal approach provides a straightforward way of analyzing these structures by expanding the beam over modes of the photonic crystal structure. This, however, requires a detailed mode matching process, which can be a tedious task. At the same time, in most dispersion-based applications of photonic crystals we are not interested in the details of the beam profile inside the periodic structure. In most these cases, a description of the behavior of the envelope of the optical beam is of

practical interest. It has been shown in Chapter 3 that in two-dimensional photonic crystals an amplitude transfer function (using the band structure) can be defined to model the evolution of the amplitude of the beam inside the periodic structure. Here, we extend the same idea to define the amplitude transfer function for three-dimensional photonic crystals. Local quadratic approximation of the band structure is then used to define diffraction indices that describe the diffraction of optical beams inside the periodic media.

One main concept that differentiates between the three-dimensional photonic crystals and the two-dimensional case is that the field in three-dimensional case is in general vectorial. Therefore, unlike two-dimensional case that field profiles can be expressed as scalar quantities (by decoupling transverse electric and transverse magnetic components), in the three-dimensional structures, in general, we need to consider the vectorial nature of polarization state. Nevertheless, it can be shown [124] that the polarization of the modes of three-dimensional photonic crystal structures in most practical cases have Bloch components with well-defined transverse eigenstates. In addition, these polarization states have smooth variation over the band structure. As a result, for the optical beams with limited spatial-spectral content, we can locally consider a scalar field by projecting over the dominant polarization state. In what follows, such scalar model is used in the approximate solutions.

For simplicity we consider a cubic three-dimensional lattice for the photonic crystal in our derivations. The formulation can be extended readily to other lattices and the results are not specific to the choice of lattice. Assume we have an initial distribution $p_1(x, y)$ along $z=z_1$ (i.e., a plane normal to the $z$-axis) inside the photonic crystal. We can expand this distribution over photonic crystal modes as

$$\begin{aligned} p_1(x,y) &= \int\int A(k_x,k_y)U_{\bar{k}_t}(x,y,z_1)\exp(jk_x x + jk_y y)\exp(jk_z z_1)dk_x dk_y \\ &= \int\int A(k_x)\left(\sum_m\sum_n\sum_l \tilde{E}_{mnl}(k_x,k_y)\exp[j(k_x+mK_x)x]\exp[j(k_y+nK_y)y]\exp[j(k_z+nK_z)z_1]\right)dk_x dk_y \end{aligned} \quad .(C.1)$$

The spatial Fourier transform of the field distribution can be calculated as

$$P_1(k_x,k_y)=\sum_m\sum_n\sum_l A(k_x',k_y')\tilde{E}_{mnl}(k_x',k_y')\exp\{j[k_z(k_x',k_y')+lK_z]z_1\}\Big|_{\substack{k_x'=k_x-mK_x\\k_y'=k_y-nK_y}}, \qquad \text{(C.2)}$$

or

$$\begin{aligned}P_1(k_x,k_y)=&\sum_m\sum_n\sum_l A(k_x-mK_x,k_y-nK_y)\tilde{E}_{mnl}(k_x-mK_x,k_y-nK_y)\\&\times\exp\{j[k_z(k_x-mK_x,k_y-nK_y)+lK_z]z_1\}\end{aligned}. \qquad \text{(C.3)}$$

Assuming that the beam profile covers a limited spectrum around $(k_x,k_y)=(k_{x0},k_{y0})$, we can extract the envelope of the beam by filtering the high-frequency portion of the spectrum around $(k_{x0},k_{y0})$ and moving it to the base band by shifting the spectrum. The resulting spectrum of the envelope is

$$\begin{aligned}\overline{P}_1(k_x,k_y)=&A(k_x+k_{x0},k_y+k_{y0})\exp[jk_z(k_x+k_{x0},k_y+k_{y0})z_1]\\&\times\left(\sum_l\tilde{E}_{00l}(k_x+k_{x0},k_y+k_{y0})\exp(jlK_zz_1)\right)\end{aligned}. \qquad \text{(C.4)}$$

At another monitoring plane, $z=z_2$, we have

$$\begin{aligned}\overline{P}_2(k_x,k_y)=&A(k_x+k_{x0},k_y+k_{y0})\exp[jk_z(k_x+k_{x0},k_y+k_{y0})z_2]\\&\times\left(\sum_l\tilde{E}_{00l}(k_x+k_{x0},k_y+k_{y0})\exp(jlK_zz_2)\right)\end{aligned}. \qquad \text{(C.5)}$$

If $z_2-z_1=2\pi q/K_z$ (with $q$ being an integer), the summation term in Equations (C.4) and (C.5) will be exactly the same, therefore

$$\overline{P}_2(k_x,k_y)=\overline{P}_1(k_x,k_y)\exp[jk_z(k_x+k_{x0},k_y+k_{y0})(z_2-z_1)], \qquad \text{(C.6)}$$

which means that the effect of propagation from $z=z_1$ to $z=z_2$ on the envelope of the beam can be represented as a phase change in the spectral domain similar to plane-wave-type propagation with propagation constant $k_z$. Thus, the main effect of propagation in photonic crystals on the beam envelope is the phase variations of the modes from initial plane to the observation plane.

Based on Equation (C.6), we can write the envelope transfer function of the structure from $z=z_1$ to $z=z_2$ plane as

$$H(k_x,k_y)=\frac{\overline{P}_2(k_x,k_y)}{\overline{P}_1(k_x,k_y)}=\exp[\,j(z_2-z_1)k_z\,], \tag{C.7}$$

where $k_z=k_z(k_x,k_y)$ is related to $k_x$ and $k_y$ through the dispersion relation of the structure at the constant temporal frequency of the beam. The relation is similar to what was obtained for two-dimensional structures [31], with the main difference being the extension of the envelope transfer function from a single variable function to one with two variables. Using the analogy with propagation in bulk media, we can extend the relation to the case of beam propagation along the $\zeta$ direction (normal to the constant frequency surface at the point of operation, parallel to $\mathbf{v}_g=\nabla_{\mathbf{k}}\omega$ ) as

$$H(k_\xi,k_\eta)=\frac{\overline{P}_2(k_\xi,k_\eta)}{\overline{P}_1(k_\xi,k_\eta)}=\exp[-j(\zeta_2-\zeta_1)k_\zeta(k_\xi,k_\eta)], \tag{C.8}$$

where the directions of $\xi$, $\eta$, and $\zeta$ are shown in Figure C.1.

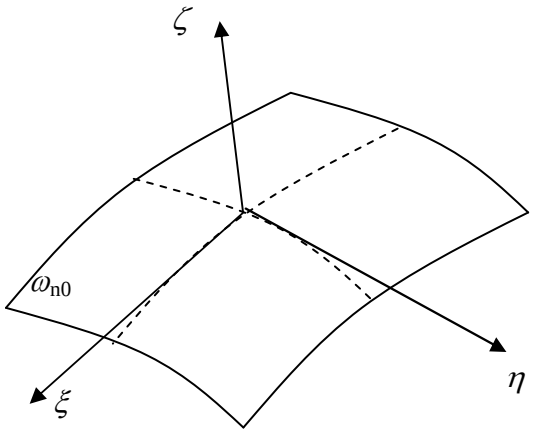


Figure C.1. A portion of an iso-frequency surface of a 3D PC in the k-space is shown. The directions tangential to the interface (i.e., $\xi$ and $\eta$) and the direction normal to the surface ($\zeta$) are defined in this figure.

Equation (C.8) can be used readily to investigate beam propagation effects inside a three-dimensionally periodic photonic crystal structure. The analogy with the propagation in normal bulk media can be further utilized if we express the exponential term of the spectral response in Equation (C.8) in terms of its Taylor expansion. Knowing that the curvature of the constant frequency surface at the operation point describes the diffraction of an optical beam launched at that point, we need to find those curvatures. Using the second order approximation,

$$k_z = k_{z0} + a_2(k_x - k_{x0}) + a_3(k_y - k_{y0}) + a_4(k_x - k_{x0})^2 + a_5(k_x - k_{x0})(k_y - k_{y0}) + a_6(k_y - k_{y0})^2, \quad \text{(C.9)}$$

a standard method can be adopted to find these curvatures [125].

Defining $W$ as the magnitude of the gradient at the operation point, we have

$$W = \sqrt{1 + a_2^2 + a_3^2}\ . \quad \text{(C.10)}$$

Then the parameters for the first fundamental form can be defined as [125]

$$\begin{cases} E = (1 + a_2^2)W \\ F = a_2 a_3 W \\ G = (1 + a_3^2)W \end{cases}, \quad \text{(C.11)}$$

and those of the second fundamental form can be calculated as

$$\begin{cases} L = 2a_4 \\ M = a_5 \\ N = 2a_6 \end{cases}. \quad \text{(C.12)}$$

Using these relations, which are coefficients of the fundamental forms of a surface in the special case of a quadratic surface, we can calculate the Gaussian curvature as

$$K = \frac{LN - M^2}{EG - F^2} \quad \text{(C.13)}$$

and the mean curvature as

$$H = \frac{1}{2}\frac{EN - 2FM + GL}{EG - F^2}. \quad \text{(C.14)}$$

Finally, the two principal curvatures can be calculated as

$$\kappa_1 = H + \sqrt{H^2 - K} \tag{C.15}$$

$$\kappa_2 = H - \sqrt{H^2 - K}\ . \tag{C.16}$$

The principal directions can be calculated by inserting these principal curvatures in the characteristic equation,

$$\begin{pmatrix} L - \kappa_i E & M - \kappa_i F \\ M - \kappa_i F & N - \kappa_i G \end{pmatrix} \bar{v}_i = 0 \quad ; \quad i = 1,2\,, \tag{C.17}$$

which gives us the principal directions projected on *xy* plane. From these directions, we can find the three-dimensional directions which are normal to the gradient direction,

$$\bar{n} = (-a_2, -a_3, 1)\,. \tag{C.18}$$

Note that in the special case that the two curvatures are equal (degenerate case), the choice of principal directions is arbitrary. Without loss of generality we assume the directions of $\xi$ and $\eta$ in Figure C.1 to be along the principal diffraction directions. Therefore, based on the analogy with bulk medium (similar to the two-dimensional case [31]) we can find the principal diffractive indices at the operation point as

$$\begin{cases} n_{e\xi} = \dfrac{1}{k_0 \kappa_1} \\ n_{e\eta} = \dfrac{1}{k_0 \kappa_2} \end{cases}. \tag{C.19}$$

As a result, for each mode of the three-dimensional photonic crystal (at a given temporal frequency), there are two principal diffraction directions in the plane perpendicular to the direction of group velocity for that mode. A principal diffractive index can be defined for each of these principal diffraction directions to describe the diffraction of an optical beam along its corresponding principal diffraction direction. The diffraction of the beam along an arbitrary direction transverse to the direction of propagation of the beam (i.e., the direction of group velocity) can be found using

$$\frac{1}{n_d^2(\theta)} = \frac{\cos^2\theta}{n_\xi^2} + \frac{\sin^2\theta}{n_\eta^2}, \tag{C.20}$$

in which $\theta$ is the angle between the arbitrary direction of interest and the $\xi$ direction in the plane perpendicular to the direction of group velocity. The same phenomenon, in principle, occurs in anisotropic media as well, but the extent of the contrast between the two principal diffractive indices can be much larger (for instance they can have opposite signs).

### C.3. Analysis of Reflection from Photonic Crystals

The analysis model is the basic mode matching between the two regions by expanding the field at each region over Bloch modes. Phase matching condition plays the main role in describing the modes excited in the transmission region for a given incident wave. The reason we use this mode matching process is that it immediately gives us information on excited photonic crystal modes such as penetration depth of evanescent modes and transmission coefficient and wavevector of propagating modes.

Here, we formulate the problem using the components of electric and magnetic fields tangential to the interface. Other formulations based on three components of the electric field or three components of the magnetic field can also be used. All these formulations are of the same order of complexity (in term of implementation issues, required memory and computation cost) but may be of interest in particular cases.

The periodic structure of the three-dimensional photonic crystal can be represented as

$$\varepsilon_r(x,y,z) = \sum_l \sum_m \sum_n \varepsilon_{lmn} \exp[-j(l\mathbf{K}_1 + m\mathbf{K}_2 + n\mathbf{K}_3)\cdot\mathbf{r}], \tag{C.21}$$

where $\mathbf{K}_1$, $\mathbf{K}_2$, and $\mathbf{K}_3$ are the reciprocal lattice vectors of the three-dimensional periodic structure. For these structures, the Floquet-Bloch theorem allows us to expand each mode of the structure as

$$\mathbf{H}_{\mathbf{k}}(\mathbf{r}) = \sqrt{\frac{\varepsilon_0}{\mu_0}} \sum_l \sum_m \sum_n \mathbf{U}_{lmn} \exp[-j(\mathbf{k} + l\mathbf{K}_1 + m\mathbf{K}_2 + n\mathbf{K}_3) \cdot \mathbf{r}] \tag{C.22}$$

$$\mathbf{E}_{\mathbf{k}}(\mathbf{r}) = \sum_l \sum_m \sum_n \mathbf{S}_{lmn} \exp[-j(\mathbf{k} + l\mathbf{K}_1 + m\mathbf{K}_2 + n\mathbf{K}_3) \cdot \mathbf{r}] \tag{C.23}$$

in which $\mathbf{k}$ is the wavevector of the mode, and $\mathbf{U}_{lmn}$ and $\mathbf{S}_{lmn}$ are the coefficients of different Bloch components of the magnetic and electric fields, respectively. For simplicity, let

$$\mathbf{k}_{lmn} = \mathbf{k} + l\mathbf{K}_1 + m\mathbf{K}_2 + n\mathbf{K}_3 . \tag{C.24}$$

To find the reflection at the interface, we use a direct mode matching process to match the modes of the incident region to those of the photonic crystal structure. For that, we need to first find the modes of the photonic crystal structure excited by the incident wave. The next step is to match the tangential fields at the interface to those of the incident region to find the amplitude coefficient of each mode.

Starting from Maxwell's equations

$$\begin{cases} \nabla \times \mathbf{E} = -j\omega\mu_0 \mathbf{H} \\ \nabla \times \mathbf{H} = j\omega\varepsilon_0\varepsilon_r \mathbf{E} \end{cases} \tag{C.25}$$

and expanding the fields over their Bloch components results in

$$\begin{cases} [\mathbf{k_y}]\mathbf{S}_z - [\mathbf{k_z}]\mathbf{S}_y = k_0 \mathbf{U}_x \\ [\mathbf{k_z}]\mathbf{S}_x - [\mathbf{k_x}]\mathbf{S}_z = k_0 \mathbf{U}_y \\ [\mathbf{k_x}]\mathbf{S}_y - [\mathbf{k_y}]\mathbf{S}_x = k_0 \mathbf{U}_z \end{cases}, \tag{C.26}$$

and

$$\begin{cases} [\mathbf{k_y}]\mathbf{U}_z - [\mathbf{k_z}]\mathbf{U}_y = -k_0 [\boldsymbol{\varepsilon}]\mathbf{S}_x \\ [\mathbf{k_z}]\mathbf{U}_x - [\mathbf{k_x}]\mathbf{U}_z = -k_0 [\boldsymbol{\varepsilon}]\mathbf{S}_y \\ [\mathbf{k_x}]\mathbf{U}_y - [\mathbf{k_y}]\mathbf{U}_x = -k_0 [\boldsymbol{\varepsilon}]\mathbf{S}_z \end{cases} \tag{C.27}$$

In these equations, the wavevector matrices are diagonal matrices with diagonal elements $\left([\mathbf{k_u}]\right)_{l,m,n} = (\mathbf{k} + l\mathbf{K_1} + m\mathbf{K_2} + n\mathbf{K_3}) \cdot \hat{\mathbf{u}}$, and the periodicity matrix, $[\boldsymbol{\varepsilon}]$, is defined as

$$\left([\boldsymbol{\varepsilon}]\right)_{(l,m,n),(q,r,s)} = \tilde{\varepsilon}_{(l-q)(m-r)(n-s)}. \tag{C.28}$$

Eliminating z components from these relations, assuming $[\boldsymbol{\eta}] = [\boldsymbol{\varepsilon}]^{-1}$, gives us

$$\begin{cases} \frac{-1}{k_0}[\mathbf{k_y}][\boldsymbol{\eta}]\left([\mathbf{k_x}]\mathbf{U}_y - [\mathbf{k_y}]\mathbf{U}_x\right) - [\mathbf{k_z}]\mathbf{S}_y = k_0\mathbf{U}_x \\ [\mathbf{k_z}]\mathbf{S}_x + \frac{1}{k_0}[\mathbf{k_x}][\boldsymbol{\eta}]\left([\mathbf{k_x}]\mathbf{U}_y - [\mathbf{k_y}]\mathbf{U}_x\right) = k_0\mathbf{U}_y \\ \frac{1}{k_0}[\mathbf{k_y}]\left([\mathbf{k_x}]\mathbf{S}_y - [\mathbf{k_y}]\mathbf{S}_x\right) - [\mathbf{k_z}]\mathbf{U}_y = -k_0[\boldsymbol{\varepsilon}]\mathbf{S}_x \\ [\mathbf{k_z}]\mathbf{U}_x - \frac{1}{k_0}[\mathbf{k_x}]\left([\mathbf{k_x}]\mathbf{S}_y - [\mathbf{k_y}]\mathbf{S}_x\right) = -k_0[\boldsymbol{\varepsilon}]\mathbf{S}_y \end{cases}. \tag{C.29}$$

To sort these relations for $k_z$, we can define $[\mathbf{k_z}] = k_z + [\mathbf{K_z}]$; thus

$$[\mathbf{M}]\begin{pmatrix}\mathbf{U}_x\\ \mathbf{U}_y\\ \mathbf{S}_x\\ \mathbf{S}_y\end{pmatrix} = k_z\begin{pmatrix}\mathbf{U}_x\\ \mathbf{U}_y\\ \mathbf{S}_x\\ \mathbf{S}_y\end{pmatrix}, \tag{C.30}$$

where

$$[\mathbf{M}] = \begin{pmatrix} -[\mathbf{K_z}] & \mathbf{0} & \frac{-1}{k_0}[\mathbf{k_x}][\mathbf{k_y}] & \frac{1}{k_0}[\mathbf{k_x}]^2 - k_0[\boldsymbol{\varepsilon}] \\ \mathbf{0} & -[\mathbf{K_z}] & \frac{-1}{k_0}[\mathbf{k_y}]^2 + k_0[\boldsymbol{\varepsilon}] & \frac{1}{k_0}[\mathbf{k_y}][\mathbf{k_x}] \\ \frac{1}{k_0}[\mathbf{k_x}][\boldsymbol{\eta}][\mathbf{k_y}] & \frac{-1}{k_0}[\mathbf{k_x}][\boldsymbol{\eta}][\mathbf{k_x}] + k_0 & -[\mathbf{K_z}] & \mathbf{0} \\ \frac{1}{k_0}[\mathbf{k_y}][\boldsymbol{\eta}][\mathbf{k_y}] - k_0 & \frac{-1}{k_0}[\mathbf{k_y}][\boldsymbol{\eta}][\mathbf{k_x}] & \mathbf{0} & -[\mathbf{K_z}] \end{pmatrix}. \tag{C.31}$$

Solving the eigenvalue problem in Equation (C.30) gives us the wavevectors of the photonic crystal modes in the *z* direction as eigenvalue, and corresponding amplitudes of the Bloch components as eigenvectors. Applying the boundary conditions afterwards gives us the amplitudes for reflected and transmitted modes.

Note that in the case that interface of the photonic crystal (chosen to be the *xy* plane, without loss of generality) contains two of the lattice vectors of the photonic

crystal structure (which is the case in most practical situations), the third reciprocal lattice vector, $K_3$, will be along the $z$ direction, and this eigenvalue problem is redundant, since theoretically if $k_{zf}$ is a solution, so is $k_{zf}+nK_3$ ($n$ being any integer number). This is the case that we will be considering in what follows. There are two conditions that a PC mode has to satisfy to be considered as one of the possible modes excited inside the PC. First, the direction of energy for that mode should be away from the interface. Second, the amplitude of the mode should not grow toward infinity. Moreover, considering the redundancy in the modes calculated in the previous section (wavevectors differing by a multiple of the lattice wavevector represent the same PC mode), only $2N_1N_2$ modes are eligible to be included in the mode matching process ($N_1$ and $N_2$ are the number of plane waves retained for $K_1$ and $K_2$ reciprocal lattice vectors, respectively).

In the first step we need to calculate the Poynting vector for each of the PC modes calculated in the previous section

$$\mathbf{S}_{\mathbf{k}} = \frac{1}{2}\mathbf{E}_{\mathbf{k}} \times \mathbf{H}_{\mathbf{k}}^{*}. \tag{C.32}$$

Therefore, the Poynting vector normal to the interface can be calculated as

$$S_z = \frac{1}{2\omega}\left\{-\mathbf{U}_y^T\mathbf{S}_x + \mathbf{U}_x^T\mathbf{S}_y\right\}. \tag{C.33}$$

The sign of Poynting vector determines whether the mode has its power propagating toward or against the interface. Only those PC modes which take power away from the interface are physically acceptable according to power conservation requirement. Thus, we retain $2N_1N_2$ PC modes which are not redundant and satisfy the causality condition, in the photonic crystal region. In the incident region, in addition to the incident plane wave, we consider $N_1N_2$ TE plane waves and $N_1N_2$ TM plane waves for reflected orders from the PC structure. Therefore, the field matching equations can then be written as

$$\delta_{lm,00}U_{i,00x} + U_{r,lmx}^{TE} + U_{r,lmx}^{TM} = \sum_{t=1}^{2N_1N_2} a_t \sum_n U_{t,lmnx} \exp[-j(k_{zt} + nK_z)z] \tag{C.34}$$

$$\delta_{lm,00}U_{i,00y} + U^{TE}_{r,lmy} + U^{TM}_{r,lmy} = \sum_{t=1}^{2N_1N_2} a_t \sum_n U_{t,lmny} \exp[-j(k_{zt} + nK_z)z] \qquad \text{(C.35)}$$

$$\delta_{lm,00}S_{i,00x} + S^{TE}_{r,imx} + S^{TM}_{r,imx} = \sum_{t=1}^{2N_1N_2} a_t \sum_n S_{t,lmnx} \exp[-j(k_{zt} + nK_z)z] \qquad \text{(C.36)}$$

$$\delta_{lm,00}S_{i,00y} + S^{TE}_{r,imy} + S^{TM}_{r,imy} = \sum_{t=1}^{2N_1N_2} a_t \sum_n S_{t,lmny} \exp[-j(k_{zt} + nK_z)z] \qquad \text{(C.37)}$$

In these relations, the TE and TM components of the reflected plane-waves satisfy

$$\mathbf{S}^{TE}_{r,lm} \parallel (k_{r,lmx}\hat{\mathbf{x}} + k_{r,lmy}\hat{\mathbf{y}}) \times \hat{\mathbf{z}} \qquad \text{(C.38)}$$

$$k_0 \mathbf{U}^{TE}_{r,lm} = \mathbf{k}_{r,lmx} \times \mathbf{S}^{TE}_{r,lm} \qquad \text{(C.39)}$$

$$\mathbf{U}^{TM}_{r,lm} \parallel (k_{r,lmx}\hat{\mathbf{x}} + k_{r,lmy}\hat{\mathbf{y}}) \times \hat{\mathbf{z}} \qquad \text{(C.40)}$$

$$k_0 n_1^2 \mathbf{S}^{TM}_{r,lm} = \mathbf{U}^{TM}_{r,lm} \times \mathbf{k}_{r,lmx}, \qquad \text{(C.41)}$$

in which

$$k_{r,lmz} = \sqrt{n_1^2 k_0^2 - k_{r,lmx}^2 - k_{r,lmy}^2}\,. \qquad \text{(C.42)}$$

By solving the linear system of equations in (C.34)-(C.37), we obtain both the amplitudes of the reflected plane-waves as well as the amplitudes of the PC modes excited in the photonic crystal region. In this work, we will use these relations to analyze reflection at the interface of different photonic crystal structures and to investigate some of the effects associated with that.

Figure C.2 shows schematically a cubic woodpile structure that can be realized through direct laser writing in a polymer material. The calculated reflection spectra for both transverse electric (TE) and transverse magnetic (TM) incident polarizations are shown in Figure C.3. In our simulations, we have used 7 plane-wave components for the expansion in each direction. The calculated values obtained at this size have an error of less than 5% in the reflected order powers, which is sufficient for most practical applications. It can be seen that at low frequencies, an average index model can be used

to describe these reflections. At frequencies in the vicinity of the bandgap, however, strong Bragg reflection is observed. Inside the stop band, total reflection of the wave to the incident region is observed (note that a semi-infinite photonic crystal is considered in these simulations).

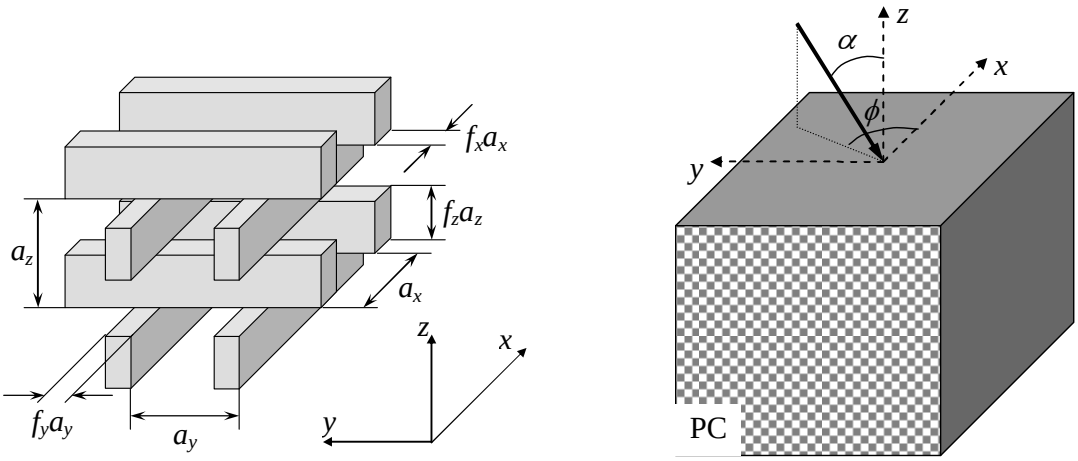


(a) (b)

Figure C.2. (a) Schematic demonstration of the cubic woodpile lattice considered throughout this appendix is shown. Lattice constants and filling factors in different directions of this lattice are marked on this figure. (b) The setup for reflection calculation is shown, with $\alpha$ being the angle between the incident wavevector and the normal to the interface ($z$), and $\phi$ being the angle between the plane of incidence and the $xz$-plane.

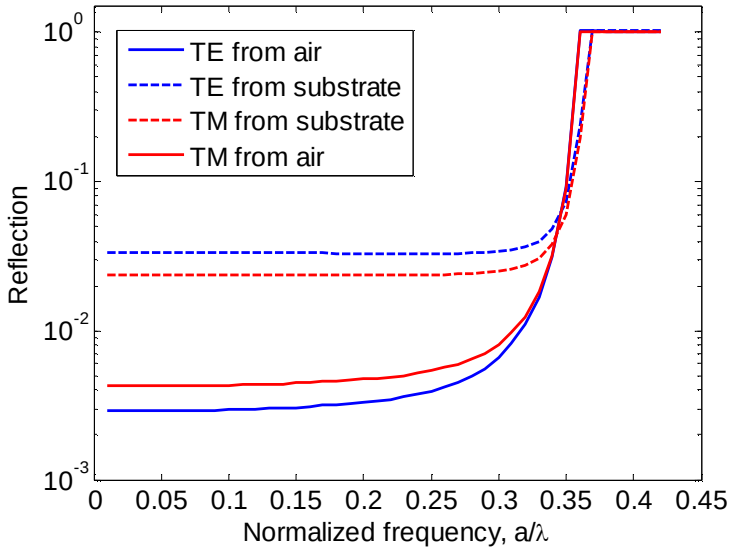


Figure C.3. Reflection at the interface of a cubic woodpile photonic crystal structure with $\varepsilon_r = 2.5$, $f_x = f_y = 0.3$, $f_z = 0.5$, $a_x = a_y = a$, and $a_z = 1.2a$ is shown with $z_0$=0 at normal incidence. Two cases with TE and TM polarizations (i.e., electric field and magnetic field along the *y* direction) are considered with incident wave coming either from the air ($\varepsilon_i = 1.0$) or substrate ($\varepsilon_i = 2.5$) regions.

## C.4. Effective Impedance Model

Analysis of reflection using the rigorous method provided in the previous section gives the exact solution (within computational limitations) for the reflection at the interface of a 3D PC. However, the process is computationally intense, and provides limited insight into the process of reflection at the interface of the PC. We have previously proposed an effective impedance model for the analysis of reflection at the interface of 2D PCs [113]. The effective impedance model suggests that the continuity of field and conservation of power at the interface are needed for an impedance matching condition (to couple the light efficiently into or out of a PC structure). Here we extend this model to analyze reflection at the interface of 3D PCs. For simplicity, we consider a TM-polarized incident wave (with magnetic field perpendicular to the plane of incidence), and define the effective impedance for a PC mode as

$$\eta = \frac{2S_n}{\left|\left\langle H_{\text{int}} \right\rangle\right|^2}, \tag{C.43}$$

where $\left\langle H_{\text{int}} \right\rangle$ is the average tangential field of the PC mode along the interface, and $S_n$ is the Poynting vector of the mode normal to the interface. Note that the effective impedance is defined for each photonic crystal mode and depends on the interface at which the PC is truncated. Therefore, by choosing the incident region or a different termination of the PC, it is possible to realize an impedance matching condition to couple the light completely into the PC structure (with no reflection). Note that the definition of this effective impedance requires that both the incident region and the transmission region to be single-mode. In low-contrast 3D PCs usually more than one mode are present, but the polarization of the incident wave can be selected such that excitation of other modes is negligible.

Figure C.4(a) shows the calculated reflection for a plane wave incident from a bulk medium with $\varepsilon_r = 2.5$ to a cubic woodpile PC with $a_x = a_y = a$, $a_z = 1.2a$, $f_x = f_y = 0.3$, and $f_z = 0.5$ (parameters as defined in Figure C.2) with TM incident polarization at an angle $\alpha = 7°$; the interface of the PC is assumed to be at $z_0 = 0.75a_z$. Both results from the rigorous mode-matching scheme and the effective impedance model are plotted in Figure C.4(a) and are in very good agreement. Figure C.4(b) shows the effective impedance of the PC modes excited at different frequencies in Figure C.4(a). The impedance matching condition in this figure occurs around normalized frequency of 0.34 which corresponds to the complete transmission range in Figure C.4(a). Another important behavior in the effective impedance of PCs is that in the vicinity of mode gap (depending on whether the average field goes to zero or a finite non-zero value), it is possible to obtain very large or very small values of effective impedance to match the PC modes of interest to the incident region.

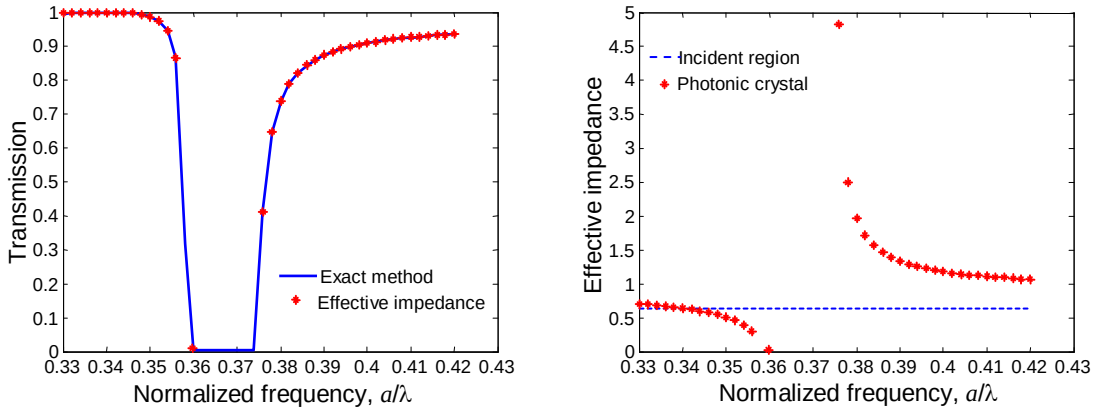


(a) (b)

Figure C.4. (a) Calculated reflection for a plane wave incident from substrate ($\varepsilon_r = 2.5$) to a cubic woodpile PC with $a_x = a_y = a$, $a_z = 1.2a$, $f_x = f_y = 0.3$, and $f_z = 0.5$ (parameters as defined in Figure C.3) with TM incident polarization (magnetic field along the *y* direction) at an angle $\alpha = 7°$ is shown. The interface of the PC is assumed to be at $z_0 = 0.75a_z$. (b) Calculated effective impedance of the photonic crystal modes excited in (a) is shown (marked by stars) and compared with that of the incident region (dashed line).

Figure C.5 shows the reflection from the PC in Figure C.4 for two different terminations at $z_0 = 0.25a_z$ and $z_0 = 0.75a_z$ along with the calculated effective impedances. It can be seen that the behavior of the effective impedance is highly dependent on the choice of the interface. In particular, by controlling the location of the interface, it is possible to move the high-transmission range (in the vicinity of the impedance matching condition) to different frequency ranges for specific applications of interest.

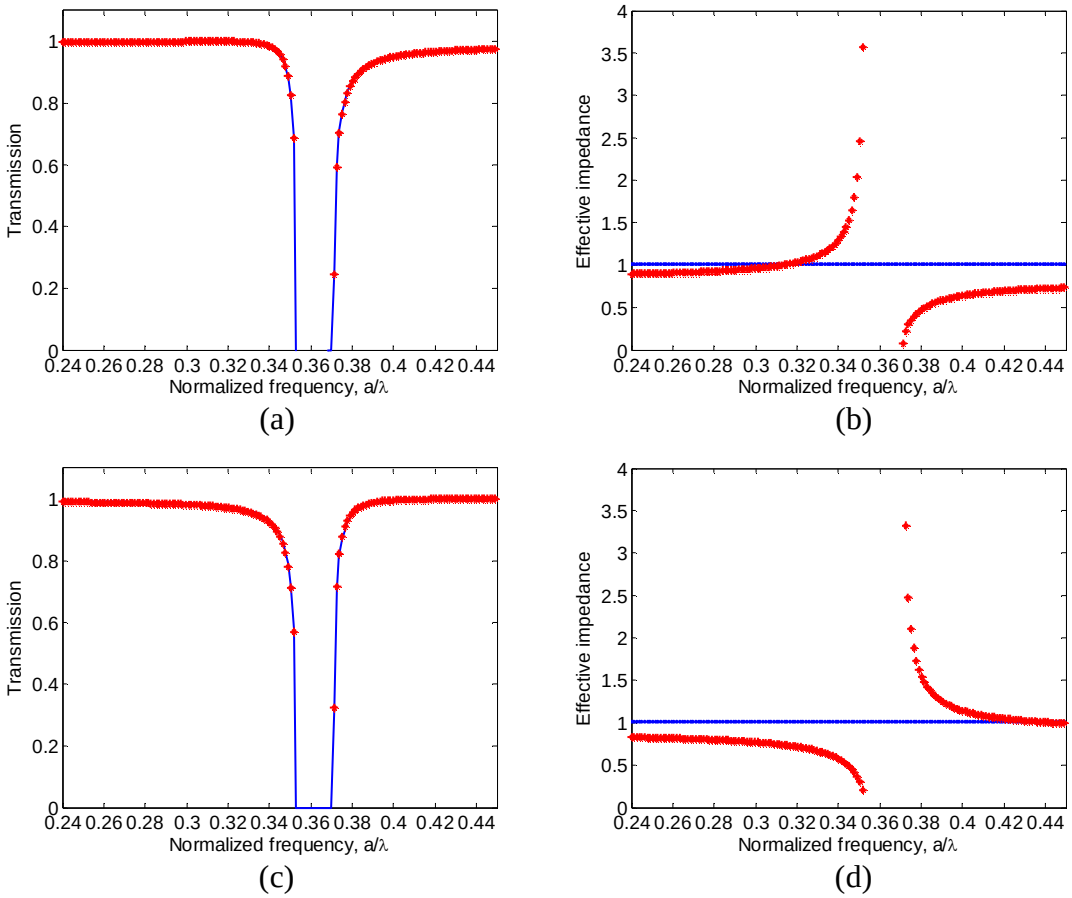


Figure C.5. Calculated reflection for a plane wave incident from air ($\varepsilon_r = 1.0$) to the same cubic woodpile PC in Figure C.4 with TM incident polarization at an angle $\alpha = 7°$ is shown. The interface of the PC is assumed to be at $z_0 = 0.25a_z$ in (a), and the corresponding effective impedance is shown in (b). The calculated reflection and effective impedance for an interface at $z_0 = 0.75a_z$ are shown in (c) and (d), respectively.

# REFERENCES


[1] K. Kato and Y. Tohmori, "PLC Hybrid Integration Technology and Its Application to Photonic Components," IEEE J. Select. Top. Quant. Electron., vol. 6, pp. 4-13 (2000).

[2] L. Eldada and L. W. Shacklette, "Advances in Polymer Integrated Optics," IEEE J. Select. Top. Quant. Electron., vol. 6, pp. 54-68 (2000).

[3] S. Fan, A. Mekis, S. G. Johnson, J. D. Joannopoulos, "Manipulating light with photonic crystals," AIP Conf. Proc., vol. 560, pp. 57-76 (2001).

[4] J. Joannopoulos, R. Meade, and J. Winn, *Photonic Crystals: Molding the Flow of Light*, Princeton University Press, Princeton, NJ, 1995.

[5] C. M. Soukoulis, "The history and a review of the modeling and fabrication of photonic crystals," Nanotechnol., vol. 13, pp. 420-423 (2002).

[6] E. Yablonovitch, "Inhibited spontaneous emission in solid-state physics and electronics," Phys. Rev. Lett., vol. 58, pp. 2059-2062 (1987).

[7] S. John, "Strong localization of photons in certain disordered dielectric superlattices," Phys. Rev. Lett., vol. 58, pp. 2486-2489 (1987).

[8] M. Okano, A. Chutinan, and S. Noda, "Analysis and design of single-defect cavities in a three-dimensional photonic crystal," Phys. Rev. B, vol. 66, pp. 165211-1-6 (2002).

[9] A. Figotin and A. Klein, "Localization of light in lossless inhomogeneous dielectrics," J. Opt. Soc. Am. A, vol. 15, pp. 1423-1435 (1998).

[10] A. Scherer, O. Painter, J. Vuckovic, M. Loncar, and T. Yoshie, "Photonic crystals for confining, guiding, and emitting light," IEEE Tran. Nanotechnol., vol. 1, pp. 4-11 (2002).

[11] S. Mookherjea and A. Yariv, “Pulse propagation in a coupled resonator optical waveguide to all orders of dispersion,” Phys. Rev. E, vol. 65, pp. 056601-1-6 (2002).

[12] S. G. Johnson and J. D. Joannopoulos, “Designing synthetic optical media: photonic crystals,” Acta Materialia, vol. 51, pp. 5823-5835 (2003).

[13] T. Baba, D. Mori, K. Inoshita, and Y. Kuroki, “Light localizations in photonic crystal line defect waveguides,” IEEE J. Sel. Top. Quantum Electron., vol. 10, pp. 484-491 (2004).

[14] T. P. White, L. C. Botten, R. C. McPhedran, and C. Martjin de Sterke, “Ultracompact resonant filters in photonic crystals,” Opt. Lett., vol. 28, pp. 2452-2454 (2003).

[15] Y. Akahane, T. Asano, H. Takano, B. –S. Song, Y. Takana, and S. Noda, “Two-dimensional photonic-crystal-slab channel-drop filter with flat-top response,” Opt. Express, vol. 13, pp. 2512-2530 (2005).

[16] Y. Akahane, M. Mochizuki, T. Asano, Y. Tanaka, and S. Noda, “Design of a channel drop filter by using a donor-type cavity with high-quality factor in a two-dimensional photonic crystal slab,” Appl. Phys. Lett., vol. 82, pp. 1341-1343 (2003).

[17] E. Chow, A. Grot, L. W. Mirkarimi, M. Sigalas, and G. Girolami, “Ultracompact biochemical sensor built with two-dimensional photonic crystal microcavity” Opt. Lett., vol. 29, pp. 1093-1095 (2004).

[18] M. F. Yanik, S. Fan, and M. Soljacic, “High-contrast all-optical bistable switching in photonic crystal microcavities,” Appl. Phys. Lett., vol. 83, pp. 2739-2741 (2003).

[19] J. Vuckovic, M. Loncar, H. Mabuchi, and A. Scherer, “Design of photonic crystal microcavities for cavity QED,” Phys. Rev. E, vol. 65, 016608-1-11 (2001).

[20] D. Felbacq, B. Guiza, and F. Zolla, “Wave propagation in one-dimensional photonic crystals,” Opt. Commun., vol. 152, pp. 119-126 (1998).

[21] I. V. Shadrivov, A. A. Sukhorukov, and Y. S. Kivshar, “Beam shaping by a periodic structure with negative refraction,” Appl. Phys. Lett., vol. 82, pp. 3820-3822 (2003).

[22] L. Wu, M. Mazilu, and T. F. Krauss, “Beam steering in planar-photonic crystals: From superprism to supercollimator,” J. Lightwave Technol., vol. 21, pp. 561-566 (2003).

[23] Z. Ruan and S. He, “Open cavity formed by a photonic crystal with negative effective index of refraction,” Optics Lett., vol. 30, pp. 2308-2310 (2005).

[24] H. –Y. Ryu, S. –H. Kwon, Y. –J. Lee, and Y. –H. Lee, “Very-low-threshold photonic band-edge lasers from free-standing triangular photonic crystal slabs,” Appl. Phys. Lett., vol. 80, pp. 3476-3478 (2002).

[25] S. –H. Kwon, H. –Y. Ryu, G. –H. Kim, Y. –H. Lee, and S. –B. Kim, “Photonic bandedge lasers in two-dimensional square-lattice photonic crystal slabs,” Appl. Phys. Lett., vol. 83, pp. 3870-3872 (2003).

[26] D. N. Chigrin, S. Enoch, C. M. Sotomayor Torres, and G. Tayeb, “Self-guiding in two-dimensional photonic crystals,” Opt. Express, vol. 11, pp. 1203-1211 (2003).

[27] D. N. Chigrin, S. Enoch, C. M. Sotomayor Torres, and G. Tayeb, “Self-guiding in two-dimensional photonic crystals,” Proc. SPIE, vol. 4655, pp. 63-72 (2002).

[28] J. Witzens, M. Loncar, and A. Scherer, “Self-collimation in planar photonic crystals,” IEEE J. Select. Topics Quant. Electron., vol. 8, pp. 1246-1257 (2002).

[29] J. Shin and S. Fan, “Conditions for self-collimation in three-dimensional photonic crystals,” Opt. Lett., vol. 30, pp. 2397-2399 (2005).

[30] M. Qiu, L. Thylén, M. Swillo, and B. Jaskorzynska, “Wave propagation through a photonic crystal in a negative phase refractive-index region,” IEEE J. Select. Topics Quant. Electron., vol. 9, pp. 106-110 (2003).

[31] B. Momeni and A. Adibi, “An approximate effective index model for efficient analysis and control of beam propagation effects in photonic crystals,” J. Lightwave Technol., vol. 23, pp. 1522-1532 (2005).

[32] A. V. Andreev, A. V. Balakin, I. A. Ozheredov, and A. P. Shkurinov P. Masselin, G. Mouret, and D. Boucher, “Compression of femtosecond laser pulses in thin one-dimensional photonic crystals”, Phys. Rev. E, vol. 63, pp. 016602-1-9 (2000).

[33] K. Hosomi and T. Katsuyama, “A dispersion compensator using coupled defects in a photonic crystal,” IEEE J. Quant. Electron., vol. 38, pp. 825-829 (2002).

[34] E. Cubukcu, K. Aydin, E. Ozbay, S. Foteinopolou and C. M. Soukoulis, “Subwavelength resolution in a two-dimensional photonic-crystal-based superlens,” Phys. Rev. Lett., vol. 91, pp. 207401-1-4 (2003).

[35] H. Kosaka, T. Kawashima, A. Tomita, M. Notomi, T. Tamamura, T. Sato, and S. Kawakami, “Superprism phenomena in photonic crystals: Toward microscale lightwave circuits,” J. Lightwave Technol., vol. 17, pp. 2032-2038 (1999).

[36] H. Kosaka, T. Kawashima, A. Tomita, M. Notomi, T. Tamamura, T. Sato, and S. Kawakami, “Self-collimation phenomena in photonic crystals,” Appl. Phys. Lett., vol. 74, pp. 1212-1214 (1999).

[37] L. Wu, M. Mazilu, T. Karle, and T. F. Krauss, “Superprism phenomena in planar photonic crystals,” IEEE J. Quant. Electron., vol. 38, pp. 915-918 (2002).

[38] K. B. Chung and S. W. Hong, “Wavelength demultiplexers based on the superprism phenomena in photonic crystals,” Appl. Phys. Lett., vol. 81, pp. 1549-1551 (2002).

[39] H. Kosaka, T. Kawashima, A. Tomita, M. Notomi, T. Tamamura, T. Sato, and S. Kawakami, “Superprism phenomena in photonic crystals,” Phys. Rev. B, vol. 58, pp. R10096-R10099 (1998).

[40] H. Kosaka, T. Kawashima, A. Tomita, M. Notomi, T. Tamamura, T. Sato, and S. Kawakami, “Photonic crystals for micro lightwave circuits using wavelength-dependent angular beam steering,” Appl. Phys. Lett., vol. 74, pp. 1370-1372 (1999).

[41] K. Oda, H. Toba, “Optical FDM-add/drop multiplexing ring network utilizing fiber Fabry Perot filters and optical circulators,” IEEE Photon. Technol. Lett., vol. 5, pp. 825-827 (1993).

[42] B. E. Little, S. T. Chu, H. A. Haus, J. Foresi, and J.-P. Laine, “Microring resonator channel dropping filters,” J. Lightwave Technol., vol. 19, pp. 998-1005 (1997).

[43] C. –W. Kuo, C. –F. Chang, M. –H. Chen, S. –Y. Chen, and Y. –D. Wu, “A new approach of planar multi-channel wavelength division multiplexing system using asymmetric super-cell photonic crystal structures,” Opt. Express, vol. 15, pp. 198-206 (2007).

[44] A. Sharkawy, S. Shi, and D. W. Pratrher, “Multichannel wavelength division multiplexing with photonic crystals,” Appl. Opt., vol. 40, pp. 2247-2252 (2001).

[45] M. Koshiba, “Wavelength division multiplexing and demultiplexing with photonic crystal waveguide couplers,” J. Lightwave Technol., vol. 19, pp. 1970-1975 (2001).

[46] P. C. Clemens, G. Heise, R. Marz, H. Michel, A. Reichelt, and H. W. Schneider, “8-Channel Optical Demultiplexer Realized as $SiO_2$/Si Flat-Field Spectrograph,” IEEE Photon. Technol. Lett., vol. 6, pp. 1109-1111 (1994).

[47] M. Fallahi, K. A. McGreer, A. Delage, R. Normandin, I. M. Templeton, R. Barber, F. Chatenoud and G. Champion, “Demonstration of grating demultiplexer in GaAs/AlGaAs suitable for integration,” Electron. Lett., vol. 28, pp. 2217-2218 (1992).

[48] J. –J. He, B. Lamontagne, A. Delage, L. Erickson, M. Davies, and E. S. Koteles, “Monolithic integrated wavelength demultiplexer based on a waveguide Rowland circle grating in InGaAsP/InP,” J. Lightwave Technol., vol. 16, pp. 631-638 (1998).

[49] S. Janz, A. Balakrishnan, S. Charbonneau, P. Cheben, M. Cloutier, A. Delage, K. Dossou, L. Erickson, M. Gao, P. A. Krug, B. Lamontagne, M. Packirisamy, M. Pearson, and D.-X. Xu “Planar waveguide Echelle gratings in Silica-On-Silicon,” IEEE Photon. Technol. Lett., vol. 16, pp. 503-505 (2004).

[50] T. Fukazawa, F Ohno, and T Baba, “Very compact arrayed-waveguide-grating demultiplexer using Si photonic wire waveguides,” Japan. J. Appl. Phys., vol. 43, L673-L675 (2004).

[51] P. Dumon, W. Bogaerts, D. Van Thourhout, D. Taillaert, V. Wiaux, S. Beckx, J. Wouters, and R. Baets, "Wavelength-selective components in SOI photonic wires fabricated with deep UV lithography," First IEEE Int. Conf. on Group IV Photonics, pp. 28-30, 2004.

[52] Y. Barbarin, X. J. M. Leijtens, E. A. J. M. Bente, C. M. Louzao, J. R. Kooiman, and M. K. Smit, "Extremely small AWG demultiplexer fabricated on InP by using a double-etch process," IEEE Photon. Technol. Lett., vol. 16, pp. 2478-2480 (2004).

[53] D. Wang, G. Jin, Y. Yan, and M. Wu, "Design of a flat-field miniature spectrometer," Proc. SPIE, vol. 4223, pp. 27-30 (2000).

[54] M. Born and K. Huang. *Dynamical Theory of Crystal Lattices*. Oxford University Press, Oxford, 1954.

[55] D. –S. Song, S. –H. Kim, H. –G. Park, C. –K. Kim, and Y. –H. Lee, "Single-fundamental-mode photonic-crystal vertical-cavity surface-emitting lasers," Appl. Phys. Lett., vol. 80, pp. 3901-3903 (2002).

[56] R. D. Meade, A. M. Rappe, K. D. Bromme, J. D. Joannopoulos, and O. L. Alerhand, "Accurate theoretical analysis of photonic band-gap materials," Phys. Rev. B, vol. 48, pp. 8434-8437 (1993).

[57] A. Taflove, *Computational Electrodynamics. The Finite Difference Time Domain Method*. Norwood, MA: Artech House, 1995.

[58] P. R. Villeneuve, S. Fan, S. G. Johnson, and J. D. Joannopoulos, "Three-dimensional photon confinement in photonic crystals of low-dimensionality," IEE Proc. Optoelectron., vol. 145, pp. 384-390 (1998).

[59] C. Jamois, R. B. Wehrspohn, J. Schilling, F. Muller, R. Hillebrand, and W. Hergert, "Silicon-based photonic crystal slabs: two concepts," IEEE J. Quantum Electron., vol. 38, pp. 805-810 (2002).

[60] S. Fan, J. D. Joannopoulos, "Analysis of guided resonances in photonic crystal slabs," Phys. Rev. B, vol. 65, pp. 235112-1-8 (2002).

[61] M. Qiu, “Band gap effects in asymmetric photonic crystal slabs,” Phys. Rev. B, vol. 66, pp. 033103-1-4 (2002).

[62] N. Kawai and K. Inoue, N. Carlsson, N. Ikeda, Y. Sugimoto, and K. Asakawa, and T. Takemori, “Confined band gap in an air-bridge type of two-dimensional AlGaAs photonic crystal,” Phys. Rev. Lett., vol. 86, pp. 2289-2292 (2001).

[63] N. Carlsson, N. Ikeda, Y. Sugimoto, K. Asakawa, T. Takemori, Y. Katayama, N. Kawai, and K. Inoue, “Design, nano-fabrication and analysis of near-infrared 2D photonic crystal air-bridge structures,” Opt. Quantum Electron., vol. 34, pp. 123-131 (2002).

[64] S. –I. Takayama, H. Kitagawa, Y. Tanaka, T. Asano, and S. Noda, “Experimental demonstration of complete photonic band gap in two-dimensional photonic crystal slabs,” Appl. Phys. Lett., vol. 87, pp. 061107-1-3 (2005).

[65] S. G. Johnson, S. Fan, P. R. Villeneuve, J. D. Joannopoulos, and L. A. Kolodziejski, “Guided modes in photonic crystal slabs,” Phys. Rev. B, vol. 60, pp. 5751-5758 (1999).

[66] T. F. Krauss, R. M. De La Rue, and S. Brand, “Two-dimensional photonic-bandgap structures operating at near infrared wavelengths,” Nature, vol. 383, pp. 699-702 (1999).

[67] H. Benisty, C. Weisbuch, D. Labilloy, M. Rattier, C. J. M. Smith, T. F. Krauss, R. M. De La Rue, R. Houdre, U. Oesterle, C. Jouanin, and D. Cassagne, “Optical and confinement properties of two-dimensional photonic crystals,” J. Lightwave. Technol., vol. 17, pp. 2063-2077 (1999).

[68] E. Chow, S. Y. Lin, S. G. Johnson, P. R. Villeneuve, J. D. Joannopoulos, J. R. Wendt, G. A. Vawter, W. Zubrzycki, H. Hou, and A. Alleman, “Three-dimensional control of light in a two-dimensional photonic crystal slab,” Nature, vol. 407, pp. 983-986 (2000).

[69] A. R. McGurna, P. Bhattacharya, J. Sabarinathan, W. –D. Zhoub, P. –C. Yu, “Photonic crystal slabs,” Physica B, vol. 338, pp. 178-181 (2003).

[70] P. Paddon and J. F. Young, “Two-dimensional vector-coupled-mode theory for textured planar waveguides,” Phys. Rev. B, vol. 61, pp. 2090-2101 (2000).

[71] K. Sakoda, *Optical Properties of Photonic Crystals*, Berlin: Springer, 2001.

[72] R. Trebino, *Frequency-Resolved Optical Gating: The Measurement of Ultrashort Laser Pulses*, Kluwer Academic Publishers, Chapter 2, 2000.

[73] M. Notomi, "Theory of light propagation in strongly modulated photonic crystals: refractionlike behavior in the vicinity of the photonic band gap," Phys. Rev. B, vol. 62, pp. 10696-10705 (2000).

[74] P. Lalanne, "Effective medium theory applied to photonic crystals composed of cubic or square cylinders," Appl. Opt., vol. 35, pp. 5369-5380 (1996).

[75] J. Witzens and A. Scherer, "Efficient excitation of self-collimated beams and single Bloch modes in planar photonic crystals," J. Opt. Soc. Am. A, vol. 20, pp. 935-940 (2003).

[76] M. Augustin, R. Iliew, C. Ettrich, D. Schelle, H. –J. Fuchs, U. Peschel, S. Nolte, E. –B. Kley, F. Lederer, and A. Tunnermann, "Self-guiding of infrared and visible light in photonic crystal slabs," Appl. Phys. B, vol. 81, pp. 313-319 (2005).

[77] X. Yu and S. Fan, "Anomalous reflections at photonic crystal surfaces," Phys. Rev. E, vol. 70, pp. 055601-1-4 (2004).

[78] X. Yu and S. Fan, "Bends and splitters for self-collimated beams in photonic crystals," Appl. Phys. Lett., vol. 83, pp. 3251-3253 (2003).

[79] T. Yamashita and C. J. Summers, "Evaluation of self-collimated beams in photonic crystals for optical interconnect," IEEE J. Select. Areas Commun., vol. 23, pp. 1341-1347 (2005).

[80] B. Momeni, J. Huang, M. Soltani, M. Askari, S. Mohammadi, M. Rakhshandehroo and A. Adibi, "Compact wavelength demultiplexing using focusing negative index photonic crystal superprisms," Opt. Express, vol. 14, pp. 2413-2422 (2006).

[81] N. K. Berger and B. Fischer, "Compensation of spatial dispersion for periodic optical patterns using a quasi-periodic multilayer," International Quantum Electronics Conference (IQEC), pp. 728-729, 2004.

[82] M. Qiu, L. Thylen, M. Swillo, and B. Jaskorzynska, “Wave propagation through a photonic crystal in a negative phase refractive-index region,” IEEE J. Select. Topic. Quantum. Electron., vol. 9, pp. 106-110 (2003).

[83] T. Matsumoto, K. –S. Eom, and T. Baba “Focusing of light by negative refraction in a photonic crystal slab superlens on silicon-on-insulator substrate,” Opt. Lett., vol. 31, pp. 2786-2788 (2006).

[84] C. Luo, S. G. Johnson, J. D. Joannopoulos, and J. B. Pendry, “Subwavelength imaging in photonic crystals,” Phys. Rev. B, vol. 68, pp. 45115-1-15 (2003).

[85] B. Gralak, S. Enoch, and G. Tayeb, “Anomalous refractive properties of photonic crystals,” J. Opt. Soc. Am. A, vol. 17, pp. 1012-1020 (2000).

[86] T. Baba and T. Matsumoto, “Resolution of photonic crystal superprism,” Appl. Phys. Lett., vol. 81, pp. 2325-2327 (2002).

[87] B. Momeni and A. Adibi, “Optimization of photonic crystal demultiplexers based on the superprism effect,” Appl. Phys. B, vol. 77, pp. 555-560 (2003).

[88] L. Wu, M. Mazilu, J. –F. Gallet, and T. F. Krauss, “Square lattice photonic-crystal collimator,” Photon. Nanostruct. Fund. Applic., vol. 1, pp. 31-36 (2003).

[89] A. Lupu, E. Cassan, S. Laval, L. El Melhaoui, P. Lyan, and J. M. Fedeli, “Experimental evidence for superprism phenomena in SOI photonic crystals,” Opt. Express, vol. 12, pp. 5690-5696 (2004).

[90] J. Witzens, T. Baehr-Jones, and A. Scherer, “Hybrid superprism with low insertion losses and suppressed cross-talk,” Phys. Rev. E, vol. 71, pp. 026604-1-9 (2005).

[91] B. Momeni and A. Adibi, “Preconditioned superprism-based photonic crystal demultiplexers: analysis and design,” Appl. Opt., vol. 45, pp. 8466-8476 (2006).

[92] T. Matsumoto, S. Fujita and T. Baba, “Wavelength demultiplexer consisting of photonic crystal superprism and superlens,” Opt. Express, vol. 13, pp. 10768-10776 (2005).

[93] B. E. Nelson, M. Gerken, D. A. B. Miller, R. Piestun, C. C. Lin, and J. S. Harris Jr., “Use of a dielectric stack as a one-dimensional photonic crystal for wavelength demultiplexing by beam shifting,” Opt. Lett., vol. 25, pp. 1502-1504 (2000).

[94] M. Gerken and D. A. B. Miller, “Multilayer thin-film structures with high spatial dispersion,” Appl. Opt., vol. 42, pp. 1330-1345 (2003).

[95] C. Luo, M. Soljacic, and J. D. Joannopoulos, “Superprism effect based on phase velocities,” Opt. Lett., vol. 29, pp. 745-747 (2004).

[96] T. Matsumoto and T. Baba, “Photonic crystal k-vector superprism,” J. Lightwave Technol., vol. 22, pp. 917-922 (2004).

[97] A. Bakhtazad, A. G. Kirk, “1-D slab photonic crystal k-vector superprism demultiplexer: analysis, and design,” Opt. Express, vol. 13, pp. 5472-5482 (2005).

[98] M. Koshiba, Y. Tsuji, and M. Hikari, “Time-domain beam propagation method and its application to photonic crystal circuits,” J. Lightwave Technol., vol. 18, pp. 102–110, Jan. 2000.

[99] G. Tayeb and D. Maystre, “Rigorous theoretical study of finite-size two dimensional photonic crystals doped by microcavities,” J. Opt. Soc. Am. A, vol. 14, pp. 3323–3332, Dec. 1997.

[100] S. Boscolo and M. Midrio, “A fast algorithm for the simulation of propagation in large-area 2-D photonic crystal devices,” J. Lightwave Technol., vol. 20, pp. 1869-1875 (2002).

[101] S. –Y. Lin, V. M. Hietala, L. Wang, and E. D. Jones, “Highly dispersive photonic band-gap prism,” Opt. Lett., vol. 21, pp. 1771-1773 (1996).

[102] A. S. Jugessur, A. Bakhtazad, A. G. Kirk, L. Wu, T. F. Krauss, and R. M. De La Rue, “Compact and integrated 2-D photonic crystal super-prism filter-device for wavelength demultiplexing applications,” Opt. Express, vol. 14, pp. 1632-1642 (2006).

[103] B. Momeni and A. Adibi, “Systematic design of superprism-based photonic crystal demultiplexers,” IEEE J. Select. Areas Communic., vol. 23, pp. 1355-1364 (2005).

[104] J. Huang, C. M. Reinke, A. Jafarpour, B. Momeni, M. Soltani and A. Adibi, “Observation of large parity-change-induced dispersion in triangular-lattice photonic crystal waveguides using phase sensitive techniques,” Appl. Phys. Lett., vol. 88, pp. 071111-1-3 (2006).

[105] M. Qiu, “Effective index method for heterostructure-slab-waveguide-based two-dimensional photonic crystals,” Appl. Phys. Lett., vol. 81, pp. 1163-1165 (2002).

[106] J. Witzens, M. Hochberg, T. Baehr-Jones, and A. Scherer, “Mode matching interface for efficient coupling of light into planar photonic crystals,” Phys. Rev. E, vol. 69, pp. 046609-1-9 (2004).

[107] T. Baba, and D. Ohsaki, “Interfaces of photonic crystals for high efficiency light transmission,” Japan. J. Appl. Phys., vol. 40(1), pp. 5920-5924 (2001).

[108] P. Rabiei and A. F. J. Levi, “Efficient optical coupling to Bloch waves,” CLEO '01, pp. 590-591, 2001.

[109] S. Kuchinsky, V. Golyatin, and A. Kutikov, “Coupling in PBG material with high group index,” Proc. SPIE, vol. 5000, pp. 59-70 (2003).

[110] M. V. Berry and K. E. Mount, “Semiclassical approximations in wave mechanics,” Rep. Prog. Phys., vol. 35, pp. 315-397 (1972).

[111] K. Sakoda, M. Sasada, T. Fukushima, A. Yamanaka, N. Kawai, and K. Inoue, “Detailed analysis of transmission spectra and Bragg-reflection spectra of a two-dimensional photonic crystal with a lattice constant of 1.15 μm,” J. Opt. Soc. Am. B, vol. 16, pp. 361-365 (1999).

[112] R. Biswas, Z. Y. Li, and K. M. Ho, “Impedance of photonic crystals and photonic crystal waveguides,” Appl. Phys. Lett., vol. 84, pp. 1252-1254 (2004).

[113] B. Momeni, A. A. Eftekhar, and A. Adibi, “Effective impedance model for analysis of reflection at the interfaces of photonic crystals,” Opt. Lett., vol. 32, pp. 778-780 (2007).

[114] B. Momeni, E. Shah Hosseini, M. Askari, S. Mohammadi, M. Soltani, and A. Adibi, "Compact photonic crystal demultiplexers and spectrometers," Proc. SPIE, vol. 6480, pp. 648012-1-12 (2007).

[115] S. Y. Lin, J. G. Fleming, D. L. Hetherington, B. K. Smith, R. Biswas, K. M. Ho, M. M. Sigalas, W. Zubrzycki, S. R. Kurtz, and J. Bur, "A three-dimensional photonic crystal operating at infrared wavelengths," Nature, vol. 394, pp. 251-253 (1998).

[116] M. Deubel, G. von Freymann, M. Wegener, S. Pereira, K. Busch, C. M. Soukoulis, "Direct laser writing of three-dimensional photonic-crystal templates for telecommunications," Nature Materials, vol. 3, pp. 444-447 (2004).

[117] R. Guo, Z. Li, Z. Jiang, D. Yuan, W. Huang, and A. Xia, "Log-pile photonic crystal fabricated by two-photon photopolymerization," J. Opt. A: Pure Appl. Opt., vol. 7, pp. 396-399 (2005).

[118] M. Deubel, M. Wegener, S. Linden, G. von Freymann, and S. John, "3D-2D-3D photonic crystal heterostructures fabricated by direct laser writing," Opt. Lett., vol. 31, pp. 805-807 (2006).

[119] Y. C. Zhong, S. A. Zhu, H. M. Su, and H. Z. Wang, J. M. Chen, Z. H. Zeng and Y. L. Chen, "Photonic crystal with diamondlike structure fabricated by holographic lithography," Appl. Phys. Lett., vol. 87, pp. 061103-1-3 (2005).

[120] J. H. Moon, J. Ford, and S. Yang, "Fabricating three-dimensional polymeric photonic structures by multi-beam interference lithography," Polymers Adv. Technol., vol. 17, pp. 83-93 (2006).

[121] J. H. Moon, S. Yang; S. –M. Yang, "Photonic band-gap structures of core-shell simple cubic crystals from holographic lithography," Appl. Phys. Lett., vol. 88, pp. 121101-1-3 (2006).

[122] J. Shin and S. Fan, "Conditions for self-collimation in three-dimensional photonic crystals," Opt. Lett., vol. 30, pp. 2397-2399 (2005).

[123] J. Mizuguchi, Y. Tanaka, S. Tamura, and M. Notomi, "Focusing of light in a three-dimensional cubic photonic crystal," Phys. Rev. B, vol. 67, pp. 75109-1-7 (2003).

[124] M. Badieirostami, B. Momeni, and A. Adibi, “Polarization state for modes of low contrast three-dimensional photonic crystal structures,” in preparation.

[125] J. J. Stoker, *Differential Geometry*, New York: John Wiley & Sons Inc., 1969, Chapter 4.

[126] B. Momeni and A. Adibi, “Adiabatic matching stage for coupling of light to extended Bloch modes of photonic crystals,” Appl. Phys. Lett., vol. 87, pp. 171104-171106 (2005).

[127] J. T. Veredeyen, *Laser Electronics*, Prentice Hall, Chapter 3, 1995.

[128] S. Shi, A. Sharkawy, C. Chen, D. M. Pustai, and D. W. Prather, “Dispersion-based beam splitter in photonic crystals,” Opt. Lett., vol. 29, pp. 617-619 (2004).

[129] M. G. Moharam, D. A. Pommet, E. B. Grann, and T. K. Gaylord, "Stable implementation of the rigorous coupled-wave analysis for surface-relief gratings: enhanced transmittance matrix approach," J. Opt. Soc. Am. A, vol. 12, pp. 1077-1086 (1995).

# VITA

## BABAK MOMENI

Momeni was born in Tehran, Iran. He received a B.Sc. and M.Sc. both in Electrical Engineering from Sharif University of Technology, Tehran, Iran in 1999 and 2001, respectively, before coming to Georgia Tech to pursue a doctorate in Electrical Engineering with specialization in Optics and Photonics. He has also received a Masters in Physics from Georgia Tech in 2007. When he is not working on his research, Mr. Momeni enjoys reading, running, listening to music, and playing soccer with friends.